ORSAY LAL 10-28
N° D'ORDRE : 9798 Mars 2010

UNIVERSITE PARIS XI
UFR SCIENTIFIQUE D'ORSAY

THESE

Présentée

Pour obtenir

Le GRADE de DOCTEUR EN SCIENCES

DE L'UNIVERSITE PARIS XI ORSAY

par

Trong Hieu TRAN

Sujet : Mesures de précision de la section efficace des processus courant chargé et courant neutre à grand Q^2 à HERA avec le faisceau d'électrons polarisés

Soutenue le **26 Mars 2010** devant la Commission d'examen

M.	Guy	**WORMSER**	Président
M.	Bertrand	**LAFORGE**	Rapporteur
Mme.	Emi	**KOU**	Rapporteur
M.	Cristinel	**DIACONU**	Examinateur
M.	Zhiqing	**ZHANG**	Directeur

Pour ma famille
et mes proches

Contents

Introduction

The physics of scattering started in 1909 by the highlighting Rutherford experiment [1] in which α particles from a radioactive source were allowed to strike a thin gold foil and were found at large deflection angles and some even found to be back-scattered. The only way that Rutherford could explain this was to consider the atom as having a very small nucleus containing the positive charge with the electrons orbiting around it. The nucleus contains of relatively high central charge concentrated into a very small volume in comparison to the rest of the atom and containing the bulk of the atomic mass. The incoming positively charged alpha particles would be repelled by a large electrostatic (Coulomb) force due to the positive nucleus, and give large scattering angles. It was Rutherford himself in 1919 who discovered that the nucleus contains positive charge in discrete units which he called protons by the scattering of α particles but off nitrogen gas. Later on, Rutherford surmised that the nucleus must contain a neutral particle in order to account the mass of the atom. The main evidence for the neutron came from an experiment by James Chadwick in 1932 ([2, 3]). A more detailed examination of the nucleus structure needs particles of higher energies which can be produced by particle accelerators. The era of accelerator physics began in the 1950s, when Robert Hofstadter and colleagues [4] studied the scattering of electron on large nucleus. It was revealed that the high energy electron can scatter from the proton within the nucleus.

A question arised: do nucleons have their own inside structures? To answer this question, much higher energy particles which do not strongly interact with the nucleon should be used for the probing of their structure. Many experiments used neutrinos or muons to enter the nucleons. However, the electron is proven to be the best candidate as it is small, penetrating, easily produced and accelerated.

The direct evidence of the existence of quarks is provided by the Deep Inelastic Scattering. The electron is accelerated to very high energies and thus can probe the proton since the associated wavelength implies that it can collide with individual constituents which are small compared to the proton.

The first electron-proton scattering was realized at SLAC in 1967 [5] and provided first comparison of the proton form factor to the theoretical models. Later experiments ([6, 7])

showed that the proton was not an extended object with uniform charged density but an object made of point-like charged particles. Feynman explained the results with a model where the proton was built up of point-like particles and antiparticles, named partons. These partons were later identified as the quarks, introduced several years before by Gell-Mann explaining the increasing number of particles found in particle beam experiments [8]. In 1969, Richard Feynman introduced the Quark Parton Model [9] which allows deep inelastic scattering to be seen as the incoherent sum of point-like elastic scattering of spin-$\frac{1}{2}$ nucleon constituents. However, the quarks have never been observed as free particles and this among other things was incorporated in the gauge theory of strong interactons, quantum chromodynamics: the mediators of the strong force are the gluons. This explains why in the deep inelastic scattering only half of the momentum of the proton was carried by the charged quarks.

Besides the electromagnetic and strong interactions, particles can also interact among each other via the weak interaction. In 1930 Wolfgang Pauli proposed a yet unobserved particle to explain the continuous distribution of the energy of the emitted electrons in a β decay. In 1932, Enrico Fermi called this particle a neutrino and developed a theory of β decay in which the neutrino carried away the missing energy and momentum [10]; β decay can be seen as the decay of one of the neutron to a proton via the weak interaction.

Although electromagnetism and weak forces appear very different at low energies, theory models them as two different aspects of the same force. Above an energy threshold, they could merge into a single electroweak force. The unification of the electroweak force was firstly contributed by Abdus Salam, Sheldon Glashow and Steven Weinberg ([11, 12]). The evidence of electroweak interaction was experimentally established in two stages: the first being the discovery of Neutral Current in neutrino scattering by the Gargamelle collaboration in 1973 [13, 14], and the second in 1983 by the UA1 and the UA2 collaborations [15, 16] that involved the discovery of the W and Z gauge bosons in proton-antiproton collisions at the converted Super Proton Synchrotron (SPS, [17]).

A facility which allows at the same time to probe the proton structure and to explore the electroweak interaction was HERA [18]. HERA used electron-proton scattering at a center of mass energy of 319 GeV, equivalent to a fixed-target experiment with a lepton energy of 50 TeV. The large kinematic domain providing an increase by two orders of magnitude in resolving power used to measure the valance quark, sea quark and gluon densities within the proton not only in Q^2, the four-momentum transfer squared, but also in x, the momentum fraction carried by the struck parton. HERA became operational in 1992 and ended in July 2007 with the integrated luminosity of $\sim 1\text{fb}^{-1}$ delivered by both H1 [19] and ZEUS [20] detectors. The highest reachable Q^2 value of 40000 GeV^2 corresponds to a distance of 10^{-16} cm, which is a factor 1000 smaller than the proton

radius. With this revolving power as well as the polarization of the electron beam, exciting physics topics can be studied such as substructure of quarks and electrons, Charged and Neutral Currents, tests of Quantum Chromodynamics, searches for new currents and for new particles.

This thesis concerns the measurement of inclusive cross section of the charged and neutral current processes of the electron-proton Deep Inelastic Scattering where the electron is polarized. The organization is as follows. The first chapter will be devoted to a theoretical introduction to Deep Inelastic Scattering. The HERA facility and the H1 experiment setups are described in chapter 2. Some aspects of the event and kinematics reconstructions used by the H1 collaboration as well as the simulation programs will be presented in chapters 3 and 4. The procedures for the measurement of Charged and Neutral Current cross sections will be described in chapters 5 and 6 with the event selections, correction methods and the cross section measurement results. In chapter 7 one will find that the combined data of HERA analyzed by H1 collaboration with highest luminosity can give a precise estimation for different aspects of the Standard Model.

Chapter 1

Theoretical framework

Contents

This chapter is devoted to the discussion on the theoretical basis of the deep inelastic scattering; namely, we introduce the DIS kinematics. The cross sections and their relation to the structure functions of the proton are shown. Furthermore, the radiative corrections will be discussed and a brief overview of the induced background processes in ep scattering will also be presented.

1.1 Deep Inelastic Scattering and structure functions

Deep Inelastic Scattering (DIS) is the name given to a process used to probe the inside of hadrons (particularly the baryons, such as protons and neutrons), using point-like beams such as electrons, muons and neutrinos. It provided first convincing evidence of the existence of the quarks. The idea is that at high energies, the wavelengths associated with the electron are much smaller than the size of a proton. Hence the electrons can probe distances that are small compared to the proton, i.e. deep within the proton. The high energies tend to disrupt the proton, so that it produces other particles (hadrons). This means the scattering is inelastic because the target has been disassociated in the process.

At HERA, the DIS is realized by the interaction of electrons (positrons) with protons via exchange of gauge bosons. According to the type of exchanged bosons, the DIS processes are classified into two sorts:

- Neutral Current process (NC DIS), $ep \to eX$: mediated by the exchange of neutral gauge bosons (photon or Z^0 boson). The final state is formed by the scattered electron and hadrons,

- Charged Current process (CC DIS), $ep \to \nu_e X$: the exchanged boson is W^+ or W^-. The characteristic of this process is the production of a neutrino (which is not directly detected) instead of the scattered electron.

The schematic diagram for the NC DIS process is shown in figure 1.1 where k and k' stand for the four-momenta vectors of the initial electron (positron) and the final electron, P is the four-momenta vector of the incoming proton. The kinematics of the inclusive[1] DIS processes at a given proton-electron center-of-mass energy squared, $s = (k + P)^2$ is determined by two independent Lorentz invariant variables, which could be any of the

[1] A DIS reaction is called inclusive when the hadrons produced in the final state X are not differentiated.

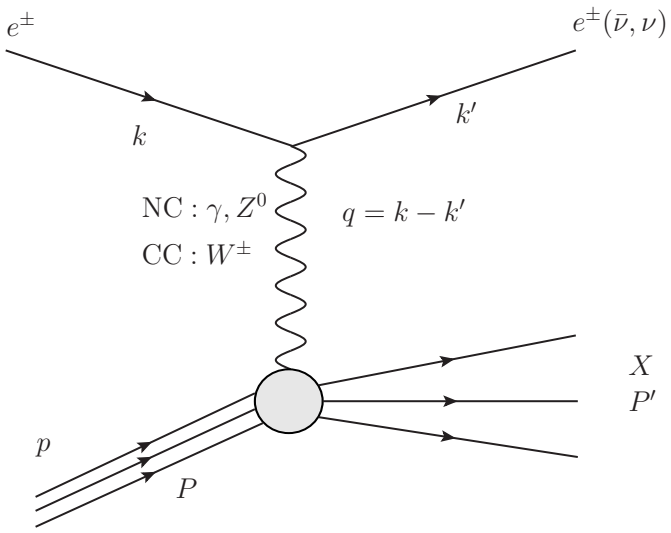

Figure 1.1: Schematic diagram for Deep Inelastic Scattering. Quantities k and k' are the four-momenta of the incoming and outgoing leptons, P is the four-momentum of a nucleon. The 'circle' at the proton vertex indicates our ignorance of the detailed structure: X indicates a sum over all the possible hadronic final states.

following:

$$Q^2 = -q^2 = (k - k')^2, \qquad Q^2 \in [0, s] \tag{1.1}$$

$$x = \frac{Q^2}{2P \cdot q}, \qquad x \in [0, 1] \tag{1.2}$$

$$y = \frac{q \cdot P}{k \cdot P}, \qquad y \in [0, 1] \tag{1.3}$$

$$W^2 = (q + P)^2, \qquad W^2 \in [M_p^2, s], \tag{1.4}$$

$$\nu = \frac{p \cdot P}{M} \tag{1.5}$$

The square of the four-momentum transfer (the invariant mass of the exchanged vector boson), $q^2 < 0$, is space-like and determines the hardness of the interaction, or in other words, the resolving power of the interaction. For the cases where $EE' \sin^2 \theta/2 \gg m_l^2 m_{l'}^2$ it can be written as:

$$Q^2 \approx 4EE' \sin^2 \theta/2 \tag{1.6}$$

where θ is the lepton's scattering angle with respect to the lepton beam direction.

The differential cross section for a DIS process can be expressed in terms of x, y, Q^2 as

$$\frac{\mathrm{d}^2\sigma^{\ell^{\pm}p}}{\mathrm{d}x\mathrm{d}y} = \frac{4\pi\alpha^2 s}{Q^4} \left[xy^2 F_1^{\ell^{\pm}p}(x, y) + (1 - y) F_2^{\ell^{\pm}p}(x, y) \right] \tag{1.7}$$

where mass terms have been ignored. By defining the longitudinal structure function as $F_L = F_2 - 2xF_1$, the cross section may also be written as

$$\frac{d^2\sigma^{\ell^\pm p}}{dxdy} = \frac{4\pi\alpha^2 s}{Q^4}\left[Y_\pm F_2(x,Q^2) - y^2 F_L(x,Q^2)\right], \tag{1.8}$$

where $Y_\pm = 1 \pm (1-y)^2$ are the helicity functions. The longitudinal structure function $F_L(x,Q^2)$ is zero in the naive quark parton model, but does contribute, in higher orders in QCD, through gluon radiation. Its contribution is significant only at high y, due to the factor y^2.

Bjorken scaling

The Bjorken scaling refers to an important feature of a large class of dimensionless physical quantities: it suggests that the observed strongly interacting particles (hadrons) behave as collections of point-like constituents when probed at high energies.

In 1969, Bjorken proposed the following scaling properties: in the limit $Q^2 \to \infty$, $W^2 \to \infty$, at fixed x. Namely at mean values, $x \sim 0.2$, the scattering, i.e. the structure function F_2, is independent of Q^2 (cf. figure 1.2), e.g. $F_i(x,Q^2) \to F(x)$. This suggests that the probing "virtual photon" scatters against something point-like. These point-like particles are referred to a "parton" by Feynman.

1.2 The quark parton model

We now proceed further with the idea that the 'partons' are quarks (and anti-quarks). In QPM, the $ep \to eX$ process can be reduced to the parton level process $eq \to eq$. The double-differential cross section of this process yields

$$\frac{\mathrm{d}^2\hat{\sigma}}{\mathrm{d}x\mathrm{d}Q^2} = \frac{4\pi\alpha^2}{Q^4}[1+(1-y)]^2\frac{1}{2}e_q^2\delta(x-\xi) \tag{1.9}$$

where ξ is the momentum fraction carried by the quark, i.e. $P_q = \xi P$ where P_q is the in-coming quark momentum. The delta function in equation (1.9) comes from the massless condition of the quark. Comparison between equations (1.7) and (1.9) may lead to $\hat{F}_2 = 2xF_1 = xe_q^2\delta(x-\xi)$. However, the experimental observation shows that the structure function is evidently a distribution in x rather than a delta function, thus the naive parton model proposes the structure function as

$$F_2(x) = 2xF_1(x) = \sum_{q,\bar{q}} e_q^2 xq(x) \tag{1.10}$$

where $q(x)$ is the probability distribution, often called parton distribution function (PDF), which is to be determined by experiments.

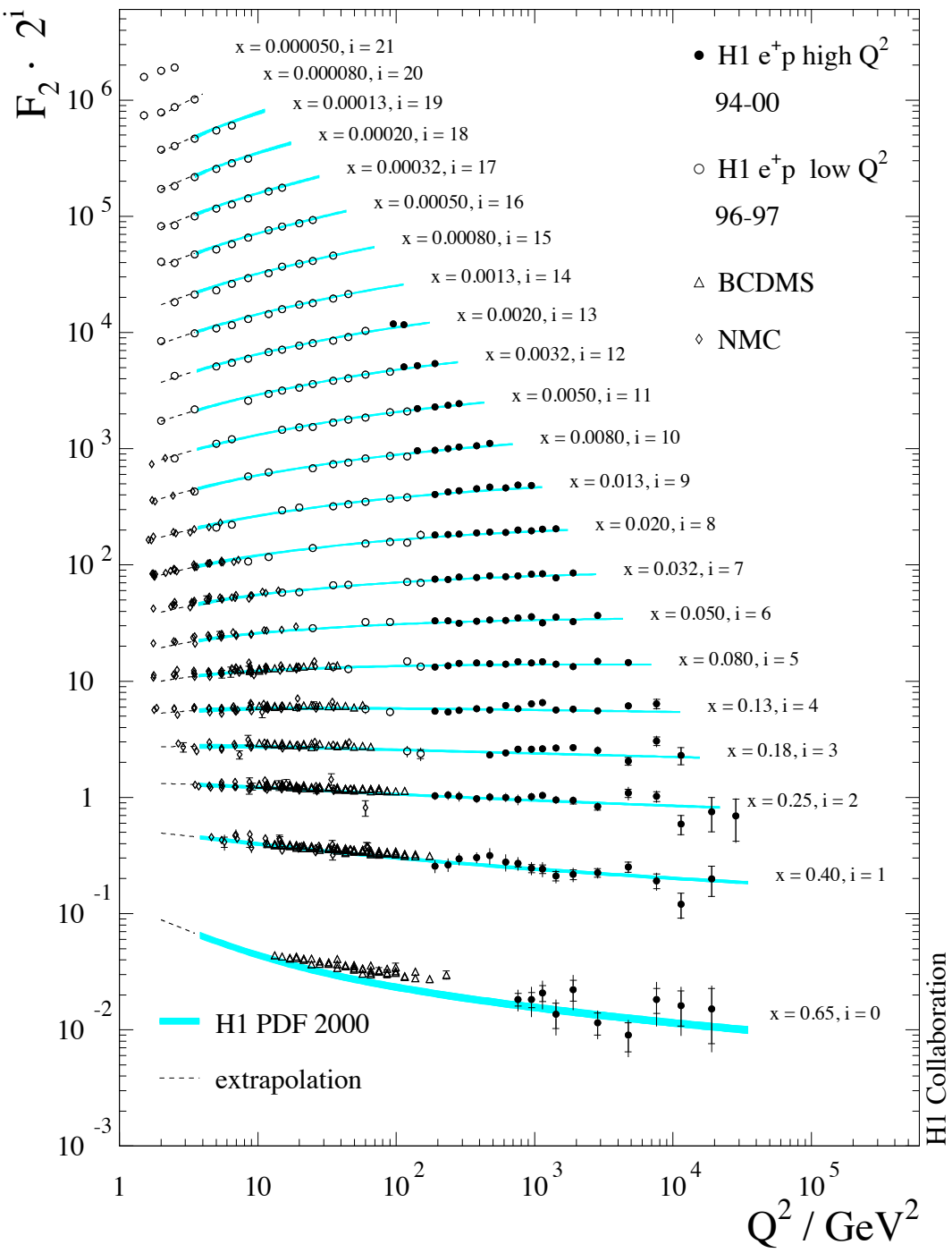

Figure 1.2: The proton structure function F_2 shown for the different HERA datasets. The measurements are compared to the corresponding Standard Model expectation determined from the H1PDF 2000 fit [21] (error bands). The dashed curves show the backward extrapolation of the fit. Also shown are the F_2 data from BCDMS [22] and NMC [23]. The inner and outer error bars represent respectively the statistical and total errors.

Sum rules

The quark distributions inside the proton must satisfy some constraints. Since the proton has strangeness zero, we have a *sum rule* (treating only u, d and s flavours)

$$\int_0^1 \mathrm{d}x[s(x) - \bar{s}(x)] = 0. \tag{1.11}$$

From the proton charge, we obtain another sum rule:

$$\int_0^1 \mathrm{d}x \left\{ \frac{2}{3}\left[u(x) - \bar{u}(x)\right] - \frac{1}{3}\left[d(x) - \bar{d}(x)\right] \right\} = 1. \tag{1.12}$$

By introducing the idea of 'valence' quarks (those of the elementary constituent of quark model) and 'sea' quarks ($q\bar{q}$ pairs created virtually) then, in a proton, the u and d quark distributions would be parameterized by the sum of the valence and the sea contributions

$$u = u_v + \bar{u} \tag{1.13}$$

$$d = d_v + \bar{d} \tag{1.14}$$

while the anti-quark and strange quark distributions are taken to be pure sea

$$\bar{u} = \bar{d} = s = \bar{s} = q_s \tag{1.15}$$

where we have assumed that the 'sea' is flavour-independent. Such a model replaces the six unknown functions now in play by three, and is consequently more predictive. We have thus the sum rules

$$\int_0^1 \mathrm{d}x\ u_v(x) = 2 \tag{1.16}$$

$$\int_0^1 \mathrm{d}x\ d_v(x) = 1 \tag{1.17}$$

which are known as *counting rules*.

Another important sum rule emerges from the picture of $xq_i(x)$ as the fractional momentum carried by quark i. This is the *momentum sum rule*

$$\int_0^1 \mathrm{d}x\ x\left[u(x) + \bar{u}(x) + d(x) + \bar{d}(x) + s(x) + \bar{s}(x)\right] = 1 - \epsilon \tag{1.18}$$

where ϵ is interpreted as the fraction of the proton momentum that is not carried by quarks. The integral in equation (1.18) is directly related to the cross sections and its evaluation implies $\epsilon \simeq \frac{1}{2}$. This gave impetus to the development of the theory of QCD (cf. section 1.4) in which the deficit in momentum is carried by the gluons.

1.3 Neutral and Charged Current cross sections with polarized electron beam

1.3.1 Polarized Neutral Current cross section

Now we introduce the weak interaction. The NC scattering of an polarized lepton with helicity λ off unpolarized proton ($e^{\pm}_{\lambda}p \to e^{\pm}X$) may be written as [24]

$$\left.\frac{\mathrm{d}^2\sigma^{\pm}_{\lambda}}{\mathrm{d}x\mathrm{d}Q^2}\right|_{\mathrm{NC}} = \frac{2\pi\alpha^2}{xQ^4}\lambda H^{\pm}_{\lambda}(x,Q^2), \tag{1.19}$$

with

$$\begin{aligned} H^{\pm}_{\lambda} &= Y_+\tilde{F}^{\pm}_{2\lambda}(x,Q^2) - y^2\tilde{F}^{\pm}_{L\lambda}(x,Q^2) \mp Y_-x\tilde{F}^{\pm}_{3\lambda}(x,Q^2), & (1.20)\\ \tilde{F}^{\pm}_{2\lambda}(x,Q^2) &= \sum_i x(q_i(x)+\bar{q}_i(x))A^{\pm}_i(\lambda,Q^2), & (1.21)\\ x\tilde{F}_{3\lambda}(x,Q^2) &= \sum_i x(q_i(x)+\bar{q}_i(x))B^{\pm}_i(\lambda,Q^2). & (1.22) \end{aligned}$$

The couplings of the fermions to the currents depend on the lepton helicity λ:

$$\begin{aligned} A^{\pm}_i(\lambda,Q^2) &= \frac{1-\lambda}{2}A^{R/L}_i(Q^2) + \frac{1+\lambda}{2}A^{L/R}_i(Q^2), & (1.23)\\ B^{\pm}_i(\lambda,Q^2) &= \frac{1-\lambda}{2}B^{R/L}_i(Q^2) + \frac{1+\lambda}{2}B^{L/R}_i(Q^2), & (1.24) \end{aligned}$$

with

$$\begin{aligned} A^{L,R}_i(Q^2) &= e_i^2 - 2e_i(v_l \pm a_l)v_iP_Z + (v_l \pm a_l)^2(v_l^2+a_l^2)P_Z^2 & (1.25)\\ B^{L,R}_i(Q^2) &= \mp 2e_i(v_l \pm a_l)a_iP_Z \pm 2(v_l \pm a_l)v_ia_iP_Z^2. & (1.26) \end{aligned}$$

The vector and axial-vector couplings of the fermions are given by

$$v_f = T_{3f} - 2e_f\sin^2\theta_W, \qquad a_f = T_{3f} \tag{1.27}$$

where the definition holds for both charged leptons and quarks, T_{3f} is the third component of the weak isospin, θ_W - the Weinberg angle or weak mixing angle which is scheme dependent and is defined in the on-mass-shell scheme [25] as $\cos\theta_W = M_W/M_Z$ (M_W and M_Z are correspondingly the masses of W and Z bosons). The Z^0 propagator appears in the quantity P_Z as

$$P_Z = \frac{Q^2}{Q^2+M_Z^2}\frac{1}{\sin(2\theta_W)}. \tag{1.28}$$

The unpolarized cross section can be obtained by

$$\left.\frac{\mathrm{d}^2\sigma^{\pm}}{\mathrm{d}x\mathrm{d}Q^2}\right|_{\mathrm{NC}} = \frac{1}{2}\sum_{\lambda=\pm1}\left.\frac{\mathrm{d}^2\sigma^{\pm}_{\lambda}}{\mathrm{d}x\mathrm{d}Q^2}\right|_{\mathrm{NC}} \equiv \frac{2\pi\alpha^2}{xQ^2}H^{\pm}(x,Q^2). \tag{1.29}$$

In fact $H^{\pm}(x,Q^2)$ can be obtained by $H^{\pm}_{\lambda}(x,Q^2)\big|_{\lambda=0}$. The explicit formula for the structure function then yields

$$H^{\pm}(x,Q^2) = Y_+\tilde{F}_2^{\pm}(x,Q^2) \mp Y_- x\tilde{F}_3^{\pm}(x,Q^2) \tag{1.30}$$

where

$$\begin{aligned} \tilde{F}_2^{\pm}(x,Q^2) &= F_2^{\gamma}(x) - v_l P_Z F_2^{\gamma Z}(x) + (v_l^2+a_l^2)P_Z^2 F_2^Z(x) & (1.31)\\ x\tilde{F}_3^{\pm}(x,Q^2) &= -a_l P_Z x F_3^{\gamma Z}(x) + 2a_l v_l P_Z^2 x F_3^Z(x) & (1.32)\end{aligned}$$

with F_2, $F_2^{\gamma Z}$ and F_2^Z related to the sum of the quark and anti-quark densities

$$\Big[F_2(x),\ F_2^{\gamma Z}(x),\ F_2^Z(x)\Big] = \sum_i [e_i^2, 2e_i v_i, v_i^2+a_i^2]x[q_i(x)+\bar{q}_i(x)] \tag{1.33}$$

standing for contributions respectively from pure photon exchange, γZ^0 interference and pure Z^0 exchange. The term $xF_3^{\gamma Z}$ and xF_3^Z

$$\Big[xF_3^{\gamma Z}(x), xF_3^Z(x)\Big] = \sum_i [2e_i a_i, 2v_i a_2]x[q_i(x)-\bar{q}_i(x)] \tag{1.34}$$

have the similar meanings. The dominant correction to $\tilde{F}_2^{\pm}(x,Q^2)$ arises from the Z^0 exchange term (the F_2^Z term in equation (1.31)) since v_l is small with respect to a_l.

Reduced Neutral Current cross section

In our results, we often use the so-called "reduced cross section" which is defined as

$$\tilde{\sigma}^{\pm}_{\mathrm{NC}} = \frac{1}{Y_+}\frac{Q^4 x}{2\pi\alpha^2}\left.\frac{\mathrm{d}^2\sigma^{\pm}}{\mathrm{d}x\mathrm{d}Q^2}\right|_{\mathrm{NC}}. \tag{1.35}$$

1.3.2 Polarized Charged Current cross section

The double differential Charged Current cross section for collisions of polarized electron (positron) with unpolarized protons may be expressed as

$$\left.\frac{\mathrm{d}^2\sigma^{\pm}_{\lambda}}{\mathrm{d}x\mathrm{d}Q^2}\right|_{\mathrm{CC}} = (1+\lambda)\frac{G_F^2}{4\pi x}\left[\frac{M_W^2}{M_W^2+Q^2}\right]^2 (Y_+F_2^{\mathrm{CC}} \mp Y_- xF_3^{\mathrm{CC}}), \tag{1.36}$$

where x is the Bjorken variable and y characterizes the inelasticity of the interaction, F_2^{CC} and xF_3^{CC} the charged current structure functions.

The structure functions for charged current processes with left-handed polarization are defined as

$$\begin{aligned} F_2^{\mathrm{CC}} = 2xF_1^{\mathrm{CC}} &= 2x[u(x)+c(x)+\bar{d}(x)+\bar{s}(x)] & (1.37)\\ xF_3^{\mathrm{CC}} &= 2x[u(x)+c(x)-\bar{d}(x)-\bar{s}(x)] & (1.38)\end{aligned}$$

and $F_2^{\mathrm{CC}} = 2xF_1^{\mathrm{CC}} = F_3^{\mathrm{CC}} = 0$ for $e^- p \to \nu_e X$ with right-handed polarization.

The unpolarized cross section reads

$$\left.\frac{\mathrm{d}^2\sigma^{\pm}}{\mathrm{d}x\mathrm{d}Q^2}\right|_{\mathrm{CC}} = \frac{1}{2}\sum_{\lambda=\pm 1}\left.\frac{\mathrm{d}^2\sigma^{\pm}_{\lambda}}{\mathrm{d}x\mathrm{d}Q^2}\right|_{\mathrm{CC}} \tag{1.39}$$

Reduced Charged Current cross section

Similarly to the reduced neutral current cross section, the reduced charged current cross section can be defined as

$$\tilde{\sigma}^{\pm}_{\mathrm{CC}} \equiv \frac{2\pi x}{G_F^2}\left(\frac{M_W^2 + Q^2}{M_W^2}\right)^2 \left.\frac{\mathrm{d}^2\sigma^{\pm}}{\mathrm{d}x\mathrm{d}Q^2}\right|_{\mathrm{CC}}. \tag{1.40}$$

1.4 Quantum Chromodynamics (QCD)

Quantum Chromodynamics is a modern field theory which describes strong interactions with the exchange of colored gluons between quarks inside the proton. In the QCD, quarks and gluons can interact to make up hadrons.

The two peculiar properties of the QCD are:

- Asymptotic freedom, which means that in very high-energy reactions, quarks and gluons interact very weakly. This prediction of QCD was first discovered in the early 1970s by David Politzer, Frank Wilczek and David Gross [26, 27].
- Confinement, which means that the force between quarks does not diminish as they are separated [28]. Because of this, it would take an infinite amount of energy to separate two quarks; they are bound into color-neutral hadrons such as the proton and the neutron.

1.4.1 Running coupling constant

These phenomena can be well explained by the scale dependence of the strong couping constant α_s. The scale dependence is governed by the so-called remormalization group equation [29]

$$\beta(\alpha_s) = \mu\frac{\partial\alpha_s(\mu)}{\partial\mu} \tag{1.41}$$

where $\beta(\alpha_s)$ is called β-function, α_s is the coupling parameter and μ is the energy scale. The β-function is calculable in QCD:

$$\beta(\alpha_s) = -\beta_0\frac{\alpha_s^2}{4\pi} - \beta_1\frac{\alpha_s^3}{16\pi^2} + \ldots \tag{1.42}$$

with

$$\beta_0 = (33 - 2n_f)/3, \quad \beta_1 = 102 - \frac{38}{3}n_f, \tag{1.43}$$

where β_0 and β_1 are the first coefficients occuring in the perturbative expansion in α_s and n_f denoting the number of active flavors, i.e. the quark flavors with masses smaller than μ.

For example in the one-loop approximation, i.e. regarding only the term with β_0 the solution to the equation 1.41 leads to the renormalization scale dependence on the coupling constant α_s

$$\alpha_s(\mu^2) = \frac{\alpha_s(\mu_0^2)}{1 + b \cdot \alpha_s(\mu_0^2) \ln(\mu^2/\mu_0^2)} \tag{1.44}$$

where $b = \beta_0/4\pi$ and μ_0^2 being suitably chosen reference scale. This equation shows one behavior of the coupling constant α_s which is called "running". The solution to the equation 1.41 including the 3-loop corrections is known [29]. An example is presented in figure 1.3. One can see that the coupling constant decreases as the scale increases (asymptotic freedom) which is the consequence of the negative sign in equation (1.42).

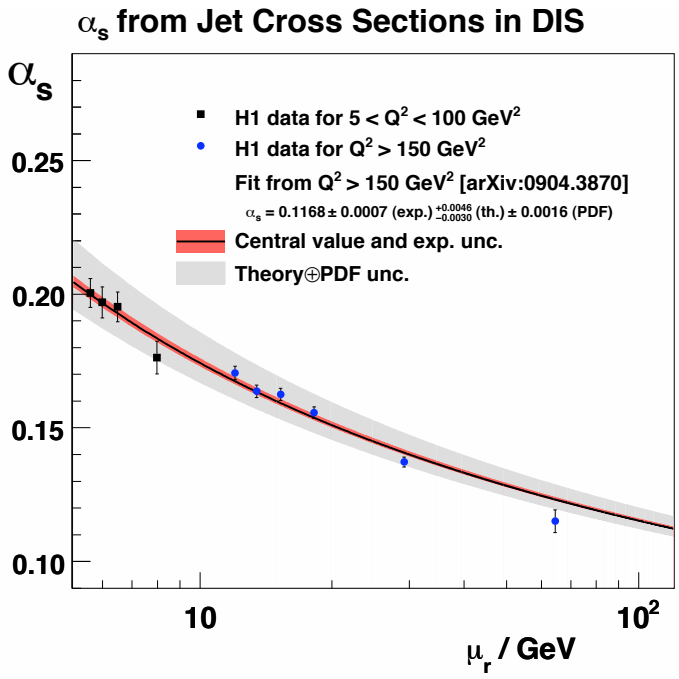

Figure 1.3: Values of $\alpha_s(\mu_r = \sqrt{(Q^2 + P^2_{T,\mathrm{obs}})/2})$ obtained by a simultaneous fit of all jet cross sections in each Q^2 bin (squares) measured in [30] together with the fit in different bins at high Q^2 (circles) [31]. The solid line shows the two loop solution of the renormalization group equation obtained by evolving the $\alpha_s(M_Z)$ extracted from jets at high Q^2.

1.4.2 Structure functions in QCD

In the QPM, the 'scaling hypothesis' predicts that in the limit ($Q^2 \to \infty$, and $\nu \to \infty$) with $x = Q^2/2M\nu$ fixed, the structure functions scale as are independent of Q^2 (i.e., $F_i(x, Q^2) \sim F_i(x)$). This property is related to the assumption that the transverse momentum of the partons in the infinite-momentum frame of the proton is small. In QCD, however, the radiation of hard gluons from the quarks violates this assumption, leading to logarithmic scaling violations, which are particularly large at small x (cf. figure 1.2). The radiation of gluons produces the evolution of the structure functions. The higher Q^2, the more gluons radiate, that in turn split into $q\bar{q}$ pairs. This process leads both to the softening of the initial quark momentum distributions and the growth of the gluon density and the $q\bar{q}$ sea as x decreases.

As a result, the structure function in QCD is described in terms of scale-dependent parton distributions. For $Q^2 \gg M^2$, the structure function is of the form:

$$\tilde{F}_2(x, Q^2) = \sum_i \hat{\sigma}_i \left(\frac{x}{z}, \frac{Q^2}{\mu^2}, \frac{\mu_F^2}{\mu}, \alpha_s(\mu^2) \right) \otimes x q_i(z, \mu_F, \mu^2), \tag{1.45}$$

where, as illustrated in figure 1.4, i is the parton label and $f \otimes g$ denotes a convolution integral

$$f \otimes g = \int_x^1 \frac{dy}{y} f(y) g(\frac{x}{y}), \tag{1.46}$$

of the hard vector-boson-parton cross section $\hat{\sigma}$ and the parton distribution function xq. The hard cross section $\hat{\sigma}$ can be calculated in perturbative QCD:

$$\hat{\sigma} \left(\frac{x}{z}, \frac{Q^2}{\mu^2}, \frac{\mu_F^2}{\mu}, \alpha_s(\mu^2) \right) = \hat{\sigma}_0 \delta \left(1 - \frac{x}{z} \right) + \alpha_s(\mu^2) \hat{\sigma}_1 \left(\frac{x}{z}, \frac{Q^2}{\mu^2}, \frac{\mu_F^2}{\mu} \right) + \mathcal{O}(\alpha_s^2) \tag{1.47}$$

where $\hat{\sigma}_0$ is the leading order contribution in the QPM (figure 1.4(b)). In performing calculations beyond leading order, various divergences arise and the renormalization scale μ is introduced to regulate these divergences. The factorization scale μ_F serves to define the separation of short-distance from long-distance scale. Roughly speaking, any propagator that is off-shell by μ_F or more will contribute to $\hat{\sigma}$ while it is grouped into xq below this scale. Since the physical structure function $\tilde{F}_2(x, Q^2)$ is independent of the scheme and scale dependent, these dependences of $\hat{\sigma}$ must be compensated by corresponding dependences of the parton distribution functions xq. In the inclusive DIS analysis, these scales are usually chosen to be Q^2, the characteristic large momentum scale of the process, to avoid logarithms of large ratios $\ln(Q^2/\mu^2)$ and $\ln(\mu_F^2/\mu^2)$.

The two most commonly used schemes are the modified minimal subtraction $\overline{\text{MS}}$ ([32, 33]) and DIS. The $\overline{\text{MS}}$ scheme is appealing for its theoretical elegance and calculational simplicity. The DIS scheme, on the other hand, is appealing for its close correspondence

to the experiment. In this scheme, one demands that, order-by-order in perturbation theory, all corrections to the structure functions $\tilde{F}_2$ be absorbed into the distributions of the quarks and antiquarks, such that the higher order formula for $\tilde{F}_2$ is the same as the leading-order formula. On the other hand, both $\tilde{F}_L$ and $x\tilde{F}_3$ acquire nontrivial order α_s corrections. For example, the structure function $\tilde{F}_L(x, Q^2)$ reads

$$\tilde{F}_L(x, Q^2) = \frac{\alpha_s(Q^2)}{\pi} \int_x^1 \frac{dz}{z} \left(\frac{x}{z}\right)^2 \left[\frac{4}{3}\tilde{F}_2(z, Q^2) + 2c\left(1 - \frac{x}{z}\right) z g(z, Q^2)\right], \tag{1.48}$$

where $c = N_f$ for neutrino scattering and $c = \sum_i e_i^2$ for charged lepton scattering.

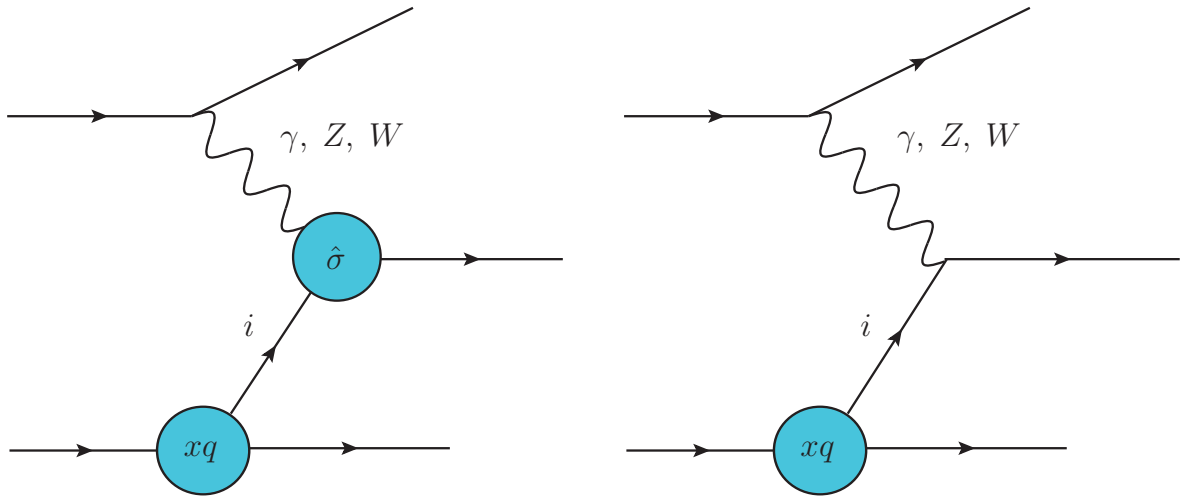

(a) (b)

Figure 1.4: Schematic diagram showing QCD corrections and factorization theorem in DIS (a) and diagram in QPM (b).

1.4.3 DGLAP equations and parton density extraction

The parton distribution q_a corresponds, at a given x, to the density of the parton a in the proton integrated over transverse momentum up to μ. Its evolution in μ is described in QCD by a DGLAP equation [34, 35, 36] which has the schematic form

$$\frac{\partial q_a}{\partial \ln \mu^2} \sim \frac{\alpha_s(\mu^2)}{2\pi} \sum_b (P_{ab} \otimes q_b), \tag{1.49}$$

where the P_{ab}, which describe the parton splitting $b \to a$, are given as a power series in α_s. Although perturbative QCD can predict, via equation 1.49, the evolution of the parton distribution functions from a particular scale, μ_0, these DGLAP equations cannot

predict them at any particular μ_0. Thus they must be measured at a starting point μ_0 before predictions of QCD can be compared to the data at other scales, μ.

The PDFs can be determined from data for deep inelastic scattering lepton-nucleon scattering and for related hard-scattering processs initiated by nucleons.

This analysis uses the parton densities extracted by performing a next-to-leading order (NLO) QCD fit on data collected by the H1 Collaboration at proton beam energies of $E_p = 820$ GeV and $E_p = 920$ GeV at HERA-I. The parton densities are parameterized using polynomial functions in x at an initial scale Q_0^2 GeV^2. The parton densities are then evolved in Q^2 using the NLO DGLAP equations and fitted to the experimental data. The fit results is shown in figure 1.5 for $Q^2 = 10$ GeV^2 which illustrates the rather dramatic influence of the DGLAP evolution on the sea-quark and gluon densities. At $Q^2 = 1.9$ GeV^2 the sea-quark density rises towards low x, in contrast to the gluon distribution which has a valence quark-like shape. The Q^2 evolution rapidly changes the low-x behaviour of the gluon distribution, which starts to rise similarly to the sea-quark distribution towards low x.

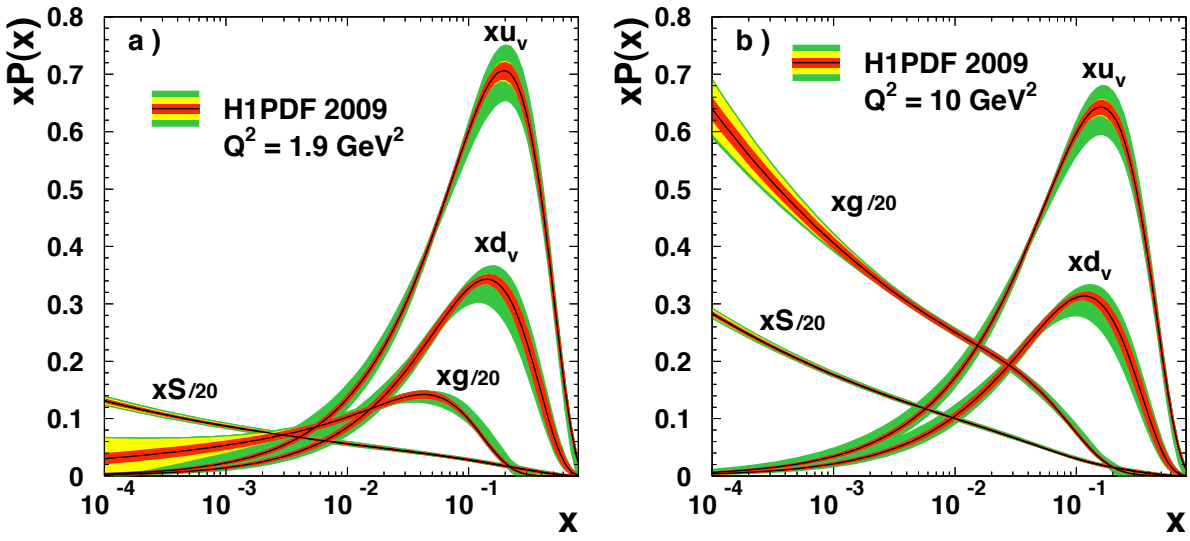

Figure 1.5: Parton distributions as determined by the H1PDF 2009 QCD fit at $Q^2 = 1.9$ GeV^2 (a) and at $Q^2 = 10$ GeV^2 (b) [37]. The inner error bands show the experimental uncertainty, the middle error bands include the theoretical model uncertainties of the fit assumptions, and the outer error band represents the total uncertainty including the parameterisation uncertainty.

1.5 Radiative corrections

A realistic goal for physics analyses at HERA is to reach a precision of 1% on the cross section measurement, so that electroweak radiative corrections of order $\mathcal{O}(\alpha_{\rm em})$ have to be taken into account. The radiative corrections are electroweak corrections at higher order of the DIS cross section given in the previous sections.

One distinguishes the corrections into two types: QED corrections, which are the photon radiation in the initial and final state, and "purely electroweak" corrections, which are corrections of vertex, propagators and box diagrams.

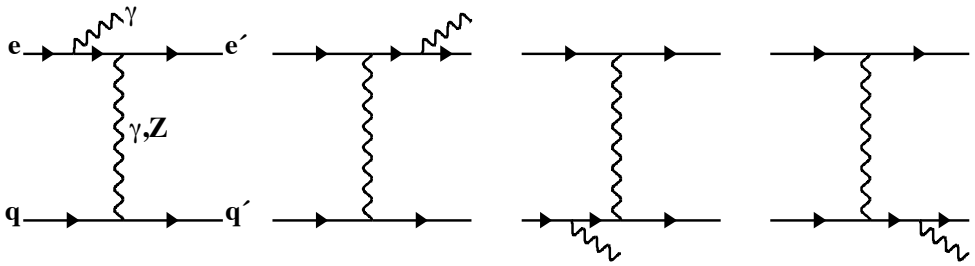

Figure 1.6: Illustration of QED corrections for the case of NC DIS with radiation of a photon from the lepton or the quark in the initial or final state.

The QED corrections are particularly important to be taken into account. These corrections are illustrated in figure 1.6 in which there is a photon emitted in the initial state or ISR (Initial State Radiation) and in the final state or FSR (Final State Radiation) by the charged lepton or the quark. In these processes, the (real) photon is not always identified. In principle there is also interference between ISR and FSR. The radiation of a photon from the quark is small compared to that of a photon from the lepton and can be neglected.

Consider first the situation when the kinematics are reconstructed using the scattered electron only (e-method for example, see section 3.1.1) and the radiation is from the initial lepton. The reaction is of the type $e^{(k)}p^{(p)} \rightarrow e^{(k')}\gamma^{(l)}X$ (where the symbols in brackets indicate the corresponding four-momenta). The effect of the initial state radiation (ISR) of a photon of four-momentum l is to lower the actual centre of mass energy in the ep interaction from $s = (k+p)^2$ to $s' = (k-l+p)^2$. The true kinematics are correctly reconstructed from the hadron side

$$Q_h^2 = -(k-k'-l)^2 \qquad x_h = \frac{Q_h^2}{2p\cdot(k-k'-l)} \qquad y_h = \frac{p\cdot(k-k'-l)}{p\cdot(k-l)}. \tag{1.50}$$

For collinear ISR, the lepton side and true variables are related by

$$Q_h^2 = z_i Q_l^2 \qquad x_h = \frac{x_l y_l z_i}{y_l + z_i - 1} \tag{1.51}$$

where z_i is the fractional energy loss from the initial state lepton $z_i = (E - E_\gamma)/E$.

Similar expressions can be deduced for the case of collinear radiation from the final state lepton (FSR). The size of the radiative contribution is characterized by $\ln(m_l^2/Q^2)$ where m_l is the electron or muon mass, and equal energy are thus generally more severe for ep than μp scattering. For a measurement at (x_l, y_l), the radiative correction is calculated by intergrating over the region $x_l \leq x \leq 1$, $0 \leq y \leq y_l$ which implies prior knowledge of the cross section being measured.

An additional correction, $1 + \Delta^{\text{weak}}$, arise from the effects of the photon-lepton vertex corrections combined with the self energies of the external fermion lines and the effects of the fermion loops of the exchanged photon self energy. The weak corrections are typically less than 1% (cf. [21]).

These procedures are typically done by correcting the measured cross section for QED radiative effects, either by using event simulation packages which include radiative effects, or from analytical calculations. The ratio between the radiative cross sections and the Born cross sections is used as correction factors.

1.6 Other processes in ep collisions

In this section, we summarize some other processes which mainly enter in our analysis as backgrounds.

1.6.1 Photoproduction

The term "photoproduction" regroups all processes of neutral current in which the transverse momentum square $Q^2 \approx 0$. They are usually called γp: the exchanged photon is quasi-real.

At HERA, the photoproduction is the dominant process with total cross section $\sigma_{\gamma p} \approx 150$ μb [38]. Most of theses processes are "soft", i.e. with small transverse momentum (a few GeV), the electron is scattered at $\theta \sim 0°$. We thus have

$$y = 1 - \frac{E'_e}{E_e} \cos^2\left(\frac{\theta}{2}\right) \cong 1 - \frac{E'_e}{E_e}. \tag{1.52}$$

We can therefore interpret y as the fraction of incident lepton momentum carried by the emitted photon. The total cross section can be decomposed as

$$\sigma_{ep\to eX} = \int \mathrm{d}y f_{\gamma/e}(y) \sigma_{\gamma p}(y, Q^2) \tag{1.53}$$

where $f_{\gamma/e}(y)$ is the probability for a photon of energy yE_e to be found in the electron. The cross section of the photoproduction is much larger than expected for a pure electromagnetic process.

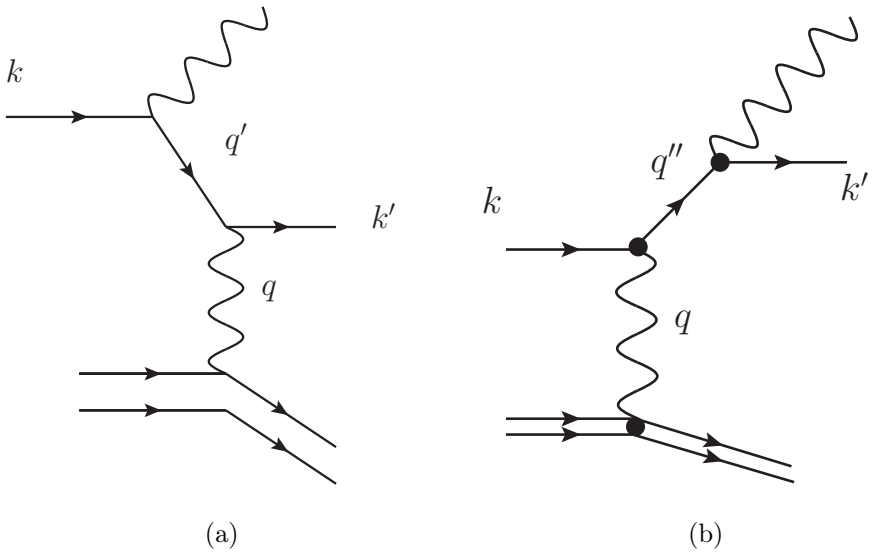

Figure 1.7: Schematic diagrams for QED Compton scattering.

Indeed the cross section of the photoproduction can be separated into two processes: *direct* and *resolved*. The direct part can be simply interpreted as an interaction of the quasi-real photon with the proton. The resolved part represents the fluctuation of the photon into a hadronic final state which will interact with the proton and as a QCD process have a large correction.

1.6.2 QED Compton

The Compton scattering is characterized by the emission of a quasi-real photon by a proton, this photon interacts with the initial electron. The interaction has type: $ep \to e\gamma X$. Figure 1.7 shows the two main contributions, where q' and q'' are propagators of the leptons outside of the mass-shell.

We have the cross sections in the following form:

$$\mathrm{d}\sigma \propto \left(\frac{1}{q'^2 - m_e^2}\right)^2 \left(\frac{1}{q^2}\right), \quad \text{and} \quad \mathrm{d}\sigma \propto \left(\frac{1}{q''^2 - m_e^2}\right)^2 \left(\frac{1}{q^2}\right). \tag{1.54}$$

Here the contribution of the interference was taken into account. From the relative values of q^2, q'^2 and q''^2 we have very different processes:

- when $q'^2 \approx m_e^2$ or $q''^2 \approx m_e^2$ and $q^2 \approx 0$ we are in the Bethe-Heitler regime, the incident lepton, the scattered lepton and the photon are collinear, i.e. the final photon is emitted along the incident (final) electron line. We will see that this process is used for the luminosity measurement,

- when $q'^2 \approx m_e^2$ or $q''^2 \approx m_e^2$ but q^2 is large, we are in the radiative DIS regime, the emitted photon is collinear to the lepton,
- when $q^2 \approx 0$ but q'^2 or q''^2 are large, it is the regime of the quasi-real QED Compton.

In the QED Compton regime, $e^\pm + \gamma^* \to e^\pm + \gamma$, the hadronic vertex does not transfer the transverse momentum to the pair $e + \gamma$ by the fact that $P_T^2 = Q^2(1-y)$ and $Q^2 \simeq 0$. The conservation of the transverse momentum reads

$$P_T(\gamma^*) = P_T(e,\gamma) = |\vec{p}_T(e) + \vec{p}_T(\gamma)| \approx 0. \tag{1.55}$$

The electron and the photon are thus balanced in transverse momentum. The measurement of the polar angles of the electron θ_e and of the photon θ_γ allows one to constrain the scattered energy E_e and E_γ for a given value of the initial energy of the electron E_0

$$E_{\gamma,e} = \frac{2E_0 \sin\theta_{e,\gamma}}{\sin\theta_e + \sin\theta_\gamma - \sin(\theta_e + \theta_\gamma)}. \tag{1.56}$$

This relation will be used for the verification of the electromagnetic energy scale of the detector.

Other processes can take place at HERA like: Drell-Yan [39], $W^\pm$ production ($\sigma_{\text{tot}}(e^\pm \to e^\pm X W^\pm) \approx 1$ pb, cf. [40]), Z^0 production processes which are considered as ep induced background to DIS and have very small contribution.

Chapter 2

The detector H1 at HERA

Contents

2.1 HERA accelerator

The first electron-proton collider in the world which will be the only such facility for many years HERA [18] (Hadron-Electron Ring Anlage) was located at DESY (Deutches Elektronen SYnchrotron) in Hamburg, Germany.

In HERA, the two beams circulate in opposite directions in an underground tunnel with 6.3 km of circumference.

The initial 500 MeV electrons are supplied by the linear accelerator (LINAC) and accelerated by the machine DESY-II up to 7.5 GeV. They will be filled into the machine PETRA-II and accelerated up to 12 GeV and then injected in the electron machine of HERA to be accelerated up to 27.6 GeV.

The protons are produced from H^- ions which are accelerated up to 50 MeV in the LINAC. Then two electrons will be removed from H^- when it is crossing a metal leaf and the protons will be accelerated to 7.5 GeV by the machine DESY-III. They will be accumulated to 70 packages and injected to the proton machine where they will attend the nominal energy, 920 GeV providing a center-of-mass energy of $\sqrt{s} = 319$ GeV. The kinematics range of HERA is more than two orders of magnitude larger than the range accessible in fixed target experiments (cf. figure 2.2).

In the storage ring, the superconducting magnets can provide a magnetic field of about 5 T. Both electron and proton rings can store up to 210 bunches. Most of bunches are colliding bunches but there is a small number of bunches called *pilot* in each beam without colliding partners which are used to measure and subtract background associated to the other beams. The spatial distribution of electrons in a bunch is Gaussian with a width of $\sigma_x \approx 111\mu m$, $\sigma_y \approx 30\mu m$ transversal to the beam direction and of $\sigma_z \approx 1$ cm in the beam direction. The proton beams have a length of 190 mm while it is 10 mm for electron beams. All proton beams are surrounded by four satellite bunches which are divided symmetrically before and after the central bunch. Two of them are at 4.8 ns (1.44 m) and the other two are at 19.2 ns (5.76 m). These satellites, which can contain up to 10% protons, appear during the compression of the bunches of the pre-acceleration step and injection.

At the two colliding experiments (H1, at the North Hall [19], and ZEUS at the South Hall [20]) the particle beams are directed against each other and collisions between protons and electrons take place with a time interval between two bunch-crossing (BC) of 96 ns.

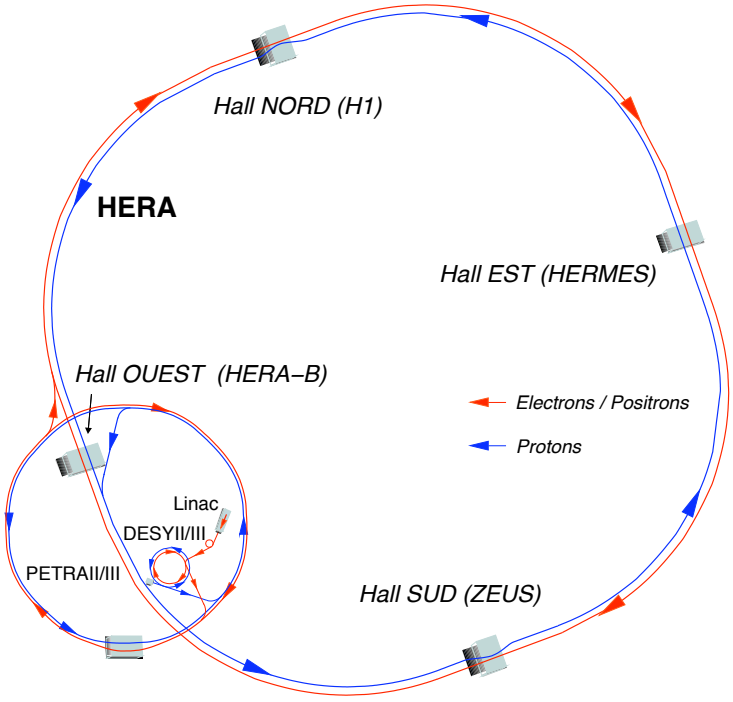

Figure 2.1: Schematic view of HERA and its detectors including two colliding (H1, ZEUS) and two fixed target experiments (HERA-B, HERMES). 27.6 GeV of energy of the electron beam and 920 GeV of that of the proton beam give a center-of-mass energy of $\sqrt{s} = 319$ GeV.

2.2 The upgrade project at HERA

2.2.1 Polarization at HERA

One important improvement at HERA-II compared to the first phase was the installation of new spin rotators at the interaction points of the two experiments H1 and ZEUS. [1]

The starting point for the description of polarized electron behavior in a storage ring is the concept of *spin-flip synchrotron radiation emission*, the celebrated Sokolov-Ternov effect [41]. When electrons (positrons) are moving on curved orbits, such as those prescribed by the magnetic guide fields of a storage rings, they emit synchrotron radiation. By calculating transition rates in terms of exact Direct wavefunctions for electrons moving in a homogenous magnetic field, it is found that a very small fraction of the emitted photons will cause a spin slip between the "up" and "down" quantum states of the electron's spin. For electron with spins initially aligned along the magnetic field, the probabilities

[1] Before the year 2000, HERA operated with two spin rotators around the HERMES experiment. After this upgrade, the HERA ring contains three pairs of spin rotators.

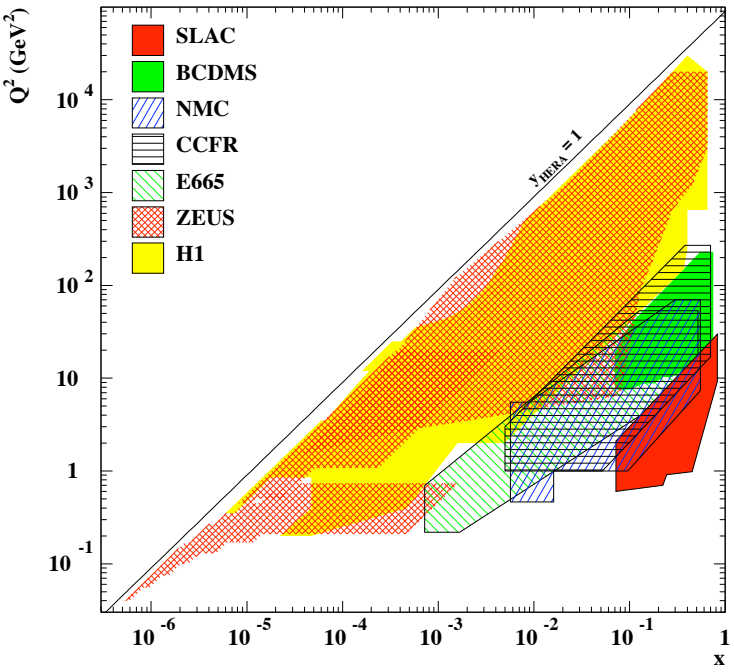

Figure 2.2: Kinematics in (x, Q^2) plane at HERA compared to other fixed target experiment.

for transitions from the up to down state and down to up state differ, leading to build up of polarization antiparallel to the field. Positrons become polarized parallel to the field. The transition rates for electrons are

$$W_{\uparrow\downarrow} = \frac{5\sqrt{3}}{16}\frac{r_e\gamma^5\hbar}{m\,|\rho|^3}\left(1+\frac{8}{5\sqrt{3}}\right) \tag{2.1}$$

$$W_{\downarrow\uparrow} = \frac{5\sqrt{3}}{16}\frac{r_e\gamma^5\hbar}{m\,|\rho|^3}\left(1-\frac{8}{5\sqrt{3}}\right) \tag{2.2}$$

where the arrows indicate the relative direction of the spin in the initial and final states, γ is the electron Lorentz factor, ρ the bending radius of the magnetic field and

$$r_e = \frac{e^2}{4\pi\epsilon m_e c^2} = 2.8179\times10^{-15}\ \text{m} \tag{2.3}$$

is the classical electron radius.

For positrons plus and minus signs are interchanged. An initially unpolarized stored $e^{+/-}$ beam gradually becomes polarized following the exponential law

$$P_{ST}(t) = P_{eq,ST}\left(1-e^{-t/\tau_{ST}}\right) \tag{2.4}$$

where the maximum attainable (equilibrium) polarization is given by

$$P_{eq,ST} = \frac{W_{\uparrow\downarrow}-W_{\downarrow\uparrow}}{W_{\uparrow\downarrow}+W_{\downarrow\uparrow}} = \frac{8}{5\sqrt{3}} \simeq 0.9238 \tag{2.5}$$

and the build-up rate is

$$\tau_{ST}^{-1} = \frac{5\sqrt{3}}{8}\frac{r_e\gamma^5\hbar}{m\,|\rho|^3}. \tag{2.6}$$

The build up rate depends strongly on energy (γ^5) and bending radius (ρ^{-3}). Its reciprocal, τ_{ST}, is typically of the order of minutes or hours. For HERA at an operation of 27.6 GeV, $\tau_{ST} \approx 40$ min.

To achieve the longitudinal electron polarization for the *ep* interactions, the transverse polarization is rotated into longitudinal just before the interaction point and, in order to maintain stable beam polarization, it must be rotated back to vertical immediately after the interaction point.

Polarization measurement

There are two techniques to measure the polarization in electron scattering: Möller scattering, $ee \to ee$, and Compton scattering, $\gamma e \to \gamma e$. The first method is experimentally simple, but limited to beam currents $I_e \leq 5\mu A$. The second method is more complicated to implement but is fast and accurate, and is therefore used in experiments operating with high beam currents. There are two polarimeters which independently measure the degree of transverse and longitudinal polarization at HERA: the Transverse Polarimeter (TPOL) and the Longitudinal Polarimeter (LPOL). Both longitudinal and transverse electron polarization measurements at HERA rely on the same physical principle: spin dependent Compton scattering of circularly polarized laser light (photons) off polarized electron beams.

The QED Compton is a well-known process, its cross section reads [42]

$$\frac{\mathrm{d}^2\sigma}{\mathrm{d}E'_\gamma \mathrm{d}\phi} = \Sigma_0 + S_1\Sigma_1(E'_\gamma)\cos(2\phi) + S_3P_Y\Sigma_{2Y}(E'_\gamma)\sin(\phi) + S_3P_Z\Sigma_{2Z}(E'_\gamma) \tag{2.7}$$

where S_1 and S_3 are the linear and circular components of the photon beam polarization, P_Y and P_Z are the transverse and longitudinal components of the electron beam polarization, Σ_i are calculable terms depending on the photon energy. From the equation above one can see that

- a measurement of the polarization can be performed by switching the sign of S_3 (maximizing the circular polarization $S_3 = \pm 1$ and thus minimizing the linear term $\sqrt{S_1^2 + S_2^2} \to 0$). This results in an asymmetry which is proportional to P_Z;
- if the polarization of the laser beam is known, the longitudinal polarization of the electrons can be determined from the photon energy distribution; to determine the transverse polarization, in addition to the energy distribution, the azimuthal distribution of the photon has to be measured.

As the spin rotator system does not change the degree of lepton beam polarization, the measurement of TPOL and LPOL is expected to be the same in magnitude.

The TPOL

The transverse polarization is determined by measuring the spatial vertical "up-down" asymmetry of the energy distribution of single back scattered Compton photons. The photons are produced in a 10 W Ar laser and are circularly polarized. The Compton photons are detected in a vertically segmented calorimeter which measures their energies in the upper (E_{up}) and lower (E_{down}) halves. The experimentally measured asymmetry A_{exp} is equal to

$$A_{\text{exp}} = \frac{E_{\text{up}} - E_{\text{down}}}{E_{\text{up}} - E_{\text{down}}} \tag{2.8}$$

which relates to the coordinates $y = r\sin(\phi)$ of the impact point, the radius $r = r(E = E_{\text{up}} + E_{\text{down}})$ is a well known function of the scattered photon energy and of the distance to the impact point. The average asymmetry $\langle A \rangle$ is measured for the circular polarizations left and right of the laser. The transverse polarization is given by

$$P_Y = \frac{1}{A_{\text{TPOL}}} \frac{1}{S_3} \times (\langle A \rangle_L - \langle A \rangle_R). \tag{2.9}$$

The analyzing power A_{TPOL} depends on the transformation $\eta \to y$, on the properties of the calorimeters but also on the electron beam parameters.

The global error on the measurement of TPOL is around 3.5%, dominated by the systematic error of the transformation $\eta \to y$.

The LPOL

The polarimeter LPOL is situated close to the experience HERMES between the spin rotators. It measures the longitudinal polarization. From equation 2.7 one needs only to measure the cross section as a function of energy of the scattered photon to obtain P_Z. The LPOL operates with a laser of frequency 100 Hz, 3 ns long with 100 mJ per pulse. The schema of the operation is shown in figure 2.3.

When a laser impulse interacts with an electron bunch, many photons are scattered at once and enter the calorimeter which measures the distribution of the integrated energy $\langle E \rangle_{S3}$. One says that the operation is at the *multi-photon* mode. The P_Z can be extracted from the measured photon energy belonging to different photon polarization states as

$$P_Z = \frac{1}{A_{\text{LPOL}}} \frac{1}{\bar{S}_3} \frac{\langle E \rangle_L - \langle E \rangle_R}{\langle E \rangle_L + \langle E \rangle_R} \tag{2.10}$$

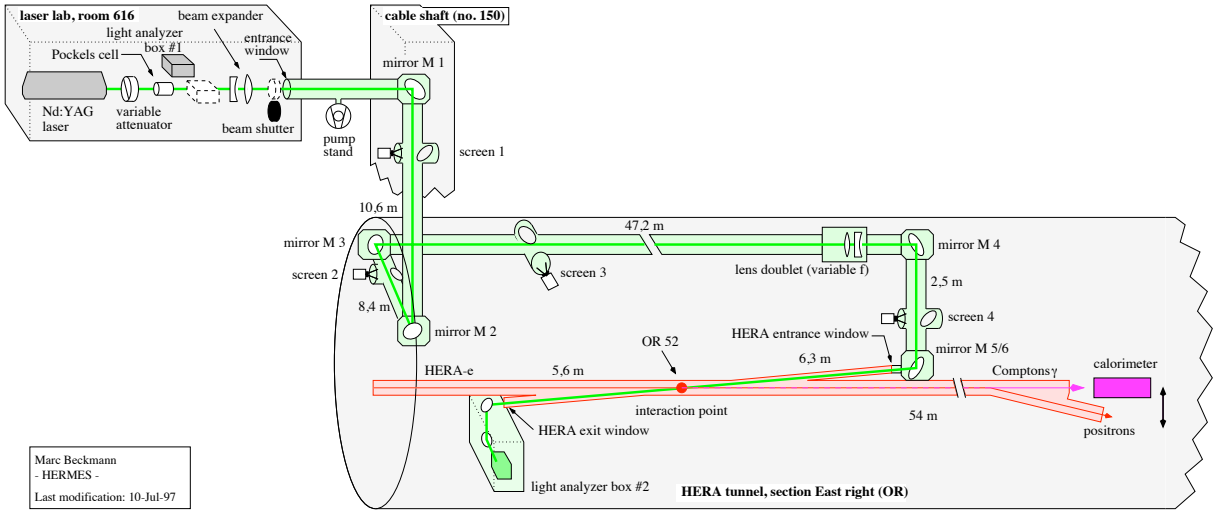

Figure 2.3: Layout of the longitudinal polarimetry at HERA.

where A_{LPOL} is the analyzing power of LPOL. Figure 2.4 shows the obtained energy for the two polarization type of the laser. The main disadvantage of this measurement is the control of the energy scale of the calorimeter since the measured energy in the multi-photon mode is of the order of TeV. The total error on a polarization measurement is about 1.6%.

The new LPOL or POLCA

The POLCA is a longitudinal polarimeter constructed with purpose to measure the polarization with 1% precision per bunch and per minute. It needs thus to operate in *few-photon* mode with a laser of high power. The Fabry-Pérot cavity is used for such a high-power laser. The layout of the cavity is shown in figure 2.5. A detailed description of the cavity can be found in [43].

By analyzing the energy distribution of the photon, one can extract the polarization of the bunch. One of the advantages of the few photon mode is an easy control of the energy scale of the calorimeter.

2.2.2 Luminosity at HERA-II

In scattering and accelerator physics, luminosity is the number of particle per unit area per unit times the opacity of the target, usually expressed in $\mathrm{cm}^{-2}\mathrm{s}^{-1}$ or in barn per second (1 barn = 10^{-28} m^{-2}). At HERA the instantaneous luminosity depends on the bunch crossing frequency f, on the numbers of protons N_p and of electrons N_e per bunch

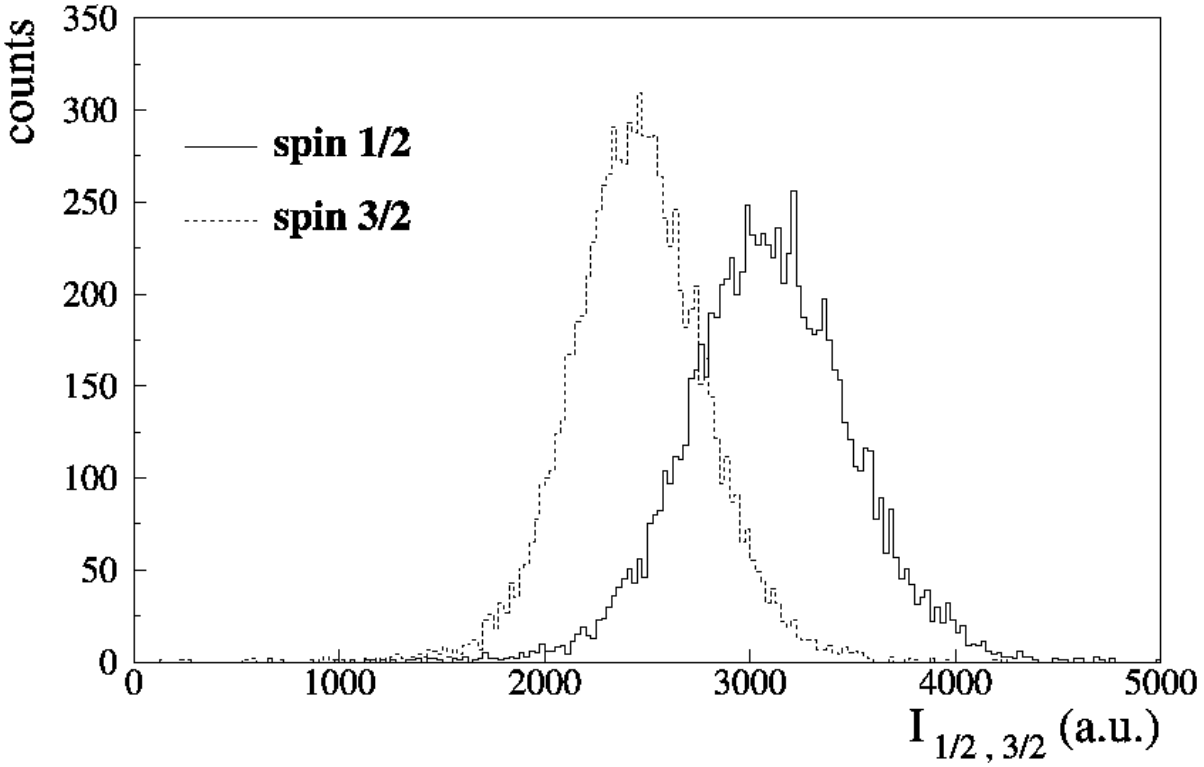

Figure 2.4: Distribution of the energy obtained in the LPOL for $S_3 = R$ (spin 3/2) and for $S_3 = L$ (spin 1/2). The polarization is extracted from the difference of the average from the figure.

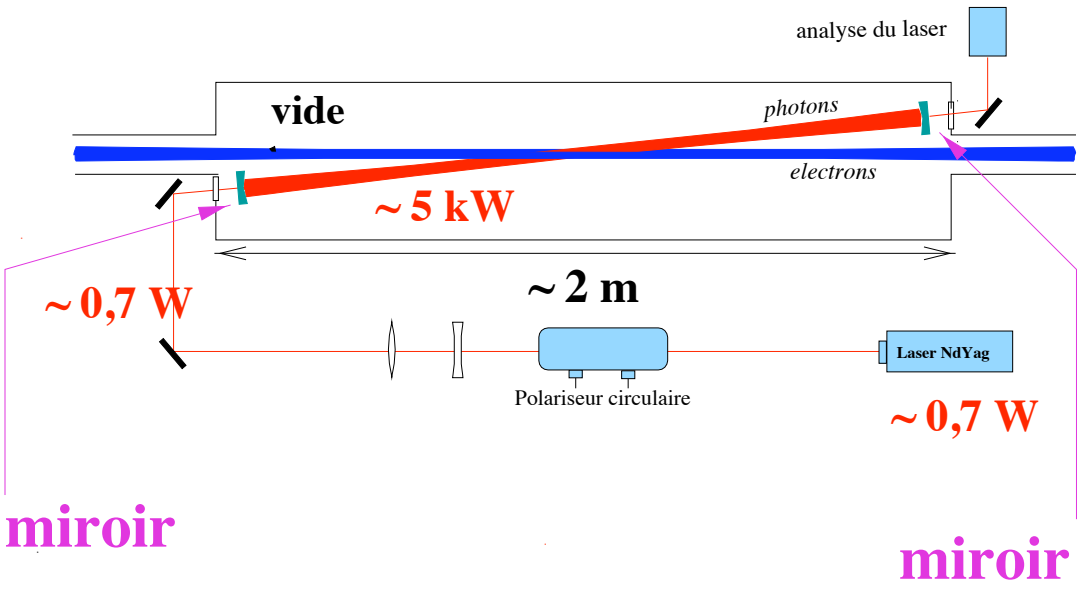

Figure 2.5: Simplified scheme of the implementation of a Fabry-Pérot cavity inside the electron beam pipe.

and also their Gaussian transverse beam profile σ_x and σ_y in the x and y directions at the interaction point which can be written as follows:

$$\mathcal{L} = \frac{f N_e N_p}{4\pi\sigma_x\sigma_y}. \tag{2.11}$$

The instantaneous luminosity is the coefficient of proportionality which allows to relate the produced collision rate $\mathrm{d}N/\mathrm{d}t$ to the cross-section σ:

$$\frac{dN}{dt} = \mathcal{L}\sigma. \tag{2.12}$$

The accumulated luminosity L during a period T of data taking is called *integrated luminosity*:

$$L = \int_0^T \mathcal{L}(t)dt. \tag{2.13}$$

The first data taking of HERA was started on 1992 and ended on July 2007. The period of data taking between 1992 and 2000 is called HERA-I. The second phase occurring between 2003 and 2007 after a shutdown period for the upgrade project is called HERA-II. The goal of this upgrade is to provide the longitudinal polarization to the H1 and ZEUS experiments and to improve of sensitivity for detecting of non Standard Model

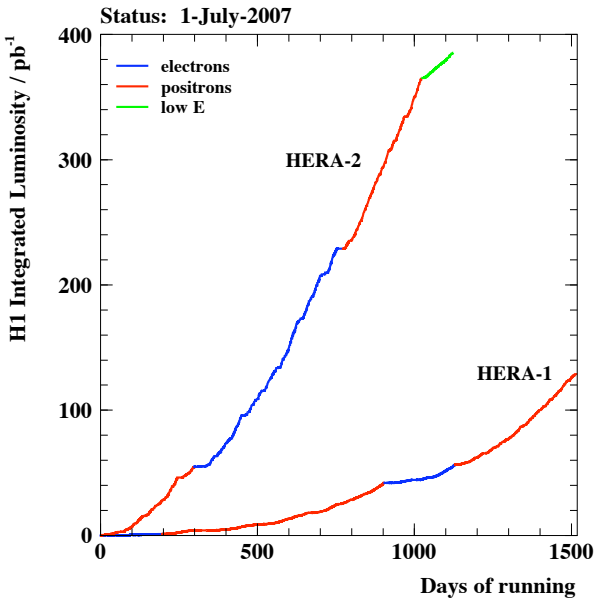

Figure 2.6: H1 integrated luminosity until the end of July 2007.

physics, extend the range of physics experiments to higher Q^2 and increase the luminosity by a factor of three (cf. figure 2.6). The luminosity of HERA-I in the year 2000 was up to 1.79×10^{31} cm^{-2}s^{-1} while that of HERA-II was increased and reached the value 4.80×10^{31} cm^{-2}s^{-1}.

2.3 The H1 detector

The H1 detector [19] was built as a general purpose detector to measure many aspects of high-energy electron-proton interactions.

The structure along the beam axis is asymmetric due to the fact that the incoming proton has a significantly higher momentum than the electron, most of the particles produced in an *ep* collision are Lorentz-boosted in the proton direction. More instrumentations were placed in the outgoing proton direction which is called *forward* direction. Reversely, the electron beam direction is referred to as the *backward* direction. Consider the so-called H1 coordinate system with the origin at the nominal interaction point and the axes chosen so that x-axis points to the centre of the HERA ring, y-axis is upwards directed and z-axis points along the beam direction. Consequently, the forward region corresponds to $\theta < 90°$ or $z > 0$ and the backward region corresponds to $\theta > 90°$ or $z < 0$.

The organization of the H1 detector is like that of other detectors in colliding experiments: tracking detectors, calorimeters, a superconducting magnet and muon detectors

cover the beam axis and are installed in layers. Besides these main detectors, there are also the detectors distributed in the very forward region and the luminosity detectors or various electron taggers which are placed in the backward region.

This arrangement allows H1 to cover a full solid angle, identify and measure the four-momenta of almost all particles produced from ep interactions.

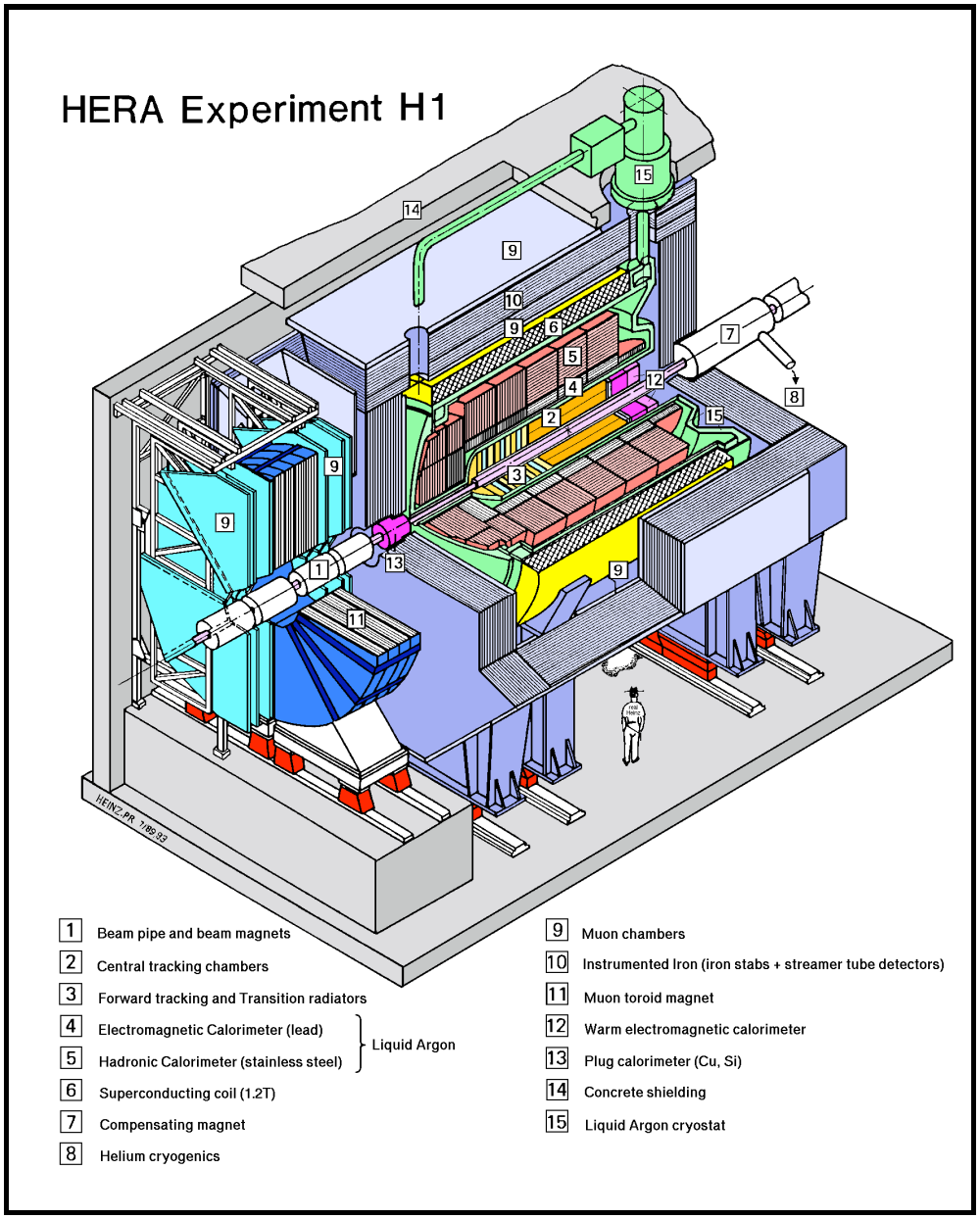

Figure 2.7: General view of the H1 detector with detector components.

The total volume occupied by H1 is $12 \times 10 \times 15$ m^3 (Length×Width×Height) and measures 2800 tons. A general view of the H1 detector can be found in figure 2.7. The

region around the interaction point is surrounded by tracking detectors 2 or 3. They are used to detect tracks left behind the charged particles as well as the interaction point.

The tracking system is enclosed by the Liquid Argon Calorimeter (LAr) which is used to measure the energy and direction of particles in the central region to the forward region. The LAr is separated into electromagnetic 4 and hadronic parts 5, both of these two parts are inserted in a cryostat 15. A magnetic field of 1.16 T provided by the superconducting solenoid 6 deflects the course of the charged particles and allows their momentum as well as their charge to be determined from their curvature and from the direction of the curvature. At the backward direction the calorimeter SpaCal 12 (Spaghetti Calorimeter) allows a precise measurement of the scattered electron. The calorimeter PLUG placed at the forward region completes the acceptance of the detector. In the case where one part of the particles produced from ep collisions leak from the Liquid Argon calorimeter they will be catched by a Tail Catcher (TC) which ensures also the return of the magnetic field.

The so-called *Instrumented Iron* 10 is surrounded by chambers dedicated for the muon identification realized by the Central Muon Detector (CMD) 9. The cover at the forward region is completed by Forward Muon Chamber (FMC) inserted in a field produced by Muon toroid magnet 11. The detector is covered by a concrete shielding 14.

Let us notice that there are other detectors which are not presented here since they are placed in the tunnels. In the electron beam direction after the interaction point, the photon detector used to measure the luminosity and the electron detector ETAG (Electron TAGger). In the proton beam direction, the Forward Neutron Calorimeter, as its name says, is used to identify scattered neutrons from the reaction $ep \to e'nX$. The Forward Proton Spectrometer (FPS) located between 50 m and 100 m is made of four Roman Pots (insertions to the beam pipe, housing scintillating fibre hodoscopes). The pots are used to detect scattered final state protons.

2.4 Tracking detectors

The tracking detectors were built with purpose for reconstruction of the particle trajectories, momentum measurement and accurate determination of the interaction point, they consist of central jet chambers (CJC1, CJC2), central trackers for measuring the z

coordinate (CST, COZ), the central multiwire proportional chambers for fast triggering (CIP), forward tracking detector (FTD), backward tracking detector (BDC) and forward, central and backward silicon microvertex detectors (FST, CST, BST). The two silicon devices CST and BST were added during the upgrade.

Central Tracking Detector

The CJC1 and CJC2 [44] are two large and concentric drift chambers consist of cylindrical tracking subdetectors arranged concentrically around the beam-axis. They are used for an accurate reconstruction of the transverse momentum and azimuthal angle of the charged particles.

The inner chamber CJC1 consists of 30 cells with 24 sense wires in each cell covering a polar angular range of $22.5° < \theta < 157.5°$. The outer chamber CJC2 consists of 60 cells with 32 sense wires each and has an angular acceptance of $39° < \theta < 141°$. From the measured drift time single hits are reconstructed with a spatial resolution of $\sigma = 170\mu$m in the $r - \phi$ plane and 22 mm in z. In addition, the event timing can be determined with the precision of about 1 ns, allowing the determination of the interaction time which is very powerful for rejection of non-ep background. The CJCs provide a measurement of the transverse momentum, p_T, with a resolution:

$$\frac{\Delta p_T}{p_T^2} \sim 0.01\ (\mathrm{GeV}^{-1}). \tag{2.14}$$

The Central Inner Proportional Chamber [45], CIP2k, is a cylindrical multi-wire proportional chamber with diameter ≈ 40 cm and consists of five radial layers. The chamber is positioned between the Central Silicon Tracker (CST) and the central drift chamber. The CIP2k allows fast ($\sim 2\ \mu s$) z-vertex position determination and thus efficient background rejection.

The Central Outer Z-chamber (COZ) is a drift chamber with sense wires perpendicular to the beam axis, complementing the accurate $r - \phi$ measurement provided by CJC chambers with an accurate z-position of the particle tracks. It is placed in between CJC1 and CJC2. Its spatial resolution in the z-direction depends on the polar angle of the transversing charged particle within the range $\sigma = 200 - 500\mu$m.

Additional planar chambers improve the track determination in the forward region: the MWPCs and transition radiators in HERA-I were replaced during the HERA upgrade by three planar drift chambers. The Forward Tracker is a set of drift chambers designed to detect tracks in the range from about 5 to 25 degrees from the interaction point. There are three Supermodules, each consisting of three Planar (P) chambers (Orientations)and a new(Q) planar chamber. The Planar drift cells each have four wires, oriented with

respect to the y axis at 0 degrees, +60 degrees and −60 degrees in the three Orientations; the Q cells each has 8 wires at +30 degrees and +90 degrees. A Planar Orientation has 28 rectangular cells with all wires parallel; the wires are read out at one end only, and hence measure only the drift coordinate.

Silicon Trackers (FST, CST, BST)

The Central Silicon Tracker [46] consists of two coaxial cylindrical silicon sensor layers with 12 and 30 modules at radii of 5.75 cm and 9.75 cm, respectively. Each module contains six silicon sensors. Both CST layers have 35.6 cm active length in the z-coordinate.

CST is the closest detector to the beam pipe. The spatial resolution of CST in an order of magnitude better than the central tracker chambers. Therefore it is used to complement and improve the CTD measurement. The Forward and Backward Silicon Trackers were not used directly in these analyses.

The momentum resolution of the tracking devices decreases with increasing of the transverse momentum ($\sigma_{P_T}/P_T \approx 0.003 P_T[\text{GeV}]$ [47]), therefore, the low momentum charged particles are usually measured with high precision.

2.5 Calorimetry

Calometers are used to measure the energy and position of the particles and serve for the identification of different types of particles. Calorimeters are sensitive not only to charged but also to neutral particles by detecting their charged secondaries. Calorimeters play a very important role at high energies since the relative energy resolution improves as $\Delta(E)/E \sim E^{-1/2}$ at large E, and in addition, they can provide reasonably fast signal which is important for making the trigger decisions.

The H1 calorimeter system contains four separate detectors:

- the Liquid Argon calorimeter (LAr) covering the central and forward region of the H1 detector
- the very forward part being complemented by the PLUG calorimeters
- the Spaghetti Calorimeter (SpaCal) placed in the backward region
- the Tail Catcher measuring the energy leaking out of the LAr calorimeter.

2.5.1 The Liquid Argon calorimeter

The Liquid Argon calorimeter [48] covers the central and forward parts of the H1 detector within the angular range of $4° < \theta < 153°$. Liquid argon is chosen because of the stability, ease of calibration and homogeneity of response. The calorimeter consists of layers of stainless steel and lead as the passive absorbing materials, and liquid argon as the active material and composed by two parts: electromagnetic (closer to the interaction point) and hadronic. The LAr calorimeter is segmented along the beam axis into eight self supporting 'wheels' as shown in the figure 2.8 which are (in the order from right to left): Backward Electromagnetic Barrel (BBE), Central Barrels (CB1, CB2, CB3), Forward Barrels (FB1, FB2) and the Inner and Outer Forward (IF1, IF2 and OF1, OF2). Each wheel consists of an electromagnetic part and a hadronic part except the BBE which has only one electromagnetic part and the IF2/OF2 are uniquely hadronic. The wheels BBE, CB and FB are divided into eight identical octants in the $x-y$ plane as shown in figure 2.9 except for the wheels IF/OF which are assembled into two parts.

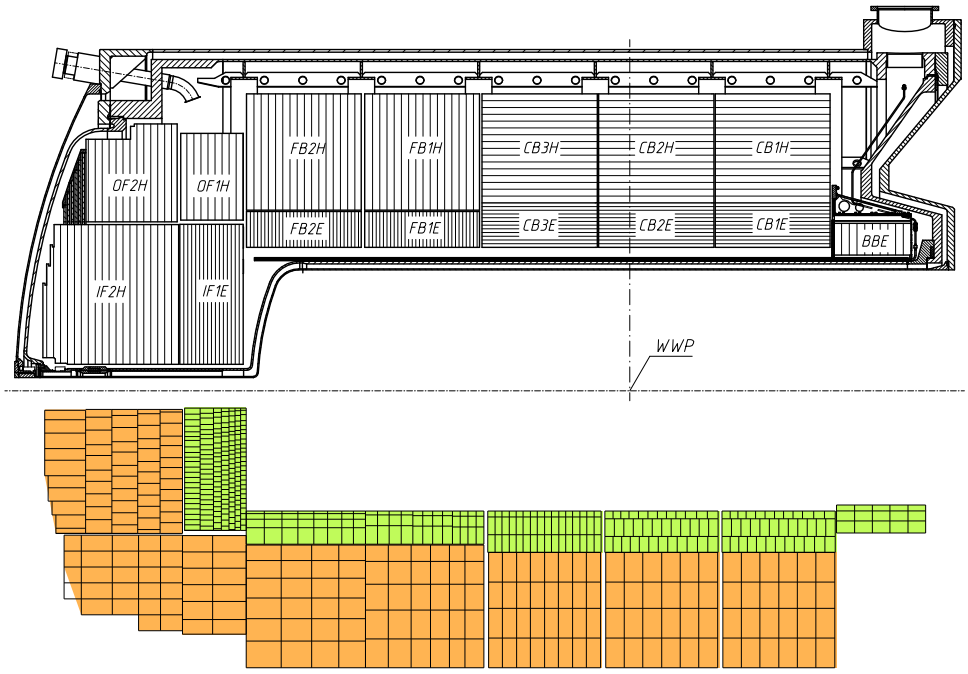

Figure 2.8: Longitudinal cross section of the Liquid Argon calorimeter. The upper part shows the wheels structure with the orientation of the absorber plates (indicated by horizontal and vertical lines respectively). The structure in cells is presented in the lower part.

The inactive parts of the detector (dead zones) between the wheels are called *z-crack* and those between octants are called *ϕ-crack*. Remark that the cracks between hadronic

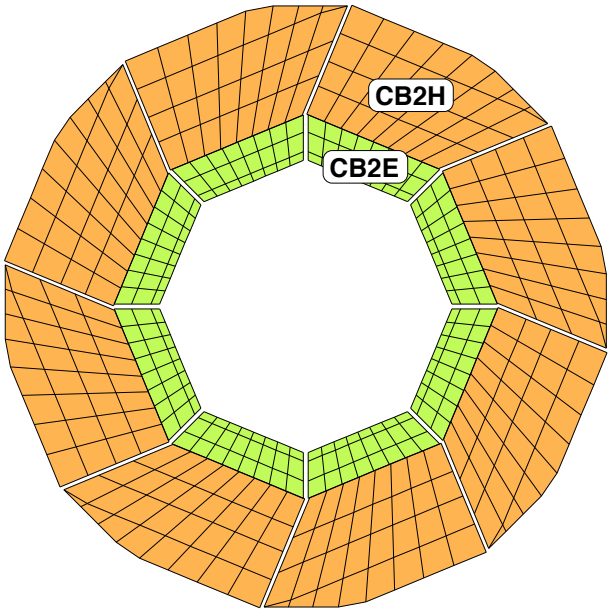

Figure 2.9: Transversal cross section of the CB2 wheel of the Liquid Argon calorimeter. The wheel is divided into eight octants. Only the cracks between electromagnetic parts point to the nominal interaction point.

wheels do not point to the interaction point in order to limit the energy losses. The treatment of these inactive regions is necessary during the analyses. The set of octants are segmented into 45000 cells of which around 30000 are for the electromagnetic part and 15000 are for the hadronic part. Each cell is related to a read-out channel.

The granularity of the electromagnetic cells varies between 1 (forward region) to 2.5 (backward region) of Molière radius[2] in order to obtain a good resolution of the transversal structure of the showers produced by the particles at several GeV or more.

The orientation of the absorber plates was chosen such that the angle of incidence was not smaller than 45° (cf. figure 2.10). Therefore, this orientation is vertical in the forward and backward, and parallel to the beam in the central region. One counts 3 to 4 layers in the electromagnetic part and 4 to 5 layers in the hadronic part. The thickness of the electromagnetic part of the LAr calorimeter varies between 22 and 30 radiation lengths while its total depth of reaches 5 to 8 times hadronic interaction length (see also figure 2.10).

[2]The Molière radius is a characteristic constant of a material giving the scale of the transverse dimension of the fully contained electromagnetic showers initiated by an incident high energy electron or photon. By definition, it is the radius of a cylinder containing on average 90% of the shower's energy deposition. It is related to the radiation length X_0 by the approximate relation: $R_M = 0.0265 X_0 (Z+1.2)$, where Z is the atomic number.

An electromagnetic cell consists of two absorber plates made of lead with 2.4 mm of thickness and separated by a liquid argon layer with 2.35 mm of thickness. The calorimeter should cover most of the solid angle in a single cryostat. Nevertheless, the insertion of the tracker components imposes a free space for a polar angle $\theta > 154°$, which is closed by a lead / scintillator calorimeter. This leaves only the backward beam hole uncovered ($\theta > 177.5°$); the forward beam hole ($\theta < 4°$) is partly covered by the plug calorimeter.

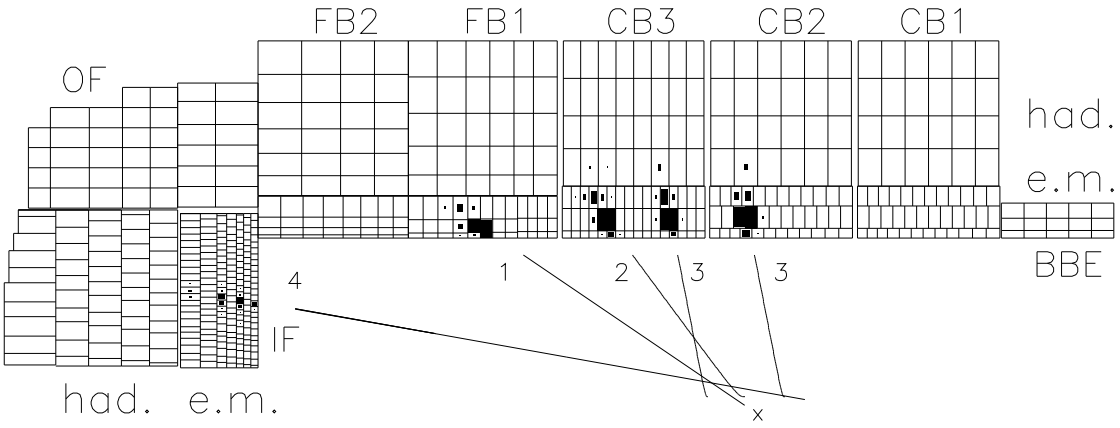

Figure 2.10: LAr cells with example for the showers formed by the electrons.

Energy measurement

The LAr has a characteristic not to be *compensated*, i.e. the response of the detector to a pion and to an electron of the same energy is different: we say the ratio e/π is different from 1. In our case, this ratio is about 1.35 for 10 GeV particles and decrease logarithmically with the energy. To correct this effect, a method of re-weighting as described in [49], [50] is used. Different cells are gathered together to be a calorimetrical *cluster* during the reconstruction.

The LAr calorimeter is affected by a relatively important noise because of the defects of the electronics which are used to shape the signal, of different cable length, and because of the pile-up energies of the particles arise from *ep* collisions and of the cosmic particles. The level of the noise is in the order of 15 to 30 MeV per cell. The addition of this noise to the entire calorimeter system yields an energy of 48 ± 3 GeV. To subtract these kinds of noise one uses the negative noise, i.e. the noise existing in the negative part of the noise distribution after the subtraction of the pedestal. During the construction of the clusters, one keeps only the cells above $+4\sigma$ and all the neighbors in a cube consisting of 3 cells. In these neighboring cells one keeps the cells with negative energy which will partially compensate the noise. There exists also an online noise subtraction called topological

which subtracts the isolated clusters in the last layer of the electromagnetic or hadronic part and far from all energetic clusters. After this online subtraction, the residual noise is in the order of several GeV.

The deposited energy is proportional to the number of secondary particles, therefore the resolution σ_E of the energy measurement will be proportional to $\sqrt{N}$ and consequently to $\sqrt{E}$, the relative resolution will be $\sigma_E/E \propto a/\sqrt{E}$. Although this term dominates the energy resolution one needs to take into account the instrumental effects independent of the energy like the noise or the pedestal subtraction which will give an contribution to the resolution which is independent of the energy such that the relative resolution is $\sigma_E/E \propto b/E$.

A third component will be due to calibration errors, to the non-linearity of the electronic chains and its contribution to the resolution is proportional to the energy such that the relative resolution is kind of $\sigma_E/E \propto c$. Numerically, $b \sim 150$ MeV and $c \sim 0.01$ which will make the statistic term dominate the resolution when we combine different terms in quadrature.

For the Liquid Argon calorimeter the energy resolution for electromagnetic particle is:

$$\frac{\sigma_E}{E} = \frac{12\%}{\sqrt{E(\text{GeV})}} \oplus 1\% \tag{2.15}$$

with $\sigma_1 \oplus \sigma_2 = \sqrt{\sigma_1^2 + \sigma_2^2}$. For the hadrons, the resolution is:

$$\frac{\sigma_E}{E} = \frac{50\%}{\sqrt{E(\text{GeV})}} \oplus 2\%. \tag{2.16}$$

2.5.2 Spaghetti Calorimeter

The "Spaghetti" Calorimeter (SpaCal) [51] covers the backward region with polar angle $153° < \theta < 177.5°$ and operates within a strong magnetic fields of 1.0 Tesla. The view of the SpaCal is shown in figure 2.11. The main design goal of the calorimeter are: good coverage of the region close to the beam pipe, high angular resolution and energy resolution of better than 2% for 30 GeV electrons. It should also be capable to provide coarse hadronic energy measurement and precise time information to suppress out-of-time background events at the first trigger level. These requirements were fulfilled by constructing two separate calorimeter sections. The inner electromagnetic section is made of 0.5 mm scintillating plastic fibres embedded in a lead matrix. Its lead-to-fibre ratio is 2.3:1 by volume. The outer hadronic section consists of 1.0 mm diameter fibres with a lead-to-fibre ratio of 3.4:1. In lead, incident particles induce electromagnetic and hadronic showers. These showers can be detected by the scintillation light emitted in the fibres when charged shower particles excite molecules in the scintillator material. The scintillation

light is collected at the backward end of the fibres and guided to *photomultiplier* tubes (PMT), which amplify the light and convert it to electric signals, these signals will be read-out to reconstruct the energy of the incident particles.

The electromagnetic section of SpaCal consists of 1172 cells and allows a spatial resolution of several milimeters for electrons. The measurement Backward Drift Chamber located in front of SpaCal. The energy resolution of the SpaCal is:

$$\frac{\sigma_e}{E} = \frac{7\%}{\sqrt{E(\text{GeV})}} \oplus 1\% \quad \text{and} \quad \frac{\sigma_e}{E} = \frac{13\%}{\sqrt{E(\text{GeV})}} \oplus 4\% \tag{2.17}$$

for electromagnetic and hadronic part respectively. Several calibration methods allow to control the electromagnetic energy scale at about 1%.

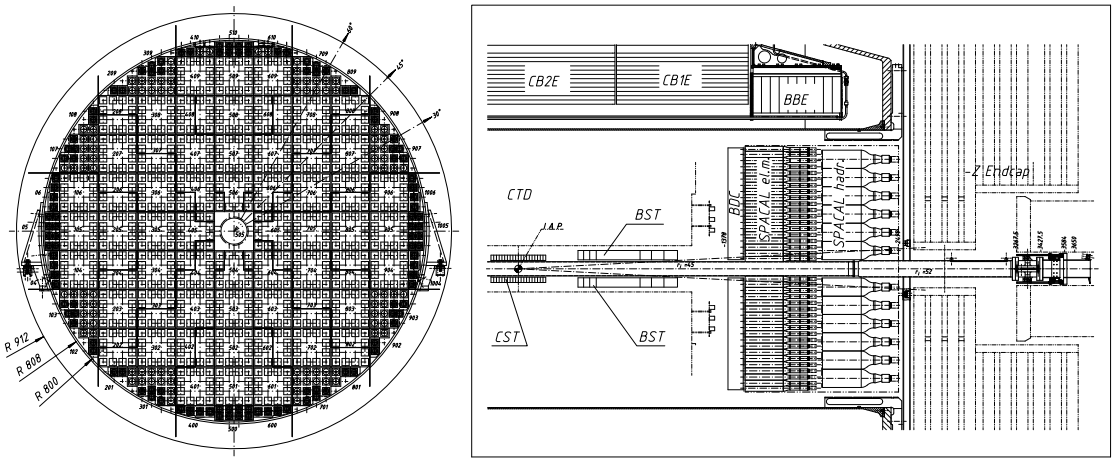

Figure 2.11: Left: view of the SpaCal in the $x - y$ plane. Right: view of the SpaCal in the $r - z$ for the configuration HERA-I.

2.6 Very forward detectors

H1 has spectrometers downstream of the main detectors in the proton beam direction to measure high energy protons, as well as calorimeters at zero degrees to measure high energy neutrons. These are used in the study of diffractive scattering as well as in the study of leading-particle production.

A forward proton spectrometer (FPS) has been installed since 1995 at 81 and 90 m away from the interaction point and detects leading protons in the momentum range from 580 to 740 GeV and scattering angles below 1 mrad. The FPS has been extended with stations at 80 and 63 m since 1997. In all stations the protons are detected with scintillating fiber hodoscopes. The detector elements are mounted inside plunger vessels,

so called Roman Pots, which are retracted during injection and are brought close to the beam after stable luminosity conditions are reached.

The forward neutron calorimeter (FNC) is located at 107 m downstream of the interaction point. The calorimeter consists of interleaved layers of lead and scintillating fibers. It has a total depth of 9.5λ and has an acceptance $> 90\%$ for neutrons with a production angle below 1 mrad.

2.7 Luminosity detector and electron taggers

2.7.1 Principle of luminosity measurement

The luminosity system is designed as a multipurpose device. Its main task is a fast relative luminosity measurement with a statistical precision of 2% s^{-1} at nominal conditions, In addition it provides electron beam monitoring for the HERA machine, absolute luminosity measurement in the interaction region with an accuracy of 5%, tagging of the photoproduction events and energy measurement for small angle scattered electrons and radiative photons from initial state radiation.

The integrated luminosity $L = \int \mathcal{L} dt$ is the ratio of the number of events per cross section: $L = N/\sigma$. It is necessary to know this number for the measurement of a cross section and inversely the precise knowledge on the cross section will allow a good measurement of luminosity. The instantaneous luminosity can be determined using the Bethe-Heitler process, which will be described below, and for a cross check the integrated luminosity can be determined using the QED Compton process.

2.7.2 Direct method – Bethe-Heitler process

At HERA, the luminosity is determined from the rate of the bremsstrahlung (Bethe-Heitler) process $ep \to ep\gamma$ [52] as this process has a large and precisely known cross section with a theoretical uncertainty of 0.5%. This process is studied in the condition where the incident electron, the photon and the scattered electron are co-linear. The large cross section of the order 170 mb allows us to obtain a large statistics. The luminosity is calculated as

$$L = \frac{R_{\text{tot}} - (I_{\text{tot}}/I_0)R_0}{\sigma_{\text{vis}}} \tag{2.18}$$

where R_{tot} is the total rate of the bremsstrahlung events, R_0 is the rate in the electron pilot bunches, I_{tot}, I_0 are the corresponding electron beam currents and σ_{vis} is a visible part of the $ep \to ep\gamma$ cross section, taking into account the acceptance and the trigger efficiency of the whole system.

The H1 luminosity monitor detects scattered electrons and outgoing photons in coincidence. It contains therefore two arms: the electron tagger (ET) and the photon detector (PD). Since the angular distributions for both the electrons and photons are strongly peaked in the direction of the primary e-beam – at 27.6 GeV and polar angles are of the order of $\theta \simeq \mathcal{O}(m/E) \simeq 17\mu$rad – the detectors should be placed close to the beamline and very far from the interaction region in order to cover these small angles.

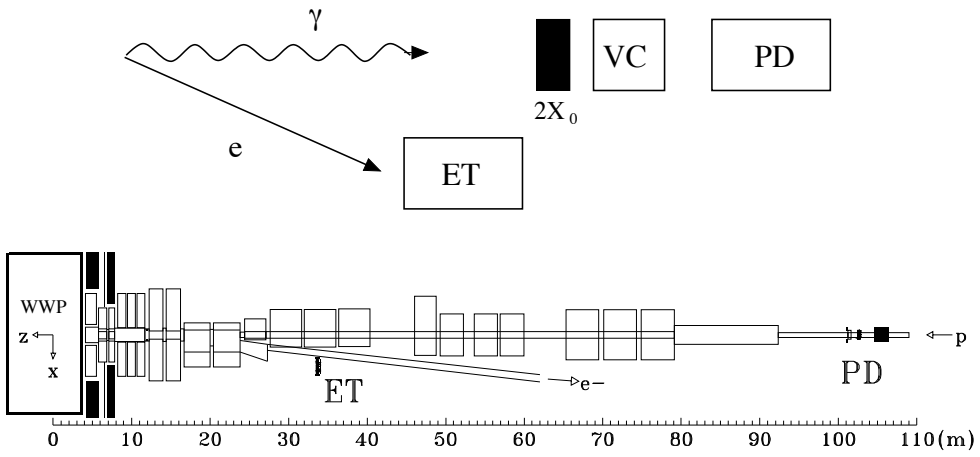

Figure 2.12: Luminometer for HERA-I

The general view of the luminosity system is shown in figure 2.12. Scattered electrons are deflected by a set of warm low-beta quadrupoles and a bending magnet located in the region 5.8m $< -z <$ 23.8m, pass exit window at $-z = 27.3$m and hit ET at $-z = 33.4$ m. The bremsstrahlung photons leave the proton beam pipe through the photon exit window at $-z = 92.3$ m, where the proton beampipe bends upward, and hit PD at $-z = 102.9$ m. A $2X_0$ Pb filter followed by a $1X_0$ water Čerenkov veto counter (VC), located in front of PD protects the detector from the high synchrotron flux. From the p-beam side PD is shielded by an iron wall of 2 m length against the proton halo. Both the ET and PD can be remotely moved from the median plane of the e beam during injection. This operation can be reserved within 1 – 2 minutes with a position accuracy of 100 μm.

The acceptance of the luminosity system for nominal electron beam conditions ($E_e =$ 27.6 GeV, zero tilt) and the expected rates at the design luminosity of $1.5 \times 10^{31}\text{cm}^{-2}\text{s}^{-1}$ (for HERA-I) are given in the table 2.1. One of the main contributions to the systematic error in the absolute luminosity measurement comes from the dependence of the system acceptance on possible variations of the electron beam angle in the interaction region. This tilt, typically of the order of 100 μrad, is controlled by the position of the beam profile at the PD with high precision, of the order of 10 μrad. The corresponding corrections to σ_{vis} are taken into account already online and can be further improved during the offline

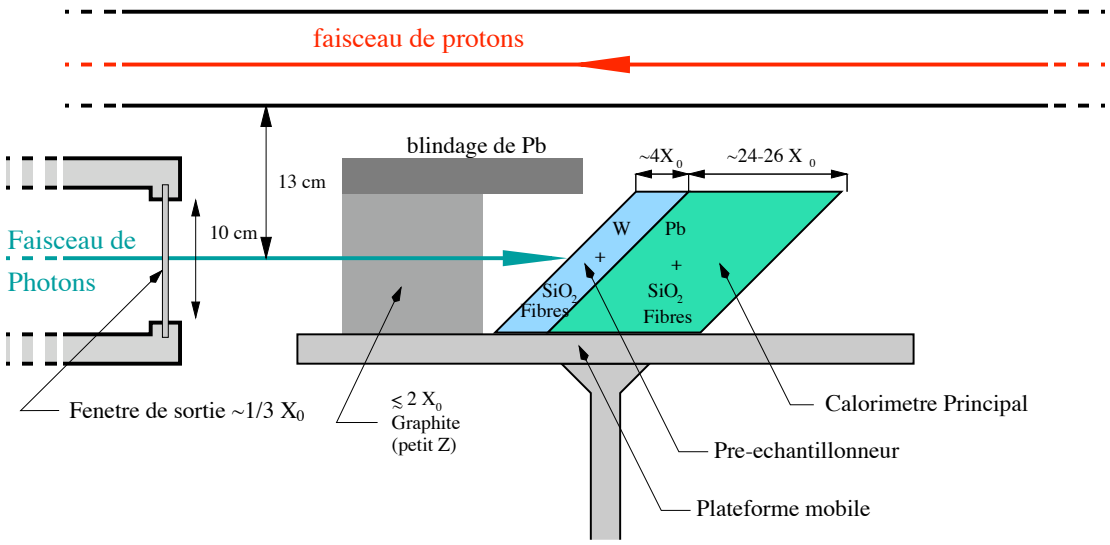

Figure 2.13: Luminometer for HERA-II

analysis.

Quasi-real photoproduction events with $Q^2 < 0.01$ GeV^2 can be tagged by the ET in the energy interval $0.2 < E'_e/E_e < 0.8$ using both the PD and VC as a veto.

2.7.3 Indirect method – QED Compton process

To determine the integrated luminosity from Compton events, one uses the formula (cf. [54]):

$$\mathcal{L}_{\text{Compton}} = \frac{N_{\text{sel}} - N_{\text{bf}}}{N_{\text{MC}}} \frac{1}{\epsilon_{\text{sel}}} \mathcal{L}_{\text{MC}} \tag{2.19}$$

where N_{sel} is the number of selected events, N_{bf} is the number of selected background events , N_{MC} is the simulated number of Compton events which passed the same reconstruction and analysis chains with the real data, ϵ_{sel} is the efficiency of the selection and $\mathcal{L}_{\text{MC}}$ is the integrated luminosity corresponding to the simulated MC set. Since one uses different samples of simulated events, the equation (2.19) can be rewritten as follows:

$$\mathcal{L}_{\text{Compton}} = \frac{N_{\text{sel}} - N_{\text{bf}}}{\sum_i \frac{N^i_{\text{MC}}}{\mathcal{L}^i_{\text{MC}}}} \tag{2.20}$$

where N^i_{MC} and $\mathcal{L}^i_{\text{MC}}$ are respectively the number of selected events and the luminosity of the MC set i of the simulated Compton events.

	unit	ET	PD
Energy interval, $E_\gamma/E_e = 1 - E'_e/E_e$		0.2 – 0.8	0.004 – 1.0
Polar angle acceptance interval	mrad	0 – 5	0 – 0.45
Average acceptance for $ep \to ep\gamma$	%	48	98
Average acceptance for photoproduction	%	36	–
σ_{vis}	mb	28	174
$ep \to ep\gamma$ rate for $E > E_{thr} = 4$ GeV (1)	MHz	0.4	1.3
Photoproduction event rate (1)	Hz	20 – 30	–
Aperture $x \times y$	mm^2	154 × 154	100 × 100
(granularity)		7 × 7	5 × 5
Chemical composition		TlCl (78%) + TlBr (22%)	
Radiation length (Molière radius)	cm	0.93 (2.10)	
Crystal length (radiation hardness)	mc (Rad)	20 ($> 6 \times 10^7$)	
Energy resolution, σ_E/E (2)	%	$1 \oplus 10/\sqrt{E}$, (E in GeV)	
Position (time) resolution, $\sigma_{x,y}(\sigma_t)$ (2)	mm (ns)	0.3 – 1.2 (< 3)	

Table 2.1: Parameters of the luminosity system. (1) at design luminosity; (2) values reached at HERA-I (cf. [53]).

The values of luminosity determined for HERA-II by QED Compton process are given in table A.1.

2.8 Time of Flight system

The Time of Flight device (ToF) [55] is located upstream of the interaction region. This choice of position represents a compromise between good coverage of the detector and time resolution. The mean of separation of particles from proton background and those from *ep* collisions at this point is 13 ns. The electron bunches have negligible size whereas the proton bunches have a spread of 2 to 3 ns FWHM.

The ToF system is a set of the following devices (see figure 2.14):

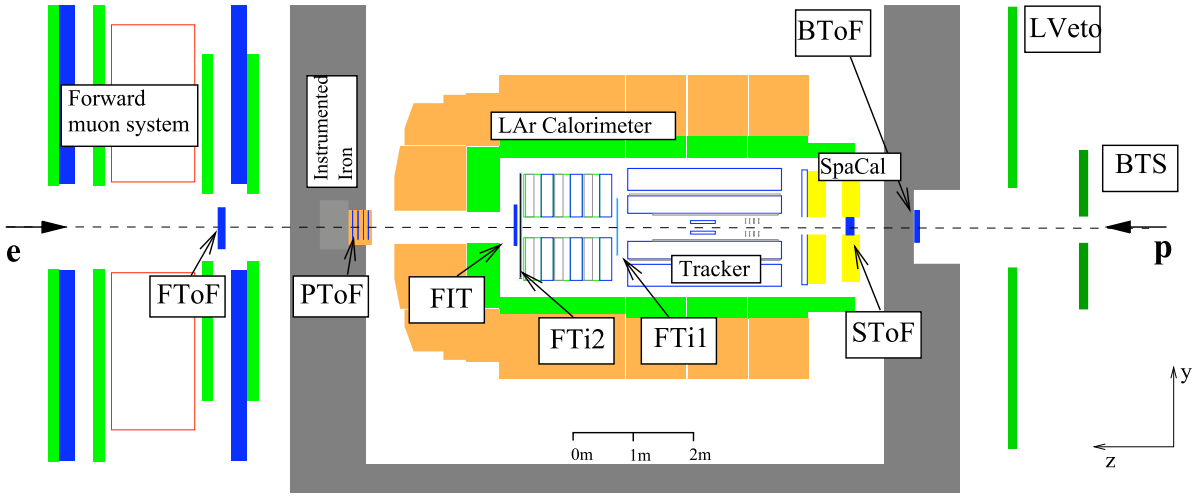

Figure 2.14: Schematic view in $y - z$ plane for different devices of the ToF system.

FToF	($z \approx 7.0$ m)	Forward ToF installed within the forward muon system
PToF	($z \approx 5.3$ m)	ToF installed behind the Plug calorimeter
FIT	($z \approx 2.7$ m)	Forward Interaction Timing system mounted behind the foward tracker
SToF	($z \approx -2.4$ m)	installed just before the hadronic SpaCal section
BToF	($z \approx -3.3$ m)	Backward ToF mounted after SpaCal
VETOWALL	($z \approx -(6.5 \div 8.1)$ m)	several small veto counters mounted close to the beam pipe

The ToF system is used to suppress a large amount of non-*ep* induced background due to timing condition (cf. section 4.5).

2.9 Trigger and event filtering

The task of a trigger system is to select physics events which are rare and to suppress background events as efficiently as possible. As the rate of the background is much higher than the true signals (see example given in table 2.2) the triggers must ensure a rapid decision, that is a time scale of the order of microseconds, from the information supplied by sub-detectors concerning the recording of an event produced by the acquisition system (DAQ). Moreover, as the readout time is long compared to the bunch crossing interval of 96 ns, the trigger system must be designed to reduce the "dead-time" and to include

Beam gas interactions			50	kHz
Cosmic μ in barrel			700	Hz
tagged γp	1.6	μb	25	Hz
$c\bar{c}$ total	1	μb	15	Hz
DIS low Q^2	150	nb	2.2	Hz
DIS high Q^2 (e in LAr)	1.5	nb	1.4	min^{-1}
Charged current DIS $p_T > 25$ GeV	50	nb	3.0	h^{-1}
W production	0.4	nb	0.5	d^{-1}

Table 2.2: Cross-section and event production rates at a luminosity of 1.5×10^{31} $\text{cm}^{-2}\text{s}^{-1}$.

complex decision, thus several trigger levels are required. At each trigger level more information is available to perform better filtering.

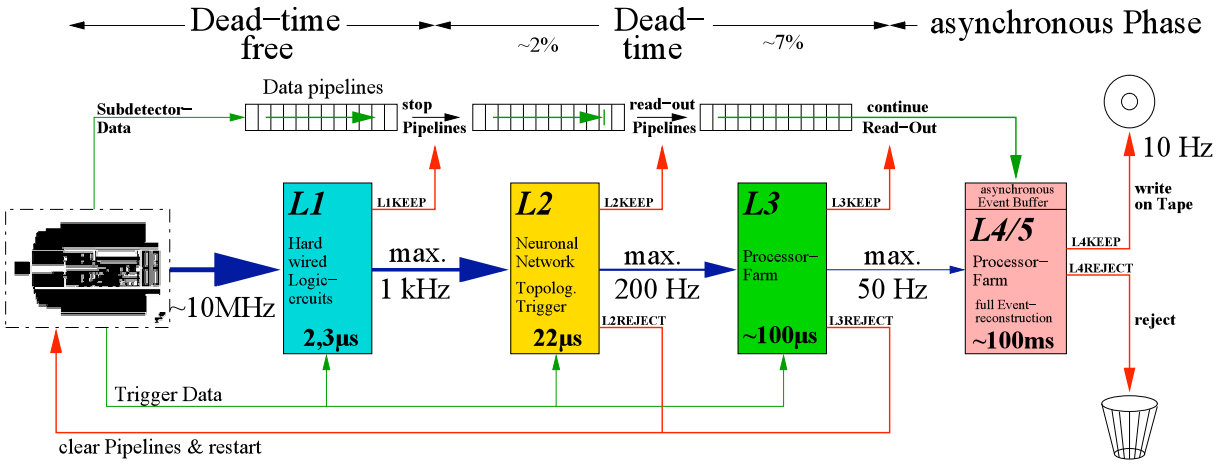

Figure 2.15: Triggering and filtering levels for H1.

2.9.1 Trigger Level One – L1

A trigger level 1 acts on the prompt information that is available in scintillation counters, proportional chambers or drift chambers with small gaps. Hardwired processors and fast electronics select a rough trigger which should not be run above 10 kHz. Not every subdetector can provide a prompt reconstruction of the event, so trigger element decisions are stored in a cyclic buffer, or 'pipe-line'. After 24 bunch crossings (2.3 μs) the trigger elements are combined into subtriggers by the central trigger logic (CTL). If the event fulfills the conditions of any subtrigger, a 'L1 keep' signal is sent and pipelines for all subdetectors are stopped and the event is passed to the next trigger level. Some

subtriggers are prescaled such that not every event fulfilling the subtrigger conditions is kept. Prescales may be applied in order to reduce the rate of triggering of some high cross section processes or so that the performance of "physics" subtriggers may be independently monitored without disturbing data taking. Some detector subsystems are able to provide coarse event timing information, they set a "T0" trigger bit if they identify an event in a given bunch crossing. The triggers which are used in this analysis will be listed as following.

Liquid Argon Trigger

As mentioned above, the LAr calorimeter consists of 45000 cells which are merged into 4844 "Trigger cells" so that each electromagnetic (or hadronic) trigger cell contains 16 (or 4) calorimeter cells. The trigger cells are arranged into "Trigger Towers" such that they point toward the nominal vertex. Trigger towers are combined into the so-called "Big Towers" so that the LAr is segmented in 14 bins in θ and up to 32 bins in ϕ with the finest granularity in the forward region. The arrangement of big towers can be seen in figure 2.16.

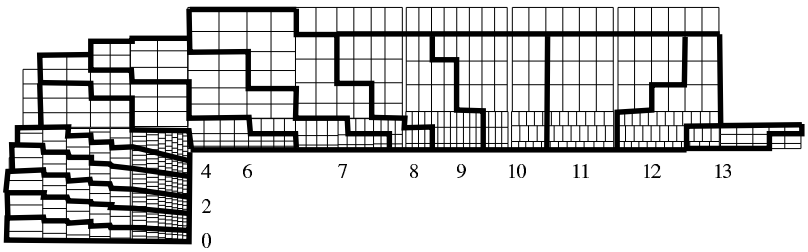

Figure 2.16: Big Towers structure of LAr. Each tower points towards the nominal interaction vertex.

The electromagnetic and hadronic signals from each BT are digitized by fast ADCs. The digital output is used to identify electron candidates. Big Towers are also combined to form global energy sums and topological quantities. These are encoded in trigger elements and sent to the Central Trigger. The important LAr trigger elements used in this analysis are:

- **LAr_el**: a potential electron signature is high (above a threshold) electromagnetic energy deposited in a BT, together with low (below threshold) energy in the associated hadronic big tower. The thresholds for the *LAr_el1* trigger element range from 5 GeV in the backward region to 25 GeV in the IF while the trigger element *LAr_el2* has looser thresholds.

- **LAr_T0**: the analogue signals from the trigger tower are processed in a special branch of the LAr Trigger system. The combined electromagnetic and hadronic signal is evaluated using a constant fraction discrimination technique [56]; this determines the T0 status for each Trigger Tower. A big tower T0 is combined (logical OR) from the constituent trigger towers. The *LAr_T0* for that bunch crossing is likewise set from a combination of big tower T0 signals.

- **LAr_Etmiss**: the energy from each BT can be weighted by $\sin\theta$ to from the transverse energy in that big tower. The three thresholds for triggering on the combined transverse energy imbalance are 3.8 GeV (low), 4.4 GeV (medium) and 5.2 GeV (high).

CIP Trigger

The proportional chamber (CIP) provides a quick information at L1 of the H1 trigger on the presence of an interaction vertex and of the tracks which helps to distinguish the *ep* proton from the background.

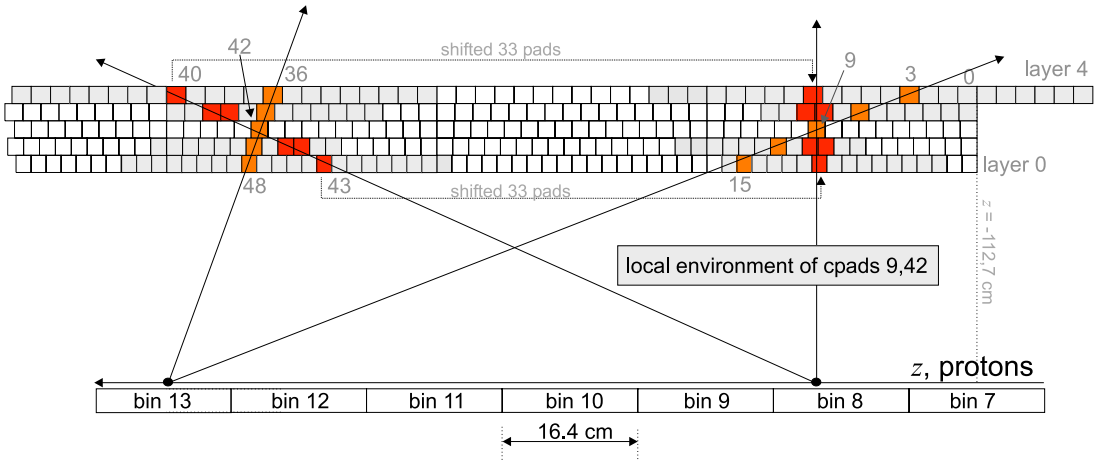

Figure 2.17: Schematic illustration of the track reconstruction method based on the impact in different cells in the proportional chamber CIP.

The method to reconstruct the interaction vertex is illustrated in the figure 2.17. The CIP tracks are combined from the impacts of at least 3 different layers (totally 5 layers) and will be extrapolated to the beam axis. The obtained longitudinal coordinate for each track is classified in a histogram on z constituted of 22 bins of 16.4 cm length each. The bins which contain a sufficiently large number of track origin are potential candidates to yield the interaction vertex position $Z_{\mathrm{vtx,CIP}}$. The precision of 20 cm of this method is enough to identify and reject the background which are produced far away from the

nominal interaction vertex or which have no defined vertex. The tracks are classified correspondingly to their position in the histogram: forward, central or backward.

VETO Triggers

The trigger elements which allow the identification of background coming from the interaction of the beam or residual gas in the beam tube are called VETO. There are two sorts of VETO triggers:

- **ToF-VETO**: this is a set of trigger elements which support the timing measurement of the detectors ToF and VETO to mark the event "background" (BG): FIT_BG, SToF_BG, BToF_BG, VETO_BG. The forward detectors FIT are used to identify the timing windows for *ep* events:FIT_IA.

- **CIP-VETO** allowing the identification of backgrounds produced in proximity of the interaction point. The conditions (CIPmul==7) and (CIPsig==0) reject efficiently the background which has high track multiplicity (≥ 100) whose origins are smeared in z.

2.9.2 Trigger Level Two – L2

The L1 trigger decisions are validated by the *second level trigger* (SLT, L2).

The SLT system consists of two independent trigger systems, the Neural Network (L2NN) and the Topological Trigger (L2TT). L2NN and L2TT have to decide within 20μs whether the event should be accepted. Otherwise it will be rejected and the central trigger restarts the pipelines (*L2-reject* signal). The L2 Trigger gets L2-information from the subdetectors. Some trigger systems generate dedicated information for the L2 trigger. This information is used to validate or reject the L1 trigger decision.

The results of the L2 trigger are given to the central trigger L2 decision logic (CTL2).

L2NN: This trigger is based on neural networks (NN). The networks have been trained with samples of *ep* and background events. For the neural network trigger, parallel processors are used. The L2NN trigger is described in detail in [57].

L2TT: The topological trigger (TT) is based on a matrix which represents the geometry of the detector in the (θ, φ) space. The L2 input data are received and are preprocessed into a Boolean projection onto the (θ, φ). A "distance to background" is calculated to find a trigger decision [58].

Following a L2 decision, the readout of the $\approx$ 270.000 channels of the H1 detector components begins.

2.9.3 Trigger Level Three – L3

The L3 trigger system, based on software algorithms running on RISC (Reduced Instruction Set Computer) multiprocessors, redefines the L2 trigger decision, potentially causing an abort of the readout if the event is to be rejected (*L3-reject* signal). It calculates invariant masses and topological quantities. The L3 Trigger was not set up prior to the HERA upgrade in 2000. The L3 algorithms benefit from the new *Fast Track Trigger* (FTT) by reconstructing tracks, looking for resonances and jet-like structures. It is able to detect different structures or topologies within 50 μs [59].

2.9.4 L4/5 Processing

For the fourth trigger level the complete detector information is transferred to the filter farms at a rate of 50 Hz. Processors reconstruct the event. The online calculation of the trajectory, energy signature and momentum of all the particles of the event are used for event classification. If the signature matches the selection criteria of an *ep*-event, all the detector information is written to tape resulting in a rate of approximately 5 Hz [60]. The events are then written to the *Production Ouput Tape* (POT) (100 kB per event). A subset of the POT information is duplicated to the *Data Summary Tapes* (DST, 10 kB per event) which is usually sufficient for most of the data analyses.

Chapter 3

Kinematics Reconstruction and Simulations

Contents

3.1 Kinematics Reconstruction

The HERA collider experiments allow DIS kinematics to be reconstructed using the scattered electron (positron), the hadronic final state or a combination of the two. This is important for maximum coverage of the kinematic range and the control of systematic uncertainties.

3.1.1 Electron method

In the electron method ('e method') [61], the energy, E'_e, and the polar angle, θ_e, of the scattered electron measured relative to the proton beam direction are used to determine the variables

$$y_e = \frac{p_p.q}{p_p.p_e} \simeq 1 - \frac{E'_e(1-\cos\theta_e)}{2E_e} \tag{3.1}$$

$$Q^2_e = \frac{P^2_{T,e}}{1-y_e} = 2E_eE'_e(1+\cos\theta_e) \tag{3.2}$$

$$x_e = \frac{Q^2}{2p_p.q} \simeq \frac{Q^2_e}{sy_e} \tag{3.3}$$

where $P_{T,e} = E'_e \sin\theta_e$, s is the center of mass energy squared, E_e (E'_e) is the energy of the initial (scattered) electron, Q^2_e is the momentum transfer to the proton, y is the fraction of the electron energy carried by the (virtual) photon in the proton rest frame, x (Bjorken x) is the fraction of the proton energy carried by the struck quark and W is the hadronic invariant mass. The $\simeq$ sign indicates that the masses of the particles are neglected.

The e method has excellent resolution in Q^2 and in x at large y. Since the incident beam energy E_e appears both in Q^2_e and in y_e, this method is thus sensitive to the initial state radiation.

3.1.2 Hadron method

For the charged current interactions the kinematic variables can only be reconstructed using the hadronic final state because the neutrino is not detected. To characterize the hadronic final state, it is convenient to introduce the quantity Σ_h, the transverse momen-

tum $P_{T,h}$, and the inclusive angle γ_h by

$$\Sigma_h = \sum_i (E_i - p_{z,i}) \tag{3.4}$$

$$P_{T,h} = \sqrt{\left(\sum_i p_{x,i}\right)^2 + \left(\sum_i p_{y,i}\right)^2} \tag{3.5}$$

$$\tan\frac{\gamma_h}{2} = \frac{\Sigma_h}{P_{T,h}}. \tag{3.6}$$

Here E_i and $p_{z,i}$ are the energy and longitudinal momentum component of the i-th particle, and $p_{x,i}$, $p_{y,i}$ are its momentum components in the plane orthogonal to the z-axis. The summation is over all hadronic final state particles, whose rest masses are neglected. The kinematic variables are then obtained from [62]:

$$y_h = \frac{\Sigma_h}{2E_e}, \quad Q_h^2 = \frac{P_{T,h}^2}{1-y_h}, \quad x_h = \frac{Q_h^2}{sy_h}. \tag{3.7}$$

This method (h method) gives moderate precision in the reconstruction of the kinematic variables because of particle losses in the beam-pipe and because of fluctuations of the detector response to hadronic final state particles.

3.1.3 Double Angle method

The kinematics variables can also be reconstructed using the electron polar angle, θ_e, and the inclusive hadronic polar angle, θ_h, which is the polar angle of the scattered quark in the QPM with massless quarks. This is the so-called Double Angle (DA) method, firstly introduced in [63]

$$Q^2_{\mathrm{DA}} = \frac{E_e}{E_p}\frac{s}{\alpha_e(\alpha_e+\alpha_h)}, \tag{3.8}$$

$$y_{\mathrm{DA}} = \frac{\alpha_h}{\alpha_e+\alpha_h}, \tag{3.9}$$

$$x_{\mathrm{DA}} = \frac{Q^2_{\mathrm{DA}}}{sy_{\mathrm{DA}}}, \tag{3.10}$$

with

$$\alpha_e \equiv \tan\frac{\theta_e}{2} = \frac{\Sigma_e}{P_{T,e}}, \tag{3.11}$$

$$\alpha_h \equiv \tan\frac{\theta_h}{2} = \frac{\Sigma_h}{P_{T,h}} \tag{3.12}$$

$$\Sigma_e \equiv E'_e - P_{z,e} \tag{3.13}$$

The DA method is sensitive to photon emission of the primary electron. It reconstructs the angle with good precision when part of the current jet disappears down the beam-pipe. This means that it is independent of fluctuations on the energy measurement of the current jet.

This method was widely used in various analyses to check and improve the energy scale of the scattered electron and of the hadronic system.

3.1.4 Sigma (Σ) method

The Σ method allows measurement [64] in large kinematic domain, and in particular in low x - low Q^2 region with small systematic errors and small radiative corrections.

One can determine y and Q^2 independently of the initial state radiation by reconstructing the incident electron energy. Since the energy-momentum is conserved, the measured quantity $E - P_z$ is equal to two times the electron beam energy, if no particle escape detection:

$$E - P_z \equiv \Sigma_h + E'_e(1 - \cos\theta_e) = 2E_e. \tag{3.14}$$

We can obtain from y_h a new expression y_Σ which gives y at the hard interaction vertex even if an ISR photon is emitted:

$$y_\Sigma = \frac{\Sigma_h}{\Sigma_h + E(1 - \cos\theta_e)}. \tag{3.15}$$

At high y, Σ_h dominates over $E(1-\cos\theta_e)$, and the fluctuation and errors on Σ_h start reducing between numerator and denominator, allowing an optimal y reconstruction when using the hadron. From E'_e, θ_e and Σ_h we determine $Q^2_{\Sigma_h}$, also independent of ISR when assuming that an initial state radiated photon which is collinear to the beam line do not carry transverse momentum

$$Q^2_{\Sigma_h} = \frac{E'^2_e \sin^2\theta_e}{1 - y_{\Sigma_h}} \equiv \frac{P^2_{T,e}}{1 - y_{\Sigma_h}}. \tag{3.16}$$

We can thus obtain x_Σ

$$x_{\Sigma_h} = \frac{Q^2_{\Sigma_h}}{s y_{\Sigma_h}} = \frac{P^2_{T,e}}{s y_{\Sigma_h}(1 - y_{\Sigma_h})}. \tag{3.17}$$

This method has high precision at high y allowing to cross check the e method in this region. Also y_Σ and Q^2_Σ are ISR independent, the radiative correction to the Σ method are smaller than to other methods.

3.1.5 Electron-sigma ($e\Sigma$) method

A combination of the e and Σ method, the $e\Sigma$ method [64], is used to optimize the kinematic reconstruction in the neutral current measurement. Q^2_e is taken from the e method and x from the Σ method. Both these variables display good resolution in the complete kinematic range and the radiative corrections remain small compared to those of the e method. The formulae for the $e\Sigma$ method are

$$y_{e\Sigma} = \frac{2E_e}{E - p_z} y_\Sigma \qquad Q^2_{e\Sigma} = \frac{P^2_{T,e}}{1 - y_e} \qquad x_{e\Sigma} = \frac{P^2_{T,e}}{s y_\Sigma (1 - y_\Sigma)}. \tag{3.18}$$

3.1.6 Modified sigma method

Another method which is used in this analysis for the NC cross section measurement is the "modified Σ method" [65]. In this method the Q^2 remains the same as in the Σ method. The only change is

$$x_\Sigma = \frac{Q^2_\Sigma}{y_\Sigma s} \longrightarrow x_{\Sigma'} = \frac{Q^2_\Sigma}{s y_\Sigma \times (1 - y_e + y_h)} \tag{3.19}$$

The term $1 - y_e + y_h$ was introduced in the denominator with purpose to have a better resolution of x at high y which is demonstrated in figure 3.1.

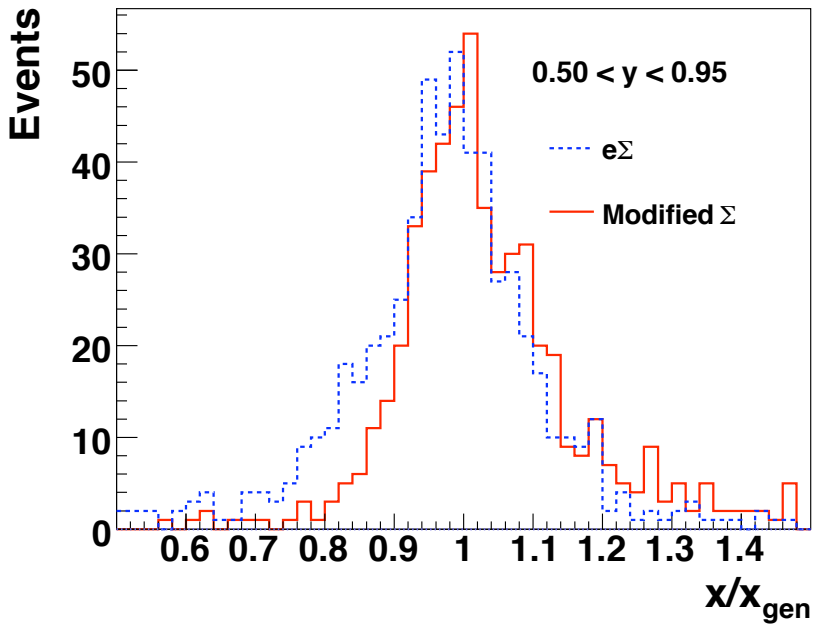

Figure 3.1: The x variable calculated by Modified Σ-method and by $e\Sigma$ method compared to the generated one at high y. The Modified Σ-method has better resolution.

3.2 Monte Carlo technique and simulation

The Monte Carlo (MC) methods have been widely used to control physics measurements. For a cross section measurement, MC can be used to determine the correction for acceptance, efficiencies, stability of the measurement, background contamination or the resolution of detector components which are often difficult to determine from data for different reasons. Because of the reliance on repeated calculation, the MC can therefore provide in principle unlimited event samples, which allow one to model the data with better precision. The simulated MC events are also very useful in defining variables, tuning cuts for selecting events from various background contributions.

For these reasons, the characteristics of the detector must be correctly simulated. The selection efficiencies, detector calibration, detector alignment can be determined from the data, the MC simulation is corrected as necessary in order to model the observed detector effects in data.

3.2.1 Detector simulation

In order to determine acceptance correction and background contributions, the detector response to events produced by various MC generation programs is simulated in detail by the H1SIM package [66] based on GEANT3 [67] which models the passage of the particles through the detector. The parameters used by this program were determined in test-beam measurements and optimized during data taking. A fast parameterization of the development of electromagnetic and hadronic showers is used in the simulation of the energy response of the calorimeters. The simulated detector readout for each event is finally led into the reconstruction software, H1REC [68]. Here, as for data, the H1REC software provides a summary of the event.

3.2.2 Generation of Neutral Current and Charged Current DIS events

The signal DIS events are generated using the DJANGO [69] MC generation program, which is based on LEPTO [70] for the hard interaction and HERACLES [71] for single photon emission off the lepton line and virtual EW corrections. LEPTO combines $\mathcal{O}(\alpha_s)$ matrix elements with higher order QCD effects using the colour dipole model as implemented in ARIADNE [72]. The JETSET program is used to simulate the hadronization process [73]. In the event generation the DIS cross section is calculated with the PDFs of [74]. The simulated cross section is reweighted using a NLO QCD fit (H1PDF 2009 fit [37]) to HERA-I data which is independent of HERA-II data.

3.2.3 Generation of background events

Monte Carlo simulations can also be used to help definition of variables and tuning of the cuts in order to discriminate signal events from background, and estimate the remaining background contamination. Backgrounds to DIS are categorized into those that can arise from *ep* physics and non-*ep* background sources. The non-*ep* background subtraction is discussed in Sec.4.5.

The background from *ep* induced processes can have detector signatures indistinguishable from DIS events. Therefore there is no alternative to estimate the contributions with Monte Carlo method. The following processes are the main background contribution.

Photoproduction

Photoproduction is the dominant background contribution to both CC and NC processes of DIS. At very low four-momentum transfer squared ($Q^2 \approx 0$), the proton interacts with a quasi-real photon (with negligible virtuality), emitted by the electron (see section1.6.1). Generally, the electron scattered through a small angle is not detected in the central part of the detector. However, a particle from the hadronic final state can be mis-identified as the scattered electron and the event could be misidentified as a DIS NC. In another case, the photoproduction events can 'obtain' a missing transverse momentum in the detector when some hadronic final state particles escape from the detection, and (or) by imperfect measurement of the hadronic final state due to limited detector acceptance and resolution. In that case the event can be misclassified as a DIS CC.

The photoproduction is simulated using the PYTHIA [75] MC with leading order PDFs for the proton taken from CTEQ 5L [76] and for the photon from GRV 98 [77].

Elastic and inelastic QED Compton

These sorts of events are treated as background processes since the exchanged photon has a low Q^2. A large four-momentum transfer between the final state electron and photon can scatter both particles into the central part of the detector. The Compton events are generated by the program WABGEN MC generator [78].

Lepton-pair production

Elastic and inelastic $\gamma\gamma$ processes producing pairs of leptons (l), $ep \rightarrow epl^+l^-(eXl^+l^-)$, are generated using the GRAPE program [79].

W-Z production

The real production of heavy gauge bosons, $ep \rightarrow eXW^{\pm}(eXZ)$ reactions which are followed by leptonic decays of the W or Z, is generated using the EPVEC [80] program.

Chapter 4

Event reconstruction and analysis

Contents

In this chapter we will give a brief description of the H1OO (H1 Object-Oriented) analysis framework [81] at HERA-II and its event reconstruction algorithm.

The main aim of the H1OO software is to substantially enhance the physics capabilities of H1 software and - at the same time - to reduce the turn-around time of physics analyses.

Data format

The data for physics analyses are stored in a three-layer system. The lowest level (ODS, Object Data Store) is produced from DST (Data Summary Tape) or POT (Production Output Tape) such that the contents of the ODS are 1-to-1 equivalent to the DST. This requirement facilitates backward conversion from ODS to DST without information loss. In practice, to avoid duplication of information on disk, the ODS layer is usually created "on the fly" when accessing the DST. The DST contents are read and an ODS information for the event is created in memory. Two additional layers μODS (micro ODS) and HAT (H1 Analysis Tag) contain calibrated and selected analysis-ready particle information (μODS) and event-level information (HAT). μODS ($\sim$ kB/event) and HAT ($\sim$ KB/event) are much smaller in size than the ODS, allowing a substantially faster selection of the events.

The selection power is further increased by providing selection flags for individual analyses at both event and particle level. Moreover, for the selection at HAT-level a RooT-eventlist [82] is generated and kept in memory throughout the analysis session. The relations between the different pieces of information for a given event are managed by the H1Tree class. This is shown schematically in figure 4.1. Direct links between particle information (μODS) and track and cluster information (ODS) are implemented with the help of the H1Pointer class.

4.1 Particle finders

In H1OO, the particle finders are performed on ODS and μODS data and the results are stored on μODS.

4.1.1 Track selection

The purpose is to select 'good' tracks and remove the double counting due to different track hypotheses. A 'good' track is the one which passes all track cuts. In a first step the track cuts, different for each track type, are applied and in a second step, the best selected track hypothesis for one particle or track is taken. So the double counting is

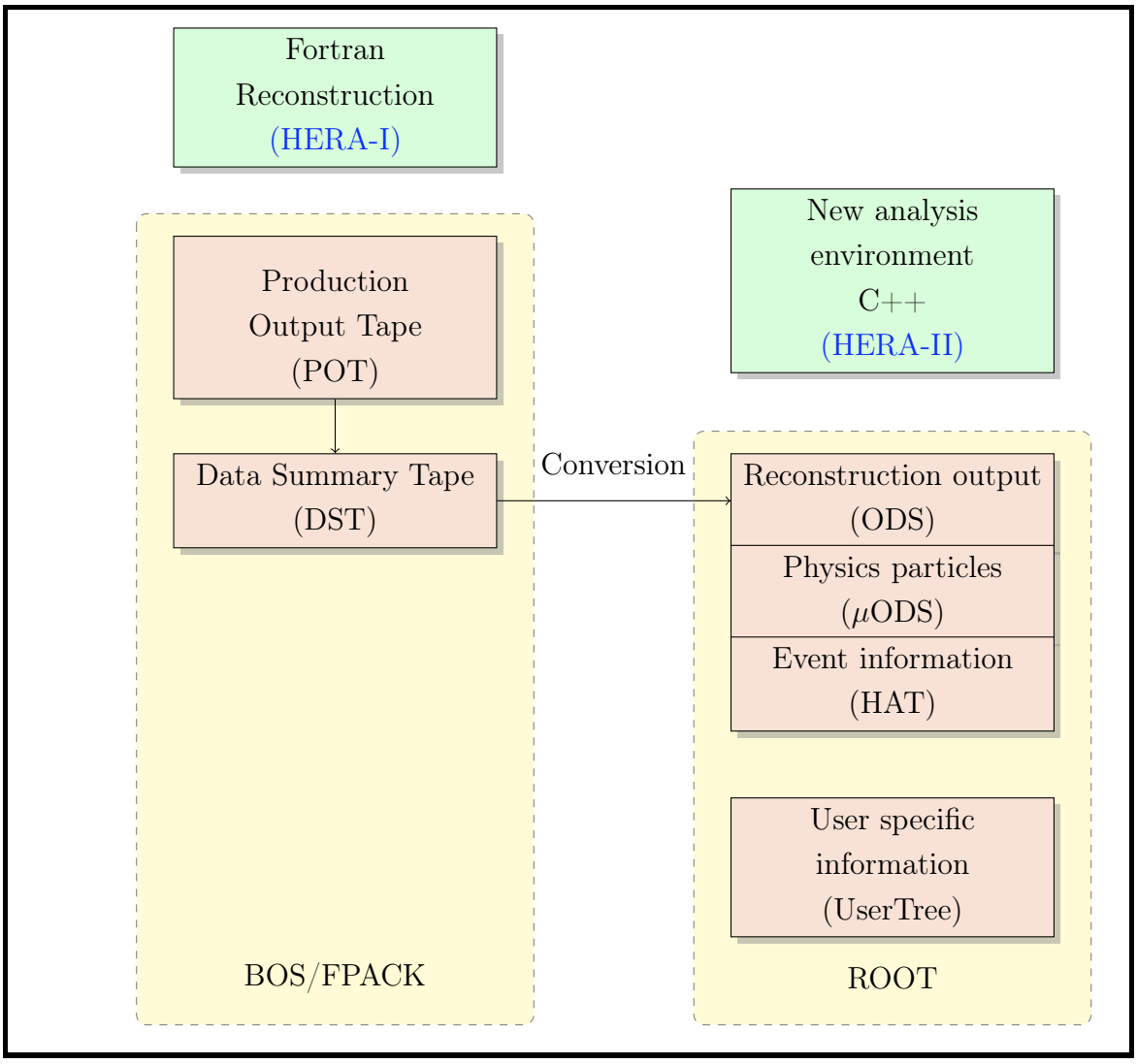

Figure 4.1: Schematic overview on different file levels. For a physics analysis, users access only μODS and HAT and eventually the User Tree.

removed. The best hypothesis candidate is the so-called 'Lee West track selection' which is originally invented by the Heavy Flavour Working Group [83][1].

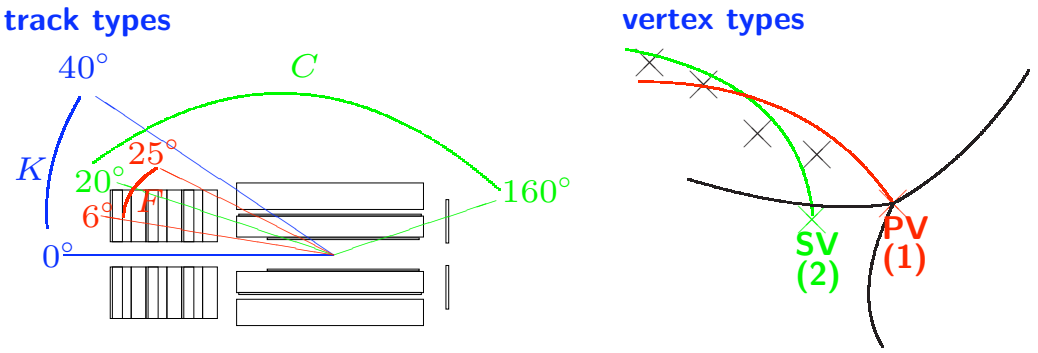

Figure 4.2: Different track types and their angular domain, and different vertex hypotheses for a single track: The selected track may be fitted to a primary or secondary vertex.

For a single track, one can have several hypotheses: the track measured only in central tracking devices (CJC, CST, z-chambers: central tracks), the track measured only with the FTD (forward track), and the combination of CJC and FTD measurement (combined track). Furthermore for a single track there can exist different vertex types: primary vertex (1), secondary vertex (2), ... (figure 4.2).

The 'good' tracks have to fulfill the cuts indicated in table 4.1 from [81]. For each single track all different selected track types are compared and the most preferred track type is chosen. If two track types are equal the track hypothesis with the most preferred vertex type is taken. Central tracks are taken in preference to combined and forward tracks and combined tracks are taken in preference to forward tracks. Furthermore tracks from the primary vertex are preferred to tracks from secondary vertices.

4.2 Electron finders

For neutral current analysis, it is indispensable to correctly identify the scattered electron in a final state with the purpose to minimize the contamination due to the processes which may have high momentum in final states and one may misidentify a pion as an electron.

[1] A Lee-West or a 'good' track is the track which passes all track cuts which are defined in [83].

Combined track (K)	**Central Tracks (C)**
$p_T > 120$ MeV	$p_T > 120$ MeV
$0° < \theta < 40°$	
$\|dca'\| \leq 5$ cm	$\|dca'. \sin\theta\| \leq 2$ cm
$R_{start} \leq 50$ cm	$R_{start} \leq 50$ cm
$R_{length} \geq 0$ cm	$R_{length} \geq 10$cm for $\theta \leq 150°$
$\Delta p/p \leq 99999.9$	$R_{length} \geq 5$cm for $\theta > 150°$
$N_{CJC\ hits} \geq 0$	$N_{CJC\ hits} \geq 0$
$\chi^2_{dtra} \leq 50$	
$\chi^2_{central-forward} \leq 50$	
Forward Tracks (F)	
$p_T > 1$ MeV	
$6° \leq \theta \leq 25°$	
$R_0 \leq 10$ cm	
$\chi^2_{dtnv} \leq 10$	
$\chi^2_{dtra} \leq 25$	
$nPrimSecPlanSeg \geq 1$	
$nPlanRadSeg \geq 2$	
$\Delta p/p \leq 9999.9$	
$p \geq 0,5$ GeV	

Table 4.1: Cuts used for the selection of good track says "Lee West" (cf. [81]). The *dca* and *dca′* are the distances of the closest approach of the track extrapolation to the vertex and the closest approach in the (x, y) plane to the vertex.

The electron finder is designed to identify electrons in the event and consists of two parts: the search for electrons in the LAr calorimeter and the search for electron in the SpaCal. The algorithms of the high Q^2 (LAr) finder and the low Q^2 algorithm are described here. In the default configuration, both searches are performed and an unlimited number of particle candidates with the flag `kIsEm` are created from clusters and tracks that fulfill the selection criteria. These clusters and tracks are locked and will not be used by other finders, e.g. for calculation of the energy in the HFS. In addition, an identified particle of type `H1PartEm` is created for each particle candidate.

All detector relevant information such as cluster radius, electromagnetic fraction, calorimeter type etc, are stored as data members of the identified electron (`H1PartEm`). The `H1PartCand` and `H1PartEm` are stored in the `H1ModsEvent`. Pointers between the two

classes allow to easily collect the full information for one candidate during analysis.

In order to be able to calculate the kinematics using scattered electron, one candidate is selected to be the scattered electron which has the highest P_T and isolated in both calorimeters LAr and SpaCal.

4.2.1 LAr electron finder

The electron finder for the LAr calorimeter is mainly based on the translation of the QESCAT fortran electron finder developed at HERA-I, whose main characteristics are described in [84].

Electron envelop

First of all, one needs to define an electromagnetic cluster and has to be sure that this object contains all the deposit energy by the electron. During the reconstruction the formation of the clusters is such that one electron corresponds to a cluster. However, if the deposit energy is closed to a crack one needs to associate more than one cluster to be able to measure correctly the electron. For this reason, from a cluster we are going to define an electron envelop, see figure 4.3: it is the cone with 7.5° around the axis which comes from the vertex to cluster barycenter. The envelop contains the electromagnetic section and the first layer of the hadronic part. All clusters with the barycenter inside this envelop will be considered as associated to the initial cluster.

The fiducial volume is a volume of the calorimeter where an electron is well measured. This volume excludes therefore the cracks. Since the trigger efficiency is relatively low and the energy is underestimated for a cluster which is closed to a ϕ-crack, i.e. when the electron passes through a crack, it looses a large amount of energy in the dead matter and the topology of the electromagnetic shower are not well measured. Hence, only the clusters with the closest distance to the crack larger than 4° and also if they contain at least 3 cells are considered.

The following characteristics are used to differentiate an electromagnetic shower to a hadronic one [84]:

- Electromagnetic fraction (EAEM): The electrons are expected to have energies such that they are stopped in the electromagnetic section of the calorimeter LAr. We define the electromagnetic fraction as $f_{\mathrm{em}} = E_{\mathrm{em}}/E_{\mathrm{tot}}$ where only the cells with positive energy are considered (E_{tot} is the total energy of the cluster).

- Transverse radius: $\sigma_R = \sqrt{(< r^2 > - < r >)}$, where r^n are moments of order n of the transverse distance (r_i).

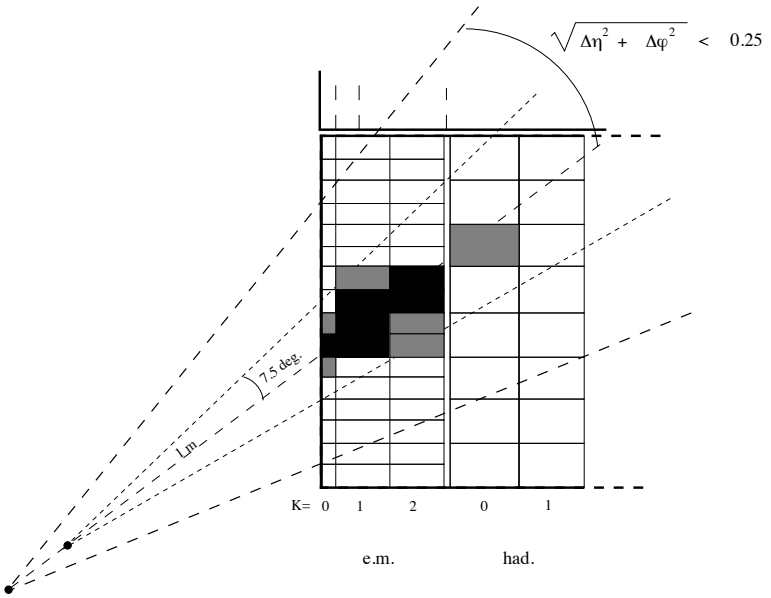

Figure 4.3: Schematic view of a electron signal in the LAr calorimeter. The electron envelop and the isolation cone are shown.

- Energy fraction in the "Hot" core (EAHN): EAHN $= E^N_{\rm Hot}/E_{\rm em}$, where $E^N_{\rm Hot}$ is the energy of the N most energetic neighbouring cells. N is defined according to the cluster position in the LAr calorimeter: $N = 4$ for BBE, $N = 8$ for CB3, FB1 and FB2 and $N = 12$ for IF.

- Isolation criteria: One uses the estimator EAIF $= E_{\rm tot}/E_{\rm iso}$ where $E_{\rm iso}$ is the energy in an isolation cone of radius $R_{\eta-\phi} = 0.25$ and $E_{\rm tot}$ is the total energy of the cluster. Then a cluster is considered as an electron if:

  - EAIF > 0.98
  - or EAIF > 0.95 and EHAD < 300 MeV where EHAD is the hadronic energy in the isolation cone.

Track-cluster matching

To differentiate the charged leptons from photons, a track associated to the cluster is also required. A track is associated to the electron cluster if its *dca* to the cluster is less than 12 cm. A track which passes all selection requirement (also called Lee West) is searched for first. If no LW matching track is found, then the search is performed for vertex fitted track (DTRA tracks) and if still not, for non-vertex fitted tracks (DTNV tracks). The algorithm chooses the closest track to the cluster. All information concerning the

matching track (θ, ϕ, P_T, ...) is stored as `H1PartEm` data members. In addition, the number of matching tracks with $dca_{\text{track-cluster}} < 12$ cm is counted for selected, vertex-fitted and non-vertex-fitted tracks are also stored as `H1PartEm` member. The track-cluster matching condition is applied only for $\theta_e > 30°$.

Isolation criteria

It is natural to use all possible information to optimize the identification of the scattered electron, particularly the topology of the event being considered. The scattered electron in a neutral current event is isolated in the calorimeter: it is alone in its own hemisphere if one excludes the fragment of the proton at very forward regions. The energy in a cone inside the electron envelop must be equal to that of the electron.

However, in some processes the electron is produced during a cascade of disintegration and it can be situated close to the particle jet. In that case, it is not well isolated (one part of the jet energy deposit is in the same place with the electron) and one cannot use the shape of the electromagnetic cluster. It thus needs to be sufficiently isolated so that one can correctly measure its energy. In H1OO, the identified electron is defined as isolated against the hadrons if the calorimeter energy is in a cone around the electron of radius $R_{\eta-\phi} = 0.5$ is less than 5% of the electron energy.

This electron finder will be used for the neutral current analysis.

4.2.2 SpaCal electron identification

For SpaCal clusters, the identification is also calorimetric. The minimal energy of the cluster is required to be at least 5 GeV. The transverse radius of the cluster is calculated using a logarithmic weighting must be less than 4 cm. Other criteria of the proximity with a track and of isolated lepton are the similar for the LAr calorimeter.

4.2.3 Jet-based identification

To be able to control the efficiency of the calorimetric identification, one uses a finder based on the tracks which is similar to a jet-finder algorithm. The selection criteria are the following:

- the good quality track (Lee West) with a transverse momentum $P_T > 2$ GeV at a distance of at least 0.5 in (η, ϕ) to the other tracks
- the deposit energy in the LAr in the cylinders of radius 30 and 50 cm around the extrapolation of the track must satisfy $E_{30}/E_{50} < 0.8$ (and 0.98 for electrons with a transverse momentum less than 3 GeV).

- the electromagnetic energy fraction in the cylinder must satisfy $f_{\text{em}} > 0.95$ (or 0.98)
- and also $0.25 < E_{\text{track}}/E_{\text{cluster}} < 3$ (or $0.25 < E_{\text{track}}/E_{\text{cluster}} < 1.5$).

4.3 Hadronic Final State finder

The default Hadron Final State finder, HADROO2 [85], is used in this analysis, it will be briefly described below. The inputs for this algorithm are tracks and clusters. The tracks selection is described above. Here we are going to detail the noise treatment which is applied to reconstruct clusters.

The clusters are aligned and beam-tilted in a proper way using run-dependent alignment factors (see Sec.6.3 for details). Calorimetric clusters are made only out of LAr or SpaCal. Iron or Plug cluster are not considered (beside the mediocre energy resolution of the Iron calorimeter, a significant fraction of Iron clusters are noise or background). If a cluster in LAr have cells in Iron or Plug, these cells are removed from the cluster. Note that the negative energy cells in clusters are kept as it must be to avoid a systematic positive bias in energy measurements.

The cluster energy momentum four-vector is made of the addition of massless cells four-vectors (in this way cluster acquire a "mass"). The position of the center of gravity is determined with a linear energy weighting of the cells positions.

4.3.1 Weighting

As the LAr has the well-known behaviour of being non-compensating, weighting algorithms are necessary to compensate the lower response to hadrons with respect to electron for a same energy. Such a weighting procedure is already applied at the reconstruction level, in H1REC, identifying clusters as originating from electromagnetic particles or from hadrons.

In the HADROO2 algorithm this classification was modified. All clusters with at least 95% of their energy in electromagnetic part and with also 50% of it in the first two layers of the electromagnetic calorimeter are taken at the electromagnetic scale. All other clusters are considered as originating from hadrons and the hadronic energy scale, determined by the H1REC weighting algorithm, is considered.

4.3.2 Noise suppression

All the measurements relying on the LAr calorimeter are affected by a relatively large amount of noise (a few GeV per event). This noise is due to detector effects such as noise

in the electronics or pile-up deposition of energy coming from non-*ep* physics like halo or cosmic muons. The impact of this noise on physics analysis is clearly not negligible. For an inclusive analysis, the distribution

$$y_h = \frac{\sum_h E_h - P_{z,h}}{2E_e} \tag{4.1}$$

is specially affected [86, 87]. At low y_h (when $E_h \sim P_{z,h}$) most of the hadrons produced in the forward direction. Any noisy cluster misidentified as part of the hadronic final state will count in the sum of equation 4.1 with a weight increasing with θ. So even relatively low energy noisy clusters in the barrel part of the LAr will strongly bias the y_h distribution.

The following strategy is applied to suppress noise: First all one-cell clusters are considered as not physical and removed, as well as clusters with energy $E_{\text{clu}} < 0.2$ GeV in LAr or 0.1 GeV in SpaCal. Then a set of noise finders are applied:

- The FSCLUS algorithm (cf. [88]): suppresses low energy isolated clusters. If the energy of a cluster is such that $E_{\text{clu}} < E_1$ the energy E_{sphere} in a sphere of radius R around the cluster is computed and if $E_{\text{sphere}} < E_2$ then the cluster is suppressed. This allows low energy cluster to survive if they are near more energetic ones (e.g. if they are due to a shower fluctuation). The values for different threshold are $E_1 = E_2 = 0.4$ GeV and $R = 40$ cm for $\theta_{\text{clu}} > 15°$, $E_1 = E_2 = 0.8$ GeV and $R = 20$ cm for $\theta_{\text{clu}} < 15°$. Consistently with the first suppression the threshold E_1 is lowered to 0.2 GeV for clusters in the electromagnetic part of LAr. Clusters near the beam pipe in the SpaCal calorimeter are also suppressed if $\sqrt{x_{\text{clu}}^2 + y_{\text{clu}}^2} < 9.6$ cm.

- The HALOID algorithm [86]: is devoted to the suppression of energy deposit due to halo muons on top of real physics events. The signature is a narrow energy deposit parallel to the beam axis. To suppress such a pattern, for each cluster it is defined two cylinders of radius $R_1 = 25$ cm and $R_2 = 65$ cm. If there is energy deposit in these cylinders in at least 4 wheels including 2 CB wheels, and if at least two of the following criteria are true:

$$E_{\text{cylinder 1}} \geqslant 0.5\, E_{\text{cylinder 2}} \tag{4.2}$$

$$N_{\text{clusters in cylinder 1}} \geqslant 0.5\, N_{\text{clusters in cylinder 2}} \tag{4.3}$$

$$N_{\text{cells in cylinder 1}} \geqslant 0.5\, N_{\text{cells in cylinder 2}} \tag{4.4}$$

  the cluster is flagged as noise and suppressed.

- The HNOISE algorithm [86]: Contrary to halo muons, cosmic muons or coherent noise do not have a characteristic pattern of energy deposit. However, on general ground, any deposit in the hadronic part of LAr should be connected to activity in the electromagnetic part or linked with tracks. The HNOISE algorithm look for clusters in the hadronic part and suppress them if the following conditions are all fulfilled:

  - There is no energy deposit in the first hadronic layer or there is energy deposit in the first hadronic layer and there is no more energetic clusters at a distance less than 75 cm.
  - There is no electromagnetic energy in a safety cylinder of 50 cm radius. The axis of this cylinder is defined by the interaction vertex and the barycenter of the considered cluster.
  - There is no vertex fitted track with a *dca* of less than 50 cm.

  This finder helps again to remove a part of the noise, as shown in [86].

- The NEWSUP algorithm [86]: The NEWSUP algorithm is inspired form FSCLUS: it is designed to suppress low energy isolated clusters. However, to remove completely the noise a threshold higher than previously applied is needed, but only in the central region of LAr where the $E - P_z$ contribution of a false particle candidate biases the y_h of the event by a large value. Contrary to FSCLUS this algorithm care about track-cluster link and if there is a vertex fitted track with $dca \leqslant 25$ cm for an electromagnetic cluster or $dca \leqslant 50$ cm in the hadronic part the corresponding cluster is not suppressed. The same thresholds as in FSCLUS are applied, except that now $E_1 = E_2 = 1.5$ GeV for $\theta > \alpha_h$. The angle α_h is chosen to be the maximum between the angle of the most backward track and the inclusive hadronic angle. The algorithm is run iteratively until there is no cluster suppressed.

All the previous procedures are optimized on MC files which include halo or noise contributions selected from real data. Figure 4.4 shows the relative contribution of the LAr calorimeter, SpaCal and tracks to y_h as a function of y. The main contribution is coming from the LAr calorimeter. SpaCal contributes only at high y. These contributions are well described by the simulation. The contribution of noise to the measured y_h is also shown. For the remaining difference of the suppressed noise between data and MC, a systematic uncertainty of 10% is assigned to the energy identified as noise in the LAr calorimeter.

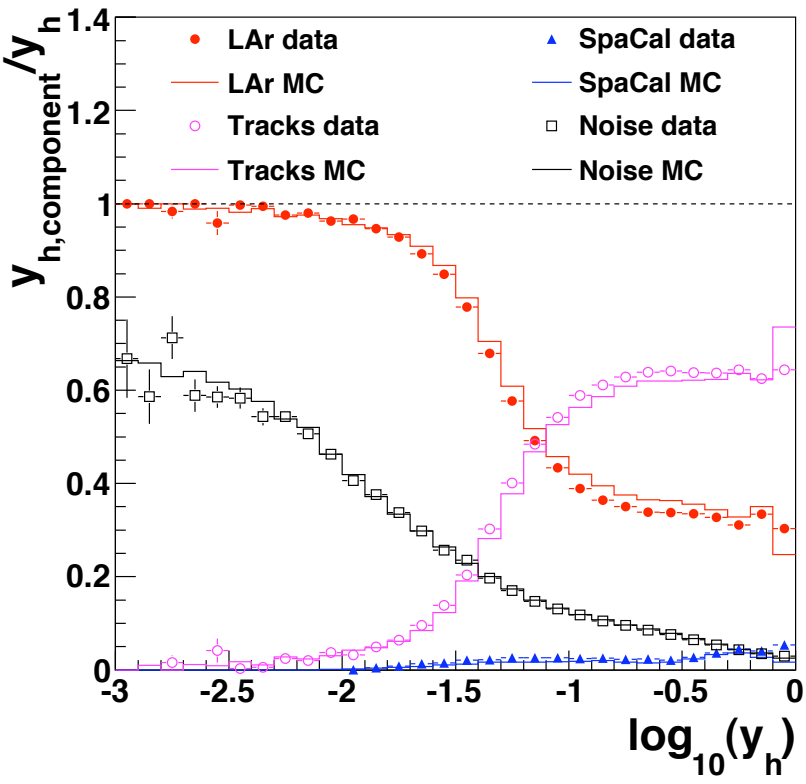

Figure 4.4: Relative contributions of the LAr, SpaCal calorimeters and tracks to the final y_h as a function of the inelasticity y and the suppressed noise contribution relative to the measured y_h. Comparison between data (points) and MC Django (histograms). Example is shown for 0607 $e^- p$ data.

4.3.3 The HADROO2 algorithm

The Hadroo2 algorithm realizes the creation of the HFS particles. Note that if there are identified electrons or muons which are not flagged as isolated, they are considered as being part of the Hadronic Final State but their four vector remains unchanged and their associated tracks and clusters are excluded from any additional treatment.

The algorithm starts with the previously described list of selected tracks and clusters. The cornerstone idea of the energy flow algorithm is the combination of the tracks and clusters. As we may have both for a charged particle, we want to keep the best measurement. To achieve this, relative resolutions of the tracker or of the calorimeter for the measurement of the same amount of energy are compared.

Comparison of tracker and calorimeter resolutions

Each track is supposed to originate from a pion, with energy

$$E^2_{\text{track}} = P^2_{\text{track}} + m^2_\pi = \frac{P^2_{T,\text{track}}}{\sin^2\theta} + m^2_\pi. \tag{4.5}$$

The error on this energy is obtained by standard error propagation using some of the track fitting error information:

$$\frac{\sigma_{E_{\text{track}}}}{E_{\text{track}}} = \frac{1}{E_{\text{track}}}\sqrt{\frac{P^2_{T,\text{track}}}{\sin^4\theta}\cos^2\theta\sigma^2_\theta + \frac{\sigma^2_{P_T}}{\sin^2\theta}} \tag{4.6}$$

where σ_{P_T} and σ_θ are the corresponding error on P_T and θ.

The corresponding error on the LAr measurement if the same energy is given by the hadronic energy resolution as

$$\frac{\sigma_E}{E}_{\text{ LAr expectation}} = \frac{\sigma_{E,\text{LAr expectation}}}{E_{\text{track}}} = \frac{0.5}{\sqrt{E_{\text{track}}}}. \tag{4.7}$$

The relative resolutions defined by Eqs. 4.6 and 4.7 are then compared to determine which of the tracker or the calorimeter provides the best measurement. The track is considered as a "good one" if

$$\frac{\sigma_{E_{\text{track}}}}{E_{\text{track}}} < \frac{\sigma_{E,\text{LAr expectation}}}{E_{\text{track}}}. \tag{4.8}$$

In this case the calorimetric energy is suppressed to avoid double counting. Each track is associated to the surface of the calorimeter as a helix, and inside LAr as a straight line. The calorimetric energy E_{cylinder} is computed as the sum of all clusters in the overlapping volume of a 67.4° cone and two cylinders of radius 25 cm in the electromagnetic part of LAr and 50 cm in the hadronic part. This volume will be referred hereafter as the "cylinder".

Then the track energy E_{track} is compared to the calorimetric energy inside the cylinder E_{cylinder}, taking into account possible fluctuations of both measurements within their standard errors. The well-measured E_{track} provides a constraint on the energy deposited by charged particles; so the calorimeter measurement is discarded unless E_{cylinder} fluctuates more than 1.96σ (the 95% Confidence Level) above E_{track}. In this case, the discrepancy is attributed to neutral particles with energy $E_{\text{cylinder}} - E_{\text{track}}$. This means that the calorimetric energy is reduced by energy of the track.

If the condition (4.8) is not satisfied then the energies E_{cylinder} and E_{track} are compared and if

$$E_{\text{track}} \in \left[E_{\text{cylinder}} - 1.96\sigma_{E_{\text{cylinder}}},\ E_{\text{cylinder}} + 1.96\sigma_{E_{\text{cylinder}}}\right] \tag{4.9}$$

(with $\sigma_{E_{\text{cylinder}}} = 0.5\sqrt{E_{\text{cylinder}}}$) the track energy is considered to be compatible with the calorimetric deposit and the calorimetric measurement is used to define a particle candidate. Otherwise, if

- $E_{\text{track}} < E_{\text{cylinder}} - 1.96\sigma_{E_{\text{cylinder}}}$, the track measurement is used and calorimetric energy is subtracted
- $E_{\text{track}} > E_{\text{cylinder}} - 1.96\sigma_{E_{\text{cylinder}}}$, the track is suppressed and a hadron is defined using the calorimetric clusters.

Once all the tracks have been treated, particles candidates are made out of remaining clusters using the calorimetric energies. The momentum of these clusters is rescaled to obtained massless particles. These particles correspond to neutral hadrons with no associated track or to charged particles with a badly measured track.

4.4 Calibration of hadronic energy

The understanding of the hadronic energy scale is crucial for numerous analyses. It is also determinant for the analyses studying the hadronic final states and the analysis of charged current events. In this section we are going to describe the principle of the hadronic calibration, the determination and application of the calibration constants.

4.4.1 Calibration principle

The principle of the so-called 'absolute' calibration is to coincide the transverse momentum of the hadronic system $P_{T,h}$ to that determined from the double-angle method, $P_{T,\text{DA}}$, using the NC events. The hadronic final state from Hadroo2 contains the tracks and clusters, one verifies that the tracks are calibrated by looking at the invariant mass of the K^0 reconstructed from the tracks of its disintegration to two pions, which is illustrated in figure 4.5. The track energy scale is better known with accuracy better than 1%. One needs thus to calibrate the $P_{T,h}$ only by changing the energy scale of the calorimetric clusters. The method of the calibration is derived from [89]. The reference quantities used for the calibration are determined with the double angle kinematics. The hadronic transverse momentum determined with this method is independent of the LAr energy calibration. The calibration is said to be absolute if the measured $P_{T,h}$ coïncides with the $P_{T,\text{DA}}$. The use of the double angle method as a reference has several consequences: first, the calibration sample chosen to determine the $P_{T,\text{DA}}$ measurement is well under control. Secondly this method does not rely on MC which is separately calibrated and no relative calibration is needed. Finally the method is also independent of the electron calibration.

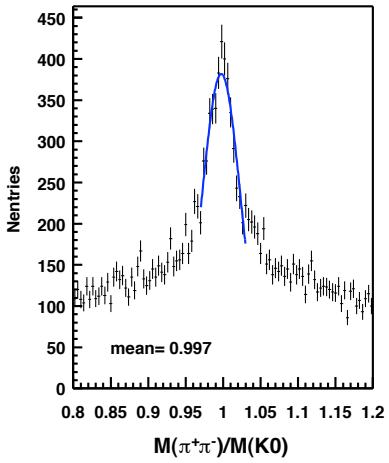

Figure 4.5: Invariant mass of the K^0 calculated from two-pions tracks of the disintegration.

4.4.2 Determination of the calibration constants

The event sample used to determine the calibration coefficients is defined by the following selection:

- Good quality selection (High Voltage, Vertex, background finders, ...),
- $Q^2 \geqslant 100$ GeV^2,
- one electron with $P_{T,e} \geqslant 10$ GeV,
- only one jet,
- good $P_{T,\mathrm{DA}}$ measurement cuts:
  - anti initial radiation state cut $P_{T,e}/P_{T,\mathrm{DA}} > 0.88$
  - anti leakage cuts: $E_{\mathrm{SpaCal}}/E_{\mathrm{Total}} < 1\%$
  - $P_T^{\mathrm{SpaCal}}/P_T^{\mathrm{Total}} < 1\%$
  - $E_{\mathrm{iron}}/E_{\mathrm{Total}} < 1\%$ or $P_T^{\mathrm{iron}}/P_T^{\mathrm{Total}} < 1\%$
  - $\mathrm{d}\theta = |\theta_{\mathrm{had}} - \theta_{\mathrm{jet}}| < 1.5$. This cut was shown to improve the double angle measurement at low P_T^{jet} and θ_{jet} (see [89]).

Figure (4.6) shows the ratio $P_{T,\mathrm{DA}}/P_{T,\mathrm{gen}}$ before and after the good $P_{T,\mathrm{DA}}$ measurement cuts for high Q^2 neutral current MC.

The improvement of the $P_{T,\mathrm{DA}}$ is clear, especially the bias of the $P_{T,\mathrm{DA}}$ to large values (due to initial QED radiation) is significantly reduced. Hence we can say that the double angle measurement are well under control. Note that no cut on the hadronic energy is used, because indeed such a cut would bias the distributions used to calibrate. In these

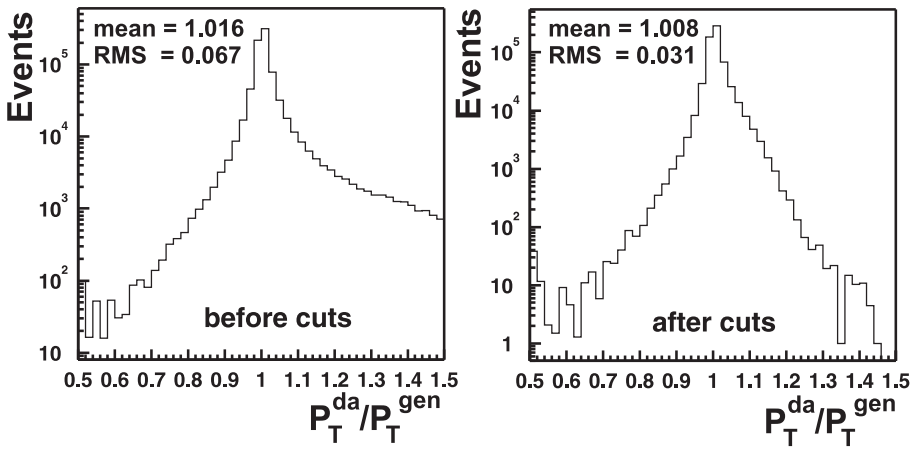

Figure 4.6: Distributions P_T^{da}/P_T^{gen} before and after application of the good quality selection of the double-angle transverse momentum.

one jet events the hadronic final state is entirely contained in a single material region of the LAr and we have an approximation of the difference between the true P_T of the jet (approximated as $P_{T,\mathrm{DA}}$) and the response (or lack of response) of the detector.

The evolution of mean values of $P_{T,\mathrm{bal}}$ distributions upon $P_{T,\mathrm{DA}}$ – called F_{ptbal} – is fitted separately for several θ regions. The functional form used for the fit is

$$F^{\theta}_{ptbal}(P_{T,\mathrm{DA}}) = A_\theta \left(1 - \mathrm{e}^{-B_\theta - C_\theta P_{T,\mathrm{DA}}}\right) \tag{4.10}$$

One example of the fit is shown in figure 4.7 for 2003-2004 e^+p data.

During the calibration procedure described in the next section each jet will then be corrected by this factor F_{ptbal}. But, as these coefficients are determined using an high P_T (greater than 10 GeV) selection, the extrapolation of F_{ptbal} to low P_T jets cannot be reliably trusted. Therefore, only jets with $P_T^{\mathrm{jet}} > 4$ GeV will be calibrated with this method.

4.4.3 Application of the calibration

In a first step all hadrons in jets will be calibrated, jet by jet. As the calibration should be applied only to clusters, we have to disentangle for each jet hadrons reconstructed from tracks and from clusters. For each jet we can define the fraction of P_T^{jet} carried by clusters before calibration C_{cls} as:

$$C_{\mathrm{cls}} = \frac{P_T^{\text{uncalibrated clusters}}}{P_T^{\mathrm{tracks}} + P_T^{\mathrm{uncalibratedclusters}}}. \tag{4.11}$$

The fraction of P_T^{jet} carried by tracks is the complement $(1 - C_{\mathrm{cls}})$. Note that here the fraction C_{cls} is an approximation because it is determined before any calibration of the

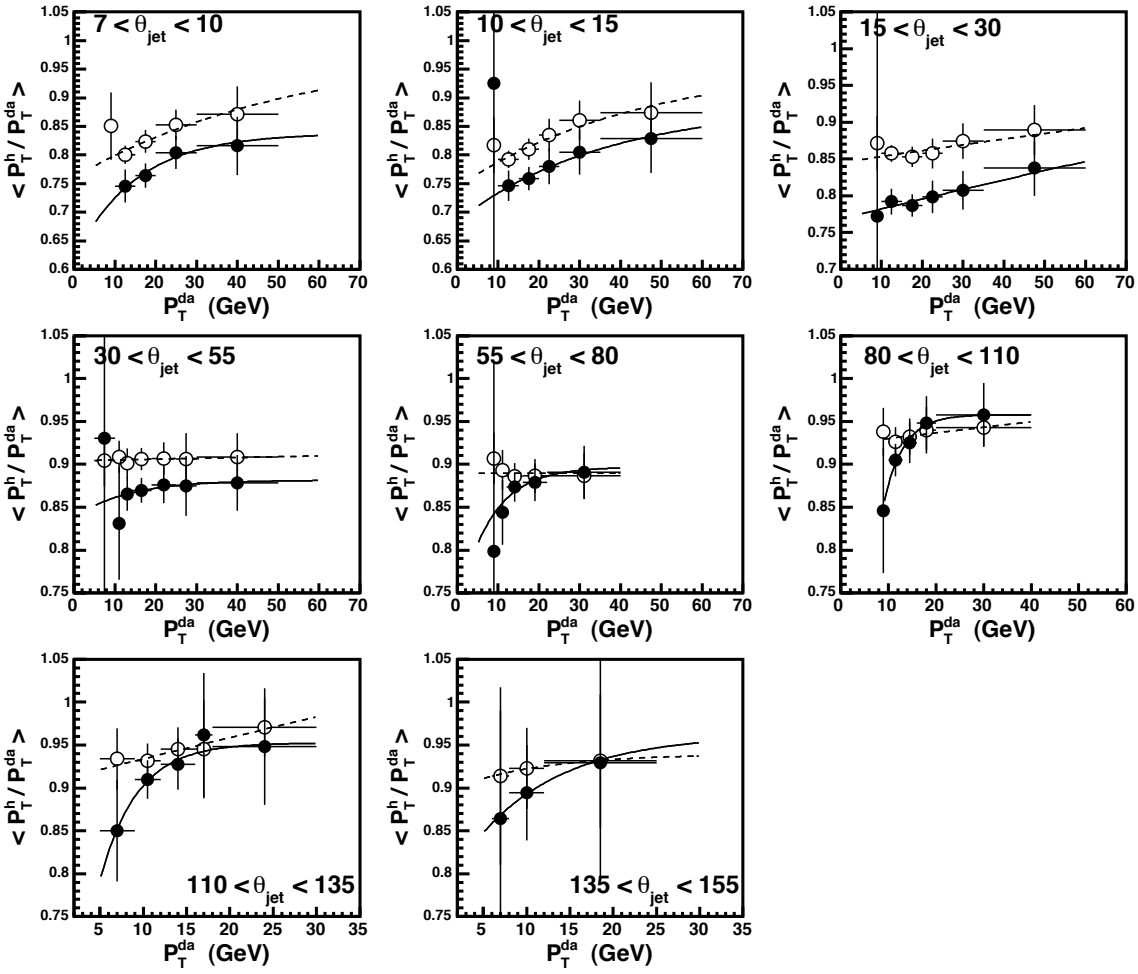

Figure 4.7: Evolution of the mean values of the $P_{T,\mathrm{bal}}$ distribtions with $P_{T,\mathrm{DA}}$ for the calibration sample in the different θ_{jet} regions. Solid and open circles stand for the data and MC, respectively. The plain and dashed lines are fits of the functional form of equation (4.10) to data and MC points, respectively. Example is for 0304 e^+p data.

energy of clusters. If F_{ptbal} is the absolute correction, it will be easy to see that the correction factor f we need to apply only to all clusters in the jets is given by

$$f = \frac{1 - F_{ptbal} \times (1 - C_{\rm cls})}{F_{ptbal} \times C_{\rm cls}}. \tag{4.12}$$

For each jet, F_{ptbal}, which was determined as functions of θ and $P_{T,\rm DA}$ (equation (4.10)), will be calculated using instead the mean polar angle of the jet $\theta_{\rm jet}$ and its transverse momentum $P_T^{\rm jet}$. Indeed $P_{T,\rm DA}$ can not be used now as, for a general selection, the double angle measurement may not be reliable and the total transverse momentum can be also shared between different jets. In order to have an approximation of the "true" transverse momentum an iterative procedure is used. The uncalibrated $P_T^{\rm jet}$ is used as the argument in equation (4.10) for a first approximation of f. The resulting $P_T^{\rm jet'}$ is then used to compute the final f which will be used to calibrate. For each jet the calibration is performed by multiplying the cluster energy by the f factor. Then in order to be consistent with the k_T jet (cf. [90, 91]) kinematics $\phi_{\rm jet}$, $\eta_{\rm jet}$, $P_T^{\rm jet}$ are properly recomputed and the final jet is massless.

4.5 Non-*ep* background rejection

Apart from the events produced by *ep* interactions, there is a large fraction of events still triggered and recorded containing particles which do not originate from the interaction of the electron with the proton beam. There are two main sources of such particles:

- *cosmic muons* produced when highly energetic cosmic particles hit the earth's atmosphere, and

- *halo muons* coming from interactions of the proton beam with the beam pipe wall or gas molecules in the beam pipe.

One means of suppressing such events is to use the timing information provided by some subdetectors. Indeed, most of the cosmics and halo events are already rejected during the data taking by including timing conditions in the trigger requirements. Another important fraction of the non-*ep* background recorded by the H1 data taking system can be suppressed by refined timing requirement. In order to identify the remaining fraction of the non-*ep* background, more sophisticated methods are necessary which are mainly based on *topological criteria* [92, 93], that is associations of tracks and clusters, the characteristic of beam-halo and cosmic muon events.

4.5.1 Background rejection with timing information

Most of non-*ep* background can be rejected by requiring the events to happen in coincidence with crossing of the electron and proton beams. Cosmics muons enter the detector uncorrelated with the electron and proton beams such that a sizeable reduction of the background can be achieved by requiring events to be measured in a small time window around the nominal bunch crossings. Since cosmic muons generally do not produce concentrated energy deposits suitable for time measurements in the LAr calorimeter, the timing information is derived from the proportional chambers CIP in the central tracking detector.

Halo events can also be significantly suppressed by the use of timing information. In beam-wall or beam-gas interaction typically a couple of secondary at varying energies are produced. Since the halo particles are in most cases almost parallel to the beam and do not traverse the proportional chambers in the central tracking detector, in general no track based timing information is available to reject halo events. Alternatively, due to the typically high calorimetric energy deposits associated with halos, a timing signals can be derived from the pulse shape of the signals in LAr bigtowers. This will be taken care by the ToF system.

For a first rejection we use the following selection

$$\left|T^0_{\mathrm{LAr}} - \left\langle T^0_{\mathrm{LAr}} \right\rangle\right| < 0.55 \text{ bunch crossing } (0.55 \times 96 = 53 \text{ ns}). \tag{4.13}$$

The size of the time window is commonly chosen to be 10% of the bunch crossing period BC for the event timing obtained from the drift chambers and 2% BC (2 ns) for the one reconstructed from the pulse shape in the calorimeter. For the use of T^0_{CJC}, one requires at least one good (Lee-West) central track for the measurement. The chosen values due to the two-peak structure in the T^0_{CJC} lead us to use the cuts

$$435 < T^0_{\mathrm{CJC}} < 510 \text{ ticks} \quad (\text{runs } 300000 \text{ to } 368000) \quad (500 \text{ ticks } = 96 \text{ ns}) \tag{4.14}$$

$$460 < T^0_{\mathrm{CJC}} < 510 \text{ ticks} \qquad (\text{runs} > 368000). \tag{4.15}$$

The value of T^0_{CJC} is quite stable as a function of time. This selection is however slack given by the fact that the resolution $\sigma_{T^0_{\mathrm{CJC}}}$ is in the order of 5 ticks (1 ns). A more strict selection is possible if one wants to take into account the fine time dependence of the $\langle T^0_{\mathrm{CJC}} \rangle$.

4.5.2 Topological finders

The topological finders are used to recognise and flag events having the signature of a high energetic penetrating particle typical for a beam-halo or cosmic muon event. The typical pattern observed in the majority of these background events is either

- Halo signature: Long, almost horizontal line of energy deposits in the LAr, possibly with matching iron tracks or tail catcher clusters in the endcaps

- Cosmic signature: Two matching iron tracks in opposite sides of the instrumented iron or one iron track matched by energy deposits concentrated inside a long cylinder with small radius in the LAr calorimeter.

Using these topologies, a set of background finder algorithms, called QBGFMAR [94], was developed to reject non-*ep* background which introduces minimal inefficiency to the MC signal events. At the analysis level, QBGFMAR is implemented in a bit coded formats and stored as the flag Ibg. A short description of each QBGFMAR finder is given in table 5.3 of [95].

Two additional sets of non-*ep* background finders, called $Ibgfm$ and $Ibgam$, have also been applied in this analysis. $Ibgfm$ is an extension of the QBGFMAR package and uses different combinations of QBGFMAR variables. The $Ibgfm$ finder is described in table 5.4 of [95]. The Ibgam bits 3, 4 and 8 are not applied since these finders cause an inefficiency much higher than 0.5% which is not acceptable.

A complement for these sets of background finders, developed in [49], was used to reject a large amount of events where there is no good quality track even there is a calometric activity in the central region. To reject this kind of events, one requires:

$$N_{\mathrm{LW}} = 0 \;\&\&\; (\gamma_h > 40^\circ \parallel \theta_{\mathrm{LAr}} > 20^\circ). \tag{4.16}$$

One remarks also the presence of events of which the number of non-vertex-fitted tracks, N_{DTNV}, is large compared to the number of vertex-fitted tracks, N_{DTRA}. These events are rejected by the condition:

$$N_{\mathrm{DTNV}}/N_{\mathrm{DTRA}} > 20. \tag{4.17}$$

The conditions 4.16 and 4.17 can suppress 60% of the remaining background and have an inefficiency of 0.15%.

A third sort of remaining events which are in the central region of the LAr with very small number of non-vertex-fitted tracks compared to large number of vertex-fitted tracks. The following condition is applied to reject these events:

$$N_{\mathrm{DTNV}}/N_{\mathrm{DTRA}} > 2 \;\&\&\; N_{\mathrm{DTRA}} < 3 \;\&\&\; \theta_{\mathrm{LAr}} > 40^\circ. \tag{4.18}$$

This cut can reject around 30% of the backgrounds and has an inefficiency of 0.3%. The rest of small fraction of events are partially rejected by requiring:

$$(d > 0.5 \;\&\&\; \theta_{\mathrm{cluster}} > 20^\circ) \parallel (d > 1 \;\&\&\; \theta_{\mathrm{cluster}} < 20^\circ) \tag{4.19}$$

where d is the distance in (η, ϕ) between any DTRA track and any cluster. This condition requires at least one track associated to a cluster.[2]

After all of these rejections, the remaining fraction of background of 1 to 2% will be rejected by eye scanning.

4.6 HERA-II datasets and MC

The high proton energy runs of second phase of HERA started in 2003 and ended in March 2007.[3] During this period, the detector was open twice, once between 2004 and 2005, and once between 2006 and 2007 for maintenance. Corresponding run type (electron or positron) and corresponding luminosity and polarization are summarized in table 4.2, the polarization profiles, i.e. luminosity versus polarization, are shown in figure 4.8. A run is considered as "good" if all the "major" systems are operational (tracking devices, LAr, luminosity system, SpaCal and central muon chambers). A run is referred to as a "medium" if at least one of the major systems is operational. These two kind of run will be kept for the analysis. If there is a serious hardware or software problem during the data taking, the run will be considered as "poor" and will be rejected. Another condition to acquiring a good run is based on the luminosity. If the minimum luminosity of a run is less than 0.2 nb^{-1} it will be rejected. An additional condition based on the polarization is also applied. For certain periods, if the polarization is below 10% or 20%, the run will not be considered. This will reject around 5% of the whole data sample.

In order to have precise analyses for each data period which can be time dependent due to different configuration and run condition of the detector, the data is therefore divided into sub-periods.

The same run selection is applied to MC samples which are simulated correspondingly to the run condition of each sub-period. The simulated MC luminosity is proportional to that of the sub-period with a factor of ~ 50. The generators for NC and CC events were mentioned in section 3.2.2 and for the background in section 3.2.3.

[2]The set of these cuts belongs to the so-called "track-cluster link" background finder. The total inefficiency is small (cf. figure 5.13(d)).

[3]The period from April 2007 to July 2007 is dedicated for low proton energy runs.

Data sample	Luminosity (pb^{-1})	Polarization (%)	Time periods
e^+p RH	98.1	$+32.5 \pm 1.2$	17/10/2003 – 01/04/2004
			02/07/2004 – 12/08/2004
			13/07/2006 – 06/12/2006
e^+p LH	81.9	-37.6 ± 1.4	08/04/2004 – 19/06/2004
			08/12/2006 – 20/03/2007
e^-p RH	45.9	$+36.9 \pm 2.3$	25/05/2005 – 06/09/2005
			05/05/2006 – 24/06/2006
e^-p LH	103.2	-26.1 ± 1.0	03/02/2005 – 18/05/2005
			09/09/2005 – 11/11/2005
			17/02/2006 – 01/05/2006

Table 4.2: Luminosity and average polarization weighted to luminosity for HERA-II. The error on polarization is total (statistic⊕systematic) error.

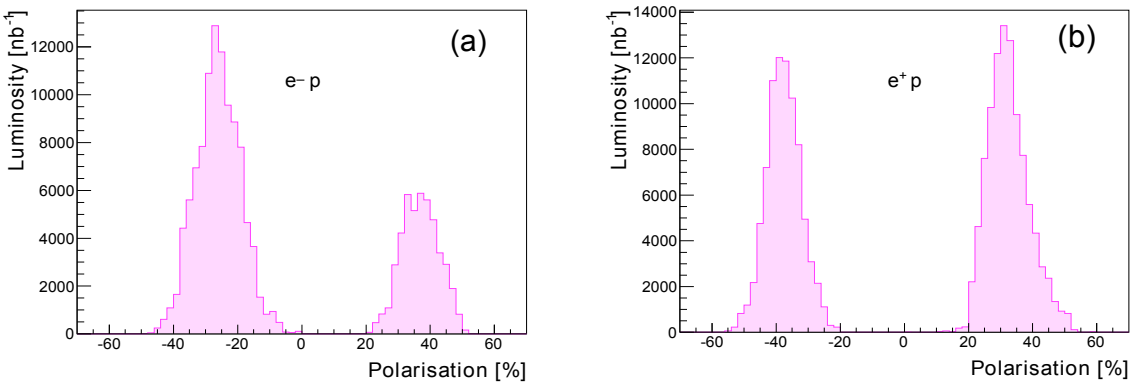

Figure 4.8: The luminosity weighted polarization profile for electron (a) and positron (b) data. The negative or positive in each plot correspond to left or right polarization.

Chapter 5

Measurement of the Charged Current cross section

Contents

This chapter is dedicated for the measurement of the Charged Current cross section. The cuts used for the selection of the CC events will be described and the optimization for the *ep* or non-*ep* background rejection will be presented. The chapter will end by giving the results of the CC cross section for the polarized electron (positron) scattering at HERA-II.

5.1 Charged Current event selection

5.1.1 Preselection

In order to reduce a large amount of non-CC events in the analyzed sample, a preselection is needed. An event can be preselected as a CC event if the following conditions are satisfied:

- only good and medium quality runs are accepted
- $P_{T,\mathrm{min}}^{\mathrm{LAr}}$ or $P_{T,\mathrm{miss}}^{\mathrm{tot}}$ is greater than 10 GeV (where P_T^{LAr} is the transverse momentum of all particles belonging to the hadronic final state which are measured in the LAr calorimeter and $P_{T,\mathrm{miss}}^{\mathrm{tot}}$ is the transverse momentum of the total hadronic final state);
- $V_{ap}/V_p < 0.35$, where $V_{\mathrm{ratio}} \equiv V_{ap}/V_p$ is the ratio of the two variables V_{ap} and V_p defined as:

$$V_{ap} = -\sum_i \frac{\vec{P}_{T,i} \cdot \vec{P}_{T,h}}{P_{T,h}} \quad \text{for} \quad \vec{P}_{T,i} \cdot \vec{P}_{T,h} < 0 \tag{5.1}$$

$$V_p = \sum_i \frac{\vec{P}_{T,i} \cdot \vec{P}_{T,h}}{P_{T,h}} \quad \text{for} \quad \vec{P}_{T,i} \cdot \vec{P}_{T,h} > 0 \tag{5.2}$$

  standing respectively for the transverse energy flow antiparallel and parallel to the direction of the transverse momentum of the event. The sums in 5.1 and 5.2 extend over all hadronic final states situated in the hemisphere which is *opposite to* or *along* $\vec{P}_{T,h}$. This variable was firstly introduced in [96]. Its definition is illustrated in figure 5.1.

- there is no "good" electron in the event. A good electron should be back-to-back with the hadronic system ($\Delta(\varphi_e, \varphi_{\mathrm{HFS}}) > 160°$) and isolated (the distance in η, φ to any jet is more than 1).

The preselected events are stored in μODS and HAT format and will be used for further selections.

s

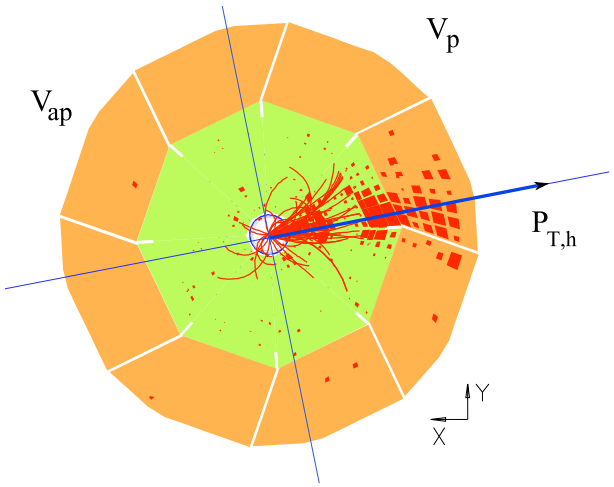

Figure 5.1: Schematic illustration of V_p, sum of projection of the cluster momentum which are parallel to the vector of total hadron final state momentum, and V_{ap} stands for the anti-parallel part.

5.1.2 Analysis selection

The following conditions are used as "standard" Charged Current cuts:

High Voltage requirement

The High Voltage (HV) requirement is an important data selection criterium which shows the operation status of the device. For example, the HV of the tracking system during a run may "trip" due to short beam instabilities resulting from a large particle flow in the detector. During such trips, the HV is temporarily switched off or reduced to protect the chambers. In contrast to the tracking system, HV is always applied for the LAr calorimeter. The HV status is checked on an event-by-event basis. The HV requirement is applied for LAr, CJC, CIP, ToF and luminosity system.

Polarisation and Luminosity

At least one of the polarimeters LPOL or TPOL is required to be in operational mode. The low polarisation and lumi below 0.2 pb^{-1} runs are also rejected in order to be sure that the detector operation was stable during the data taking.

Trigger requirement

The main characteristics of CC DIS events is the absence of balancing transverse momentum in the calorimeter. The missing transverse momentum, $P_{T,\mathrm{miss}}$, is carried by the final state neutrino which leaves the detector undetected and is defined as

$$P^2_{T,\mathrm{miss}} = P^2_X + P^2_Y = \left(\sum_i E_i \sin\theta_i \cos\varphi_i\right)^2 + \left(\sum_i E_i \sin\theta_i \sin\varphi_i\right)^2 \tag{5.3}$$

where the sum runs over all detected particles, E_i is the corresponding energy and θ_i, φ_i are respectively the polar and azimuthal angles of the particle with respect to the beam axis. The triggering of a charged current is thus based on the LAr_Etmiss trigger element and the event timing information (LAr_T0 and CIP_T0). In addition, global veto conditions (cf section 2.8) are applied to the subtriggers. The complete definitions of the charged current subtriggers as used in the present analysis are given in Table 5.1.

Subtrigger	Trigger elements	Description
ST66	(LAr_IF>1&& LAr_Etmiss>2) && (CIP_T0 || (LAr_T0 && !CIP_T0_nextBC)) && (FIT_IA || !FIT_BG)&& (!SPCLh_AToF_E_1 && !VETO_BG && !BToF_BG && !SToF_BG) && (!(CIP_MUL>7 && CIP_SIG==0))	phys. signature timing criteria veto condition
ST67	(LAr_electron_1) && (CIP_T0 || (LAr_T0 && !CIP_T0_nextBC)) && (FIT_IA || !FIT_BG) && (VETO_BG && !BToF_BG && !SToF_BG) && (!(CIP_MUL>7 && CIP_SIG==0))	phys. signature timing criteria veto condition
ST77	(CIP_SIG>0 && LAr_Etmiss>1) && (CIP_T0) && (FIT_IA || !FIT_BG) && (!BToF_BG && !SToF_BG) && (!(CIP_MUL>7) && CIP_SIG==0))	phys. signature timing criteria veto condition

Table 5.1: List of charged current subtriggers and their logical trigger element combinations.

Subtrigger 66 is designed to trigger events passing a high $E_{T,\mathrm{miss}}$ threshold in coincidence with deposited energy in the forward LAr region (LAr_IF>1). About 63% of charged current events are selected by this subtrigger.

Subtrigger 67 is designed for triggering of high Q^2 physics, especially NC events. The main element of ST67 is LAr_electron_1. This trigger is also very efficient to select the charged current events: about 82% of charged current events triggered by ST67.

Subtrigger 77 is the main charged current subtrigger. It triggers low unbalanced energy deposits in the LAr calorimeter: LAr_Etmiss>1 corresponds to low $E_{T,\text{miss}}$ threshold. This subtrigger is the most efficient for the triggering of charged current events with an efficiency of about 98%.

Figure 5.2 shows the fraction of CC events triggered by these three subtriggers.

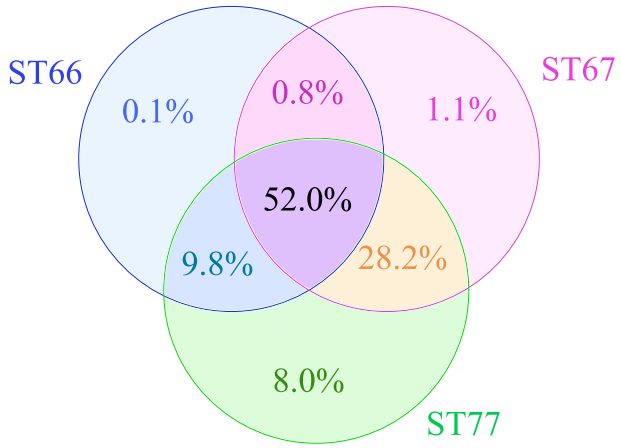

Figure 5.2: Fractions of CC events triggered by subtriggers ST66, ST67 and ST77. Example for combined $e^- p$ data.

More details on trigger description can be found in [95]. The trigger requirement is used as an OR logic: **ST66||ST67||ST77**.

Interaction vertex

The reconstructed z-vertex of the event is restricted to -35 cm $< z_{\text{vtx}} <$ 35 cm which corresponds to $\sim 3\sigma$ of the z-vertex distribution. The tracks satisfying this condition are measured in the central drift chamber (central vertex).

Transverse momentum and kinematic region

As mentioned above, one important characteristics of the charged current events is the missing transverse momentum, $P_{T,\text{miss}}$, which is caused by the undetected scattered neutrino. For the selection, it is used as the condition: $P_{T,\text{miss}} > 12$ GeV, since below this value, the trigger efficiency decreases rapidly and in contrast to that, the ep induced background increases.

An additional cut $y_h < 0.85$ is chosen also due to the poor resolution of the hadron method in x and Q^2 for high y_h and a cut $y_h > 0.03$ is determined since in the low y_h region the detector acceptance is low, the hadronic final state is partially lost in the beam pipe and thus degrading the trigger efficiency.

Background rejection

The background contribution to the CC analysis can be distinguished into two sorts: non-ep background and ep induced background.

The main ep induced background sources are: NC DIS events, photoproduction, QED Compton, lepton pair productions and W production. However, since the contributions of NC DIS and photoproduction are largest, the reoptimization focuses on the rejection of these two sources. For the reduction of the NC contribution to the CC sample, we introduced a new electron finder, see section 5.2, and revisited the anti-γp cut to against the photoproduction, see section 5.3. The non-ep background finders were introduced in section 4.5.

Timing conditions

The timing requirement for LAr and CJC are used as: $|T^0_{\mathrm{LAr}} - \langle T^0_{\mathrm{LAr}} \rangle| < 0.55$ bunch crossing ($0.55 \times 96 = 53$ ns) and $460 < T^0_{\mathrm{CJC}} < 510$ ticks or $88.3 < T^0_{\mathrm{CJC}} < 97.9$ ns for HERA-II data. Detail of the timing condition description is given in section 4.5.

5.2 New electron rejection cut for CC analysis

5.2.1 Motivation

One important contribution to the background for CC event sample is the NC events with misidentified scattered electron. One explanation for this misidentification is that for this kind of events, the electron might be scattered to the non sensitive regions of the detector, for example the cracks of the LAr or the edges of the SpaCal calorimeter. Consequently, the measured energy of the cluster is not sufficient to be reconstructed as an electron cluster and therefore the electron may not be identified by normal electron finder algorithms and therefore may not be rejected from the CC sample.

5.2.2 Description of the new electron finder

As mentioned above, the electrons which enter cracks in NC events are often misidentified due to not well measured cluster energy in the calorimeter. Due to this reason we are going

to use the information from the clusters, cells and corresponding tracks. The variables used for this finder are:

- *dca* (distance of the closest approach) of the closest track to the clusters
- $\Delta\varphi$ which is the difference on azimuthal angle between the cluster and the "hadronic final state". Here the hadronic final state should not contain the cluster being studied[1],
- isolation which is the ratio of the cell energies: sum of energy of all cells outside a cone of 10° around the barycenter of the cluster but inside another cone of 45° divided by the total energy inside the larger cone (cf. figure 5.3),
- P_T of the track associated to the cluster,
- hadronic energy fraction of the "electron" in the LAr calorimeter.

The procedure can be described as follows: First we make a loop over all clusters of the event. Inside this loop, all of possible tracks (central-fitted, forward-fitted and combined-fitted tracks) are checked in order to find the closest one to the barycenter of the cluster. If there exists at least one track and if the *dca* of the closest one is smaller than 25 cm, the track is considered as associated to the cluster. This *dca* as well as the P_T of the track are stored for further studies.

Still inside the loop, the barycenter of the cluster being considered will be taken as the center of gravity for the "electron" under searching. A second loop inside first loop will run over all cluster cells including the main one. To save time, we check only the clusters which are located not too far from the center, i.e. the conditions are required:

$$\Delta\theta = |\theta_{\text{cluster},i} - \theta_{\text{main cluster}}| < 90^{\circ} \tag{5.4}$$

$$\Delta\varphi = |\varphi_{\text{cluster},i} - \varphi_{\text{main cluster}}| < 90^{\circ}. \tag{5.5}$$

Keep in mind that the energy of an electron existing in a crack is not well measured. The idea is to regroup a set of cells existing inside a cone of 10° (this cone is originated to the interaction vertex and its axis contains both the vertex and the center of the initial cluster) to estimate the energy of the electron, E_{inner}. At the same time, the hadronic energy fraction of the cell is also regrouped. The energy of the cells laying outside this cone but inside a larger one of 45° is also counted. Let us denote this energy as E_{outer}. The schematic view of the cone is illustrated in figure 5.3.

[1]For each considered cluster, the final states will be taken as sum of all possible clusters except this one.

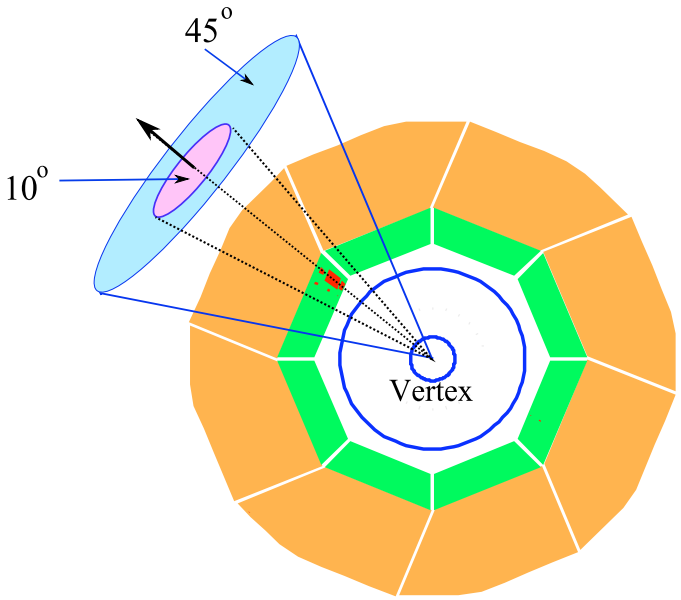

Figure 5.3: Schematic illustration of cone definition for electron finder: Inner and outer cones of $2 \times 5°$ and $2 \times 22.5°$, respectively. Both of cones are with axes containing the barycenter and the interaction vertex. The top of the two cones is at the vertex.

The isolation of the electron is then defined as:

$$Isolation = \frac{E_{\text{outer}}}{E_{\text{inner}} + E_{\text{outer}}}. \tag{5.6}$$

Moreover, a scattered electron should be back-to-back with the hadronic final state, so that the difference of φ-angle of the electron and that of the hadronic final state (which includes all clusters but not the one being checked), $\Delta\varphi_{\text{clus-hfs}}$ is calculated.

The events containing a cluster satisfying the following conditions will be stored:

- $dca_{\text{trk-clus}} < 25$ cm
- $\Delta\varphi_{\text{clus-hfs}} > 90°$
- $Isolation < 0.5$
- $P_T^{\text{track}} > 1.5$ GeV
- the electron candidate cluster is located in LAr or SpaCal calorimeters.

At the end of the main loop, the stored cluster which has largest polar angle, θ_{clus} will be chosen, and all related information of the the others will be deleted. Note that this set of parameters is used only as a preselection of NC candidates.

5.2.3 Parameters setting

For this study, we use a NC Django MC sample to be sure that all candidates are neutral current events. However the CC MC will be used to check the misidentification of the cut.

The main idea of introducing these parameters is based on the fact that:

- the scattered electrons are always back-to-back with the hadronic final state,
- moreover it must also be isolated from other particles.

The existence of the track and its small *dca* to the electron is verified to be sure that the electromagnetic particle is not a photon or π^0.

The procedure of the optimization is as follows: First we look at the correlations between different parameters $dca_{\mathrm{trk-clus}}$, $\Delta\varphi_{\mathrm{clus-hfs}}$, $Isolation$ and P_T^{track}. The correlation plots are shown in figure 5.4.

From figure 5.4(a), one can easily notice that most of the events are distributed at large $\Delta\varphi$ and small *dca* inside the triangle formed by the red line connecting two points ($\Delta\varphi = 130°$, $dca = 0$) and ($\Delta\varphi = 180°$, $dca = 20$). Similarly from figure 5.4(b), a triangle situated on the bottom-left corner can also cover most of events. The energy condition is done via the cut $P_T^{\mathrm{track}} > 3$ GeV which can be seen from figures 5.4(c), 5.4(e) and 5.4(f). All events which satisfy the conditions:

$$dca_{\mathrm{trk-clus}} < 20 \text{ cm} \tag{5.7}$$

$$isolation < 0.15 \tag{5.8}$$

$$\Delta\varphi_{\mathrm{trk-clus}} > 130° \tag{5.9}$$

$$P_T^{\mathrm{track}} > 3 \text{ GeV} \tag{5.10}$$

will be referred to as NC candidates with an electron. The hadronic energy fraction, F_{had}, is also stored for further studies.

5.2.4 Optimization

The aim of the optimization is to find the set of parameters for the cut which respects the following requirements:

- The efficiency of the selection must be highest possible.
- at the same time, the contamination must be small, i.e. for example if we use the CC MC sample for this study, the number of selected events should be minimized;

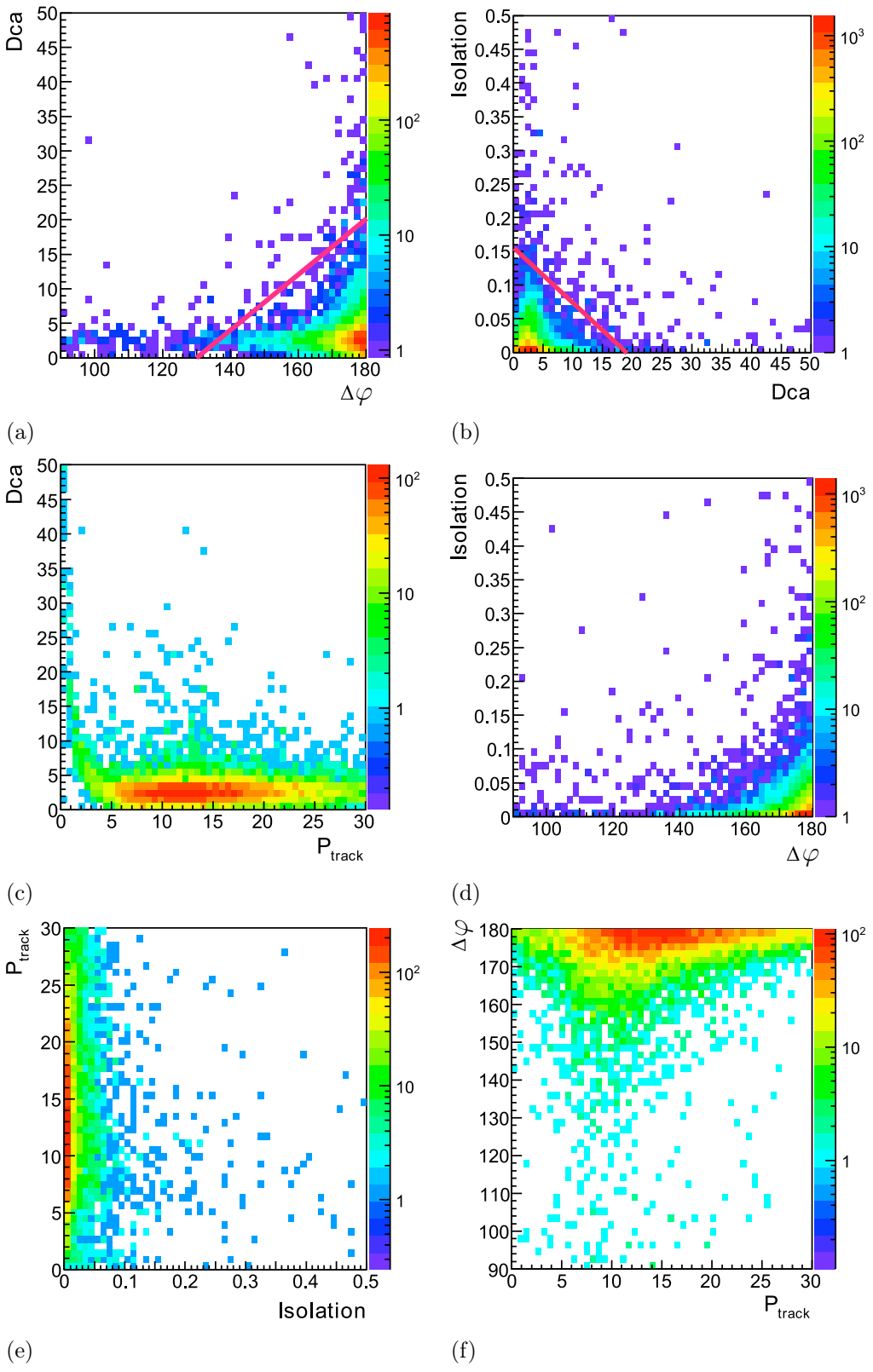

Figure 5.4: Correlation plots between different variables for electron candidates in NC events.

- an optimal cut should maximize the ratio S/B, with S and B being the numbers of signal and background (CC) events.

First of all, among the chosen parameters, one of them will be varied in the range where we expect it to be optimal, the others will be fixed. The corresponding values of the ratio S/B will then be plotted in function of the corresponding parameter in order to choose the value where the efficiency and S/B begins to saturate, i.e. where they reach the maximum value. This is shown in figure 5.5(a), the scan was performed for the *dca*.

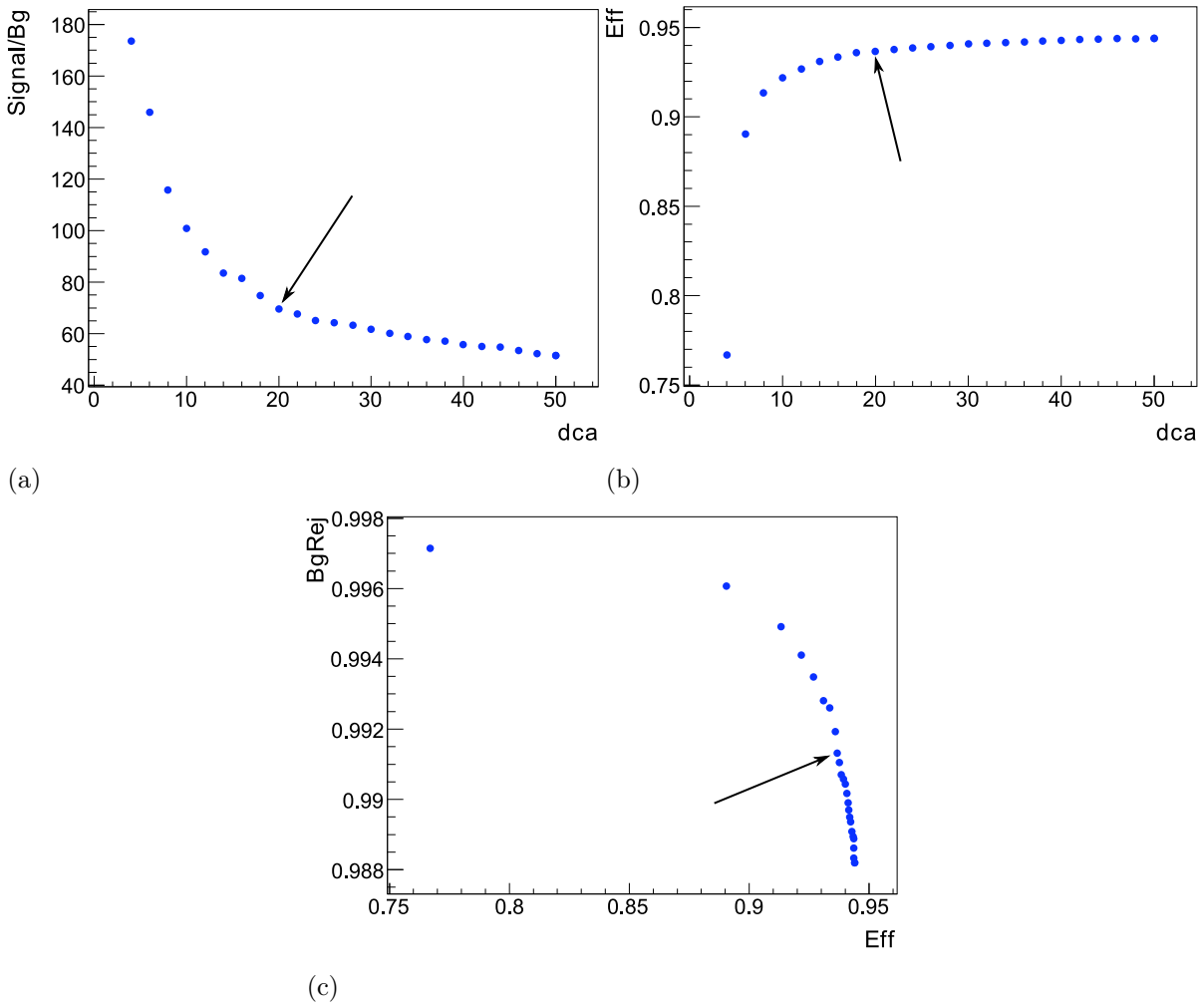

Figure 5.5: Scan for the parameter *dca*. Each point corresponds to a scan index. The arrows point to the chosen value of *dca*.

Another characteristics can be used to control the scan is the relation between the background rejection and the efficiency. The shape of the relation between these two quantities can be found in figure 5.5(c). The value for *dca* is chosen at 20 cm. For a smaller value of *dca*, the ratio S/B can increase to a much higher value but it seems not

reasonable since the efficiency will drop down to less than 90%, which is not acceptable. Contrarily, there is no need to increase the cut on *dca* to a higher value to have better efficiency since it has almost reached the maximal value.

The value of *dca* will now be fixed and similar scans will be performed one by one for the parameters *isolation*, $\Delta\varphi$, P_T^{track} and the hadronic energy fraction F_{had}. The scanned value of F_{had} is 0.3 which means that a particle which passes all previous cuts but deposits less than 70% of its energy in the electromagnetic part of the LAr will not be considered as an electron.

5.2.5 Efficiency and contamination

To check the performance of the method, let us now compare it to the official electron finder algorithm which is mainly based on the FORTRAN finder QESCAT [84]. Figures 5.6(a) and 5.6(b) show the comparison to QESCAT for the efficiency and contamination (which is the fraction of CC events passing the cuts over all CC sample). One can see that both the efficiency and the contamination are similar between the two finders. However if we look at the comparison of the reconstructed angles (θ and φ) which is shown in figure 5.7, even there is a very good agreement but there is a systematic difference in φ, the two satellites in figure 5.7(b), and at very large θ in figure 5.7(a). The large region of θ corresponds to the BBE-CB1 crack. The difference in φ is due to the fact that QESCAT missed the electron scattered in the φ-crack of the LAr. The events in that region were scanned by eye and an example is shown in figure 5.8.

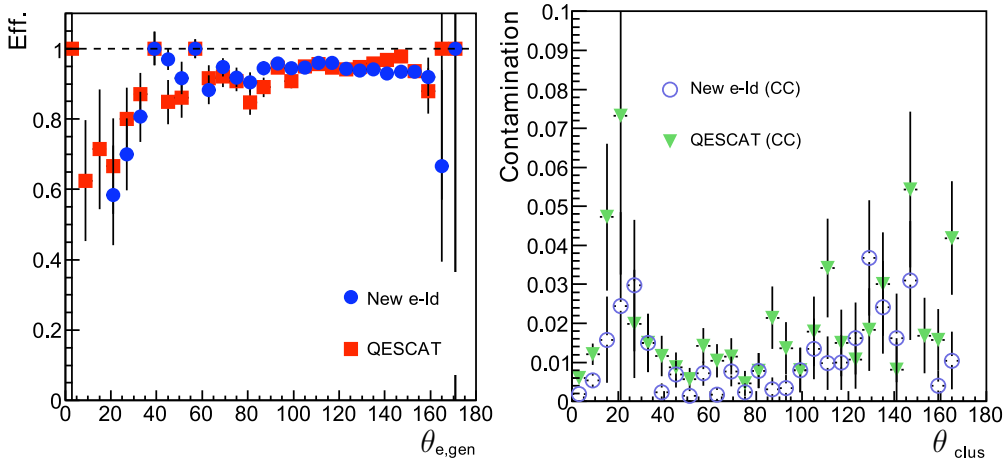

(a) (b)

Figure 5.6: Efficiency and contamination of the new electron finder compared to those of the official one, QESCAT.

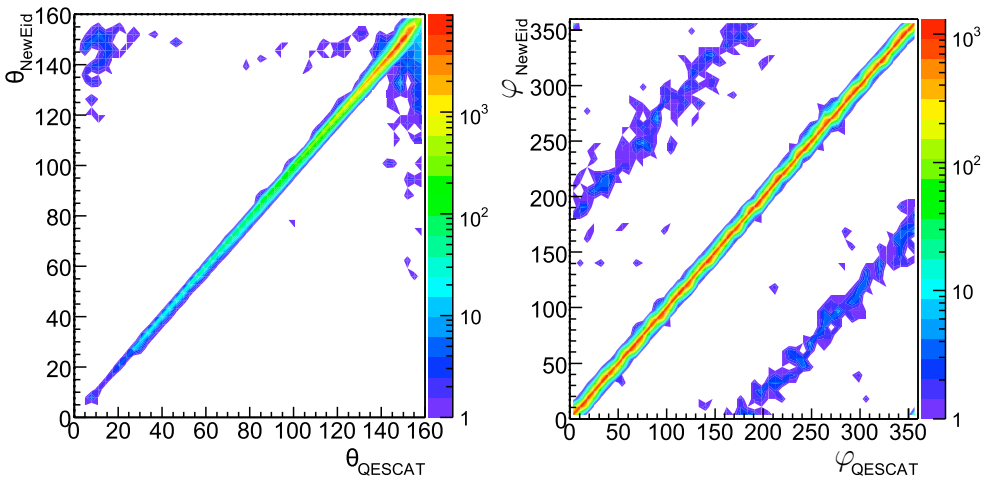

(a) (b)

Figure 5.7: Comparison of reconstructed electron polar & azimuthal angles between the new electron finder and the official one named QESCAT.

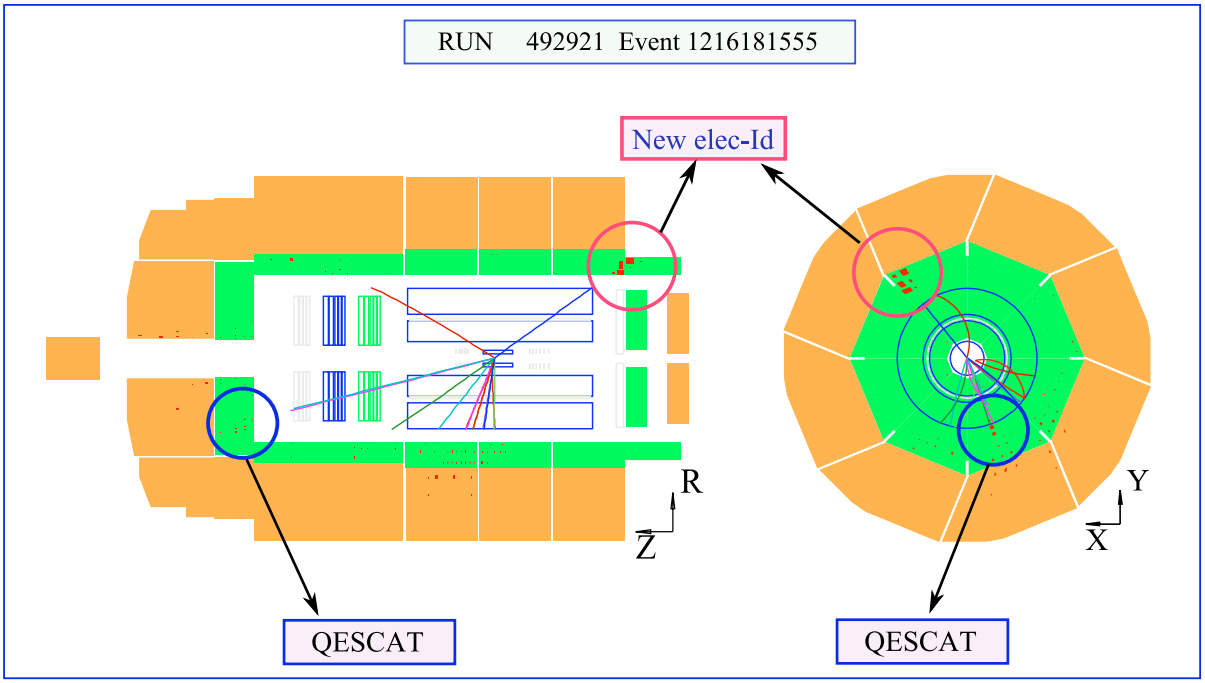

Figure 5.8: Example of event which is identified by both the new electron finder and QESCAT but with different reconstructed polar & azimuthal angles.

5.3 Re-optimization of photoproduction background rejection

In the case where a proton interacts with a quasi-real photon ($Q^2 \approx 0$), one speaks of photoproduction (cf section 1.6). Both types of photoproduction (direct and resolved)

are treated inclusively in this analysis. In photoproduction events the P_T of the event is balanced. Therefore the $P_{T,\text{miss}}$ requirement introduced above for CC events can remove most of photoproduction events from the CC sample. However, due to energy lost in the final state (e.g. fluctuation in the energy measurement for events with high E_T or events with a jet going into the crack region), photoproduction events can have $P_{T,\text{miss}}$.

Since in a CC process, the neutrino is always scattered in the opposite direction to the struck quark hence in the transverse plane the energy flow is expected to be more isotropic in the photoproduction and NC events than in CC events. The rejection of photoproduction events will be based on the energy distribution in the calorimeter. This is quantified by the ratio V_{ratio} of the two variables V_{ap} and V_p defined in section 5.1. An example from the distribution of $V_{\text{ratio}} = V_{ap}/V_p$ is shown in figure 5.9. Since at $V_{\text{ratio}} > 0.25$, the photoproduction is the dominate process, and the rates of the CC events is negligible, we apply an initial cut $V_{\text{ratio}} < 0.25$.

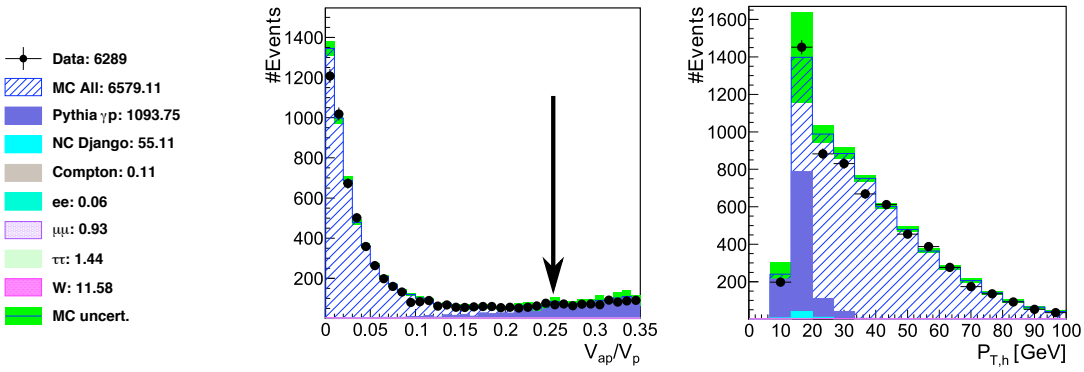

Figure 5.9: Distribution of V_{ratio} and $P_{T,h}$ for CC analysis without anti-photoproduction rejection. The contribution of photoproduction is high at large V_{ratio}. The arrow points to the cut $V_{\text{ratio}} < 0.25$.

The remaining contribution photoproduction is still large. The correlation between V_{ratio} and $P_{T,h}$ will help to reject another large amount among the rest. Figure 5.10 shows the correlation between theses two variables separately for CC MC, γp and data.

One can easily see that CC events are distributed at small V_{ratio} and increase to large value V_{ratio} when $P_{T,h}$ increases. In contrast to that, the γp events are distributed mostly at big V_{ratio} and decrease with $P_{T,h}$, at high $P_{T,h}$ (i.e. $P_{T,h} > 40$ GeV) there is almost no contribution from γp. From this observation, we can defined a cut which is illustrated in figure 5.10(c). It is constructed from two cuts: the line for $V_{\text{ratio}} = V_0$ and a parabola connecting the two points ($P_{T,h} = P_{T,0}$, $V_{\text{ratio}} = 0.35$) and ($P_{T,h} = 12$, $V_{\text{ratio}} = V_0$).

Parameters V_0, V_1 and $P_{T,0}$ are then scanned. The scan procedure is similar to what

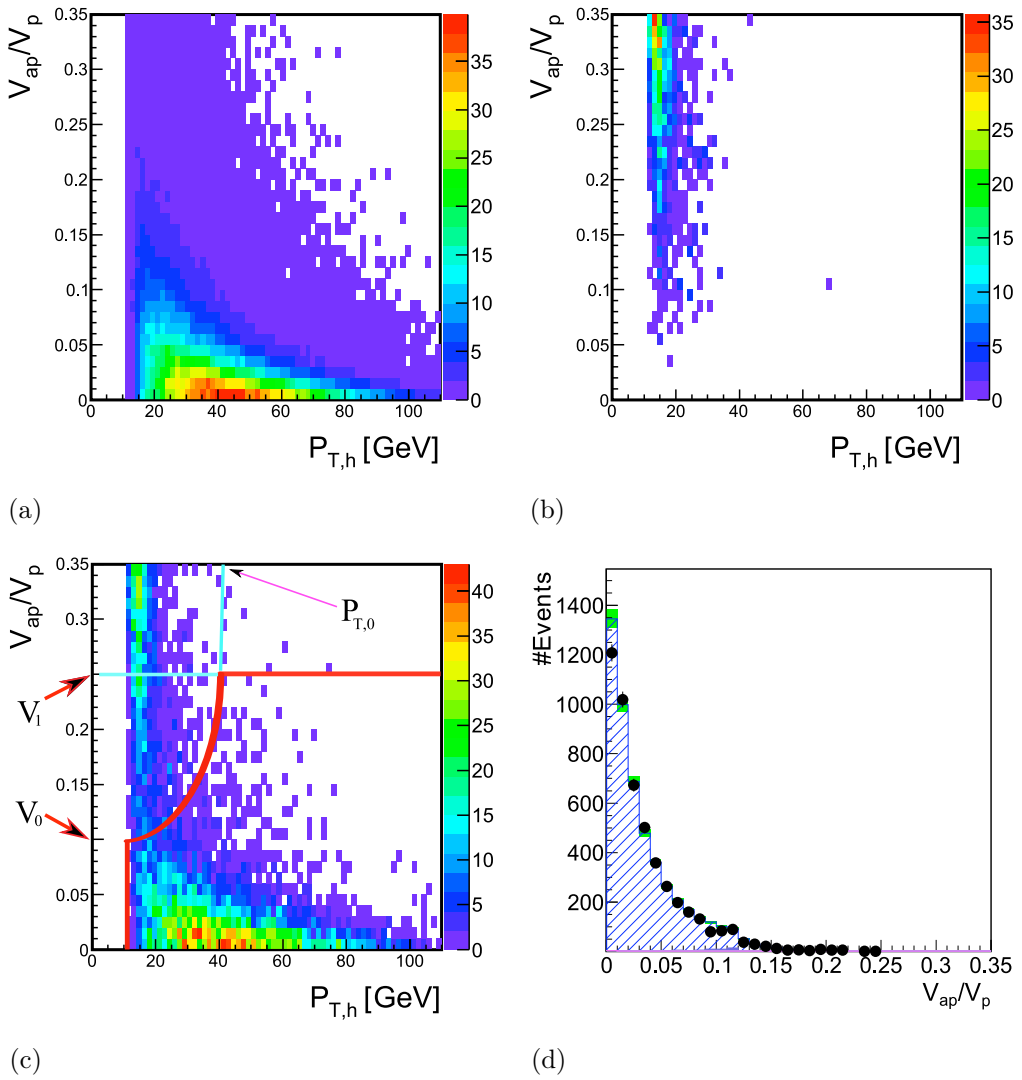

Figure 5.10: Correlation between V_{ratio} and $P_{T,h}$ for CC MC (a), photoproduction (b) and data (c). Small contribution from photoproduction obtained for final distribution of V_{ratio} (d).

was performed for the anti-NC cut (cf. section 5.2). The resulting parameters are given in table 5.2 for left- and right-handed data.

This cut is sensitive to the value of V_0, an uncertainty of ± 0.01 is thus assigned to V_0. Details of the estimation of this systematic uncertainty can be found in [95].

5.4 Efficiency estimation using pseudo-CC events

In this section, a method will be presented which is commonly used for years in the H1 Collaboration, for the determination of efficiencies for the CC analysis using the hadronic

Helicity	P_0	V_0	V_1
Left-handed	45 GeV	0.12	0.25
Right-handed	45 GeV	0.10	0.25

Table 5.2: Scanned parameters for anti-γp cut. The scanned was performed for left-handed and right-handed datasets separately.

final state of the NC data events.

5.4.1 Pseudo Charged Current events

For a cross section measurement, it is necessary to know the efficiencies of selection requirement such as triggers, background finders and vertex requirement. Some of the efficiencies may be determined from MC but it is always preferable to get the efficiencies from data. However, due to the low statistics of the CC data samples it is not possible to perform a precise determination of efficiencies. Fortunately, the hadronic states of CC and NC data events are similar, the NC data events are thus used.

The main difference between NC and CC events is the scattered electron. When the detector information of the scattered electron is "removed" from a NC event, the resulting event looks like a real CC event. Such events are called *pseudo charged current* (PsCC).

In a production of pseudo-CC sample, the scattered electron finding algorithm is applied to each selected NC event. When the electron is found, all relevant detector information, i.e. tracks and calorimetric energy, found inside the $\eta - \phi$ cone with the radius $R_{\eta-\phi} = 29$ is removed from the event. The cone radius is defined as:

$$R_{\eta-\phi} = \sqrt{\Delta\eta^2_{\text{tracks}} + \Delta\phi_{\text{tracks}}}. \tag{5.11}$$

The full event reconstruction (H1REC) is then applied to the modified NC (pseudo-CC) event mainly to redo the vertex reconstruction without the electron track.

Finally, pseudo-CC events are reweighted to the charged current cross section so that correct kinematics distributions expected for real CC events are produced: each pseudo-CC event receives a weight $w(x, Q^2)$ with which it enters in all subsequent distributions. The weight is defined as[2]:

$$w(x, Q^2) = \frac{\mathrm{d}^2\sigma_{\text{CC}}/\mathrm{d}x\mathrm{d}Q^2}{\mathrm{d}^2\sigma_{\text{NC}}/\mathrm{d}x\mathrm{d}Q^2}. \tag{5.12}$$

[2]Here, original x and Q^2 are calculated with the electron-sigma method (Sec.3.1.5) since it has a better resolution than that of the hadronic method.

The efficiency for the pseudo-CC is defined as

$$\varepsilon = \frac{N^{\text{cut}}_{\text{PsCC}}}{N^{\text{all}}_{\text{PsCC}}} \tag{5.13}$$

where $N^{\text{cut}}_{\text{PsCC}}$ is the number of weighted pseudo-CC events which fulfill standard CC selection. It is a sum of the event weights: $N^{\text{cut}}_{\text{PsCC}} = \sum w^{\text{cut}}_{\text{PsCC}}$, and $N^{\text{all}}_{\text{PsCC}}$ is the total number of weighted events: $N^{\text{all}}_{\text{PsCC}} = \sum w^{\text{all}}_{\text{PsCC}}$.

For the background and timing efficiencies, the correction applied to charged current MC is the difference (ratio) between pseudo-CC and MC. This means that the applied efficiency is from data. For the trigger efficiency, since we cannot use the trigger information from the CC MC as it is not properly simulated in MC, the correction determined from pseudo-CC is applied directly to CC MC. If there exists a difference between pseudo-CC and CC MC after these corrections, the difference is assigned as the systematic error uncertainty on the corrections.

5.4.2 Trigger efficiency

Trigger efficiency is determined from the PsCC data and will be applied on the CC MC as a function of x and Q^2 with the same bin grids being used for the cross section measurement (x and Q^2 are reconstructed using hadronic method, cf. figure 5.18). Figure 5.11 shows an example of the trigger efficiency for the period 2006-2007 e^+p right-handed.

A comparison of trigger efficiency for different sub-periods is shown in figure 5.12(a), for electron runs, and figure 5.12(b) for positron runs. The same observation is found for all sub-periods: the efficiency is low for the region $\gamma_h < 20^\circ$ (low y) which is limited by the detector acceptance, i.e. at low γ_h, the hadronic final states are very close to the beam pipe and may be lost during the triggering. At high γ_h (high y), the efficiency is limited due to relatively high energy thresholds against noise in the LAr calorimeter. The low efficiency at low Q^2 and low x is due to same reason. The efficiencies are also shown in function of $P_{T,h}$ for electron runs (figure 5.12(c)) and positron runs (figure 5.12(d)). The efficiency drops at low $P_{T,h}$, that is why there is the cut $P_{T,h} > 12$ GeV. The figures show that there is little time variation.

5.4.3 Background-timing efficiency

In this analysis, we use the background finders named *Ibg, Ibgfm, Ibgam* and the one called *track-cluster link* which is described in 4.5.2. The efficiency is determined for both pseudo-CC and CC MC in (x, Q^2) bins (cf. figure 5.18). The correction to be applied on

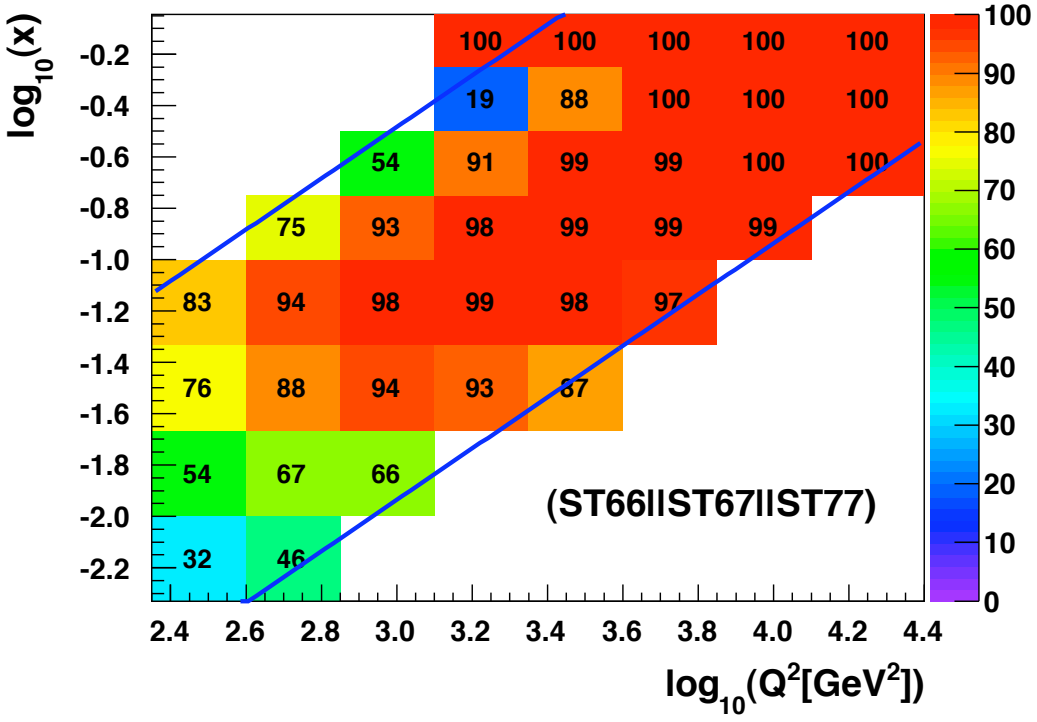

Figure 5.11: Trigger efficiency in function of x and Q^2 determined by pseudo-CC. Example for 2006-2007 e^+p right-handed period. The two lines indicate the cut $0.03 < y_h < 0.85$.

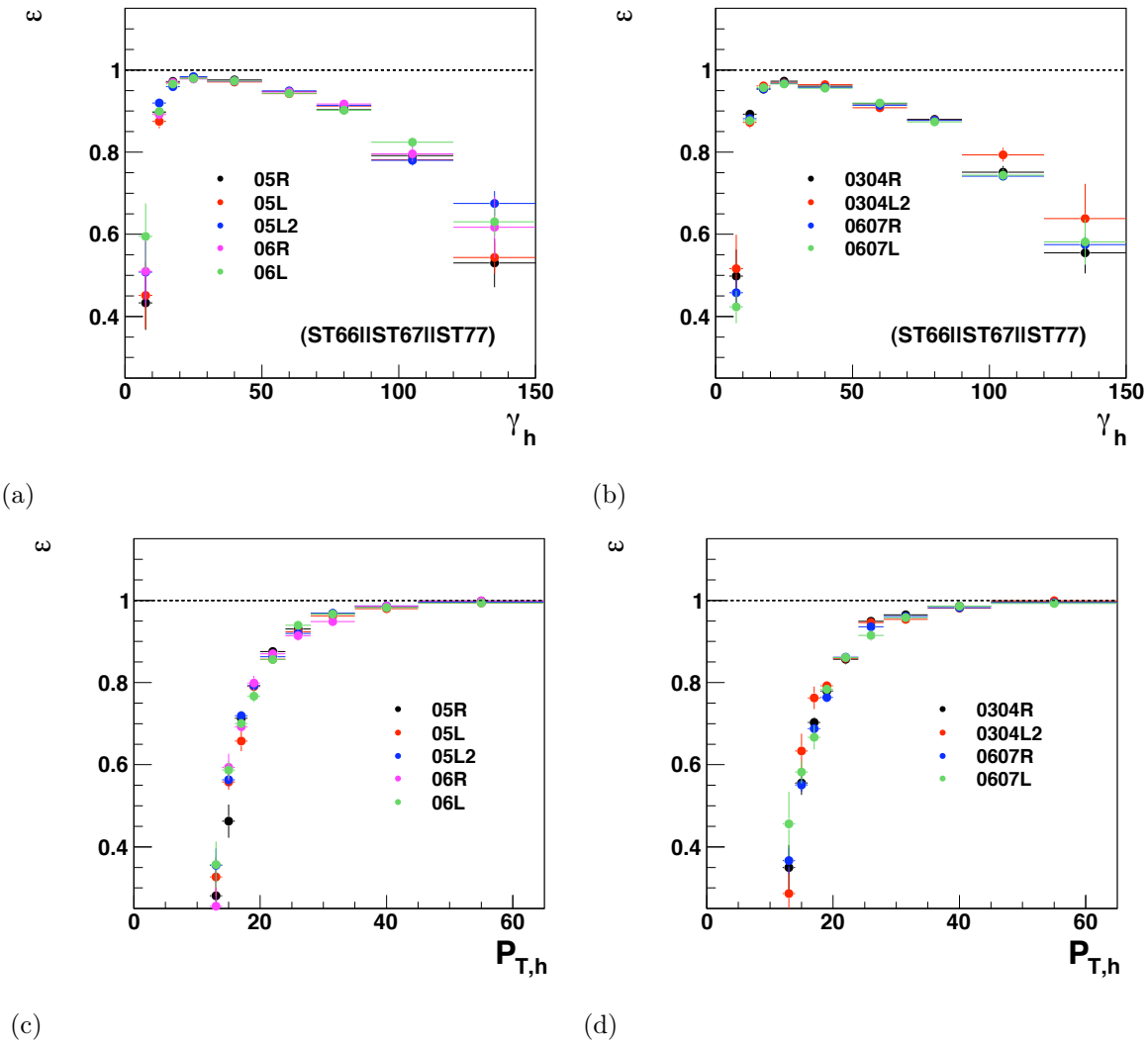

Figure 5.12: Trigger efficiency in function of γ_h determined by pseudo-CC for all electron runs (a) and positron run periods (b) and in function of $P_{T,h}$ (c, d).

the CC MC is the weight defined by the ratio:

$$w(x, Q^2) = \frac{\varepsilon_{\mathrm{PsCC}}(x, Q^2)}{\varepsilon_{\mathrm{CC\,MC}}(x, Q^2)} \tag{5.14}$$

where $\varepsilon_{\mathrm{PsCC}}(x, Q^2)$ and $\varepsilon_{\mathrm{CC\,MC}}(x, Q^2)$ are correspondingly the efficiencies in a (x, Q^2) bin determined for pseudo-CC and CC MC.

The efficiencies for individual background finders on PsCC data and the CC MC are shown in figures 5.13(a), 5.13(b), 5.13(c) and 5.13(d). The inefficiency of the track-cluster link (cf. sub-section 4.5.2) is small. More importantly, there is an overall disagreement between pseudo-CC and CC MC for the Ibgam finder and a difference at low-γ_h and high-γ_h for the finder Ibg. The picture is the same for the combined efficiency which is shown in figure 5.13(e). The CC MC therefore needs to be corrected to the pseudo-CC data.

In reality, it is shown [95] that the timing condition has a very small inefficiency, we then decided to combine the efficiency of the background finders and the timing into one and call *background finder-timing* efficiency. The efficiencies for both pseudo-CC and CC MC efficiencies are shown in figures 5.14(a) and 5.14(b).

5.4.4 Vertex reconstruction efficiency

The efficiency of the vertex reconstruction is determined from the pseudo-CC and CC MC events from equation 5.13 with $N^{\mathrm{cut}}_{\mathrm{PsCC}}$ being the number of events satisfying the vertex requirement (cf. section 5.1). The efficiency of the vertex requirement is represented in figure 5.15(a) as a function of y_h for pseudo-CC and CC MC. It increases from 30% at $y_h = 0.03$ to 100% at high y_h values. At low y_h, which corresponds to the forward detector region, the efficiency is low since the vertex requirement is based only on the central tracking detector.

From figure 5.15(b) one observes a difference between the efficiency for pseudo-CC and the CC MC at low y. A y dependence systematic uncertainty is assigned for vertex requirement efficiency (cf. section 5.6.5).

5.5 Z-vertex reweighting

Since the use of latest MC productions the run dependent of the z-vertex was properly simulated in the MC[3]. However the remaining difference of the z-vertex distribution between data and MC still requires a small correction in order to have a better agreement.

[3]In the past, the z-vertex was simulated to a given period without local time dependence.

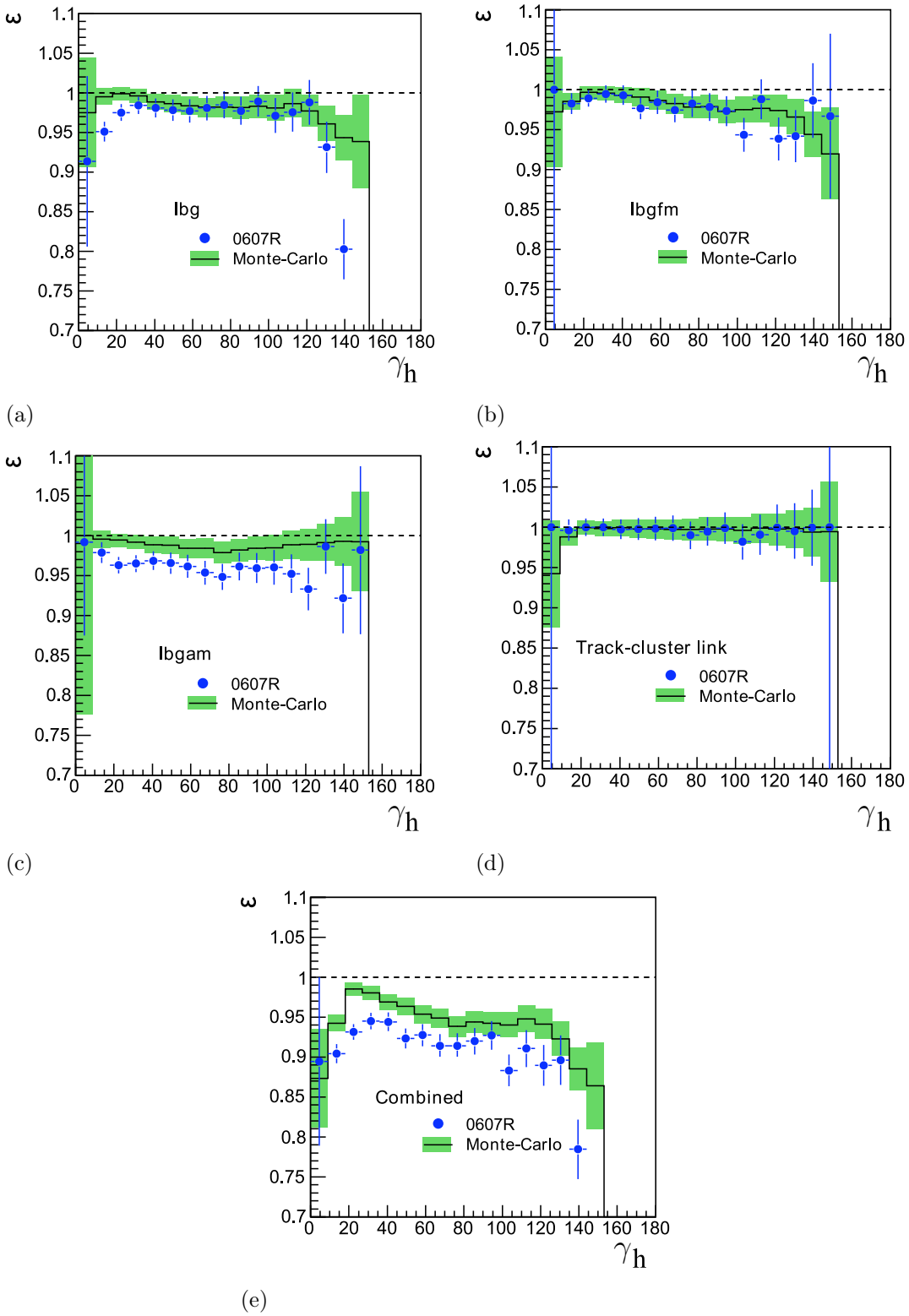

Figure 5.13: Background efficiency in function of γ_h determined by pseudo-CC and CC MC for Ibg (a), Ibgfm (b), Ibgam (c) and track-cluster link (d). The combined efficiency shows an over all difference between pseudo-CC and CC MC (e). Example for 2006-2007 e^+p right-handed data.

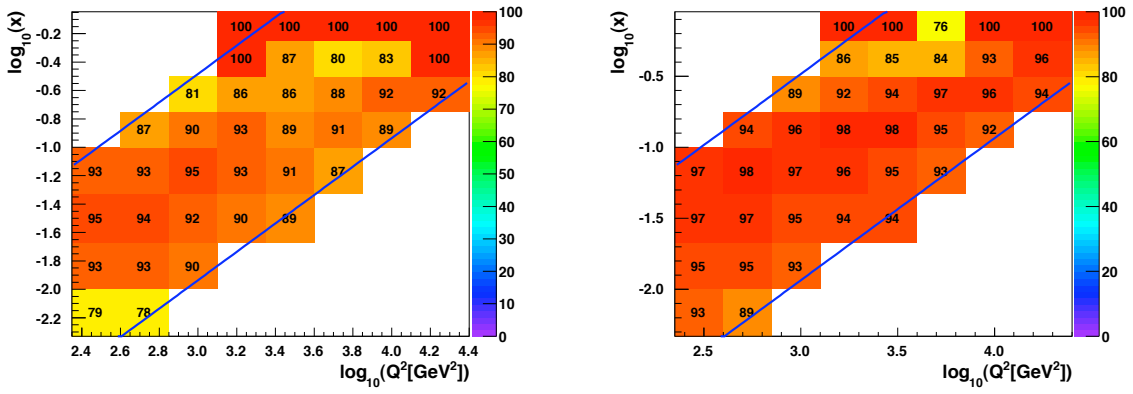

Figure 5.14: Combined background and timing efficiency in function of x and Q^2 determined by pseudo-CC (a) and CC MC (b). The lines indicate the cut $0.03 < y < 0.85$. Example for 2006-2007 e^+p right-handed data.

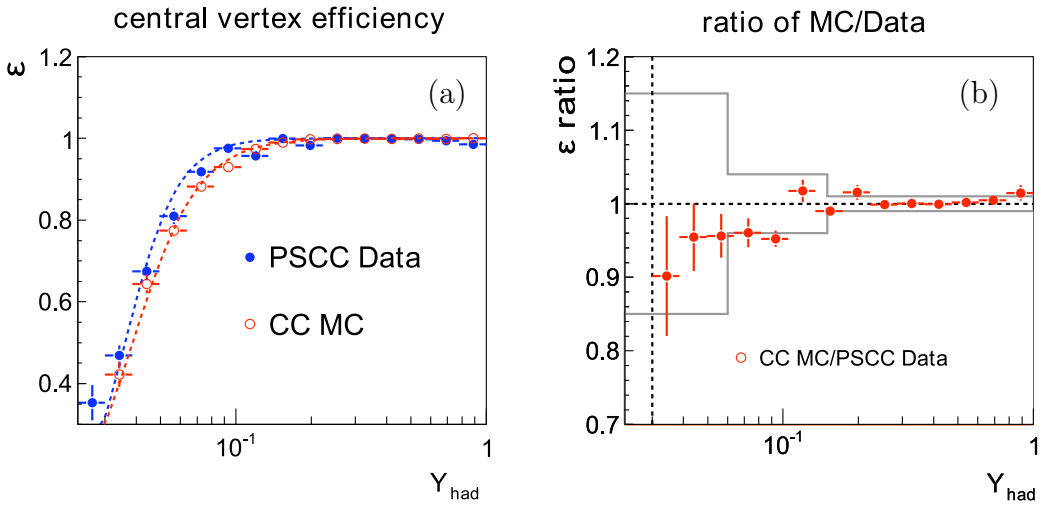

Figure 5.15: Vertex finding efficiency as a function of y_h for the pseudo-CC data and CC MC (a). Ratio of efficiency pseudo-CC data over CC MC. The assigned systematic uncertainty is indicated by the full lines. The vertical dashed line indicates the analysis cut $y_h > 0.03$ (b). Example for 2003-2004 e^+p data.

Such a correction is performed in function of the reconstructed z-vertex (in the region $-35 < z_{\text{vtx}} < 35$ cm) in the MC by adjusting its distribution to that obtained from the

data. Both distribution of data and MC are fitted with a function of type:

$$f(z) = A\exp\left(-\frac{1}{2}\frac{(z-B)^2}{C^2}\right) + D\exp\left(-\frac{1}{2}\frac{(z-E)^2}{F^2}\right) + G + Hz + Kz^2 \qquad (5.15)$$

which is a combination of two gaussians and a second-degree polynomial. One of the gaussians will take into account the width and the center of the peak, the other one will combine with the polynomial to describe the non-gaussian queue of the distribution. Such a parameterization is sufficiently flexible to reproduce the z-vertex distribution. The z-vertex distribution of the MC will then be normalized by the total number of events and then one applies a weight

$$\varepsilon_{z\text{vtx}}(z) = \frac{f_{\text{data}}^{\text{norm}}(z)}{f_{\text{MC}}^{\text{norm}}(z)} \qquad (5.16)$$

to each simulated events. The numerator and dominator correspond to the integral of the function 5.15 for data and MC. The z-vertex reweighting was done separately for each sub-period to avoid the time dependence of the distribution. Figure 5.16 shows the distribution of the CC MC before and after the reweighting where we can see a clear improvement. Here, all histograms are normalized by number of events in order to demonstrate only the effect of z-vertex reweighting.

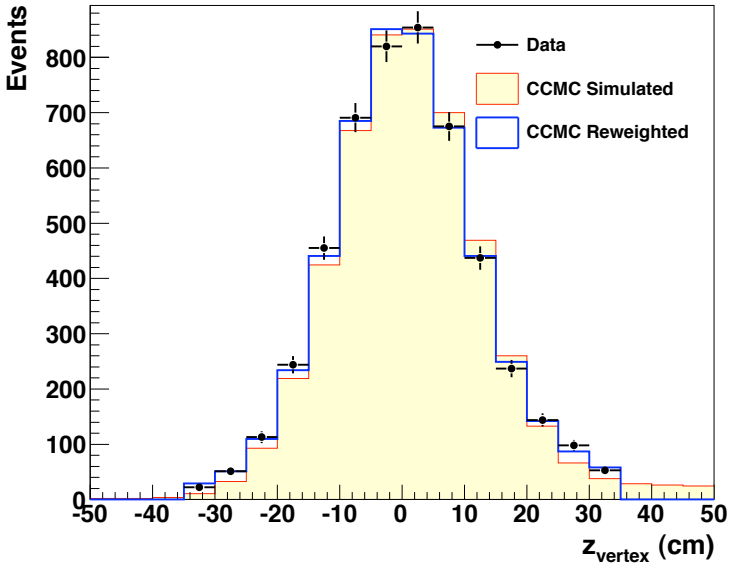

Figure 5.16: Comparison of the z-vertex distribution of the CC MC before and after reweighting to data. The MCs have been normalized to data to have the same number of events with purpose to see only the reweighting effect.

5.6 CC cross section measurement

5.6.1 Data and MC comparison

The distributions of the variables V_{ap}/V_p, P_T, $E - P_z$, Q^2 and x presented figure 5.17 as an example for the period $e^- p$ left-handed, show a good description of the data by the Standard Model prediction estimated by the H1PDF 2009 fit.

5.6.2 Binning scheme

The idea of choosing a binning for the CC analysis is to have an equidistant in the log-scale in both x, Q^2 and to have an optimal bin size according to the resolution and the statistical consideration.

The definition of the (x, Q^2) bins in this analysis is the same for the previous H1 published paper on the CC cross section measurement [97].

Bin boundaries:

$\log_{10}(Q^2)$	2.35	2.60	2.85	3.10	3.35	3.60	3.85	4.10	4.40
Q^2 GeV^2	224	398	708	1259	2239	3981	7080	12589	25119
$\log_{10}(x)$	−2.33	−2.00	−1.67	−1.33	−1.00	−0.75	−0.50	−0.25	0.00
x	0.005	0.010	0.021	0.047	0.100	0.178	0.316	0.562	1.000

Bin centers:

$\log_{10}(Q^2)$	2.48	2.70	3.00	3.30	3.48	3.70	3.90	4.18
Q^2 GeV^2	300	500	1000	2000	3000	5000	8000	15000
$\log_{10}(x)$	−2.10	−1.89	−1.50	−1.10	−0.89	−0.60	−0.40	−0.19
x	0.008	0.013	0.032	0.080	0.130	0.250	0.400	0.650

An illustration of this binning can be found in figure 5.18. The kinematic plane is restricted by the cut $0.03 < y_h < 0.85$ and $P_{T,h} > 12$ GeV.

5.6.3 Extraction of the cross section

The cross section in a bin $(x,\ Q^2)$ of a process can be expressed as

$$\sigma_{\text{bin}} = \int_x \int_{Q^2} \frac{\mathrm{d}^2\sigma(x, Q^2)}{\mathrm{d}x\mathrm{d}Q^2} \mathrm{d}x\mathrm{d}Q^2. \tag{5.17}$$

Normally, it corresponds to the integrated σ in the bin which is determined as

$$\sigma = \frac{N}{\mathcal{L}}. \tag{5.18}$$

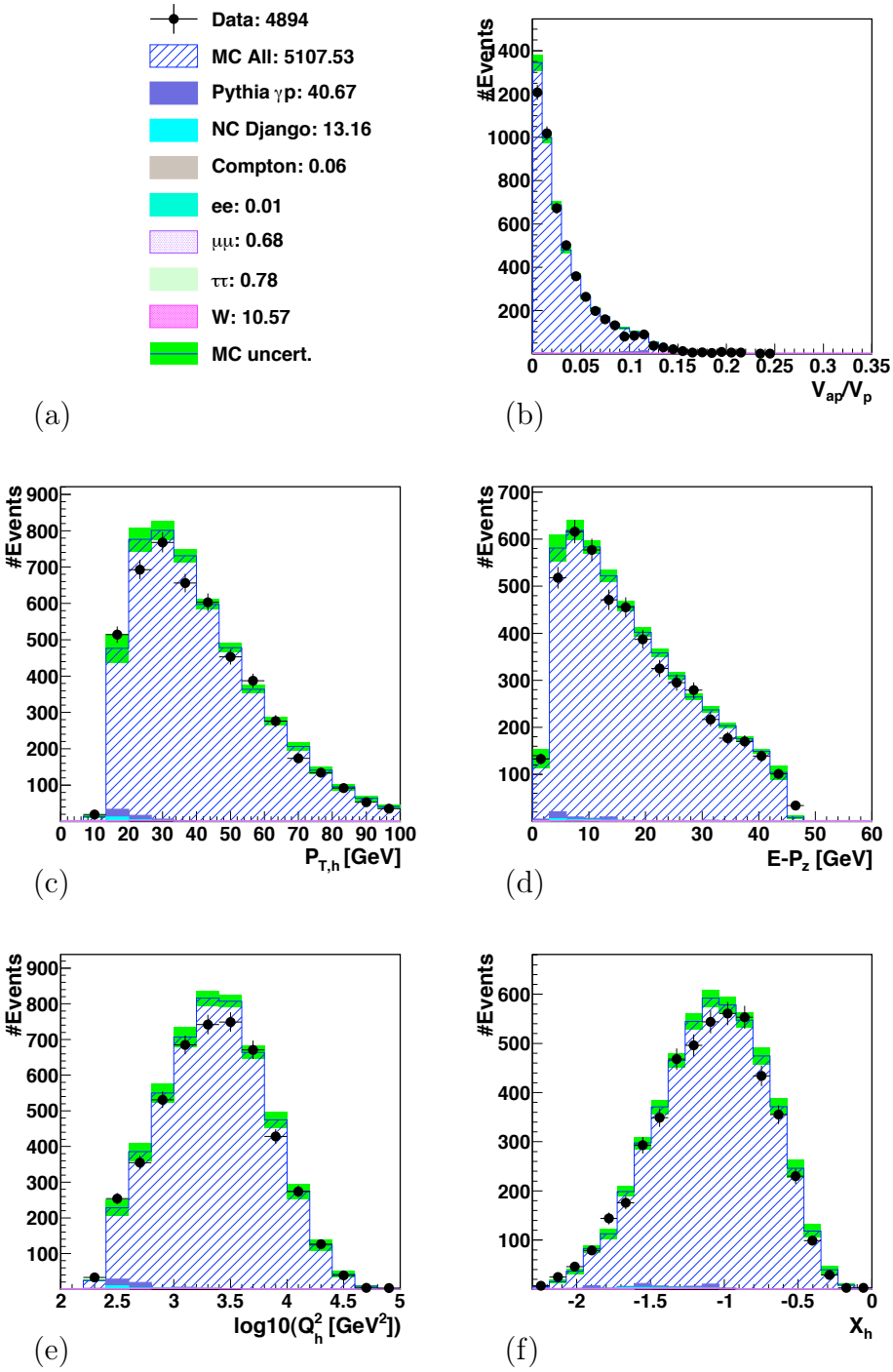

Figure 5.17: Example of data and MC comparison for period e^-p left-handed. The data are presented in closed circles and the total MC contribution are shown in histograms. The error bands are total (statistical $\oplus$ systematic) MC uncertainties. The error bars on data are statistical error.

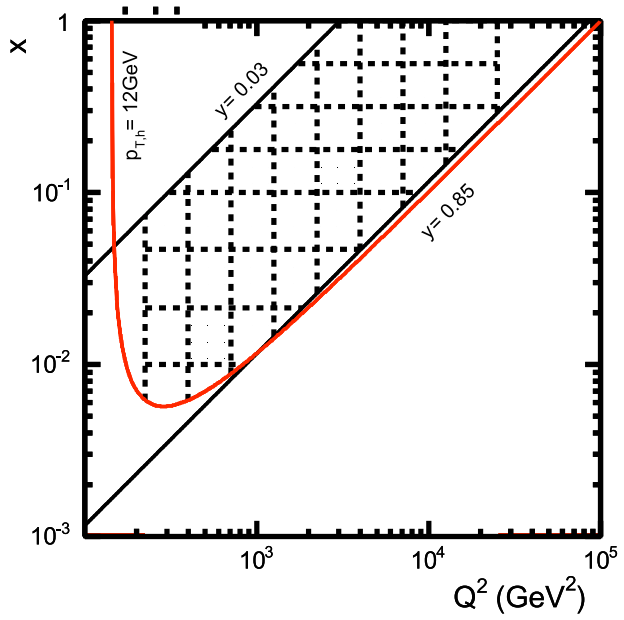

Figure 5.18: Binning in (x, Q^2) for CC analysis. The dashed lines represent the bin boundaries, the solid lines are limits defined by the y and $P_{T,h}$ cuts.

The cross section measurement is then the events counting when the integrated luminosity is known. The corrections are nevertheless needed to be taken into account in this simple formula. First of all, the presence of non-avoidable background which can contribute to the number of selected events. This can be subtracted by using the MC which gives an estimation of the number of background events $N_{\rm bg}$. Moreover, the kinematics variables used in the measurement are subject to various distortions like detector geometry effects (geometric acceptance $\mathscr{A}$) and electroweak radiative effects. One needs to account that the counted events are a bin $(x_{\rm min},\ x_{\rm max})$ and $(Q^2_{\rm min},\ Q^2_{\rm max})$ thus to measure the cross section at a point $x_{\rm C},\ Q^2_{\rm C}$ one needs to make the correction of the bin center $\delta_{\rm bc}$ which can be evaluated with help from the theoretical cross section $\sigma^{\rm th}$ used in the generation of the MC

$$\begin{aligned}\delta_{\rm bc} &= \frac{\dfrac{{\rm d}^2\sigma^{\rm th}(x_c,Q^2_c)}{{\rm d}x{\rm d}Q^2}}{\displaystyle\int_{x_{\rm min}}^{x_{\rm max}}\int_{Q^2_{\rm min}}^{Q^2_{\rm max}}\frac{{\rm d}^2\sigma^{\rm th}(x_c,Q^2_c)}{{\rm d}x{\rm d}Q^2}{\rm d}x{\rm d}Q^2} = \frac{\dfrac{{\rm d}^2\sigma^{\rm th}(x_c,Q^2_c)}{{\rm d}x{\rm d}Q^2}}{\sigma^{\rm th}_{\rm bin}} \\ &= \frac{{\rm d}^2\sigma^{\rm th}(x_c,Q^2_c)}{{\rm d}x{\rm d}Q^2}\times\frac{\mathcal{L}_{\rm MC}}{N_{\rm gen}}. \end{aligned} \tag{5.19}$$

As mentioned in section 1.5, the radiative corrections must also be taken into account as the ratio of the Born cross section and that determined from the measurement which

includes radiation effect

$$\delta_{\rm rad} = \frac{\displaystyle\int_{x_{\rm min}}^{x_{\rm max}} \int_{Q^2_{\rm min}}^{Q^2_{\rm max}} \frac{{\rm d}^2\sigma^{\rm th}(x_c, Q^2_c)}{{\rm d}x{\rm d}Q^2} {\rm d}x{\rm d}Q^2}{\displaystyle\int_{x_{\rm min}}^{x_{\rm max}} \int_{Q^2_{\rm min}}^{Q^2_{\rm max}} \frac{{\rm d}^2\sigma^{\rm th}_{\rm rad}(x_c, Q^2_c)}{{\rm d}x{\rm d}Q^2} {\rm d}x{\rm d}Q^2} = \frac{N_{\rm gen}}{N^{\rm rad}_{\rm gen}}. \tag{5.20}$$

The resulting cross section reads

$$\frac{{\rm d}^2\sigma^{\rm meas}(x_c, Q^2_c)}{{\rm d}x{\rm d}Q^2} = \frac{N^{\rm data} - N_{\rm bg}}{\mathcal{L}\mathscr{A}\varepsilon} \delta_{\rm bc}\delta_{\rm rad} \tag{5.21}$$

with ε the efficiencies determined from data. Let's define the smeared acceptance $\mathcal{A} = \mathscr{A}\varepsilon$. One uses a hypothesis that this acceptance $\mathcal{A}$ can be determined from the MC as the ratio of the number of reconstructed and selected events divided by the number of generated events $\mathcal{A} = N^{\rm rad}_{\rm MC}/N^{\rm rad}_{\rm gen}$. This hypothesis is valid only if all of the detection efficiencies of the real detector is well reproduced in the MC, which have to be treated particularly and corrected. By expressing explicitly different factors in the equation (5.21) one obtains

$$\frac{{\rm d}^2\sigma^{\rm meas}(x_c, Q^2_c)}{{\rm d}x{\rm d}Q^2} = \frac{N^{\rm data} - N_{\rm bg}}{\mathcal{L}} \frac{N^{\rm rad}_{\rm gen}}{N^{\rm rad}_{\rm MC}} \frac{N_{\rm gen}}{N^{\rm rad}_{\rm gen}} \frac{\mathcal{L}_{\rm MC}}{N_{\rm gen}} \frac{{\rm d}^2\sigma^{\rm th}(x_c, Q^2_c)}{{\rm d}x{\rm d}Q^2} \tag{5.22}$$

and after simplification

$$\frac{{\rm d}^2\sigma^{\rm meas}(x_c, Q^2_c)}{{\rm d}x{\rm d}Q^2} = \frac{N^{\rm data} - N_{\rm bg}}{N^{\rm rad}_{\rm MC}} \frac{\mathcal{L}_{\rm MC}}{\mathcal{L}} \frac{{\rm d}^2\sigma^{\rm th}(x_c, Q^2_c)}{{\rm d}x{\rm d}Q^2}. \tag{5.23}$$

This is the formula which is used in this analysis for the measurement of the double differential cross section. The same procedure is followed for ${\rm d}\sigma/{\rm d}Q^2$, ${\rm d}\sigma/{\rm d}x$ and ${\rm d}\sigma/{\rm d}y$.

In reality, the MC was generated with using fixed (old) set of PDFs, cf. section 3.2.2, we need thus to reweight each MC event with a factor:

$$w = \frac{\sigma^{\rm th}({\rm new})}{\sigma^{\rm th}({\rm old})} \tag{5.24}$$

which allows us to use the $\sigma^{\rm th}$ from the latest PDF knowledge (eg. H1PDF 2009) in the previous formulae. It should be emphasized that the measured cross sections are largely independent of the choice of the PDFs.

5.6.4 Acceptance, Purity and Stability

To quantify the acceptance of the event selection and detector effects, three variables are defined. They are the smeared acceptance $\mathcal{A}$, the purity $\mathcal{P}$ and the stability $\mathcal{S}$:

$$\mathcal{A} = \frac{N^{\mathrm{MC}}_{\mathrm{rec}}(i)}{N^{\mathrm{MC}}_{\mathrm{gen}}(i)} \tag{5.25}$$

$$\mathcal{P} = \frac{N^{\mathrm{MC}}_{\mathrm{rec+gen}}(i)}{N^{\mathrm{MC}}_{\mathrm{rec}}(i)} \tag{5.26}$$

$$\mathcal{S} = \frac{N^{\mathrm{MC}}_{\mathrm{rec+gen}}(i)}{N^{\mathrm{MC}}_{\mathrm{gen+sel}}(i)} \tag{5.27}$$

where

- $N^{\mathrm{MC}}_{\mathrm{rec}}(i)$ is the number of events reconstructed in the bin i,
- $N^{\mathrm{MC}}_{\mathrm{gen}}(i)$ is the number of events generated in bin i,
- $N^{\mathrm{MC}}_{\mathrm{rec+gen}}(i)$ is the number of events generated and reconstructed in a bin i,
- $N^{\mathrm{MC}}_{\mathrm{gen+sel}}(i)$ is the number of events generated in the bin i and passing all selection criteria (i.e. reconstructed in any bin).

The purity and stability are required to be larger than 30% and the event with acceptance less than 40% will be rejected. An example of these quantities for CC measurement is shown in figure 5.19. Both purity and stability are high at low x. With increasing Q^2 they become higher and approach the values of $\approx 80\%$.

5.6.5 Systematic uncertainties

The systematic uncertainties on the cross section measurement are discussed briefly below (cf. [95, 49, 98] and references therein for more details). Positive and negative variations of one standard deviation of each error source are found to yield errors which are symmetric to a good approximation. The systematic uncertainties of each source are taken to be fully uncorrelated between the cross section measurements unless stated otherwise.

- An uncertainty of 2% is assigned to the scale of the hadronic energy measured in the LAr calorimeter, of which 1% is considered as a correlated component to the uncertainty. This results in a total uncertainty of 1.3% on the total cross section measurements.
- A 10% uncertainty is assigned to the amount of energy in the LAr calorimeter attributed to noise, which gives rise to a systematic error of 0.3% on the total cross section measurement.

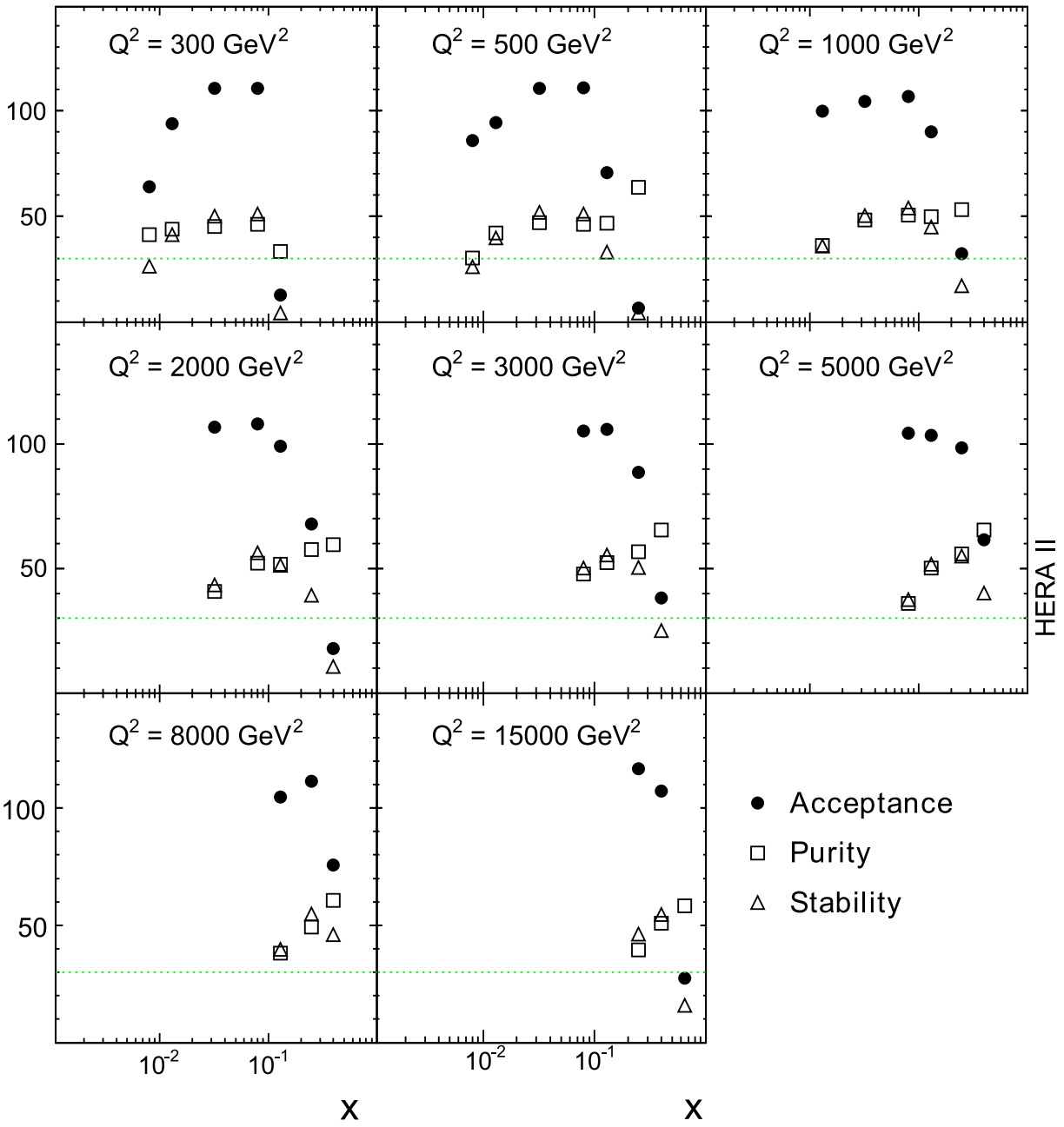

Figure 5.19: Smeared acceptance, purity and stability for the CC measurement. The dashed line indicate the limit for purity and stability cuts. Example for e^-p left-handed dataset which is similar for other periods.

- The variation of cuts against photoproduction on V_{ap}/V_p (cf. section 5.3) has an effect on the total cross section of 0.6%.

- A 30% uncertainty of the subtracted ep background is determined from a comparison

of data and simulation after relaxing the anti-photoproduction cuts, such that the sample is dominated by photoproduction events.

- The non-ep background finders introduce an inefficiency for CC events. The associated uncertainty is estimated using pseudo-CC data and found to depend on y. The uncertainty is 2% for $y < 0.1$ and 1% for y>0.1.

- A y-dependent error is assigned to the vertex finding efficiency: An uncertainty of 1% is applied for $y > 0.15$, 4% for $0.15 > y > 0.06$, and 15% for $y < 0.06$. This yields an uncertainty of $\simeq 2\%$ on the total cross section measurements.

- An uncertainty of 0.5% accounts for the dependence of the acceptance correction on the PDFs used in the MC simulation.

- An error of 0.8% is estimated for the QED radiative corrections. This accounts for missing contributions in the simulation of the lowest order QED effects and for the uncertainty on the higher order QED and EW corrections.

- A 15% of uncertainty is applied on the inefficiency of the triggers added in quadratic by 1% of uncertainty from the statistical error of the pseudo-CC events. The uncertainty applied on the cross section will be determined as: $15\% \times (1 - \varepsilon) \oplus 1\%$. This yields an uncertainty of 0.8% on the cross section measurements.

- In addition, there is a global uncertainty of 2.5–2.9% on the luminosity measurement for different e^+, e^-, left and right samples, of which 2.1% is considered as correlated.

- The relative uncertainty in the measurement of the lepton beam polarisation is taken to be 1.6% for the LPOL [99] and 3.5% for the TPOL [100], yielding a total relative polarisation uncertainty in the e^+p sample of 1.2% for the right-handed data set and 1.4% for the left-handed data set. For the e^-p data a relative uncertainty of 2.3% for the right-handed data set and 1.0% for the right-handed data set is obtained. These uncertainties are not included in the error bars of the data points.

The total systematic error is formed by adding the individual uncertainties in quadrature and amounts to about 4% on the total cross section measurements.

5.7 Results

The CC cross sections are measured for HERA-II data at the center-of-mass energy $\sqrt{s} =$ 319 GeV in the kinematic region restricted by $0.03 < y_h < 0.85$ and $P_{T,h} > 12$ GeV.

5.7.1 Double differential cross section

The double differential reduced cross sections are shown in figure 5.20 for electron data and in figure 5.21 for positron data.

The reduced cross section at different Q^2 values as functions of x together with the theoretical expectations are shown. A very good agreement between data and the expectation of the Standard Model is achieved for all periods. The difference between e^-p and e^+p or left and right-handed cross sections is expected due to the charge and polarization dependence. This can be seen also for the total CC cross sections presented below.

5.7.2 Single differential cross section

The CC single differential cross sections are found to be falling by four orders of magnitude for the measured Q^2 region between 300 GeV^2 and 30000 GeV^2 for left and right samples in $e^{\pm}p$ scattering. These are shown in figures 5.22, 5.23, 5.24 and 5.25 compared to the Standard Model expectations based on the PDFs from H1 PDF 2009. The cross sections are observed to fall with increasing Q^2 and have a more rapid decrease for $Q^2 > 2000\text{GeV}^2$. In the context of the Standard Model this is understood to arise from the falling parton densities as Q^2 (and hence also x) increases.

5.7.3 Total cross section

The total CC cross section is measured for $Q^2 > 400$ GeV, $y < 0.9$ and separately for the combined data sets: e^-p and e^+p, left and right-handed.

The compilation of the total cross sections with polarized beams (HERA-II) and unpolarized beams (HERA-I) is represented in figure 5.26 in order to have complete figure about the polarization dependence of the total CC cross section. The data exhibit a clear linear polarisation dependence of the cross sections which is maximal for left handed e^-p scattering and right handed e^+p scattering demonstrating the parity violation of purely weak charged current interactions.

In [97], a linear fit to the polarization dependence of the e^-p CC cross section data based on part of the HERA-II data was performed to obtain an upper limit on $\sigma^{\text{tot}}_{\text{CC}}(P_e = -1) = 1.9$ pb at 95% confidence level (CL). The results excludes the existence of charged current involving right-handed fermions mediated by a boson of mass below 208 GeV at 95% CL, assuming SM couplings and a massless right-handed v_e. The same analysis will be repeated once the cross sections will be finalized and an improved mass limit is expected.

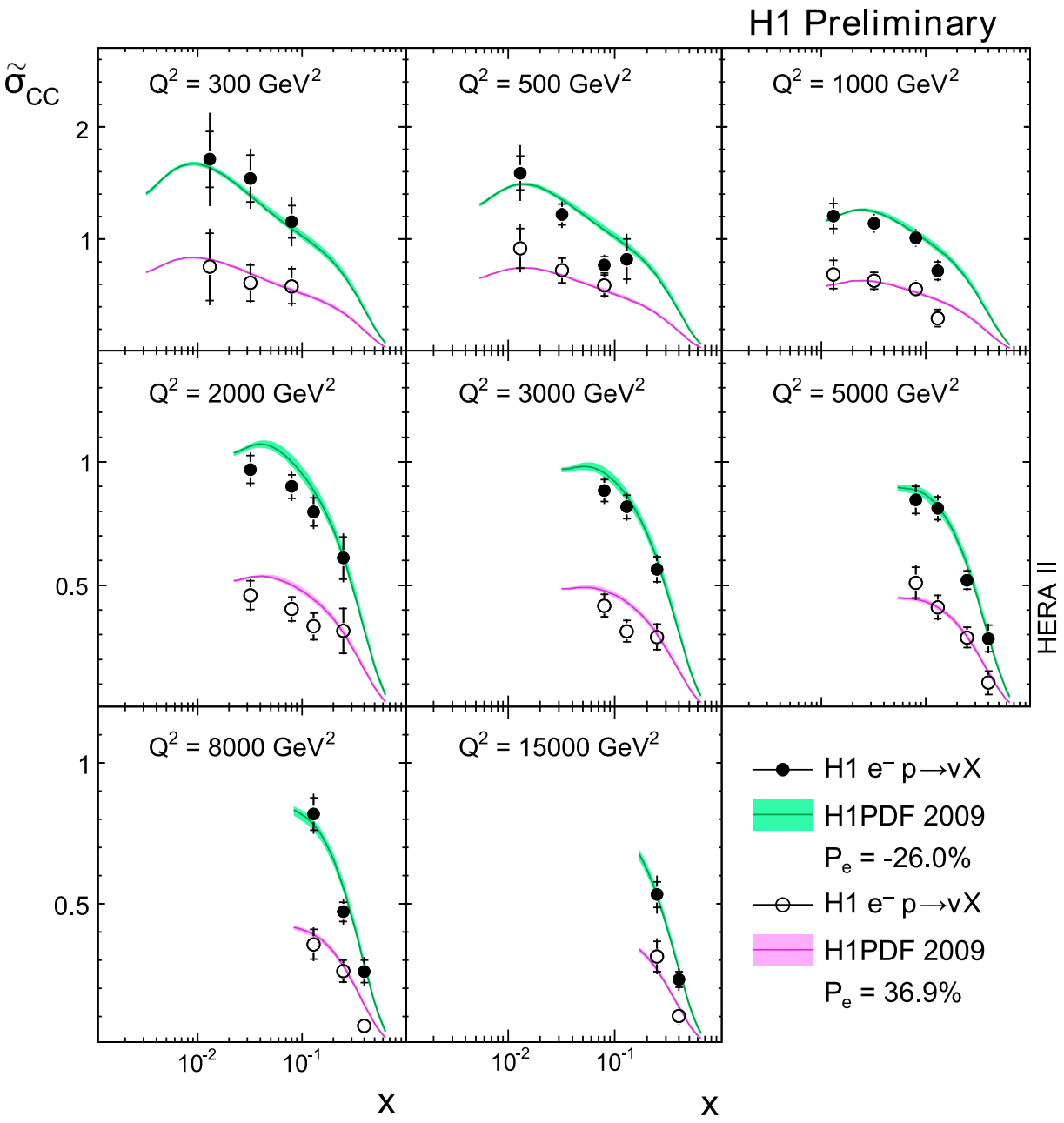

Figure 5.20: Reduced CC cross section as a function of x for different values of Q^2 for the e^-p data compared to the theoretical expectation evaluated by H1PDF 2009. The left-handed polarization electron data are shown in filled points, the right-handed data are shown in open points. The outer error bar on the data shows the total uncertainty, the inner error bar shows the statistical uncertainty. The error bands on MC show the total theoretical uncertainty (parameterization ⊕ model ⊕ experimental uncertainty).

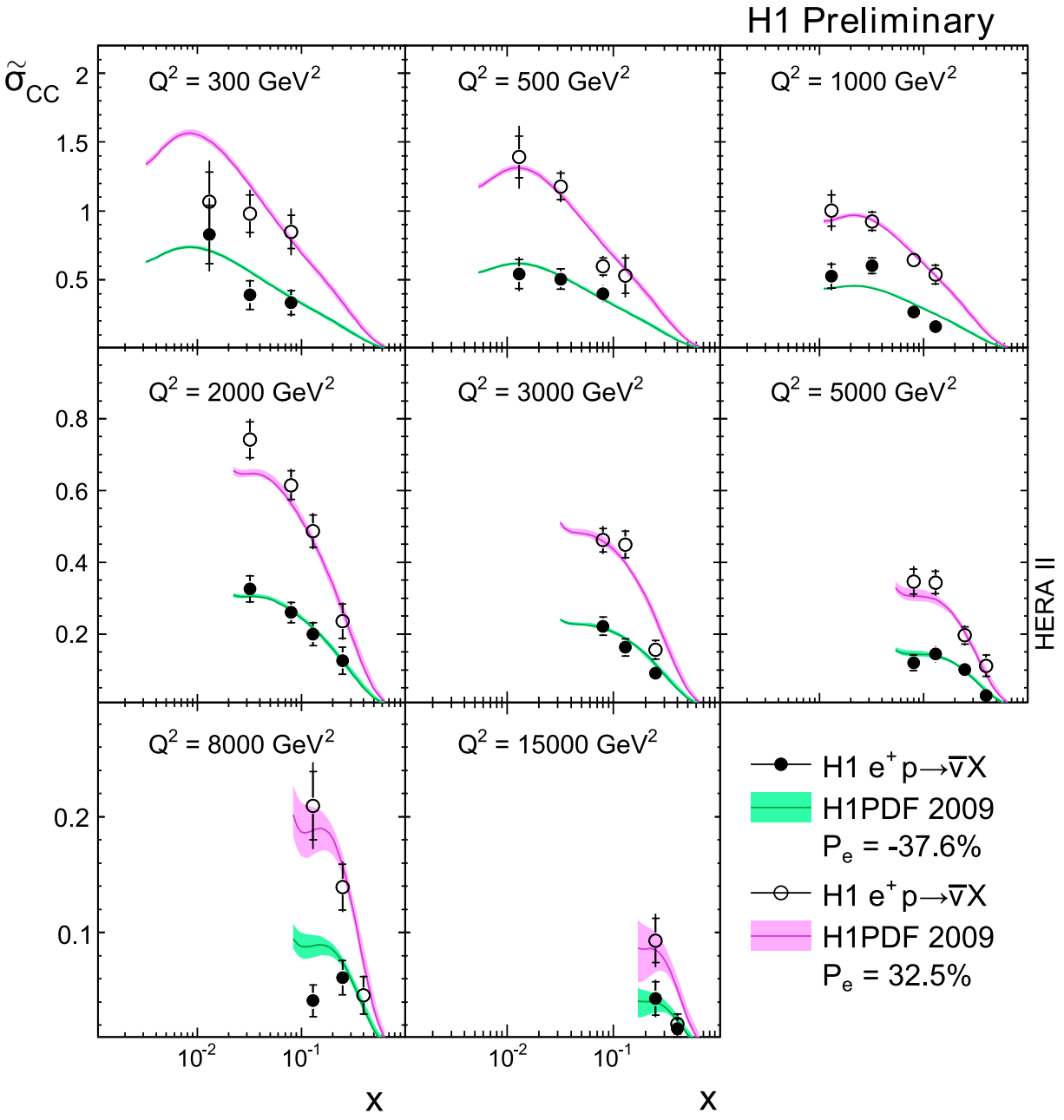

Figure 5.21: Reduced CC cross section as a function of x for different values of Q^2 for the e^+p data compared to the theoretical expectation evaluated by H1PDF 2009. The left-handed polarization electron data are shown in filled points, the right-handed data are shown in open points. The outer error bar on the data shows the total uncertainty, the inner error bar shows the statistical uncertainty. The error bands on MC show the total theoretical uncertainty (parameterization $\oplus$ model $\oplus$ experimental uncertainty).

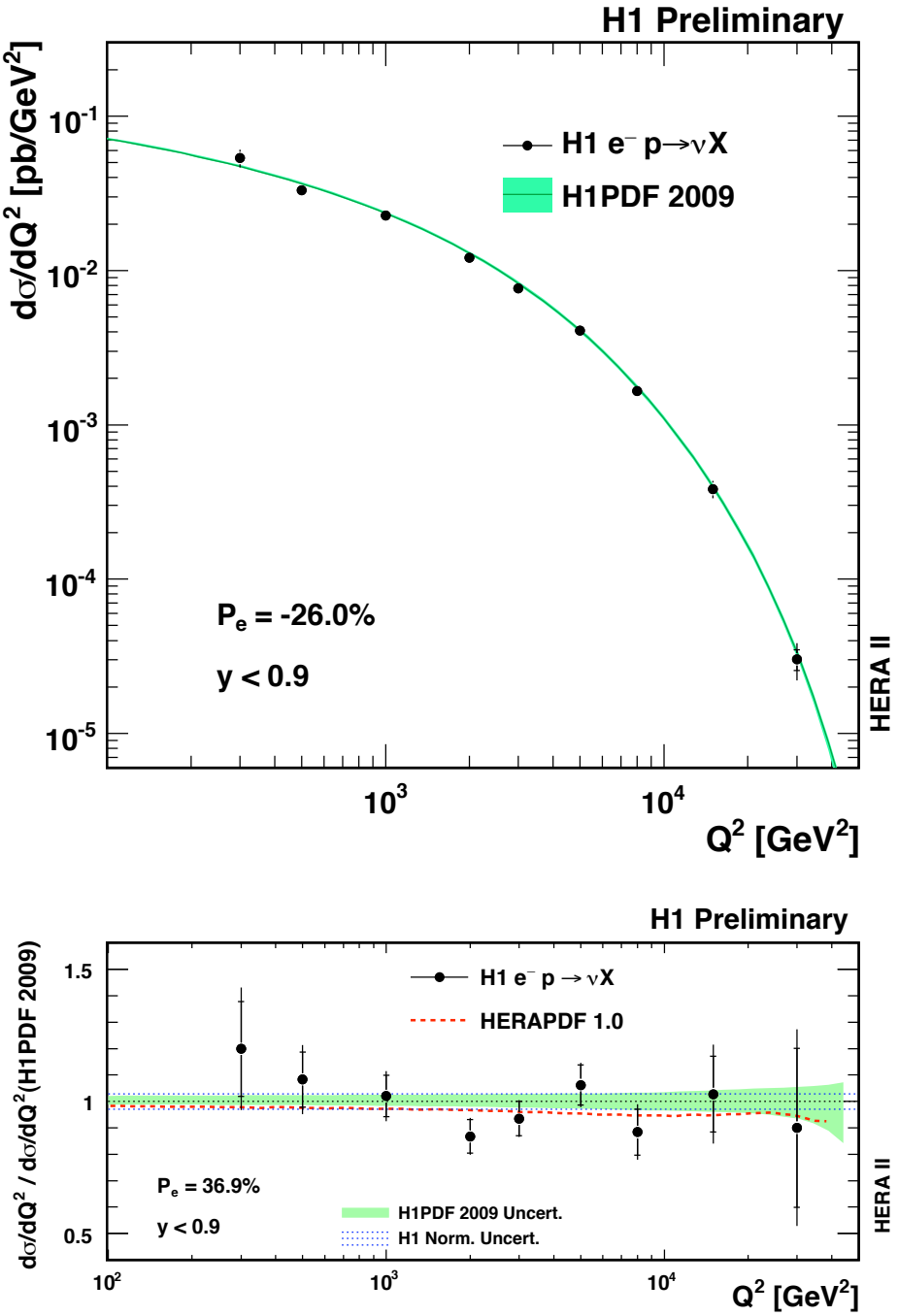

Figure 5.22: The Q^2 dependences of the CC cross section $\mathrm{d}\sigma/\mathrm{d}Q^2$ shown for the e^-p left-handed data (solid points). The results are compared with the corresponding Standard Model expectation determined from the H1PDF 2009 fit. The inner and outer error bars represent the statistical and total errors. In addition the ratio using the expectation from HERAPDF 1.0 [65, 101] is also shown (dashed line). The normalisation uncertainty is not included in the error bars and is instead represented by the blue dashed lines (bottom).

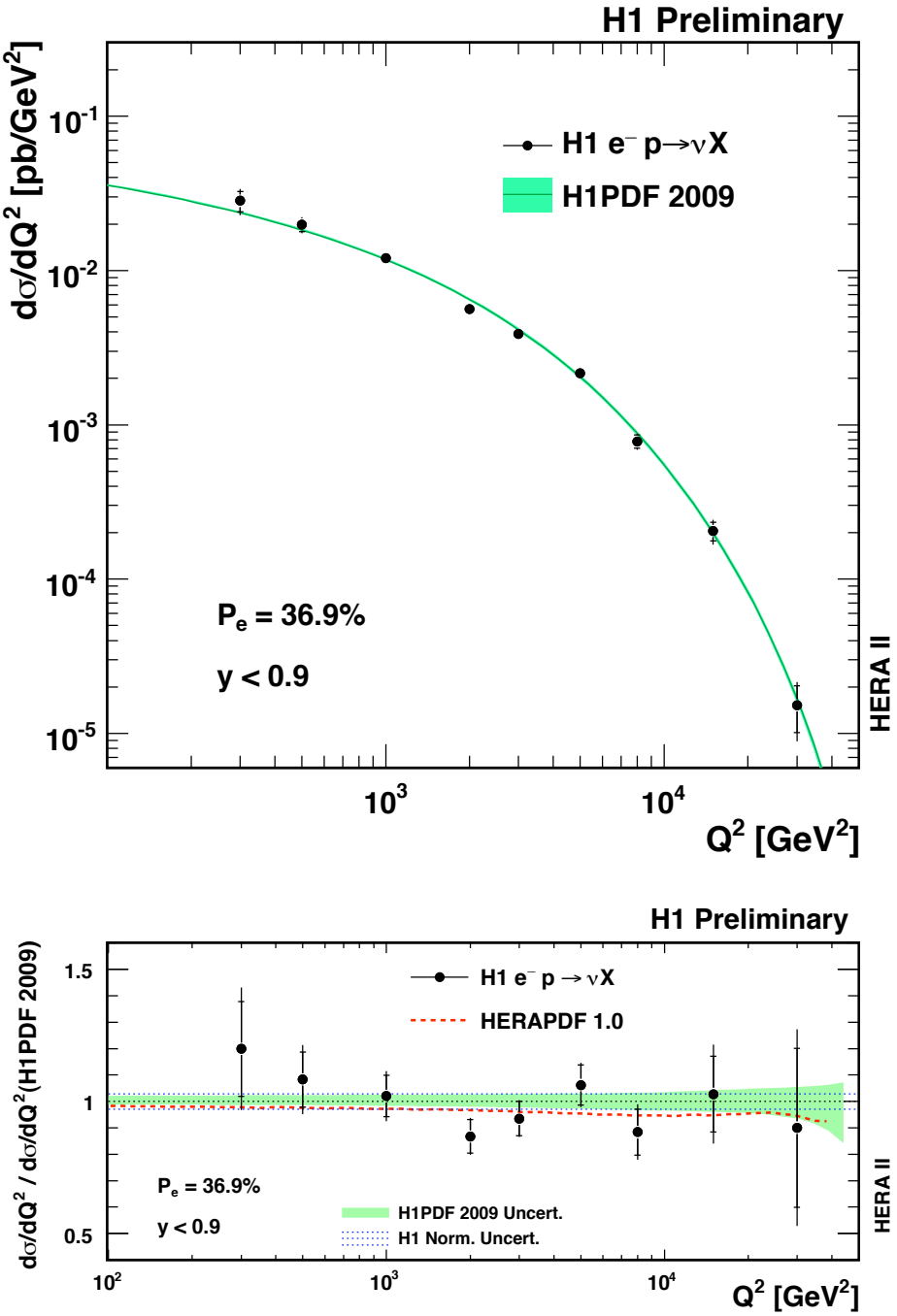

Figure 5.23: The Q^2 dependences of the CC cross section $\mathrm{d}\sigma/\mathrm{d}Q^2$ shown for the e^-p right-handed data (solid points). The results are compared with the corresponding Standard Model expectation determined from the H1PDF 2009 fit. The inner and outer error bars represent the statistical and total errors. In addition the ratio using the expectation from HERAPDF 1.0 is also shown (dashed line). The normalisation uncertainty is not included in the error bars and is instead represented by the blue dashed lines (bottom).

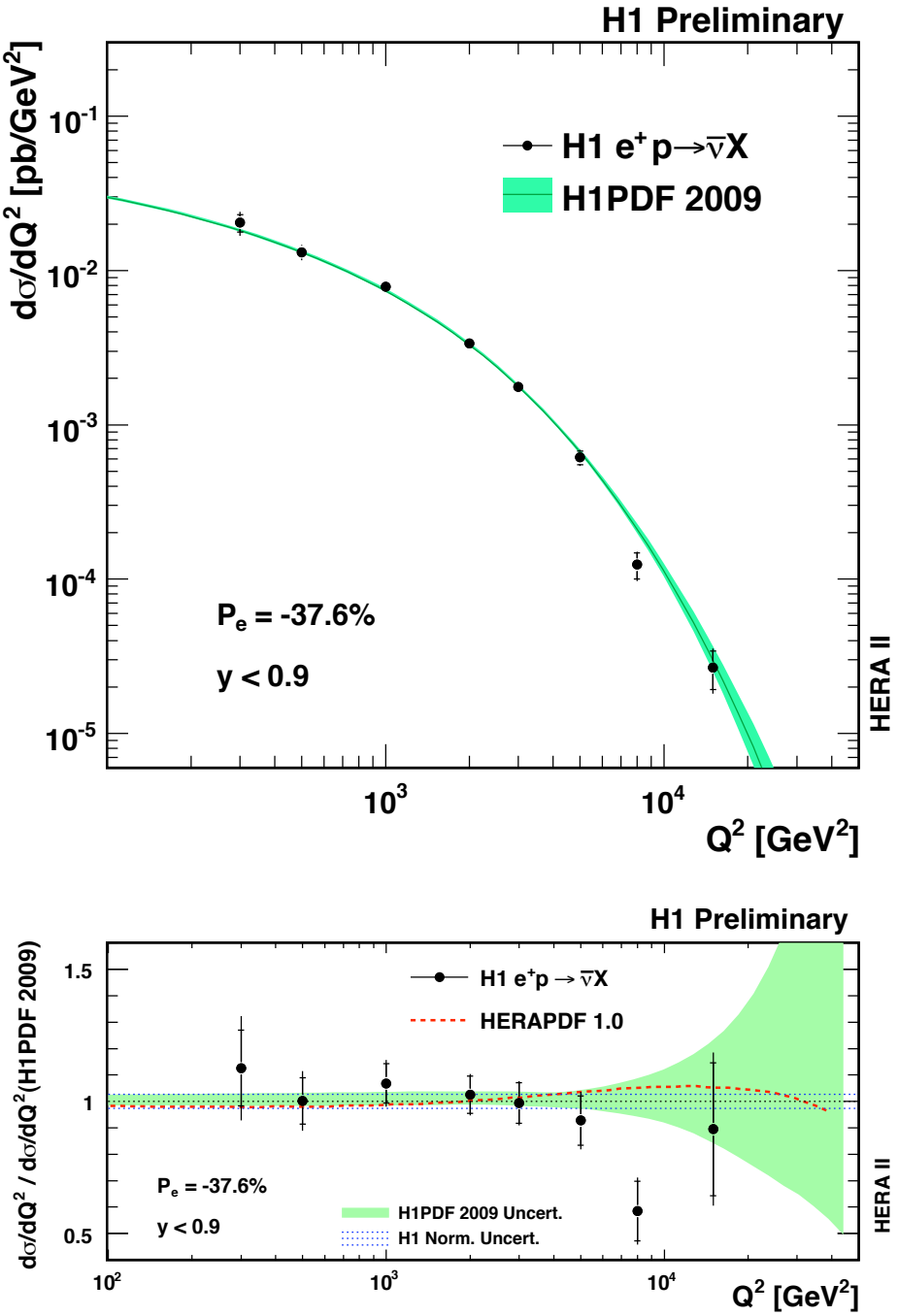

Figure 5.24: The Q^2 dependences of the CC cross section $\mathrm{d}\sigma/\mathrm{d}Q^2$ shown for the e^+p left-handed data (solid points). The results are compared with the corresponding Standard Model expectation determined from the H1PDF 2009 fit. The inner and outer error bars represent the statistical and total errors. In addition the ratio using the expectation from HERAPDF 1.0 is also shown (dashed line). The normalisation uncertainty is not included in the error bars and is instead represented by the blue dashed lines (bottom).

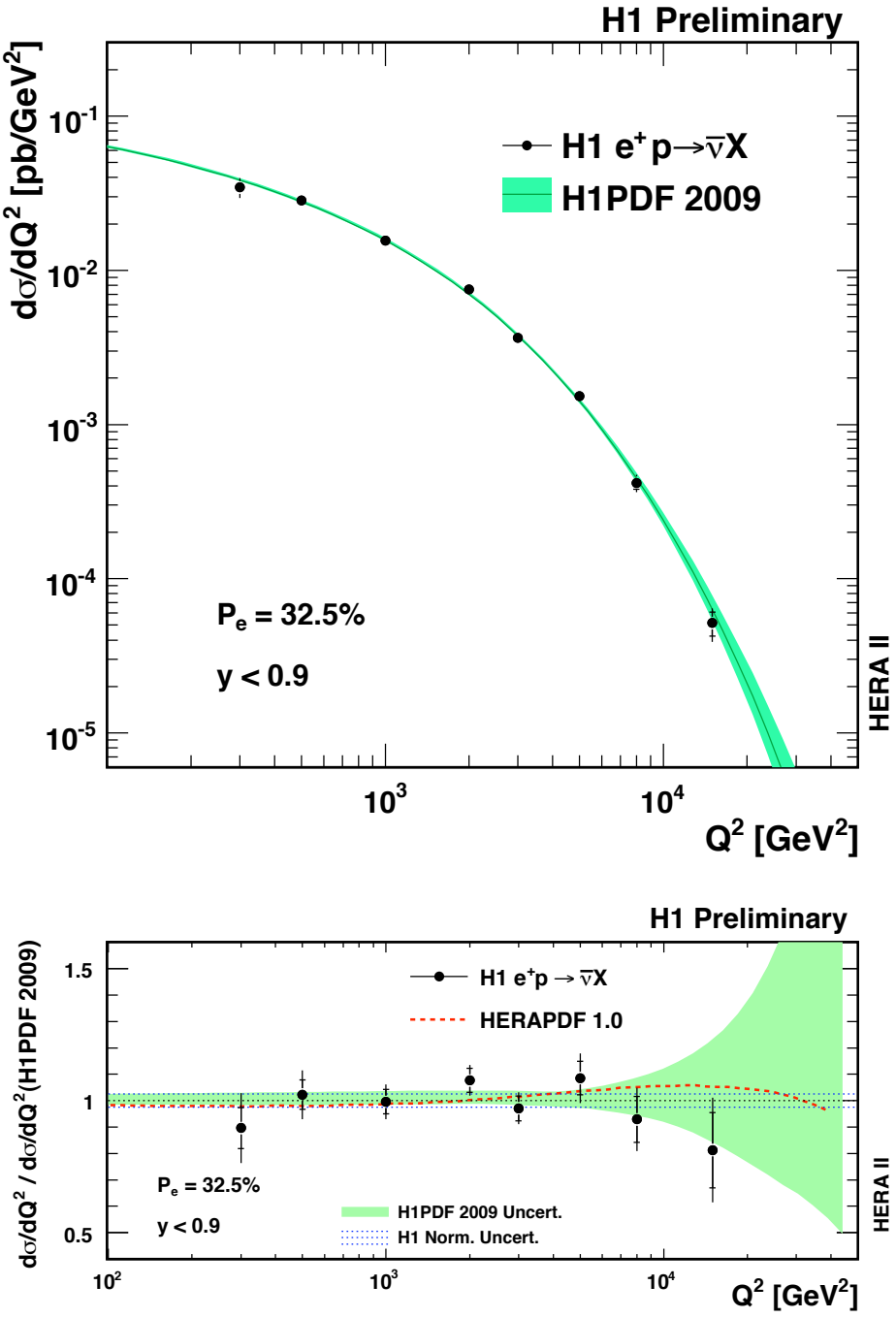

Figure 5.25: The Q^2 dependences of the CC cross section $\mathrm{d}\sigma/\mathrm{d}Q^2$ shown for the e^+p right-handed data (solid points). The results are compared with the corresponding Standard Model expectation determined from the H1PDF 2009 fit. The inner and outer error bars represent the statistical and total errors. In addition the ratio using the expectation from HERAPDF 1.0 is also shown (dashed line). The normalisation uncertainty is not included in the error bars and is instead represented by the blue dashed lines (bottom).

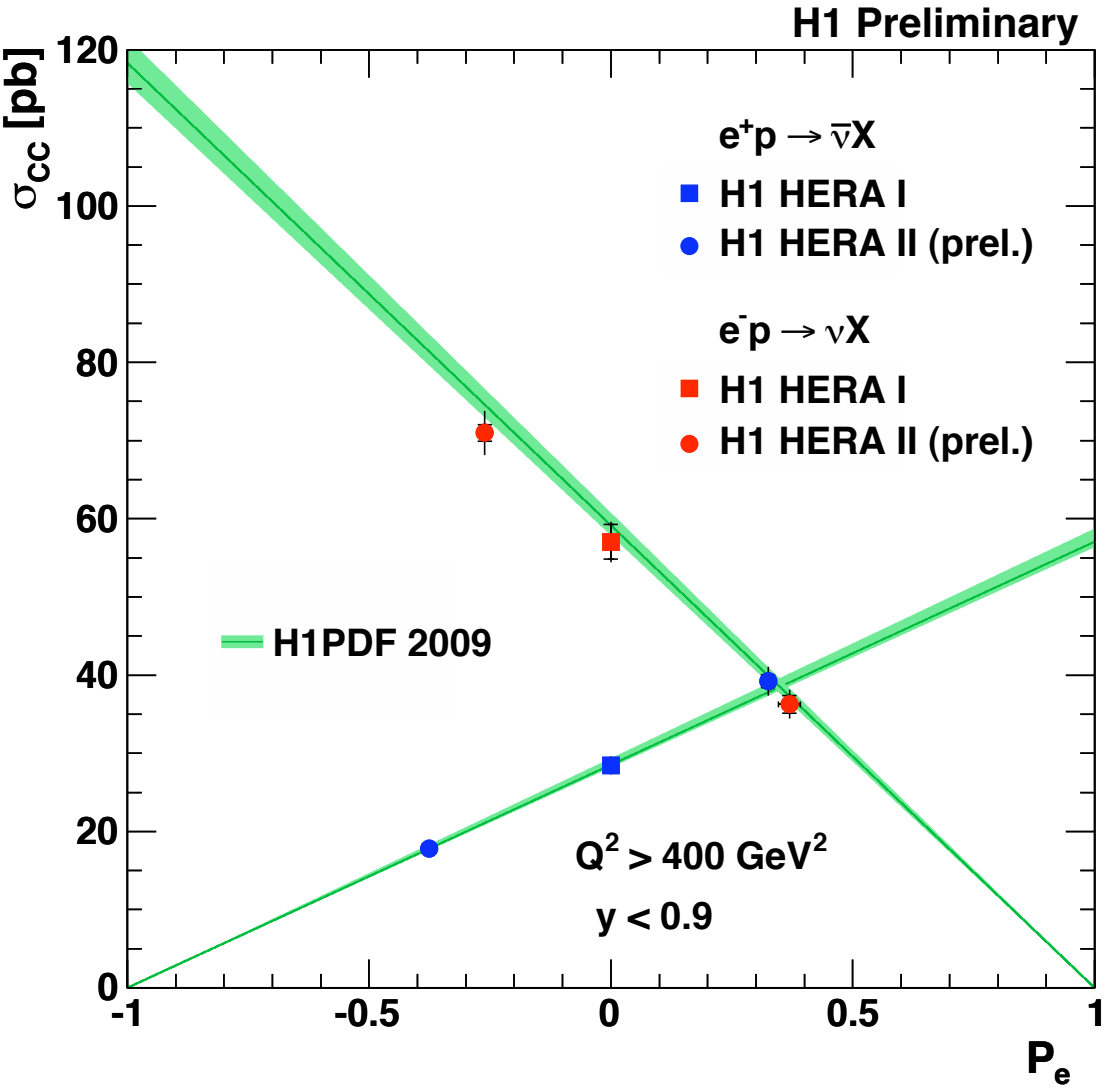

Figure 5.26: The total CC cross section $\sigma^{\text{tot}}_{\text{CC}}$ as a function of the lepton beam polarization P_e, measured for e^-p and e^+p HERA-I ([102, 103, 21]) and HERA-II data. The data are compared to the Standard Model prediction based on the H1PDF 2009 (green band). The statistical errors are indicated by inner vertical error bars, while the outer vertical error bars show the total errors. The horizontal error bars show the polarization uncertainty.

Chapter 6

Measurement of the Neutral Current cross section

Contents

In this chapter, we are going the present the analysis of the DIS NC events for the whole HERA II data. We will initially describe the cuts used to select the NC events. Some other aspects of the measurement of the scattered electron (positron) as well as the cross section measurement procedure will be presented and finally the results will be given.

6.1 Neutral Current events selection

The selection of NC events are performed in two steps. First, a preselection based on official DST is done in order to reduce a large amount of non-NC events. The corresponding μODS and HAT files will be produced in parallel. [1] These μODS/HAT files will then be used for the analysis where the NC selection will be applied.

The selection for NC events is much simpler than that for the CC since the main requirement is the identification of an electron of good quality. This will lead naturally to a rather pure NC event sample.

6.1.1 Preselection

The preselection of the NC events requires the event to have an electromagnetic particle identified in the LAr with $E_e > 8$ GeV. Since there exist satellite tails in the z-vertex distribution, we did not apply the cut $|z_{\text{vtx}}| < 50$ cm (cf. [49] for more detail).

6.1.2 Analysis selection

The following criteria are used for the selection of the NC events:

- one requires the High Voltage of the main detectors for the measurements and the trigger systems to be at the nominal functioning level: CJC1, CJC2, CIP2k, LAr, SpaCal, ToF and the luminometers (cf. section 5.1 for more detail),
- the event is triggered by the ST67 [2] (cf. section 5.1 for a description of this subtrigger),
- to ensure a highest possible trigger efficiency, one suppresses the regions where the LAr_Electron_1 is inefficient, the "fiducial volume" is applied (see section 6.7),

[1] The official μODS and HAT were produced without any preselection cut.

[2] It is demonstrated that the subtrigger ST77 can recover only a small amount of events, we did not thus use it with purpose to have a simpler analysis procedure.

- the events with electron pointing to the cracks in the LAr are removed: one of the φ-cracks of 2°, also the z-cracks regions between CB2 and CB3: $15 < z_e < 25$ cm. The electrons at the acceptance border of the BBE, $z_e < -190$ cm, are equally rejected,

- one requires the electron of highest transverse momentum to be isolated and exists in the LAr calorimetric identificator (this is a natural selection of a high Q^2 event),

- for $\theta_e > 30°$ the electron must be associated to a track and the corresponding vertex must be validated by the track (see section 6.5),

- the primary vertex must be reconstructed in the tracking devices, i.e. $|z_{vtx}| < 35$ cm,

- the non-*ep* backgrounds are also rejected, see section 4.5 for more details, here we use only the bits 0, 1, 5, 6 and 7 of the Ibg background finder which has some restrictions described in [104],

- the conservation of the energy and the longitudinal momentum $E - P_z > 35$ GeV allows to suppress the photoproduction background for the reason that in this process the scattered electron is not detected in the main detector and the corresponding $E - P_z$ is well below the expected $2E_e$,

- another region with $y_e > 0.9$ which has high rates of photoproduction background, a cut $y_e < 0.9$ is therefore introduced (see [105]),

- to reject the QED Compton events, we introduced a simple cut which identifies the events with two electromagnetic particles: if there are more than two electromagnetic particles (isolated), the two most energetic ones will be considered, if they are back-to-back, the event will be rejected by checking an additional information: the pseudo-rapidity of the most forward cluster in LAr with $E_{clus} > 400$ MeV is greater than 2, and the energy fraction of the event in the hadronic part of the LAr is more than 10%, then one of the EM particles is considered as a photon, the event will be therefore considered as a QED Compton and does not contribute to the NC sample. This cut has low inefficiency (several ‰) as expected;

- the condition $E_e > 11$ GeV is used due to low efficiency of electron identification (cf. [105] or [106])

- an additional ($y_e \leq 0.63 || Q_e^2 > 891.2$ GeV^2) cut is applied as illustrated in figure 6.12 for the separating region which is dedicated to the longitudinal structure function F_L analysis (high-y analysis) (cf. [104]);

- to ensure the quality of the polarisation, we consider only events with at least TPOL or LPOL is operational.

Finally the events of reconstructed at $Q^2 > 10000$ GeV^2 are visually scanned to reject non-ep backgrounds. The rejected non-ep background is less than about 2%.

6.2 Electron Polar Angle measurement

The track information can be used directly for the measurement of the electron polar and azimuthal angles or can be used as a reference for the measurement using electron cluster position and the interaction vertex (cf. section 6.3). The quality of track reconstruction is therefore crucial for NC analysis. One possibility to control the track reconstruction is to use the generated electron polar angle: the electron polar angle reconstructed from the track should be compatible to the generated one. An example is shown in figure 6.1(a) for the old reconstruction scheme. The difference between θ-angle of the track and that of the generated electron appeared to be biased at the order of 2 mrad (0.1°) and there was also a difference for negative and positive regions of z-vertex which triggered extensive studies on the origins of the bias.

The main cause was found to be a T0 offset in the COZ chamber. After the correction, the new MC provides indeed an essentially unbiased reference from the electron polar angle measurement as shown in figure 6.1(b). In the mean time, a few other improvements have been implemented in data:

- z-vertex bias: the nuclear interaction of the hadronic final state in the beam pipe (cf. section 6.5) may be reconstructed as a secondary vertex and it gives rise to a tail in the z-vertex distribution. The vertex fitting procedure could wrongly take this vertex as primary and this will lead to a biased θ-angle of the track. A correction is applied on the z-vertex reconstruction by a nuclear interaction finder;
- proper alignment performed for FST, FTD, BDC, BST;
- FST and BST z-vertex used (before, there were only z-vertex from CJC and CST).

Many other studies were performed and a significant improvement was achieved.

6.3 Detector alignment

A very important ingredient for the analysis of Neutral Current events is the reconstruction of kinematics which uses the polar angle of the scattered electron. The electron

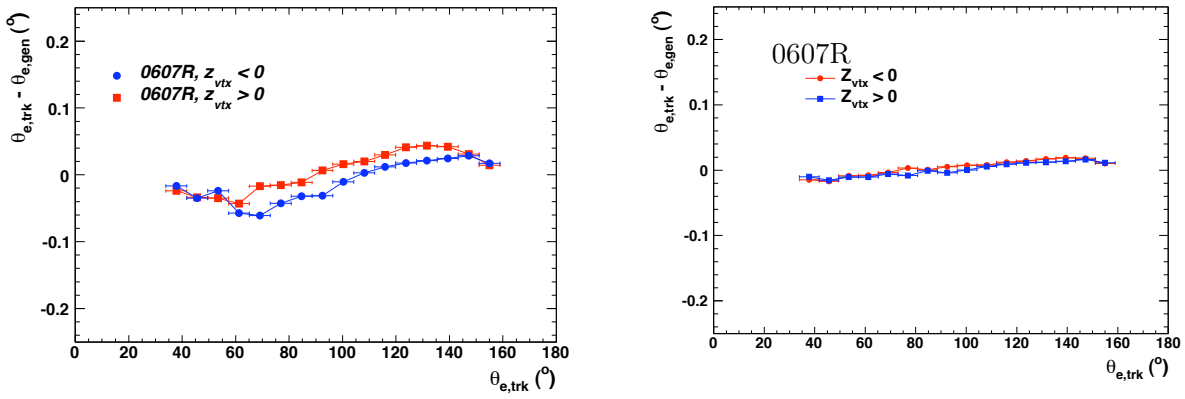

(a) (b)

Figure 6.1: The polar angle difference between the generated scattered electron and the associated track as a function of the θ polar angle of the associated track for old (a) and new (b) reconstruction schemes. The red points correspond to the negative and blue squares to the positive z-vertex regions. Example for 2006-2007 e^+p right-handed data.

polar θ_e and azimuthal ϕ_e angles can be measured by the trackers via the tracks associated to the electron or can be calculated from the position of the electron cluster in the LAr calorimeter taking into account the interaction vertex. The two determinations are complementary:

- when the trackers are fully operational, the former determination gives a better precision than the latter one. On the other hand, it suffers from occasional inefficiencies of part of the tracking system and needs a delicated modeling of the fraction of inefficient regions and its time dependence in Monte Carlo simulation
- the latter determination though intrinsically less precise is more stable as a function of time. However, it is achieved when the calorimeter is well aligned to the trackers.

6.3.1 Method

The alignment being performed in this analysis was based on the Neutral Current events sample which is used for the cross section measurement. For these events, the track associated to the scattered electron was well measured by the central outter z-chamber COZ and the central silicon microvertex detector CST[3]. Under such condition, the polar angle of the track θ_{trk} gives a good reference for the angle of the scattered electron θ_e.

[3]The alignment analysis performed in [87] used the central inner z-chamber which no longer exists in H1 after the upgrade to HERA-II.

This is demonstrated by 6.1(b) where the reconstructed electron track angle ($\theta_{\mathrm{e,trk}}$ is in good agreement with the generated angle of the scattered electron, $\theta_{e,\mathrm{gen}}$).

An alignment of the LAr calorimeter relative to the trackers is performed by comparing the positions of the track and the cluster after their extrapolation into a reference plane. For the alignment methods used in [87] or in [104], the reference plane is an octagon around the z-axis which is in the depth of 5 cm inside the LAr calorimeter. In the $x-y$ projection the reference surface has an inner radius of 105 cm, while in the backward region $z < -157$ cm the shape is a hexagon with the same radius. The track impact point is defined on the octagon after having been extrapolated from the event vertex $(x_{\mathrm{vtx}}, y_{\mathrm{vtx}}, z_{\mathrm{vtx}})$ taking into account its curvature in the magnetic field.

A projection of the cluster position on the same reference plane is done along a straight line from the vertex to the cluster since the information from the trackers should not be used for the cluster and the changes in the θ angle of the electron after the projection is expected to be small. However, the characteristic of this method may cause a problem: when the cluster is far from the octagon, the extrapolated position of the track on the octagon might be very different from that of the cluster on the same plane. To avoid this, in this analysis we use a varying octagon for each event which is taken to be the one containing the initial position of the cluster (before extrapolation).

The alignment is performed in two steps. First the change of the LAr calorimeter dimensions (shrinkage) due to the low temperature of the liquid Argon is corrected for. Then the position of the LAr is adjusted with respect to the H1 coordinate system in order to choose the one which gives the closest position of the cluster to the extrapolated track on the common plane.

Shrinkage of the LAr calorimeter

The dimensions of the LAr calorimeter had been determined at room temperature. The working temperature is 72 K which causes shrinkage of the LAr calorimeter in the z-direction.

$$z_{\mathrm{cold}} = 23.67\ \mathrm{cm} + (z_{\mathrm{warm}} - 23.67\ \mathrm{cm}) \times (1 - 0.0027) \tag{6.1}$$

which corresponds to 0.7 cm shift in the IF region ($z = 292$ cm). This is the so-called 'warm-to-cold' correction which is not applied to Monte Carlo.

Rotation and translation of the LAr calorimeter

Defining α, β and γ anti-clock-wise rotations of the LAr calorimeter around the x, y and z axes in the coordinator system of CJC, respectively. Supposing the barycenter of the scattered electron is measured in the coordinator system of the LAr is x_e, y_e, z_e. The

rotations can be expressed as follows:

$$\begin{array}{lll} x_1 = x_e & x_2 = x_1\cos\beta + z_1\sin\beta & x_3 = x_2\cos\gamma - y_2\sin\gamma \\ y_1 = y_e\cos\alpha - z_0\sin\alpha & y_2 = y_1 & y_3 = y_2\cos\gamma + x_2\sin\gamma \\ z_1 = z_e\cos\alpha + y_0\sin\alpha & z_2 = z_1\cos\beta - x_1\sin\beta & z_3 = z_2 \end{array} \tag{6.2}$$

where subscripts 1, 2 and 3 refer to the coordinates of the points after the rotations about the x, y and z-axes respectively.

Finally the position of the barycenter in the CJC coordinator system after the translations Δx, Δy and Δz in x, y and z direction correspondingly is determined as

$$x_{\text{clus}} = x_3 - \Delta x, \quad y_{\text{clus}} = y_3 - \Delta y, \quad z_{\text{clus}} = z_3 - \Delta z. \tag{6.3}$$

Parameters determination

The real rotation and translation of the LAr calorimeter with respect to the tracking system are determined by choosing the set of parameters which minimize the sum[4]:

$$\sum_i \sum_a \left(\frac{a_{\text{trk}} - a_{\text{clus}}}{\sigma_a} \right)^2 \tag{6.4}$$

with $a \equiv x$, y or z; a_{trk} and a_{clus} are correspondingly coordinates of the track and cluster impact position on the common plane; σ_a corresponds to the uncertainty of the a_{clus} measurement. The first sum runs over all data points.

Internal check

To check the validation of the alignment method we have performed the alignment procedure on MC and data in different ways:

- the shifts on x and y axis for MC are expected to be compatible to zero.
- the fitted parameters from the data were applied to correct the data and perform again the adjustment of parameters (fit) on the corrected data, the residual parameters should also compatible to zero
- a mis-alignment (arbitrary) was applied on MC and then make a fit to redetermine these parameters. Example is given in table 6.1.

Also cross checks were done by comparison with another independent method developed in [108] which gives similar results.

[4]The parameters are adjusted using the package minuit [107].

Δx (mm)	Δy (mm)
-0.15 ± 0.10	0.02 ± 0.10
α (mrad)	β (mrad)
-0.04 ± 0.08	0.09 ± 0.08

Table 6.1: Test of alignment method based on 2003–2004 e^+p MC. The shifts are compatible to zero.

6.3.2 Alignment parameters for HERA-II

In order to have an independent estimation for different wheels, we define different parameters in z which are illustrated in figure 6.2 [5]. The low statistics in the region of FB1 and FB2 leads us to choose a unique shift for both wheels (Δz_5). The different movement between different wheels BBE, CB1, CB2 and CB3 are taken into account by defining different parameters Δz_{1-4}.

The resulting parameters for all HERA-II data are shown in the table 6.2 for the 2003-2004 e^+p, 2005 e^-p, 2006 e^-p and 2006-2007 e^+p data.

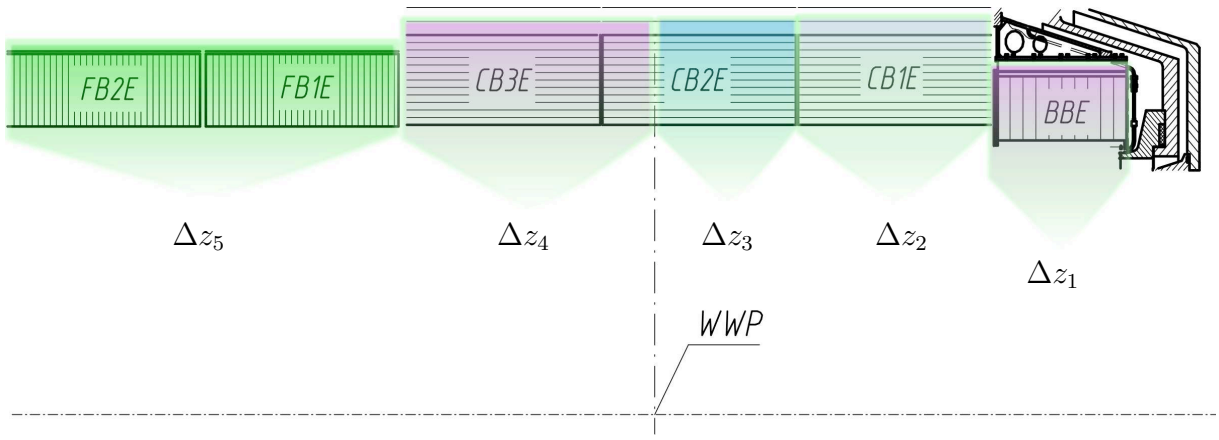

Figure 6.2: Wheel dependent parameters on z-axis. Δz_5 is common for the two wheels FB1&FB2.

As an example, figure 6.3 shows how the alignment on both 2006-2007 e^+p data and MC improves the difference $a_{\text{trk}} - a_{\text{clus}}$. Before the alignment, there was a significant

[5] A more precise parameterisation should be done by taking into account the difference in x, y axis and also different rotation for each wheel, however the results show that such a complicated parameterisation is not needed since the difference of translation in x and y between wheels is small.

	0304 (e^+p)	05 (e^-p)	06 (e^-p)	0607 (e^+p)
Δx (mm)	3.29 ± 0.08	2.29 ± 0.05	2.15 ± 0.07	2.10 ± 0.05
Δy (mm)	-3.86 ± 0.08	-3.77 ± 0.05	-4.32 ± 0.07	-4.49 ± 0.05
Δz_1 (mm)	9.83 ± 0.05	10.48 ± 0.03	10.29 ± 0.05	7.42 ± 0.03
Δz_2 (mm)	8.85 ± 0.04	9.81 ± 0.03	10.95 ± 0.04	7.79 ± 0.03
Δz_3 (mm)	2.33 ± 0.10	2.37 ± 0.07	3.01 ± 0.09	1.87 ± 0.06
Δz_4 (mm)	0.48 ± 0.25	-0.24 ± 0.16	-1.57 ± 0.23	-0.26 ± 0.16
Δz_5 (mm)	-10.21 ± 0.54	-10.26 ± 0.34	-12.96 ± 0.46	-9.18 ± 0.35
α (mrad)	0.77 ± 0.04	0.86 ± 0.03	0.08 ± 0.04	-0.29 ± 0.02
β (mrad)	-1.97 ± 0.04	-1.27 ± 0.03	-1.11 ± 0.04	-1.06 ± 0.02
γ (mrad)	-0.02 ± 0.03	-0.21 ± 0.02	-0.26 ± 0.02	-0.14 ± 0.02

Table 6.2: Alignment parameters for HERA-II data.

rotation around the y-axis. Around other axes, there were no important rotation, but the shift in y and in particular in z were sizable.

The most relevant quantity is the difference $z_{\text{trk}} - z_{\text{clus}}$ which affects directly the measurement of the polar angle of the scattered electron, θ_e. A global agreement between the MC and data was achieved after the alignment. The resulting difference $\theta_{\text{trk}} - \theta_{\text{clus}}$ was also improved and the difference between data and MC was reduced. The figure also shows how the shift on z differs for each wheel. The largest movement appeared for the region FB1–FB2 ($z_{\text{impact}} > 95$ cm). An important shift was also observed for BBE and CB1 ($z_{\text{impact}} < -60$ cm). The region of CB2 and CB3 was observed to be the least shifted part ($z_{\text{impact}} \in (-60, 20)$ cm).

A slight difference of the shifts on x and y axes was observed where the translation on y for the periods 2003-2004 e^+p and 2005 e^-p are similar but differ from the Δy for the two period 2006 e^-p and 2006-2007 e^+p. This could be explained by the fact that the detector was opened between those periods for maintenance and a small movement of subdetectors can not be excluded.

6.4 Electron calibration

In section 3.1.3 we have mentioned that the kinematic variables can be reconstructed using double-angle method which is independent of the energy measurement. It thus can be used as a reference for the control of electron energy measurement, i.e. the electron energy calibration.

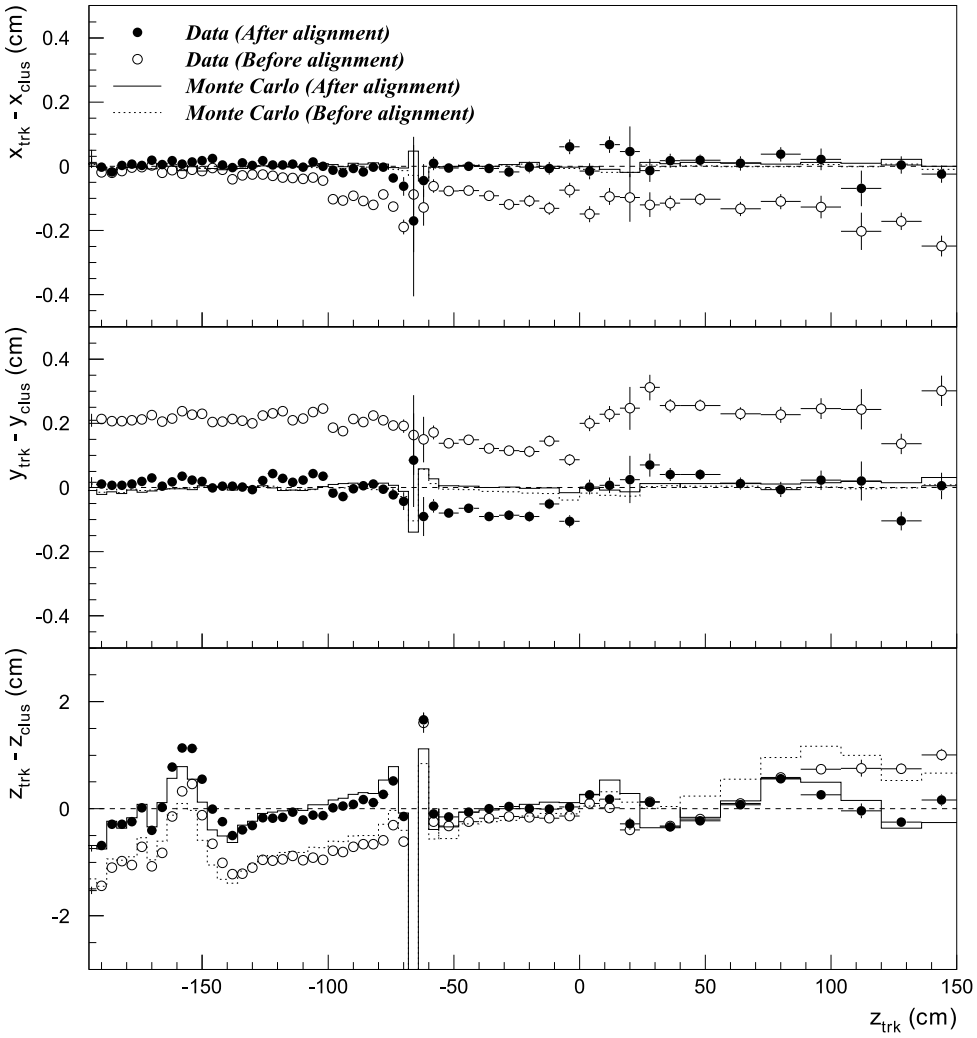

Figure 6.3: The difference of the impact point x, y and z between track and cluster as a function of z impact of the track before and after the alignment.

The electron calibration was previously performed in [108] and in [105] and is repeated for these data samples. The main idea of the calibration is to compare the electron energy measured in the LAr calorimeter and that calculated using the double-angle method for different LAr wheels.

A clean sample was used for the calibration with purpose to have a sufficient precision of the DA method. An additional cut was applied on the ratio E_e/E_{DA}: $0.85 < E_e/E_{DA} < 1.15$ to reduce the influence of the tail in the distribution. The calibration is then done in two steps:

- The wheel- and octant-wise calibration: The first calibration step was performed octant-wise for each of the BBE, CB1, CB2 and CB3 wheels. The regions are

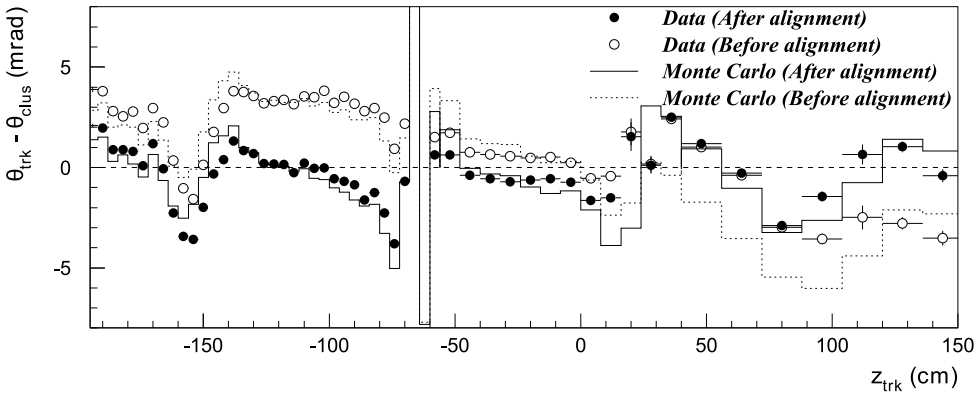

Figure 6.4: The difference of the measured polar angle between track and cluster as a function of z impact of the track before and after the alignment.

enumerated by $N_{\text{stack}} = 8N_{\text{wheel}} + N_{\text{octant}}$. Here, $N_{\text{octant}} = 0 - 7$ for $\varphi = 0 - 360°$, and the wheels are enumerated by $N_{\text{wheel}} = 0 - 3$ for BBE, CB1, CB2 and CB3. Because of the limited statistics, for the wheels FB1 and FB2 only one calibration factor per wheel is determined.

- The z-wise calibration. Further calibration factors are determined as a function of the z position of the electron impact point in the LAr calorimeter z_{LAr}. The factors are determined in 1 cm bins for $z_{\text{LAr}} < 0$; 10 cm bins for $0 \leq z_{\text{LAr}} \leq 90$ cm; 20 cm bins for $90 \leq z_{\text{LAr}} \leq 110$ cm and 50 cm bins for $z_{\text{LAr}} \geq 110$ cm. The increasing bin size is related to the decreasing statistics of the NC events (increasing Q^2).

The two-step procedure is iteratively repeated with narrowing of the averaging window for E_e/E_{DA} to $0.9 < E_e/E_{DA} < 1.1$.

In the forward region, between 5° and 45° an absolute calibration with a precision of 1% was performed in a dedicated analysis [109] by selecting an isolated high $P_T > 25$ GeV electron using all HERA-I and HERA-II data.

6.5 Vertex-track-cluster matching efficiency

The reconstruction of charged particle tracks is described in [47]. Briefly, track segments are found by fitting a helical path to the hits in space, determined in the CJC. The ep interaction region extends over a few tens of μm in the xy-plane with a mean value that typically stands constant over several runs. The known x and y position of the interaction vertex can then be used to improve the track fitting by providing an extra constraint. The z position of the vertex is obtained from these vertex fitted tracks. The tracks that can

be fitted to the interaction vertex are known as DTRA tracks. Non-vertex-fitted tracks are known as DTNV tracks. At the analysis level, in order to improve the precision of NC events measurement and to reduce the non-*ep* background, the identified electron should be associated to a track of good quality and there should be at least one vertex which is linked to the electron track. Traditionally, the CJC vertex is used. However, due to the nuclear interaction of the hadronic final state in the beam pipe, the reconstructed CJC vertex does not always match with the DTRA track and it gives rise to the tail in z-vertex distribution (see [108]). This is shown in figure 6.5. Moreover, if one uses only the CJC vertex matched by the DTRA track, the obtained efficiency of the vertex-track-cluster matching will be low ($\sim 92\%$).

A more precise study needs therefore a definition of a new strategy which has two purposes: a more precise estimation of z-vertex, allowing a better reconstruction of kinematic variables, and a higher efficiency of vertex-track finding which recovers the most possible neutral current sample.

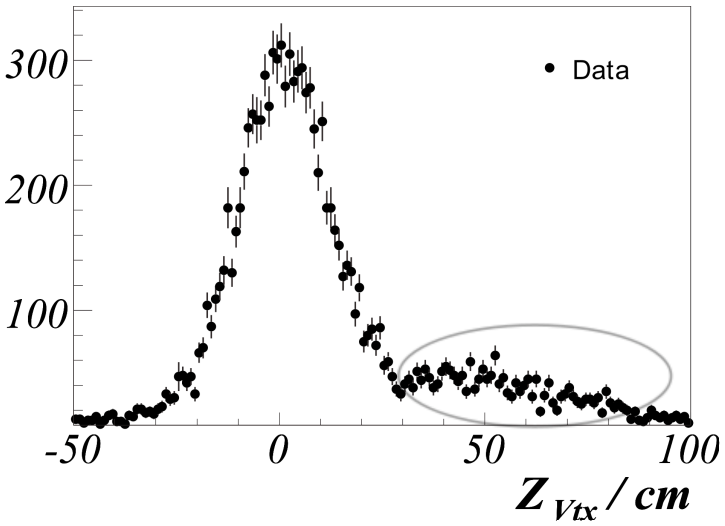

Figure 6.5: Distribution of the z-vertex for NC events with no DTRA electron track. The vertices determined from the hadronic final state give rise to the right tail of the distribution caused by nuclear interactions in the beam pipe.

6.5.1 Strategy

An event is validated, says *having an optimal vertex*, if it belongs to one of the following three subsamples:

eDTRA

A primary-vertex-fitted track, DTRA, is searched for first. Among all DTRA tracks, the one with smallest distance of closest approach (dca) to the center of gravity of the electron cluster is considered. If this distance is less than 12 cm, the track is assigned to the cluster.

eDTNV

If there is no DTRA track assigned to the cluster, then the DTNV tracks are checked. This distance is also required to be less than 12 cm so that the DTNV track could be assigned to the cluster. An additional condition for the corresponding DTNV vertex is required: its dca to the DTNV track must be less than 2 cm to ensure the quality of the vertex (as illustrated in figure 6.6, at dca larger than 2 cm, the DTNV vertex is not well reconstructed).

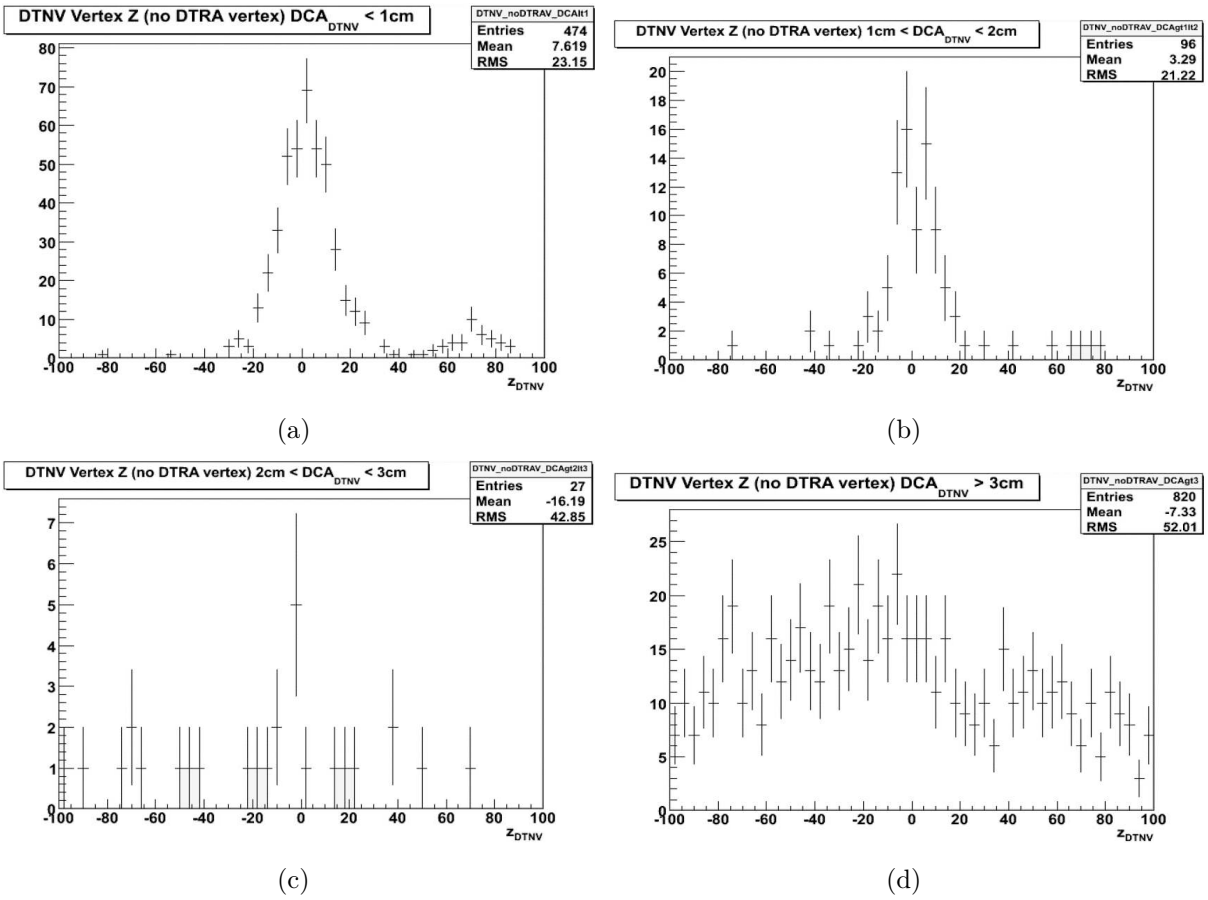

Figure 6.6: Distributions of z_{vtx}(DTNV) for different regions of its dca to the closest DTNV track: dca $<$ 1 cm (a), 1 cm $<$ dca $<$ 2 cm (b), 2 cm $<$ dca $<$ 3 cm (c) and dca $>$ 3 cm (d). The pictures show a bad resolution for dca $>$ 2 cm, the corresponding events are therefore rejected.

Moreover, in this case the CJC vertex is not matched by the DTRA track, the only reference is based on the difference $z_{\mathrm{CJC}} - z_{\mathrm{DTNV}}$:

- $z_{\mathrm{CJC}} - z_{\mathrm{DTNV}} > 10$ cm: the CJC vertex is biased (as mentioned above) the DTNV is therefore taken (eDTNV-1 sample in figure 6.7),

- for the region $z_{\mathrm{CJC}} - z_{\mathrm{DTNV}} < -10$ cm, the CJC vertex is heavily biased (long tail at negative z), the DTNV vertex is thus used in stead of the CJC vertex. Since the z_{DTNV} is biased in the positive region, the condition $z_{\mathrm{DTNV}} < 20$ cm is applied to avoid the tail (eDTNV-2 sample in figure 6.7).

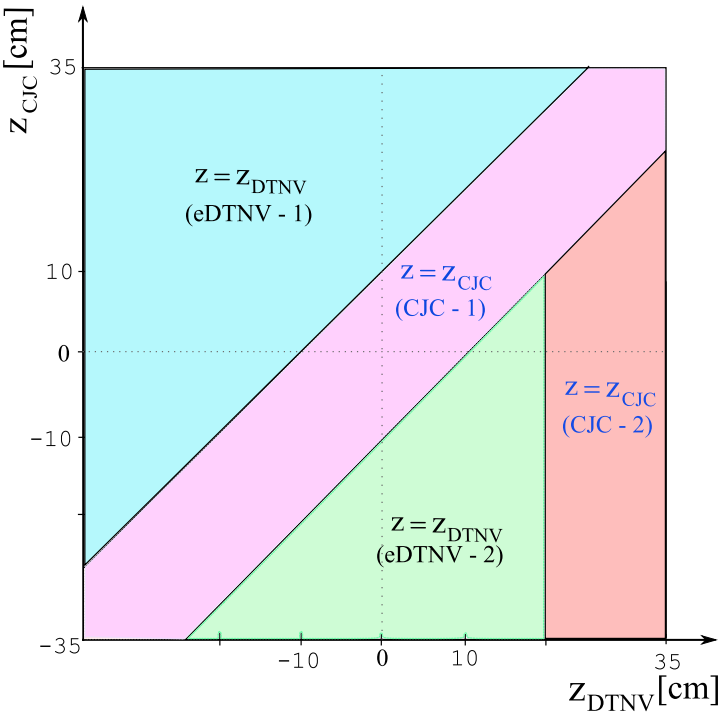

Figure 6.7: Schematic illustration for the eDTNV and CJC sample selection.

CJC

For the region $-10\mathrm{cm} < z_{\mathrm{CJC}} - z_{\mathrm{DTNV}} < 10$ cm: both CJC and DTNV vertices are unbiased, the CJC vertex is thus chosen (subsample CJC-1 in figure 6.7). Another amount of events is recovered by using also the region $z_{\mathrm{CJC}} - z_{\mathrm{DTNV}} < -10$ cm but here, as the CJC vertex is used, and it has a large tail at negative region, the additional validation is required: $z_{\mathrm{DTNV}} > 20$ cm (subsample CJC-2, figure 6.7).

A third kind of events which contribute to this sample are those which have neither the validation of the DTRA nor of the DTNV track but that of the CIP (which is a good reference for z-vertex reconstruction, see section 2.9). To be taken as a reference, the CIP is required to have at least two hits.

6.5.2 Monitor sample and efficiencies

To evaluate the vertex-track-cluster link efficiency, one uses a clean sample which is basically the NC sample (see section 6.1) but with tighter cuts with purpose to suppress *ep*

or non-*ep* background as much as possible. For that, the event is required be conserved in longitudinal momentum ($45 < E - P_z < 65$ GeV) and balanced in transverse momentum ($0.5 < P_{T,h}/P_{T,e} < 1.4$). An additional condition is applied on the energy of the scattered electron: $E_e > 18$ GeV. For events with null z-vertex, i.e. there is neither CJC nor DTNV vertices, only those with $\gamma_h < 30^\circ$ are kept. These conditions are used to reject photoproduction background. Such a clean sample is called *monitor sample*.

The efficiency of the vertex-track-cluster finding, or the *optimal vertex efficiency*, is then defined as:

$$\varepsilon = \frac{N_{e\mathrm{DTRA}} + N_{e\mathrm{DTNV}} + N_{\mathrm{CJC}}}{N_{e\mathrm{DTRA}} + N_{e\mathrm{DTNV}} + N_{\mathrm{CJC}} + N_{\mathrm{noVtx}}} \tag{6.5}$$

where N_i correspond to the number of events which belong to the subsamples eDTRA, eDTNV, CJC or without vertex. The dominator in this equation is in fact the total number of the monitor sample (N_{Monitor}).

The individual efficiencies can also be expressed as:

$$\varepsilon_{\mathrm{DTRA}} = \frac{N_{e\mathrm{DTRA}}}{N_{\mathrm{Monitor}}} \qquad \varepsilon_{\mathrm{DTNV}} = \frac{N_{e\mathrm{DTNV}}}{N_{\mathrm{Monitor}}} \qquad \varepsilon_{\mathrm{CJC}} = \frac{N_{\mathrm{CJC}}}{N_{\mathrm{Monitor}}} \tag{6.6}$$

Figures 6.8(a), 6.8(b), 6.8(c) show the individual efficiencies of three subsamples. The inefficiency is shown as well in figure 6.8(d). The agreement between data and MC for the eDTNV and CJC samples are rather good. However there is a difference of up to $\sim 1\%$ between data and MC for the eDTRA sample. The similar situation is shown in figure 6.9(a) for the combined efficiency. A correction determined in (x, Q^2) bins (cf. figure 6.12) is then needed to apply on the MC. Figure 6.9(b) shows the comparison between data and MC after correction. A good agreement is achieved and the remaining small differences of 0.5% at $Q^2 < 1000$ GeV^2 and 1% at $Q^2 \geq 1000$ GeV^2 are assigned to systematic uncertainty.

6.6 Z-vertex reweighting

For the same reason as for the z-vertex distribution of the CC events, although the z-vertex has been simulated correspondingly to the run numbers but there still presents a small difference between data and MC. The distribution therefore needs to be corrected for a better modelling of the data. All the procedure of correction is the same as for the CC analysis. The fit procedure is performed for the data of each sub-period. Figure 6.10 shows the effect of the z-vertex reweighting. The corrected MC describes quite well the data

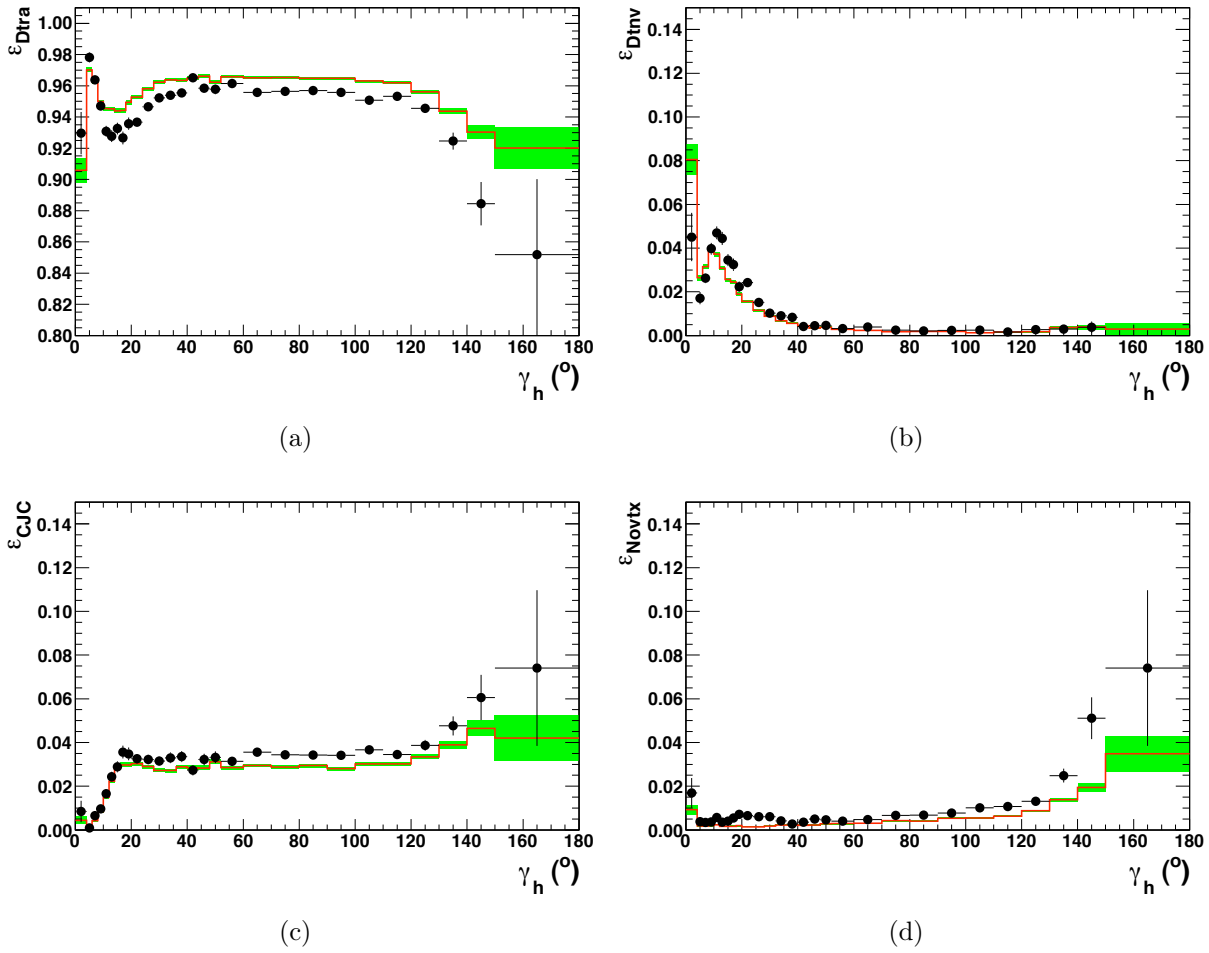

(a) (b) (c) (d)

Figure 6.8: Vertex-track-cluster link efficiencies for DTRA (a), DTNV (b) and CJC (c) no vertex-track matching (d) samples are in good agreement between data (points) and MC (histograms) for eDTNV and CJC samples with an overall disagreement of ∼1% for eDTRA sample.

6.7 Trigger efficiency and Fiducial Volume

Since in the high Q^2 NC DIS events, the electron is scattered into the LAr calorimeter, the most important trigger component for this analysis is thus LAr triggers.

The efficiency of a trigger element TE, or a combination of trigger elements, is defined as follows

$$\varepsilon_{TE} = \frac{\text{number of events triggered by MT and TE}}{\text{number of events triggered by MT}} \tag{6.7}$$

where MT is an independent monitor trigger or trigger element. The selection of monitor is given in table 6.3 (cf. [108]).

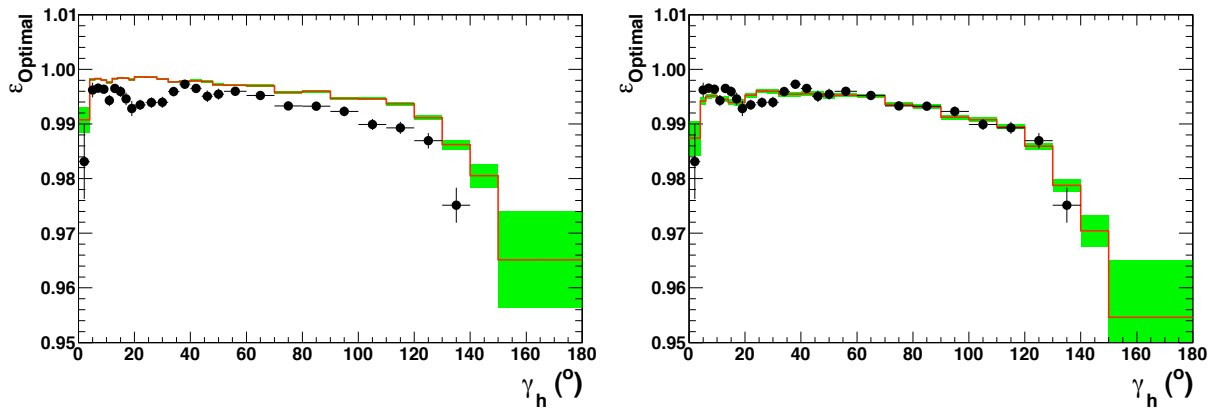

(a) (b)

Figure 6.9: Combined vertex-track-cluster link efficiency which is called "optimal vertex efficiency" before (a) and after (b) correction.

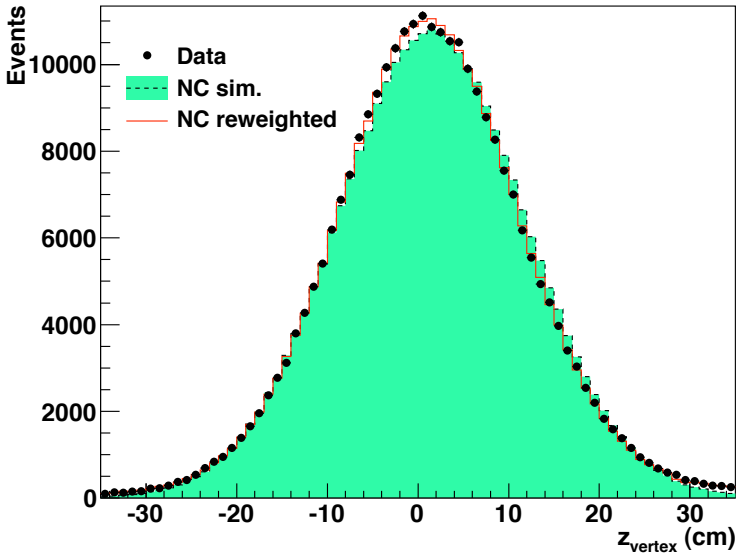

Figure 6.10: Z-vertex distribution for data (black points), simulated NC MC (green histogram) and reweighted NC MC (red line). A good agreement between data and MC achieved after the reweighting. Example shown for e^-p left-handed period which is the combination of 2005 e^-p left-handed and 2006 e^-p left-handed. The reweighting was determined separately for these two sub-periods.

LAr_electron_1 efficiency

The trigger level information on the calorimeter Big Towers is exploited to study the LAr_electron_1 TE efficiency. The LAr_electron_1 can be fired by both the scattered

LAr trigger elements	monitor trigger
LAr_electron_1	PSNC
LAr_T0	CIP_T0
CIP_T0	LAr_T0
ToF Veto	ST57 and special runs
CIP Veto	ST57 and special runs

Table 6.3: NC trigger elements and their monitor triggers

electron and the hadronic final state. The efficiency of the LAr triggering on an electron deposit is evaluated using those neutral current events in which the hadronic final state caused the LAr_electron_1 TE to fire. In turn, the efficiency for triggering on the hadronic final state is calculated with events in which an electron deposit causes the LAr_electron_1 TE to fire. An example for the combined efficiency of triggering on hadrons and on electrons is shown in figure 6.11. The efficiency is found to be very high over the bulk of the detector volume. Inefficient regions are excluded from this analysis. After this cut, the remaining efficiency will be applied on NC MC as a function of x and Q^2. This is done for each subperiod.

Timing condition

The T0 trigger elements allow the determination of the bunch crossing time. It is shown that the efficiency of the combined LAr T0 and CIP T0 is close to 100%.

Veto conditions

The veto conditions use the Time of Flight information to reject out of time background events. In addition, the CIP is able to veto background from interactions in the collimators located in the beam pipe on the basis of the z-vertex origin of tracks.

The signal inefficiency due to these veto conditions, i.e. the chance of rejecting good ep events, is continuously monitored with the subtrigger ST57. This monitor trigger is a copy of ST67 without the veto conditions applied. It is prescaled to keep the rate manageable.

The efficiencies of the CIP_veto and ToF_veto requirement are given in table 6.4.

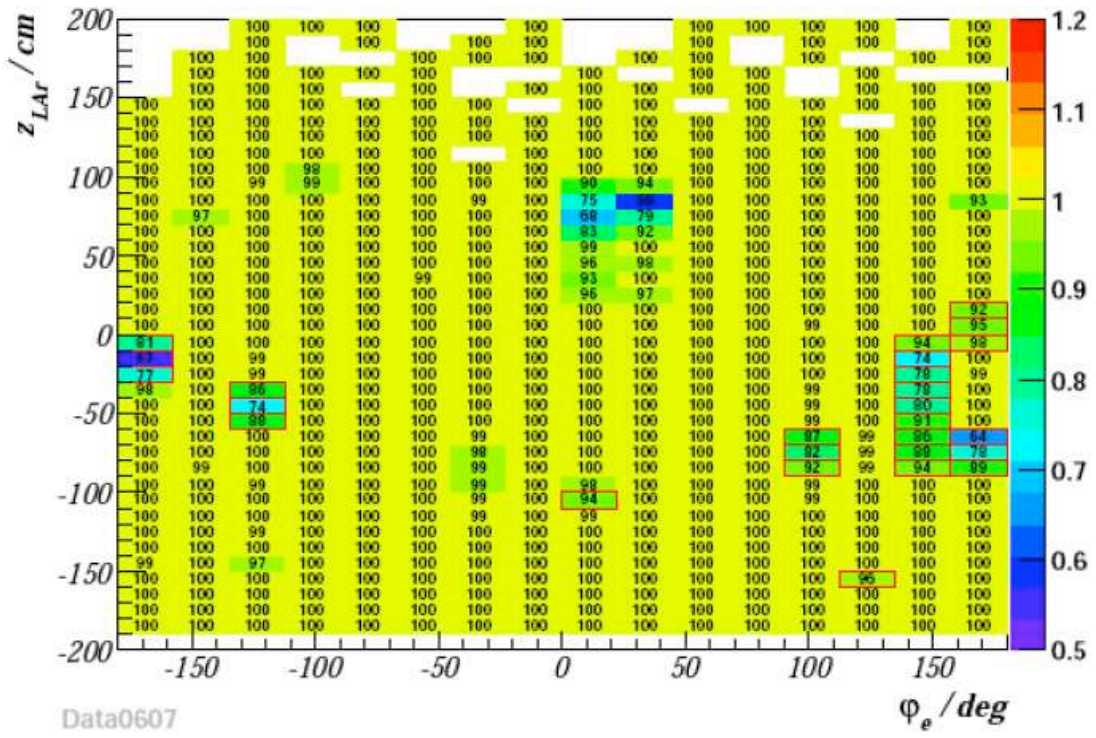

Figure 6.11: The efficiency of the trigger element LAr_electron_1, presented in a $z-\varphi$ grid for 0607e^+ data. The areas indicated by red squares are excluded regions due to low efficiency.

Fiducial Volume

The fiducial volume cuts ensure the precise measurement of the scattered electron of high Q^2 NC events. The φ and z cracks regions are excluded to obtain a reliable electron identification, a precise determination of the cluster position and good resolution of the electron energy measurement. In addition, regions of inefficient LAr trigger cells and CIP trigger pads are excluded from the analysis, taking into account their time variation. The fiducial volume definition is applied using the impact position of the scattered electron.

6.8 Cross section measurement procedure

6.8.1 Binning scheme

The cross section measurement in this analysis is performed in (x, Q^2) bins. The binning was developed for NC analyses at HERA I in [110, 111]. Here we introduced some modification to adapt the high-y analysis. The main idea is to have equidistant edges in $\log_{10}(x)$ and $\log_{10}(Q^2)$ but taking into account event statistics and detector resolution.

Period	Helicity	CIP_veto	ToF_veto
$0304e^+p$	RH	99.79%	99.30%
$0304e^+p$	LH	99.56%	99.30%
$0405e^-p$	RH	99.44%	99.09%
$0405e^-p$	LH	99.49%	99.44%
06 e^-p	L&R	99.37%	99.60%
$0607e^+p$	L&R	99.67%	99.82%

Table 6.4: CIP_veto and ToF_veto requirement efficiency for HERA-II data sets.

The same binning in Q^2 is used for both double and single differential cross section.

There are ten bins per decade in Q^2 and five bin per decade in x. At $Q^2 \geq 3000$ GeV^2 the bin size is doubled due to limited statistics. The bin boundaries and bin centers in Q^2 are:

$\log_{10}(Q^2)$ bin boundaries

1.75 1.875 2.00 2.125 2.25 2.35 2.45 2.55
2.65 2.75 2.85 2.95 3.05 3.15 3.25 3.35
3.55 3.78 4.00 4.222 4.444 4.666 4.888

Q^2 bin boundaries

56.23 74.99 99.999 133.4 177.8 223.9 281.8 354.8
446.7 562.3 707.9 891.2 1122 1412 1778 2239
3548 6000 10000 16680 27778 46334 77268

and the corresponding bin centers:

Q^2 bin centers

60 90 120 150 200 250 300 400
500 650 800 1000 1200 1500 2000 3000
5000 8000 12000 20000 30000 50000

The binning in x is however more complicated where we have to take into account the difference of statistics for different Q^2 region. At $Q^2 \leq 446.7$ GeV^2 the binning is modified to accommodate the limited x resolution. The resulting bin boundaries and bin centers are:

$\log(x)$ bin boundaries

-3.0	-2.8	-2.6	-2.4	-2.2			
-2.0	-1.8	-1.6	-1.4	-1.2			
-1.0		-0.767	-0.50		-0.2228	0	for $Q^2 \leq 446.7$ GeV^2
-1.0	-0.84	-0.68	-0.50	-0.30	-0.0228	0	for $Q^2 > 446.7$ GeV^2

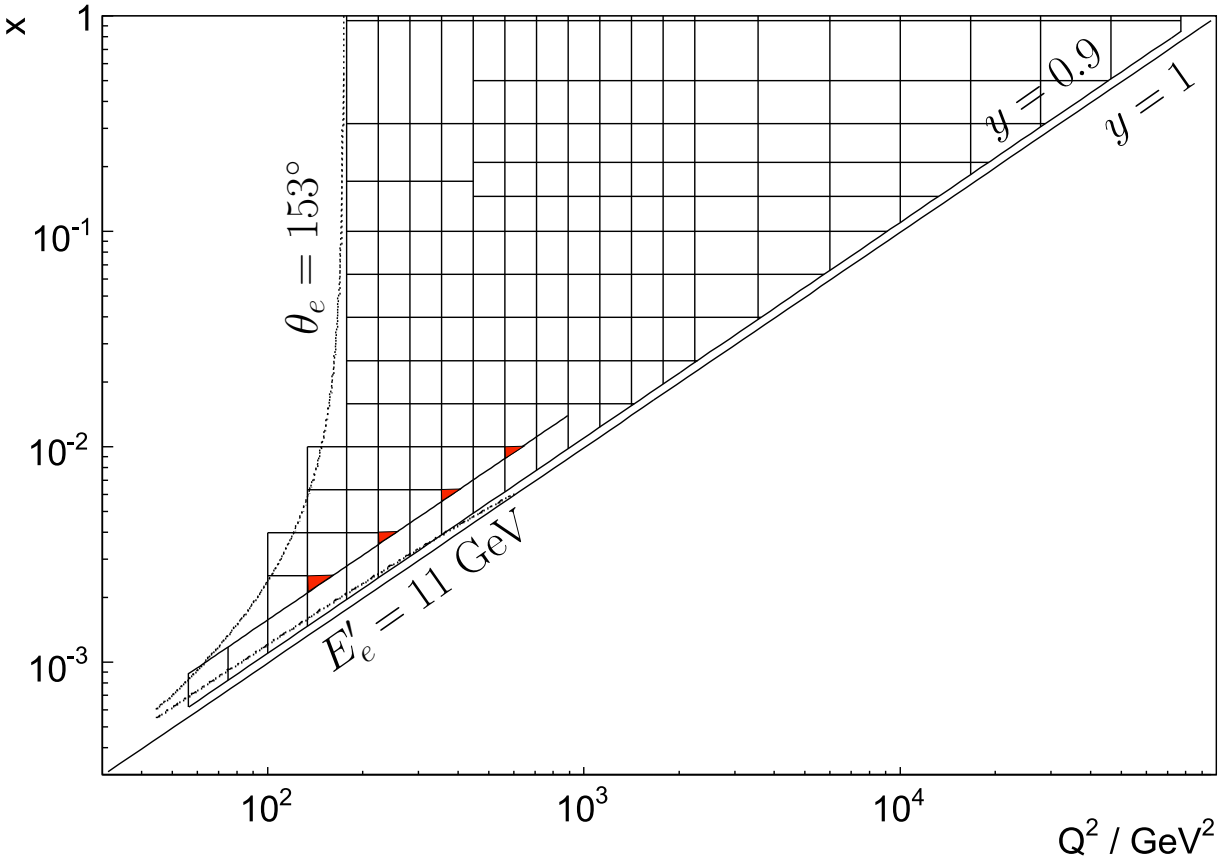

Figure 6.12: Division of the (x, Q^2) plane for the measurement of the inclusive DIS cross section. Due to the cut ($y_e < 0.63 || Q_e^2 > 891.2$ GeV^2) the four bins (red triangles) at the border of the line which have not enough statistics will be merged into the one with higher x but with the same bin center in Q^2. Also shown are the upper $y = 0.9$-cut, the $E_e = 11$ GeV cut and the line of constant $\theta_e = 153°$ which corresponds to roughly the acceptance of the LAr calorimeter.

x bin centers:

0.0013	0.0020	0.0032	0.0050	0.0080	
0.013	0.020	0.032	0.050	0.080	
0.13	0.18		0.40		0.97 (for $Q^2 \leq 446.7$ GeV^2)
0.13	0.18	0.25	0.40	0.65	0.97 (for $Q^2 > 446.7$ GeV^2)

At Q^2 = 150, 250, 400 and 650 GeV^2, the small triangular bins at smallest x are truncated by the line $y = 0.63$ are merged with the neighbouring bins at the same value of Q^2 and larger values of x to gain statistics. The illustration of the binning scheme for NC analysis is shown in figure 6.12.

For the quality requirement of the measurement in each bin, we use the same definition of Acceptance, Purity and Stability as in section 5.6.4.

6.8.2 Data and MC comparison

The comparisons between data and MC determined by H1PDF 2009 for the combined periods e^+p and e^-p are shown in figures 6.13 and 6.14, correspondingly, for the scattered electron energy E'_e, its polar angle θ_e, $E - P_z$, Q^2_e and the ratio $P_{T,h}/P_{T,e}$. One observes that there is a small deficit of the data. Apart from that, a good description of data by the MC is achieved and also the contribution of background is small.

6.8.3 Systematic Uncertainties

The systematic uncertainties on the cross section measurements are discussed briefly below (see [49, 108] and references therein for more details). Positive and negative variations of one standard deviation of each error source are found to yield errors which are symmetric to a good approximation. The systematic uncertainties of each source are taken to be fully uncorrelated between the cross section measurements unless stated otherwise.

- An uncertainty of 1% ($z_{imp} < +20$cm), 2% ($+20$cm $< z_{imp} < +100$cm) and 3% for $z_{imp} > +100$cm) is assigned to the scale of the electromagnetic energy measured in the LAr calorimeter, where z_{imp} is the z coordinate of the impact position of the scattered lepton in the LAr calorimeter. 0.5% of this uncertainty is considered as a correlated component.

- An uncertainty of 0.5% for $\theta_e < 100^\circ$ and 2% for $\theta_e > 100^\circ$ in the identification of the scattered electron or positron.

- An uncertainty in the polar angle measurement of the scattered lepton is taken to be 2 mrad for $\theta_e > 120^\circ$ and 3 mrad elsewhere.

- An uncertainty of 2% is assigned to the scale of the hadronic energy measured in the detector, of which 1% is considered as a correlated component to the uncertainty.

- A 10% correlated uncertainty is assigned to the amount of energy in the LAr calorimeter attributed to noise.

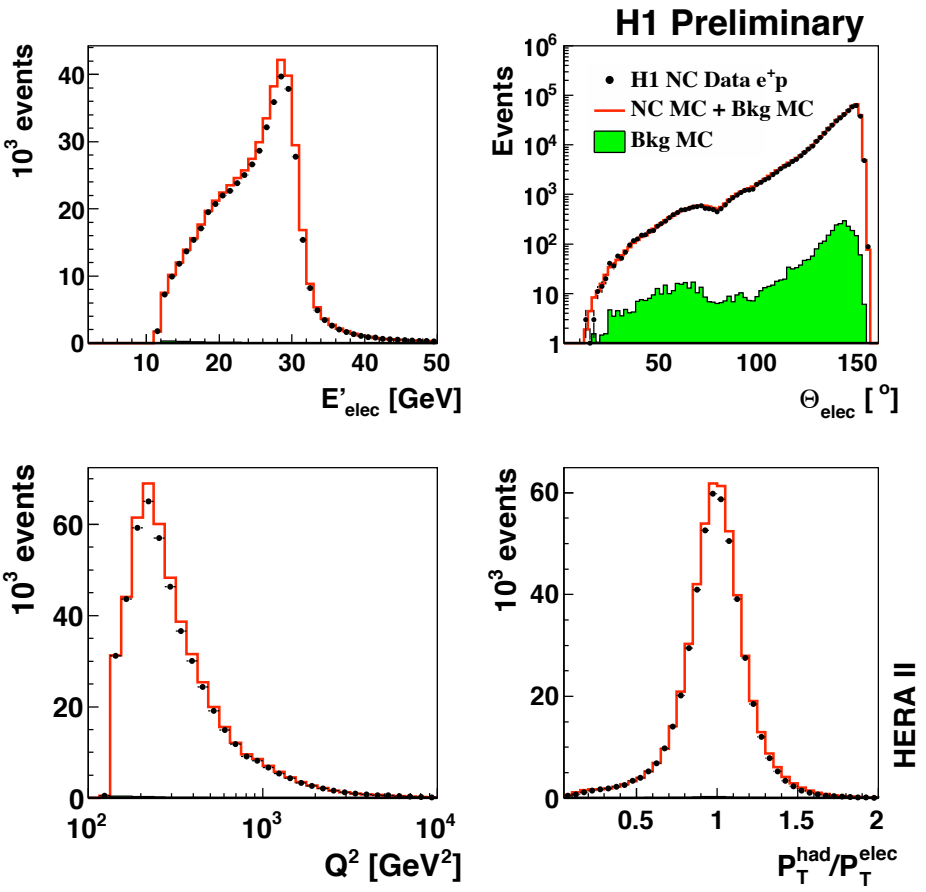

Figure 6.13: Distributions of the electron energy E'_e, the electron polar angle θ_e, Q^2 and $P_{T,h}/P_{T,e}$ for the combined e^+p data. The MC contributions from the neutral current (NC) process and the ep background (bkg) processes are shown as open histograms with the latter contribution alone being shown as shaded histograms.

- A 1% uncertainty on the trigger efficiency.
- A 30% correlated uncertainty on the subtracted ep background is determined from a comparison of data and simulation after relaxing the anti-photoproduction cuts, such that the sample is dominated by photoproduction events.
- The combined uncertainty of finding an interaction vertex and associating a track to the scattered lepton is estimated to be 0.5% at $Q^2 < 1000$ GeV^2 and 1% at $Q^2 \geq 1000$ GeV^2.
- An uncertainty of 0.5% accounts for the dependence of the acceptance correction on the PDFs used in the MC simulation.

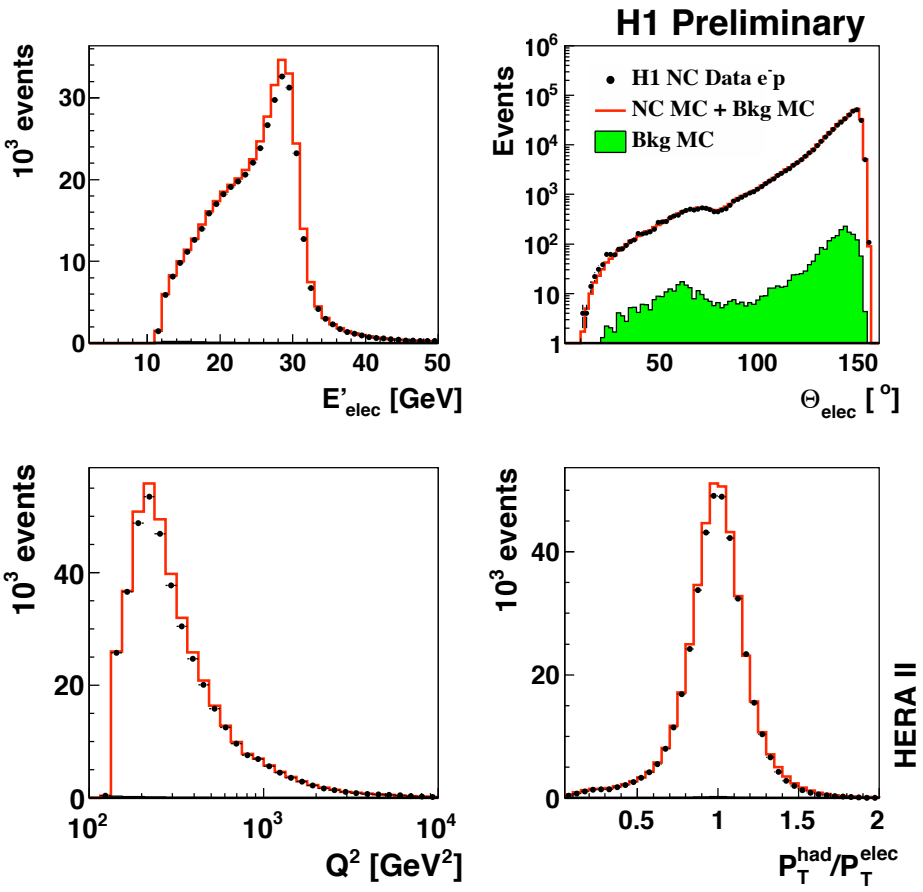

Figure 6.14: Distributions of the electron energy E'_e, the electron polar angle θ_e, Q^2 and $P_{T,h}/P_{T,e}$ for the combined e^-p data. The MC contributions from the neutral current (NC) process and the ep background (bkg) processes are shown as open histograms with the latter contribution alone being shown as shaded histograms.

- An error of 1% is estimated for the QED radiative corrections. This accounts for missing contributions in the simulation of the lowest order QED effects and for the uncertainty on the higher order QED and EW corrections.
- An uncertainty of z dependence of the proton bunch structure is estimated to be 0.5%.
- The relative uncertainty in the measurement of the lepton beam polarisation is taken to be 1.6% for the LPOL and 3.5% for the TPOL, yielding a total relative polarisation uncertainty in the e^+p sample of 1.2% for the R data set and 1.4% for the L data set. For the e^-p data a relative uncertainty of 2.3% for the R data set and 1.0% for the L data set is obtained. These uncertainties are not included in the

error bars of the data points.

- In addition, there is a global uncertainty of 2.5–2.9% on the luminosity measurement for different e^+, e^-, left and right samples, of which 2.1% is considered as correlated.

The total systematic error is formed by adding the individual uncertainties in quadrature.

6.9 Results

The results of the cross section measurement for the NC process will be presented in this section. The measurement was performed in different data periods from the whole HERA II data from 2003 to the end of the high energy runs on March 2007. The cross section will be shown only for the combined data, i.e. the four samples: e^-p left-handed, e^-p right-handed, e^+p left-handed and e^+p right-handed.

6.9.1 Double differential cross section

The measured NC double differential reduced cross section is shown in figures 6.15 and 6.16. The kinematic range for a NC double differential cross section is $200 < Q^2 < 30000$ GeV^2 and $x < 0.9$.

The measurements are in very good agreement over the full kinematic region with the predictions based on the H1PDF 2009 fit.

The reduced cross section exhibits a strong rise with decreasing x. This behaviour can be interpreted as originating from the rise of the sea quark distribution which is dominating the proton structure function $\tilde{F}_2$ at low x. This rising sea quark distribution is in turn driven by the dominant gluon density at low x. The rise with decreasing x becomes stronger as Q^2 increases. The behaviour of the cross section at lowest x (highest y) departs from the monotonic rise of $\tilde{F}_2$ indicating a contribution of the longitudinal structure function $\tilde{F}_L$ to the cross section.

At very high Q^2 the e^+p cross section for right handed polarised positrons is higher than for the left handed ones, and the e^-p cross section for left handed polarized electrons is higher than for the right handed.

6.9.2 Single differential cross section

The single differential cross sections for e^-p, e^+p, which are shown in figures 6.17 to 6.20, falling by over six orders of magnitude for the measured Q^2 region between 200 GeV^2 and 30000 GeV^2, are well described by the H1PDF 2009 fit. The error band represents

the total uncertainty as derived from the QCD analysis by adding in quadrature the experimental, model and parameterization uncertainties.

The data with both lepton charges and polarizations are well described by the predictions of the SM. The error is dominated by the systematic uncertainties except at very high Q^2.

These data can be used to search for eq contact interactions to scales far beyond the HERA center of mass energy. Indeed, the previously published analysis of the HERA-I data [112] and a preliminary analysis of the HERA-II data [113] show that for conventional contact interactions, lower limits as high as ~ 5 TeV can be set on the compositeness scale, couplings and masses of leptoquarks and squarks in R-parity violating supersymmetry are constrained to $M/\lambda > 0.3 - 1.4$ TeV, and a form factor analysis yields a bound on the radius of light quarks of $\sim 0.7 \cdot 10^{-18}$ m.

6.9.3 Polarization Asymmetry

The Standard Model predicts a difference in the cross section for leptons with different helicity states arising from the chiral structure of the neutral electroweak exchange. With longitudinally polarized lepton beam in HERA-II such polarization effects can be tested, providing a direct measure of electroweak effects in the neutral current cross sections. The polarization asymmetry, A, is defined as

$$A = \frac{2}{P_R - P_L} \cdot \frac{\sigma^{\pm}(P_R) - \sigma^{\pm}(P_L)}{\sigma^{\pm}(P_R) + \sigma^{\pm}(P_L)}. \tag{6.8}$$

To a very good approximation A measures the structure function ratio:

$$A^{\pm} \simeq \mp P_Z a_e \frac{F^{\gamma Z}}{F_2} \tag{6.9}$$

which is proportional to combination $a_e v_q$ and is thus a direct measure of parity violation. In positron scattering, A is expected to be positive and about equal to $-A$ in electron scattering. At large x, the asymmetry measures the d/u ratio of the valence quark distribution according to

$$A^{\pm} \simeq \pm P_Z \frac{1 + d_v/u_v}{4 + d_v/u_v}. \tag{6.10}$$

The polarized single differential cross sections $\mathrm{d}\sigma/\mathrm{d}Q^2$ from HERA-II are used to construct the asymmetry where it is assumed that the correlated uncertainties of each measurement cancel. The asymmetry is shown in figure 6.21.

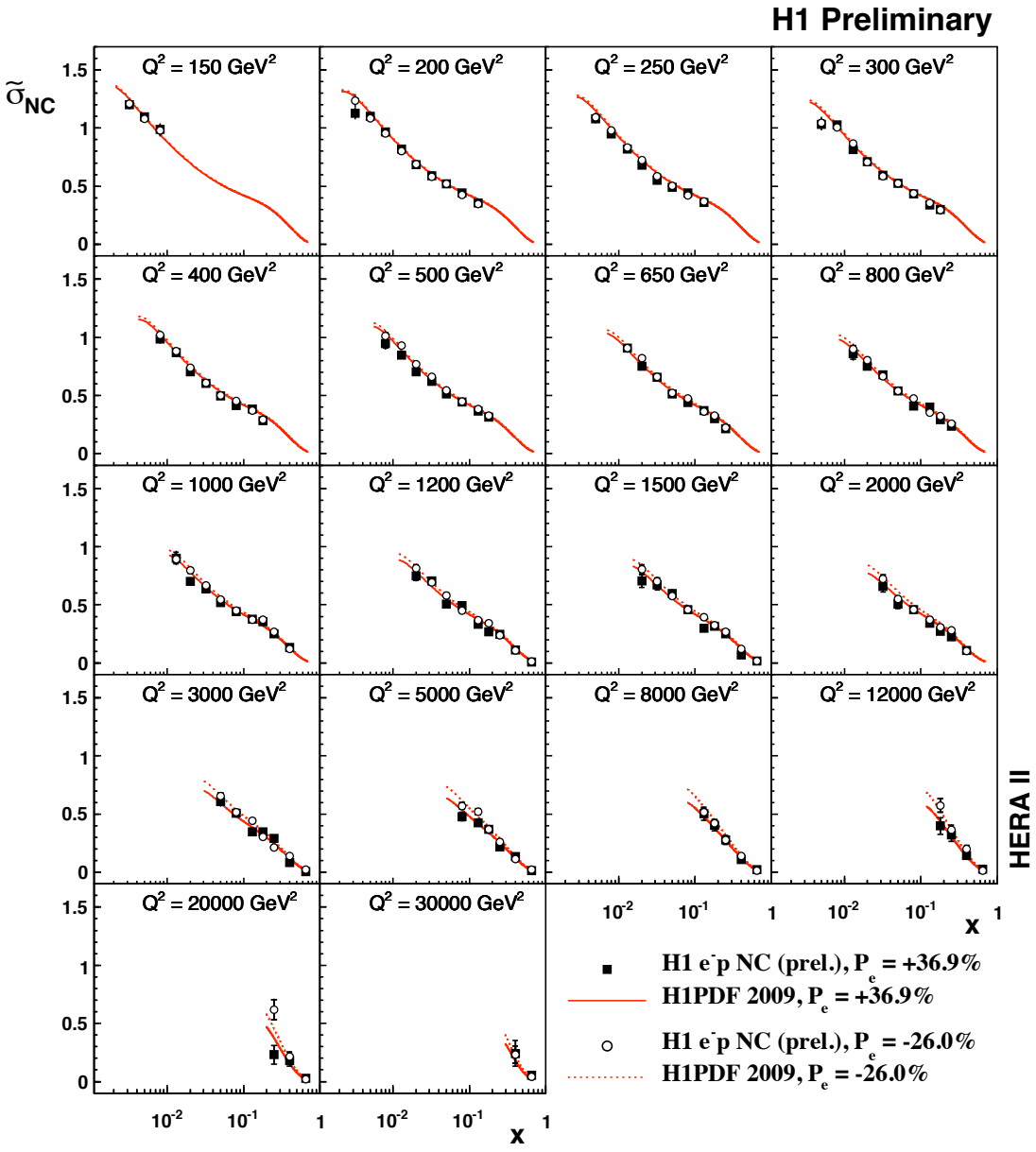

Figure 6.15: The reduced cross section $\tilde{\sigma}_{NC}$ in e^-p scattering for R (filled squares) and L (open circles) polarized samples. The data are compared to the Standard Model prediction from H1 PDF 2009. The inner error bars represent the statistical uncertainties and the outer error bars represent the total errors. The normalisation uncertainty is not included in the error bars.

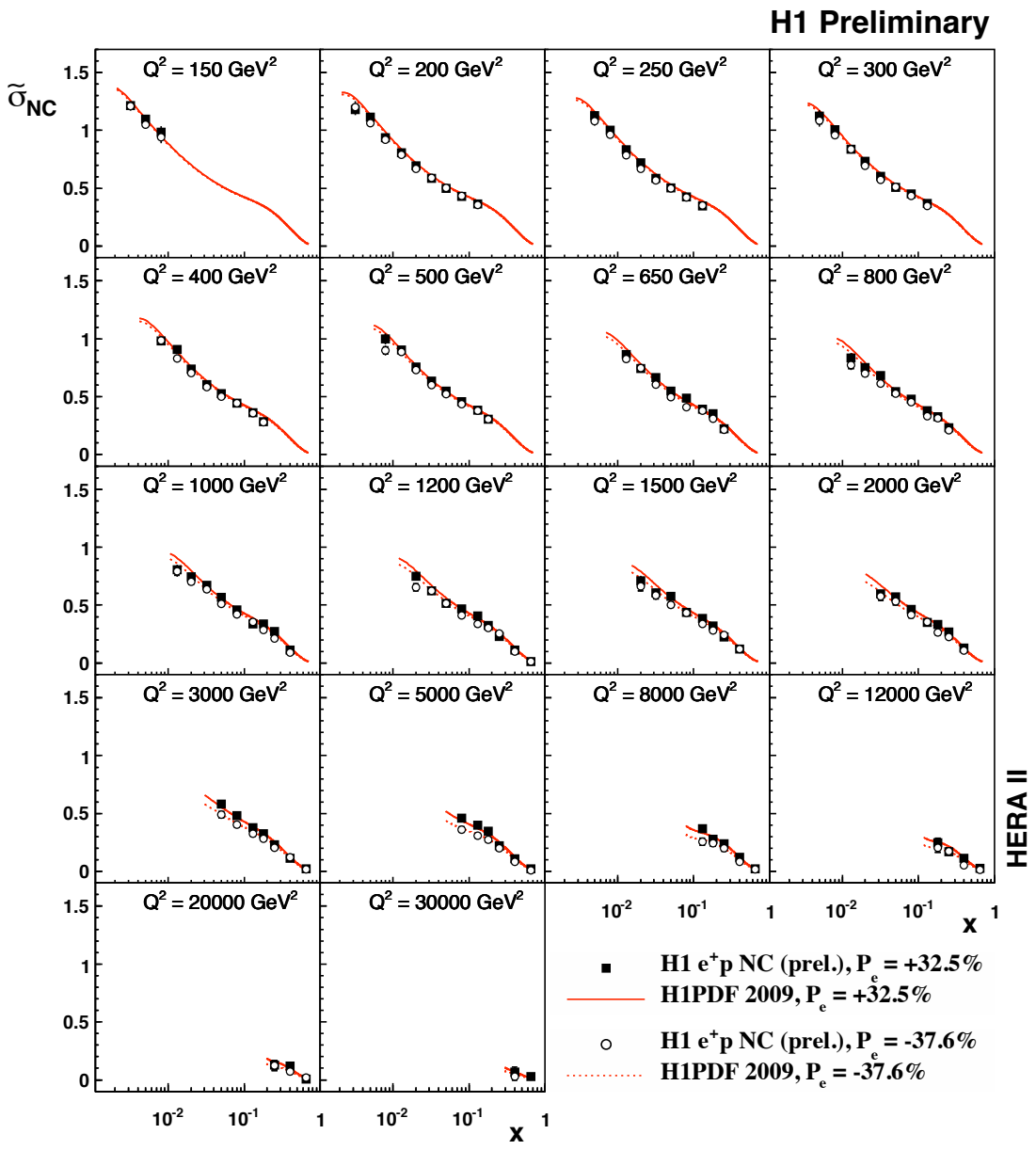

Figure 6.16: The reduced cross section $\tilde{\sigma}_{NC}$ in e^+p scattering for R (filled sqaures) and L (open circles) polarised samples. The data are compared to the Standard Model prediction from H1 PDF 2009. The inner error bars represent the statistical uncertainties and the outer error bars represent the total errors. The normalisation uncertainty is not included in the error bars.

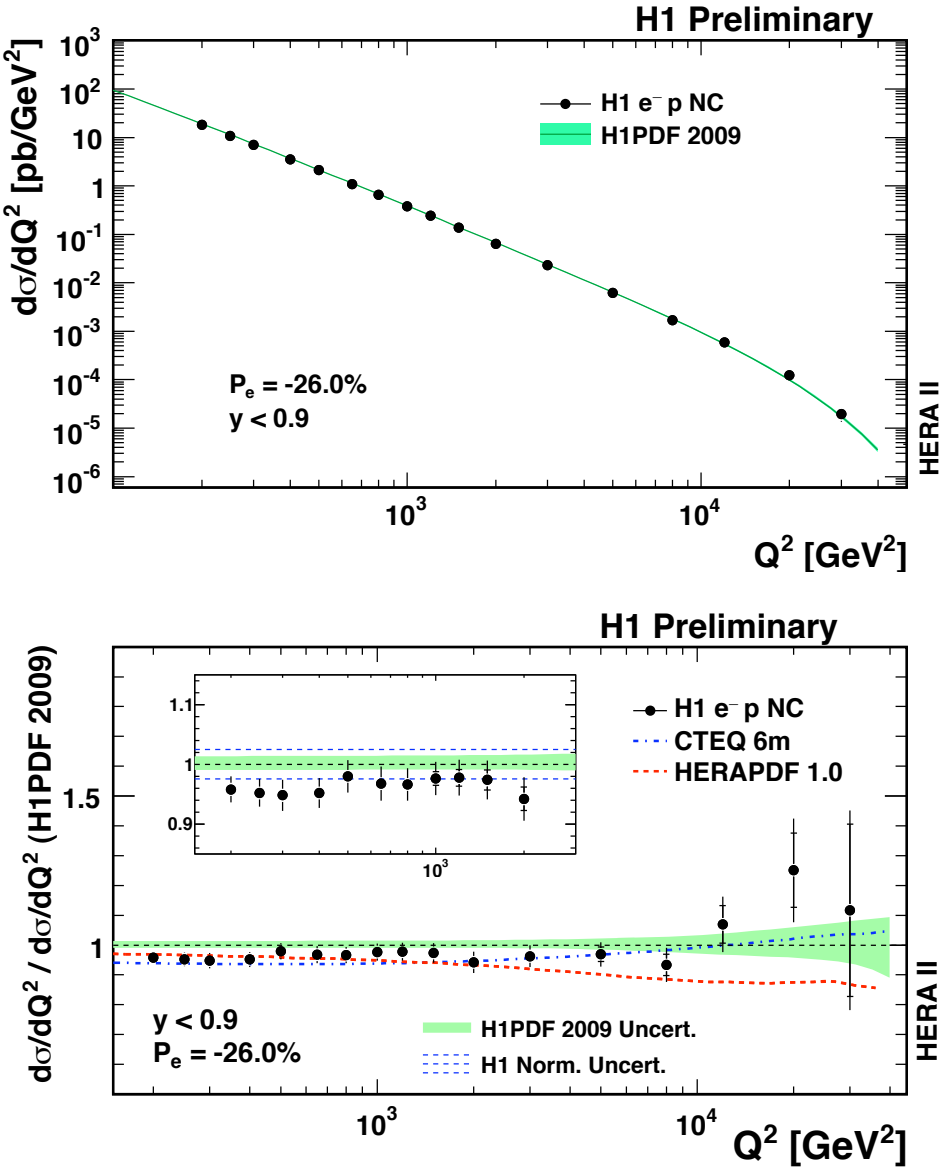

Figure 6.17: Single-differential cross section for the e^-p left-handed data compared to the Standard Model evaluated by H1PDF 2009. In addition the comparisons using CTEQ6m PDFs and HERAPDF 1.0 are also indicated. The normalization uncertainty is not included in the error bars and is instead represented by the blue dashed lines on the inset figures. The error bands on the prediction H1PDF 2009 show the total theoretical uncertainty (parameterization $\oplus$ model $\oplus$ experimental uncertainties).

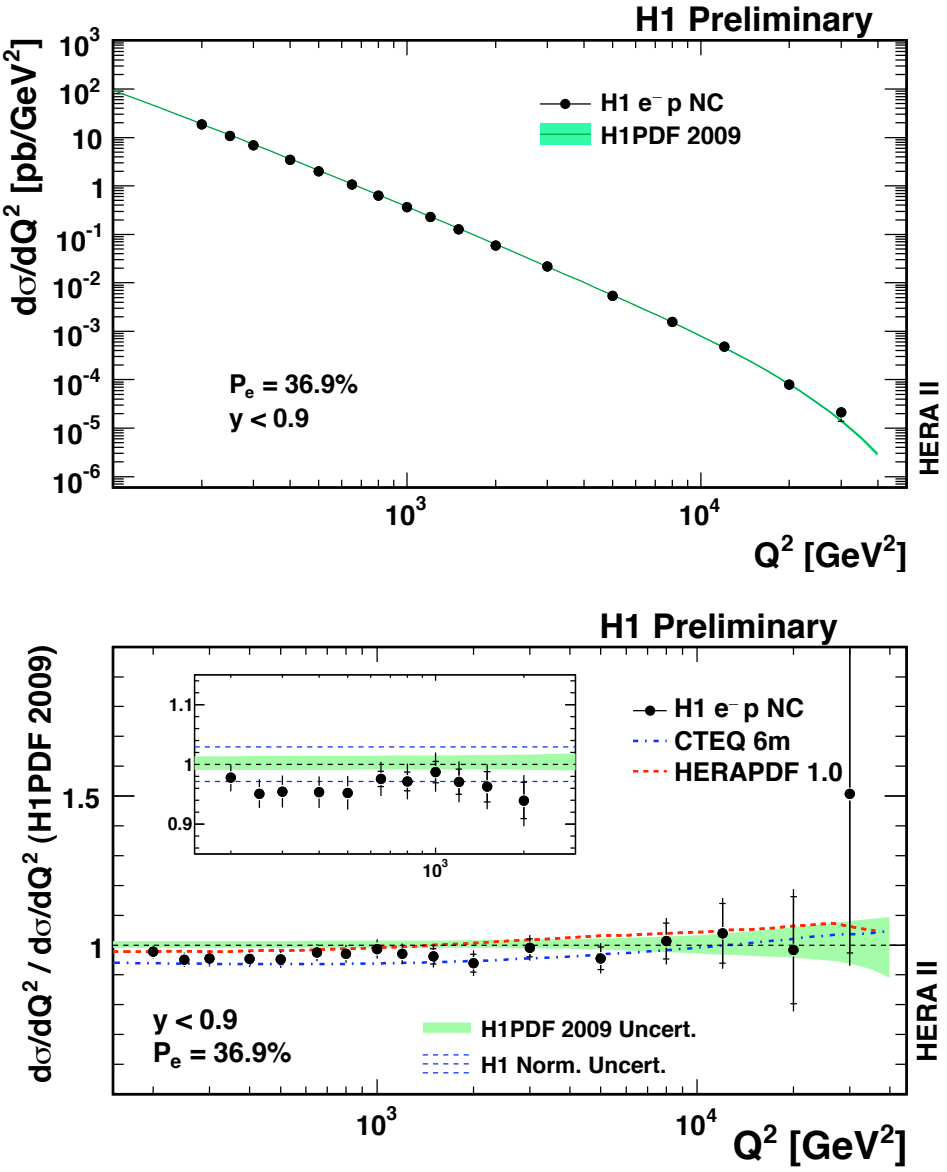

Figure 6.18: Single-differential cross section for the e^-p right-handed data compared to the Standard Model evaluated by H1PDF 2009. In addition the comparisons using CTEQ6m PDFs and HERAPDF 1.0 are also indicated. The normalization uncertainty is not included in the error bars and is instead represented by the blue dashed lines on the inset figures. The error bands on the prediction H1PDF 2009 show the total theoretical uncertainty (parameterization $\oplus$ model $\oplus$ experimental uncertainties).

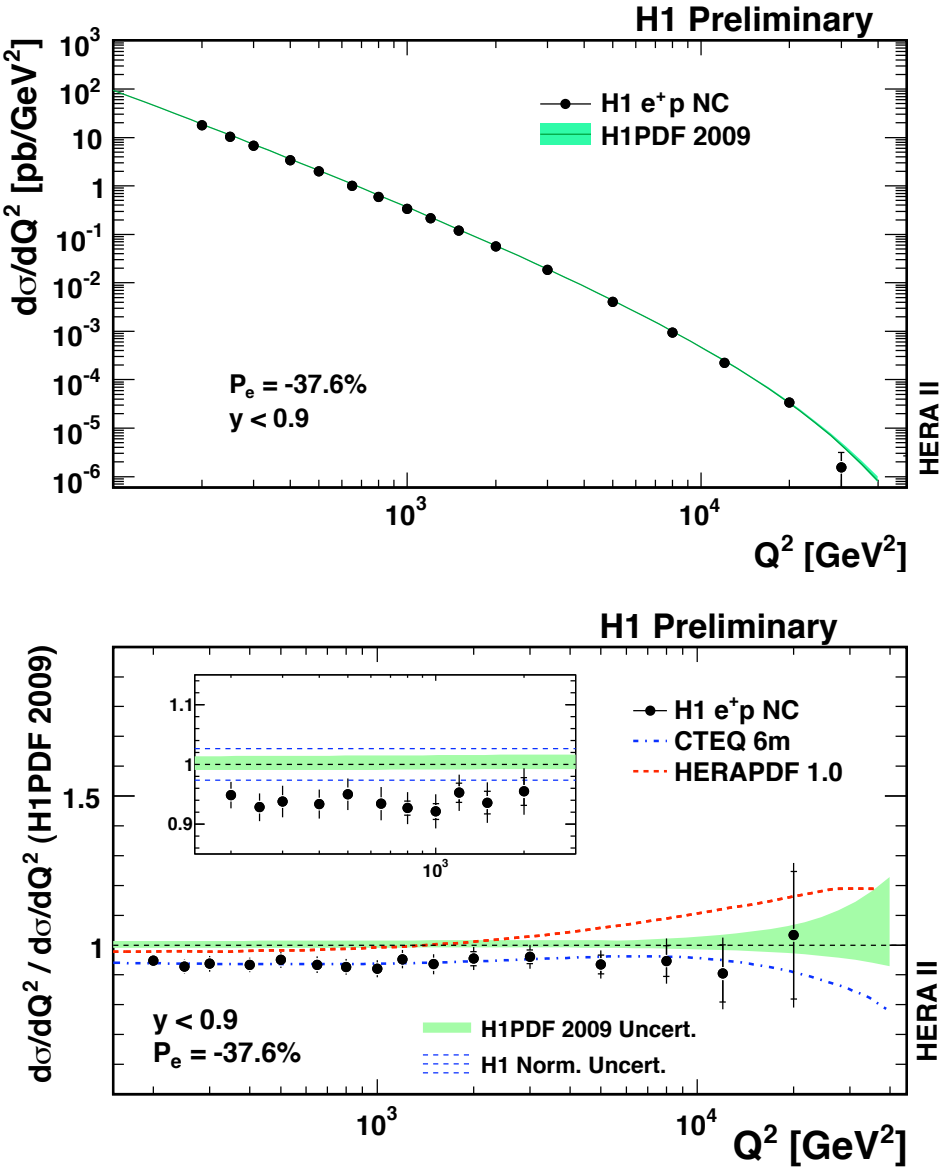

Figure 6.19: Single-differential cross section for the e^+p left-handed data compared to the Standard Model evaluated by H1PDF 2009. In addition the comparisons using CTEQ6m PDFs and HERAPDF 1.0 are also indicated. The normalization uncertainty is not included in the error bars and is instead represented by the blue dashed lines on the inset figures. The error bands on the prediction H1PDF 2009 show the total theoretical uncertainty (parameterization $\oplus$ model $\oplus$ experimental uncertainties).

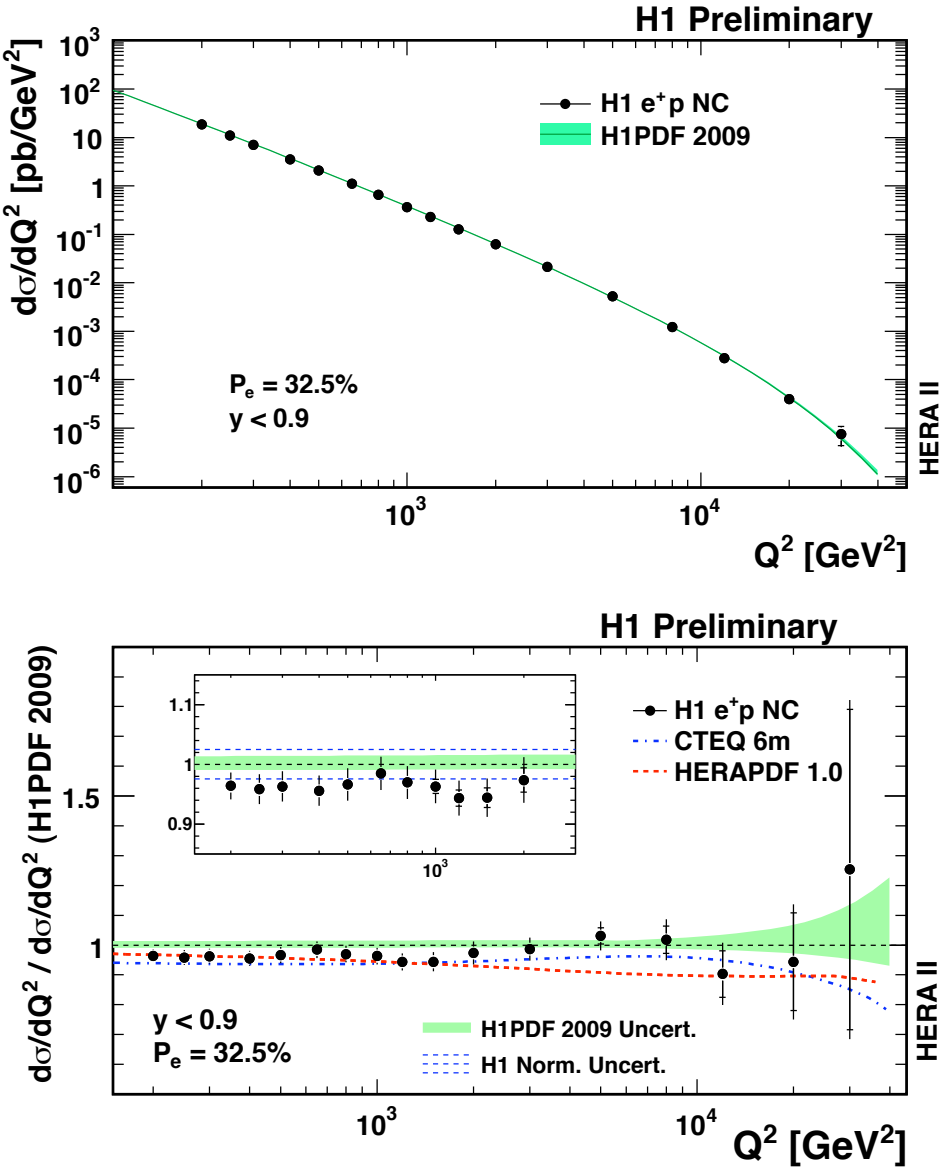

Figure 6.20: Single-differential cross section for the e^+p right-handed data compared to the Standard Model evaluated by H1PDF 2009. In addition the comparisons using CTEQ6m PDFs and HERAPDF 1.0 are also indicated. The normalization uncertainty is not included in the error bars and is instead represented by the blue dashed lines on the inset figures. The error bands on the prediction H1PDF 2009 show the total theoretical uncertainty (parameterization $\oplus$ model $\oplus$ experimental uncertainties).

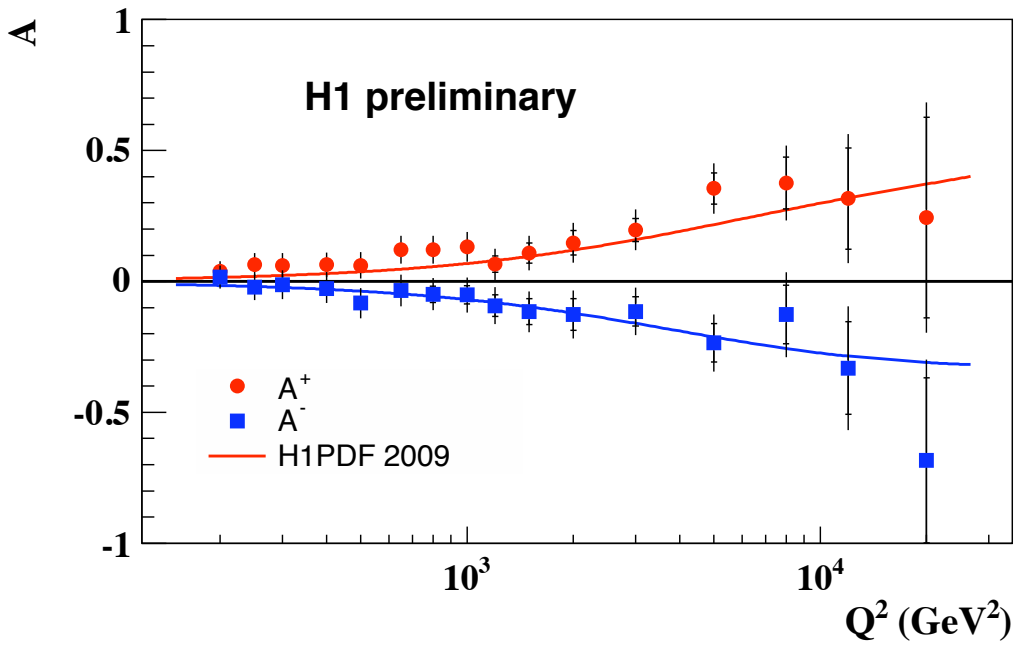

Figure 6.21: The Q^2 dependence of the polarization asymmetry A, for e^+p (red circles) and e^-p (blue squares). The data (solid points) are compared to the Standard Model prediction (full lines). The inner error bars represent the statistical uncertainties and the outer error bars represent the total errors. The normalization uncertainty is not included in the error bars.

Chapter 7

Combination of HERA-I and HERA-II data

Contents

This chapter is dedicated mainly to the combination of the whole HERA data measured by H1. The combined NC and CC cross sections will be shown. The extraction of the generalized structure function $x\tilde{F}_3$ will also be given here.

In order to improve the statistical precision on the measurements which are still limited at high Q^2, the cross sections are combined with previously published HERA-I measurements from H1. Since for some periods of HERA-I, the proton energy was at 820 GeV, it is therefore needed to correct these data to the common center-of-mass energy. For HERA-II data, the electron (positron) left-handed and right-handed are combined together. However, there still exists a residual polarization effect which needs to be corrected to provide a measurement of the unpolarized cross sections.

7.1 Combination method

Averaging

The combination method was developed in [65] which uses the χ^2 minimization method described in [114]. The χ^2 function takes into account the correlated systematic uncertainties for the cross section measurement. For a single dataset, the χ^2 is defined as

$$\chi^2_{\text{exp}}(\boldsymbol{m},\boldsymbol{b}) = \sum_i \frac{\left[m^i - \sum_j \gamma^i_j m^i b_j - \mu^i\right]^2}{\delta^2_{i,\text{stat}}\mu^i\left(m^i - \sum_j \gamma^i_j m^i b_j\right) + \left(\delta_{i,\text{uncor}} m^i\right)^2} + \sum_j b_j^2. \tag{7.1}$$

Here μ^i is the measured value at a point i and γ^i_j, $\delta_{i,\text{stat}}$ and $\delta_{i,\text{uncor}}$ are relative correlated systematic, relative statistical and relative uncorrelated systematic uncertainties, respectively. The function χ^2_{exp} depends on the prediction m^i for the measurements (denoted as the vector $\boldsymbol{m}$) and the shifts b_j (denoted as the vector $\boldsymbol{b}$) of the correlated systematic error sources. For the reduced cross-section measurements, $\mu^i \equiv \tilde{\sigma}^i$, i denotes a (x, Q^2) point, and the summation over j extends over all correlated systematic sources. The predictions m^i are given by the assumption that there is a single true value of the cross section corresponding to each data point i and each process, neutral or charged current e^+p or e^-p scattering.

Several datasets providing a number of measurements are represented by a total χ^2 function, which is built from the sum of the χ^2_{exp} functions for each dataset e

$$\chi^2_{\text{tot}} = \sum_e \chi^2_{\text{exp},\,e}. \tag{7.2}$$

The minimization procedure will search for the minimum of equation (7.2), χ^2_{min}. The ratio $\chi^2_{\text{min}}/n_{\text{dof}}$ is a measure of the consistency of the datasets, where the number of degrees of freedom, n_{dof}, is calculated as the difference between the total number of measurements and the number of averaged points.

Center-of-mass energy correction

The datasets considered for the combination contain sub-samples taken with a proton beam energy of $E_p = 820$ GeV and $E_p = 920$ GeV. Both the CC and NC scattering reduced cross-sections depend weakly on the energy via terms containing the inelasticity y. For the CC data for all values of y and for the NC data for $y < 0.35$, the uncertainty on the theoretically estimated difference between cross sections for $E_p = 820$ GeV and $E_p = 920$ GeV is negligible compared to the experimental precision. Therefore the data are corrected to a common center-of-mass energy corresponding to $E_p = 920$ GeV and then averaged.

The correction is calculated multiplicatively for the CC data which is given in full double differential form

$$\frac{\mathrm{d}^2\sigma^{e^\pm p}_{\text{CC }920}}{\mathrm{d}x\mathrm{d}Q^2} = \frac{\mathrm{d}^2\sigma^{e^\pm p}_{\text{CC }820}}{\mathrm{d}x\mathrm{d}Q^2} \left[\frac{\mathrm{d}^2\sigma^{\text{th},\,e^\pm}_{\text{CC }920}}{\mathrm{d}x\mathrm{d}Q^2} \Bigg/ \frac{\mathrm{d}^2\sigma^{\text{th},\,e^\pm}_{\text{CC }820}}{\mathrm{d}x\mathrm{d}Q^2} \right] \tag{7.3}$$

and additively for the NC data which is quoted in reduced double differential form

$$\tilde{\sigma}^{\pm}_{\text{NC }920} = \tilde{\sigma}^{\pm}_{\text{NC }820} + \Delta\tilde{\sigma}^{\text{th},\,\pm}_{\text{NC}}(x, Q^2, y_{820}, y_{920}). \tag{7.4}$$

Here y_{820} and y_{920} are the inelasticities for the two proton beam energies. The theoretical cross sections for the NC case:

$$\begin{aligned} \Delta\tilde{\sigma}^{\text{th},\,\pm}_{\text{NC}}(x, Q^2, y_{820}, y_{920}) \quad &= \tilde{F}^{\text{th}}_L(x, Q^2) \quad \left[\frac{y_{820}}{Y_{+\,820}} - \frac{y_{920}}{Y_{+\,920}} \right] \\ &+ x\tilde{F}^{\text{th}}_3(x, Q^2) \quad \left[\pm\frac{Y_{-\,820}}{Y_{+\,820}} \mp \frac{Y_{-\,920}}{Y_{+\,920}} \right] \end{aligned} \tag{7.5}$$

where $Y_{-\,820,920} = 1 \pm (1 - y_{820,920})^2$.

7.2 Charged Current combination

The datasets used for this combination are listed in table 7.1. The total integrated luminosity of the combined datasets correspond to about 160 pb^{-1} for e^-p and 230 pb^{-1} for e^+p . The combinations are shown in figures 7.1 and 7.2. The combined data are compared to the Standard Model expectation from the H1PDF 2009 fit [37] which provides

an excellent description of the Q^2 dependence of the data including the difference between the e^+p and e^-p cross sections.

For an unpolarized $e^-p \to \nu X$ scattering, similar to equations 1.37 and 1.38, one can express the structure functions as

$$F_2^{\mathrm{CC}} = 2x(u(x,Q^2) + c(x,Q^2) + \bar{d}(x,Q^2) + \bar{s}(x,Q^2)) \quad (7.6)$$
$$xF_3^{\mathrm{CC}} = 2x(u(x,Q^2) + c(x,Q^2) - \bar{d}(x,Q^2) - \bar{s}(x,Q^2)) \quad (7.7)$$

and for $e^+p \to \bar{\nu} X$ scattering:

$$F_2^{\mathrm{CC}} = 2x(d(x,Q^2) + s(x,Q^2) + \bar{u}(x,Q^2) + \bar{c}(x,Q^2)) \quad (7.8)$$
$$xF_3^{\mathrm{CC}} = 2x(d(x,Q^2) + s(x,Q^2) - \bar{u}(x,Q^2) - \bar{c}(x,Q^2)). \quad (7.9)$$

Using these expressions, one can obtain the reduced cross sections

$$\tilde{\sigma}^+_{\mathrm{CC}} = x[\bar{u} + \bar{c} + (1-y)^2(d + s + b)] \quad (7.10)$$
$$\tilde{\sigma}^-_{\mathrm{CC}} = x[u + c + (1-y)^2(\bar{d} + \bar{s} + \bar{b})] \quad (7.11)$$

where the arguments x, Q^2 have been suppressed. Here we have assumed that there is no significant top quark content in the proton and that energies are above threshold for the production of c and b quarks in the final states. From figure 7.1, it is indicated that the contribution of the d PDF dominates the e^+p cross section whereas figure 7.2 shows that the u PDF dominates the e^-p cross section at high x.

The unpolarized CC cross sections can thus be used to determine the u and d quark densities contrary to the NC cross sections which are quark flavor blind.

Dataset	$\mathcal{L}$ pb^{-1}	e^+/e^-	$\sqrt{s}$ (GeV)	Reference
94-97	35.6	e^+p	301	[102]
98-99	16.4	e^-p	319	[103]
99-00	65.2	e^+p	319	[21]
03-07	180.0	e^+p	319	this analysis
04-06	149.1	e^-p	319	this analysis

Table 7.1: Datasets used for both CC and NC cross section combination HERA-I and HERA-II. The HERA-II data have been corrected to polarization at zero.

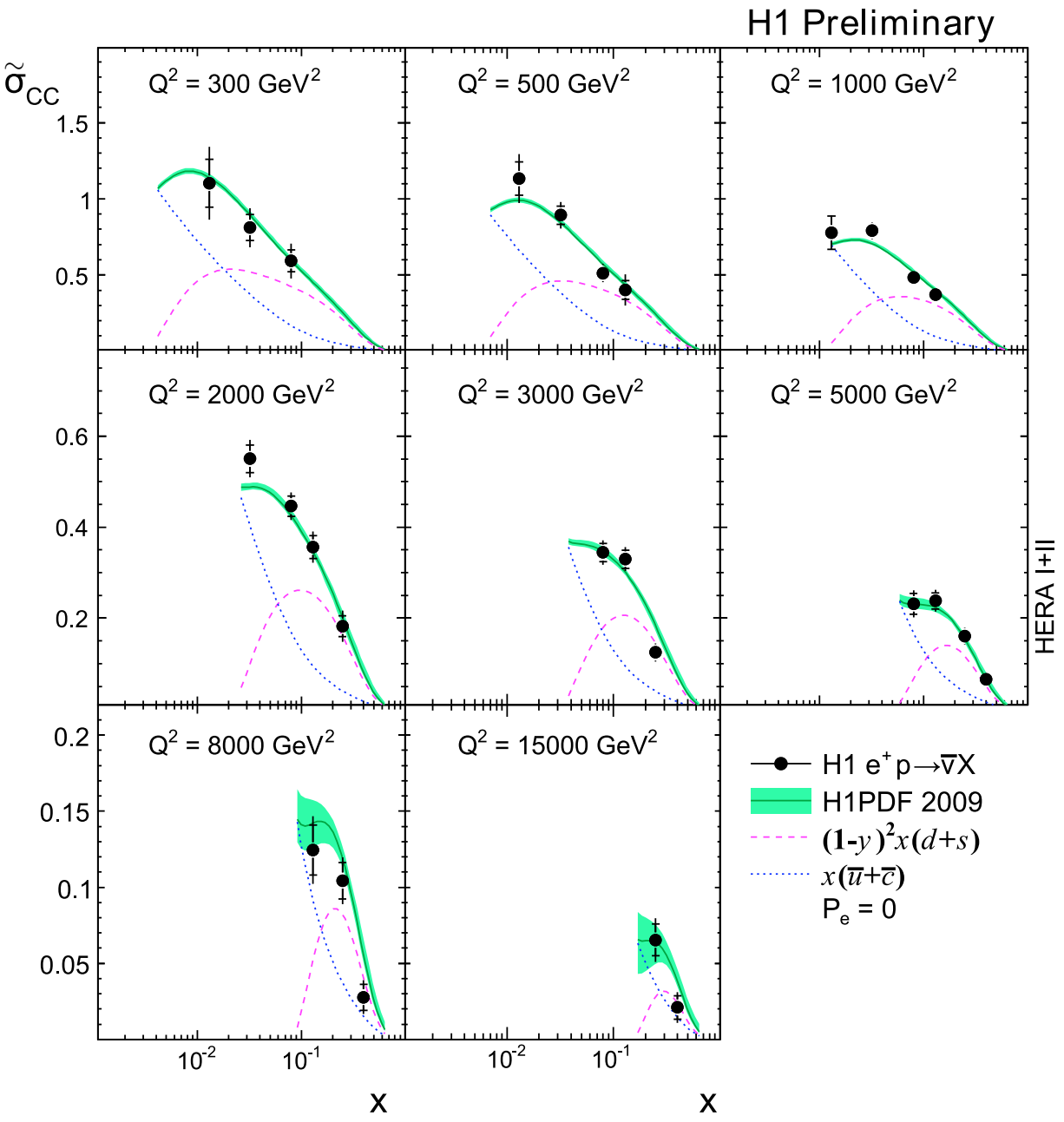

Figure 7.1: Reduced CC cross section for combined HERA-I+II data as a function of x for different values of Q^2 for the e^+p data compared to the theoretical expectation evaluated by H1PDF 2009. Data are shown in filled circle. The outer error bar on the data shows the total uncertainty, the inner error bar shows the statistical uncertainty. The error bands on the prediction show the total theoretical uncertainty (parameterization $\oplus$ model $\oplus$ experimental uncertainty). The separate contributions from quarks and anti-quarks are shown as the dashed and dashed-dotted curves.

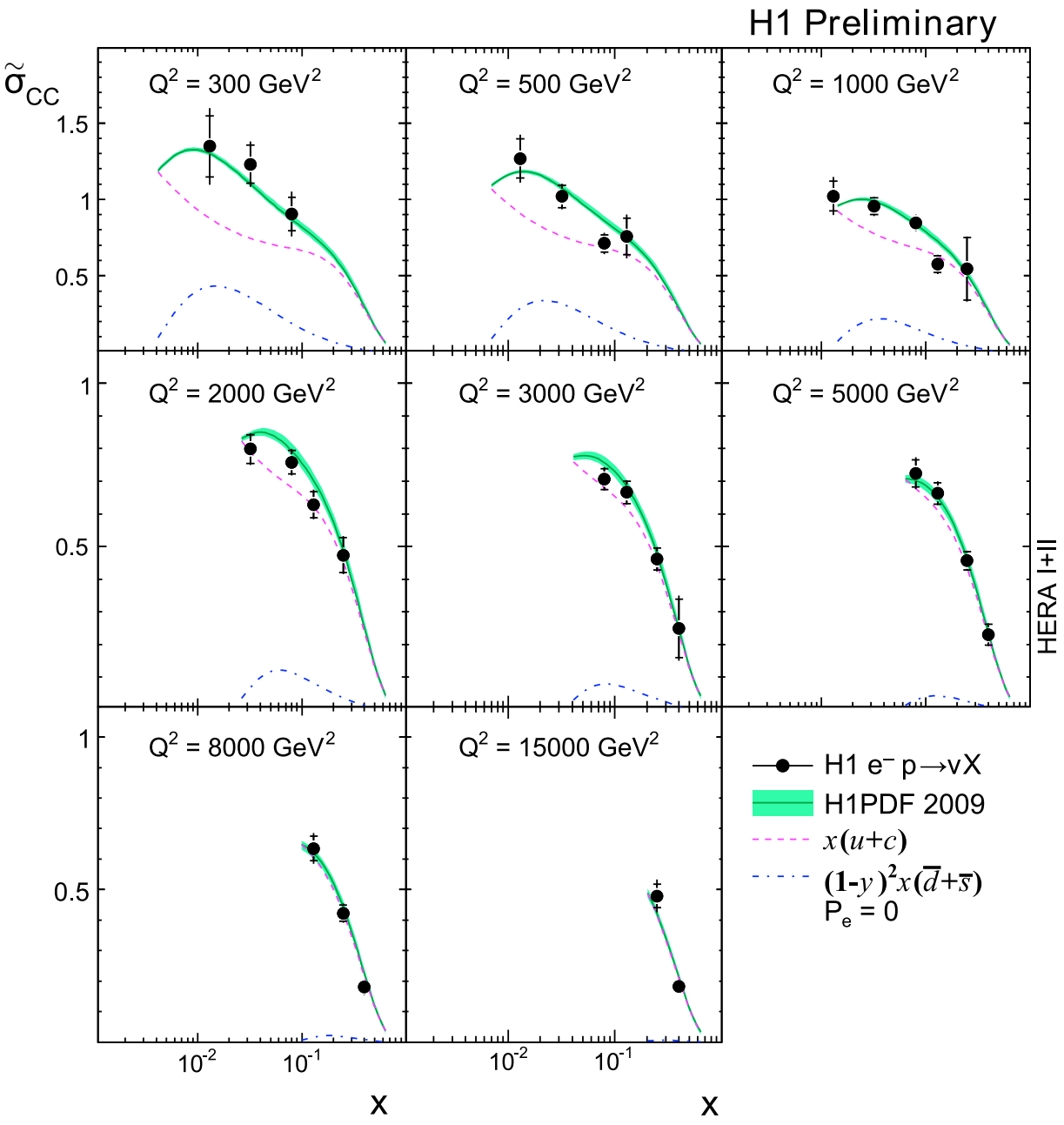

Figure 7.2: Reduced CC cross section for combined HERA-I+II data as a function of x for different values of Q^2 for the e^-p data compared with the theoretical expectation evaluated by H1PDF 2009. Data are shown in filled circle. The outer error bar on the data shows the total uncertainty, the inner error bar shows the statistical uncertainty. The error bands on the prediction show the total theoretical uncertainty (parameterization $\oplus$ model $\oplus$ experimental uncertainty). The separate contributions from quarks and anti-quarks are shown as the dashed and dashed-dotted curves.

7.3 Neutral Current combination

The same data sets were used for NC combination. The results for the unpolarized e^-p and e^+p cross sections are shown in figure 7.3. An excellent agreement between data and the prediction of the Standard Model is achieved. Again the difference of cross section for e^-p and e^+p scattering due to the $\gamma - Z$ interference is confirmed.

7.4 Structure function $x\tilde{F}_3$

From equation (1.19) one can notice that the generalized proton structure function $x\tilde{F}_3(x, Q^2)$ contributes positively to the cross section of e^-p scattering and negatively to e^+p scattering due to the constructive or destructive interference of the photon to the Z-boson. It therefore can be extracted by subtracting $\mathrm{d}^2\sigma^-/\mathrm{d}x\mathrm{d}Q^2$ and $\mathrm{d}^2\sigma^+/\mathrm{d}x\mathrm{d}Q^2$, thus eliminating the contribution of $F_2(x, Q^2)$ and $F_L(x, Q^2)$ which have the same sign in both processes. The expression for $x\tilde{F}_3(x, Q^2)$ is relating to the reduced NC cross sections as

$$x\tilde{F}_3(x, Q^2) = \frac{Y_+}{2Y_-}\left[\tilde{\sigma}^- - \tilde{\sigma}^+\right]. \tag{7.12}$$

The resulting generalized structure function $x\tilde{F}_3(x, Q^2)$ is shown in figure 7.4. It rises with Q^2 for fixed values of x due to the increasingly contribution of the Z-boson.

It can be seen from equation 1.22 that the dominant contribution to $x\tilde{F}_3(x, Q^2)$ arises from the $\gamma - Z$ interference term, since the pure Z exchange term is suppressed by the factor $Q^2/(Q^2 + M_Z^2)$ in the definition of P_Z and the vector coupling v_l is small. The $xF_3^{\gamma Z}$ can therefore be determined as

$$xF_3^{\gamma Z} \simeq x\tilde{F}_3 \frac{Q^2 + M_Z^2}{a_l P_Z Q^2}. \tag{7.13}$$

The structure function $xF_3^{\gamma Z}$ is shown in figure 7.5(a). The measurement based on the combined HERA-I and HERA-II data is in an excellent agreement with the prediction from H1PDF 2009.

Since the dependence on Q^2 is weak, the data from each Q^2 are transformed to one Q^2 value at 1500 GeV^2 and then averaged. The extracted $xF_3^{\gamma Z}$ data for all Q^2 values is shown in figure 7.5(b). The Standard Model predictions based on H1PDF 2009 and HERAPDF 1.0 [65, 101] are also shown and found to be in excellent agreement in both shape and magnitude with the data.

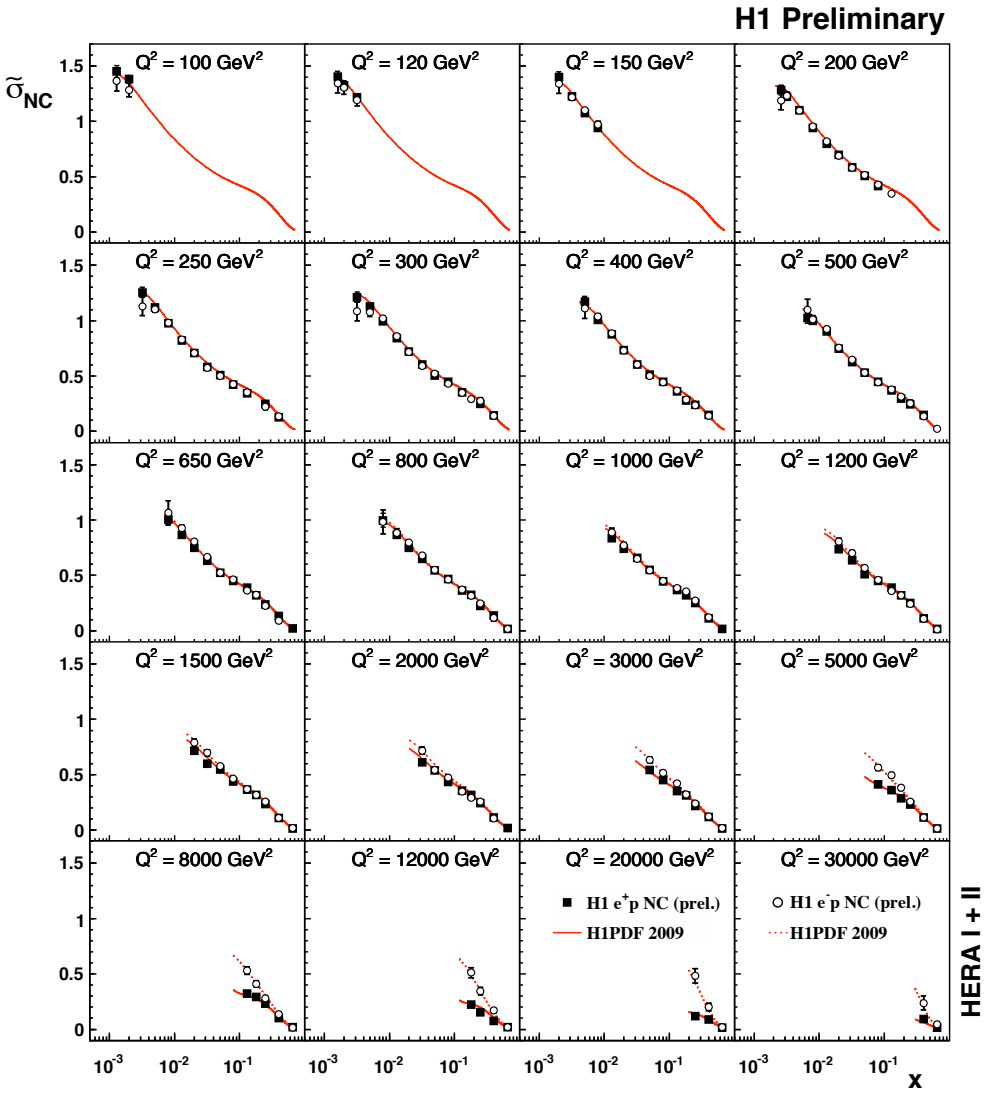

Figure 7.3: The reduced cross section $\tilde{\sigma}_{NC}$ in unpolarised $e^{\pm}p$ scattering. The data are compared to the Standard Model prediction from H1 PDF 2009. The inner error bars represent the statistical uncertainties and the outer error bars represent the total errors. The normalisation uncertainty is not included in the error bars.

7.5 Electroweak unification

The measurement of unpolarized NC and CC cross section $\mathrm{d}\sigma/\mathrm{d}Q^2$ up to highest values of Q^2 allow a visualization of the "unification of electromagnetic" and "weak" interactions [11, 162

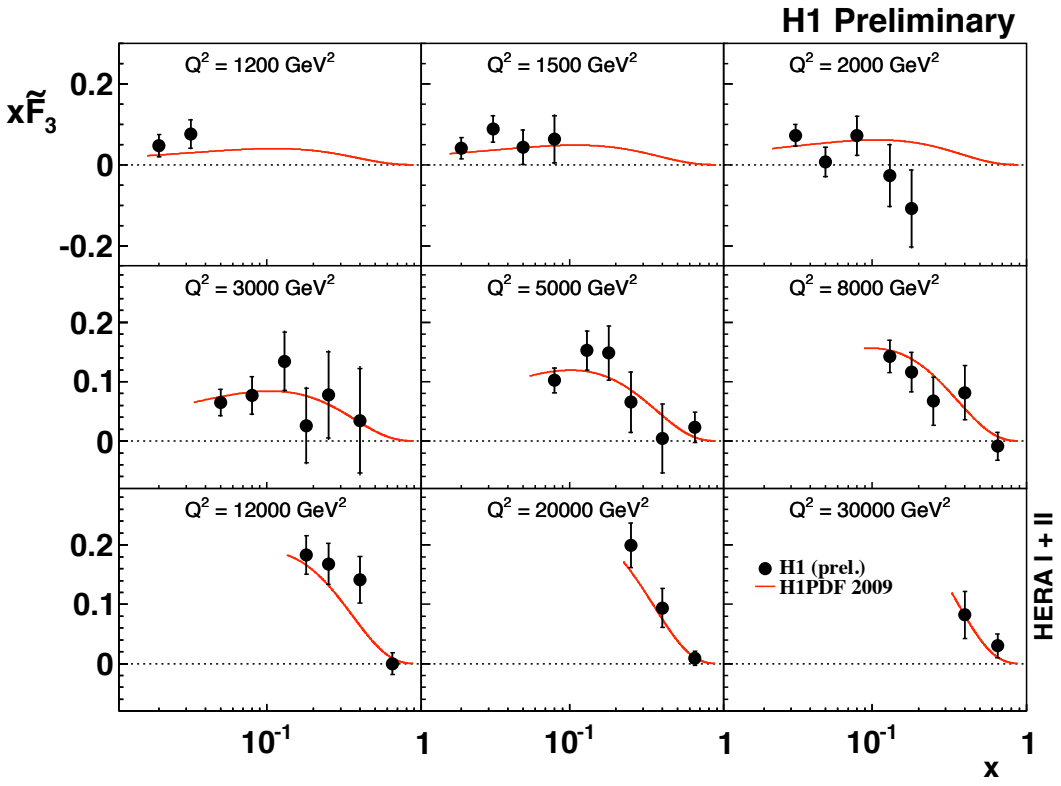

Figure 7.4: The structure function $x\tilde{F}_3$ evaluated using the combined HERA-I and HERA-II data is shown (solid points) compared to the Standard Model expecation from H1PDF 2009 (solid curve). The inner error bars represent the statistical uncertainties and the outer error bars represent the total errors which include the normalisation uncertainty.

12]. This is shown in figure 7.6, with the measurements made by H1 on the whole HERA data and ZEUS on the HERA-II data in comparison to the Standard Model expectation based on HERAPDF 1.0. Both measurements from H1 and ZEUS show an excellent agreement with the Standard Model prediction.

At low Q^2, virtual photon exchange dominates the NC interactions, and CC events are suppressed by many orders of magnitude. With increasing Q^2 both cross sections approach each other, which means that the electromagnetic and weak interaction strengths become comparable. At very high Q^2, the CC cross section for electrons is higher than for positrons. This is due to the W^- (W^+) boson exchange, which couples to up (down)-type quarks in the case of electrons (positrons). In addition, for positron scattering the helicity structure of the interaction leads to an additional suppression. In the highest Q^2

region also the NC cross section is larger for electrons than for positrons. In this region the interference between photon and Z exchange becomes relevant, which explains the observed asymmetry.

7.6 Electroweak and QCD analyses using the full HERA data

The inclusive CC and NC cross sections are not only sensitive to PDFs but also the electroweak parameters. Indeed, the NC cross section at high Q^2 depends on the weak vector (v_q) and axial-vector (a_q) couplings of up- and down-type quarks to the Z boson via structure functions. Such sensitivity on the quark couplings at HERA has been exploited by H1 collaboration in a recent publication [115].

The analysis was performed using the QCDFIT package [116] which solves the DGLAP equations [34, 35, 36] at NLO [117] in the $\overline{\text{MS}}$ renormalization scheme. The contribution of the heavy quarks is taken into account, including the top quark. All quarks are considered to be massless when Q^2 is above their mass thresholds. Since the NC cross section is dominated by the light quarks at HERA, thus it is the light quark couplings to the Z-boson that are probed. The combined electroweak-QCD analysis (or $v_u{-}a_u{-}v_d{-}a_d{-}$PDF fit) follows the same fit procedure as used in [21, 115], in which the vector and axial-vector couplings of u and d quarks together with PDF are treated as free parameters.

The fits were performed to the measured cross sections by fixing the strong coupling constant to $\alpha_s(M_Z^2) = 0.1176$. The fit procedure is based on the minimization of the χ^2 function, which is defined in [103], by taking into account the correlation between data points from systematic uncertainties.

The analysis was performed using full HERA-I and HERA-II data. These data cover a Bjorken range from 3×10^{-5} to 0.65 depending on Q^2. The results are compared to similar results obtained previously by the CDF experiment [118] and the combined LEP/SLC experiments [119]. The HERA determination of the u quark couplings has better precision than that from the Tevatron. Theses determinations are sensitive to u and d quarks separately, contrary to other measurements of the light quark-Z^0 couplings in νN scattering [120] and atomic parity violation [121] on heavy nuclei. They also resolve any sign ambiguity and the ambiguities between v_q and a_q ($q = u, d$) of the determination based on observables measured at the Z^0 resonance [119] at LEP/SLC.

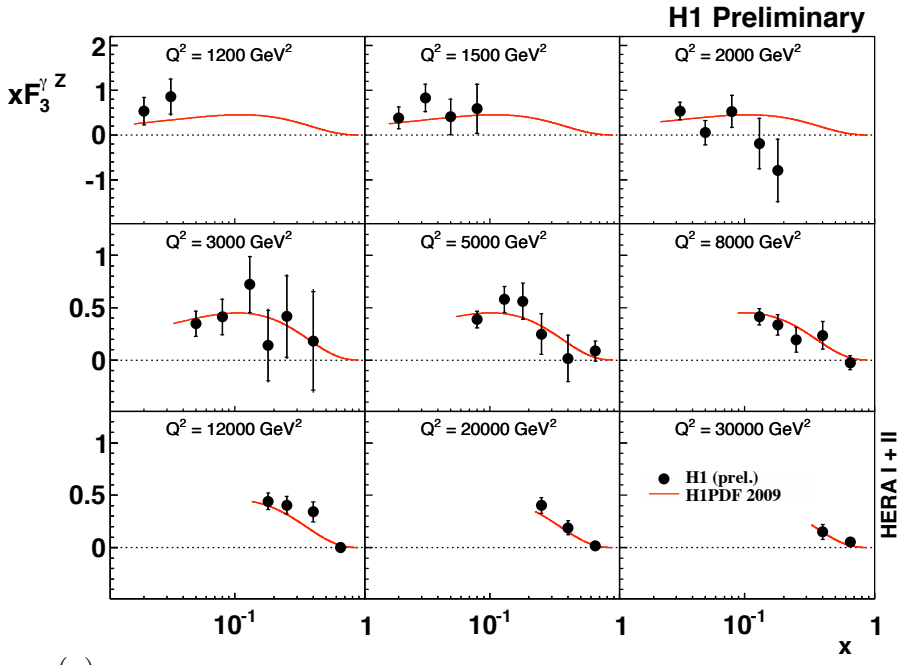

(a)

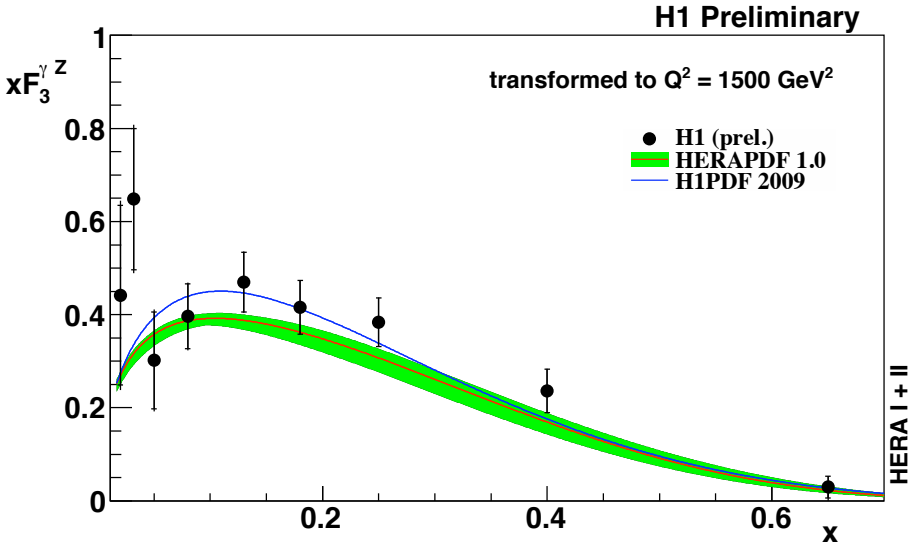

(b)

Figure 7.5: (a): The structure function $xF_3^{\gamma Z}$ extracted from all HERA-I and HERA-II data (solid points) is shown together with the Standard Model expectation from H1PDF 2009 (solid curve); (b): The structure function $xF_3^{\gamma Z}$ extracted from all HERA-I and HERA-II data (solid points) and transformed to $Q^2 = 1\,500$ GeV^2 is shown together with the Standard Model expectation from H1PDF 2009 and HERAPDF 1.0. The inner error bars represent the statistical uncertainties and the outer error bars represent the total errors which include the normalisation uncertainty.

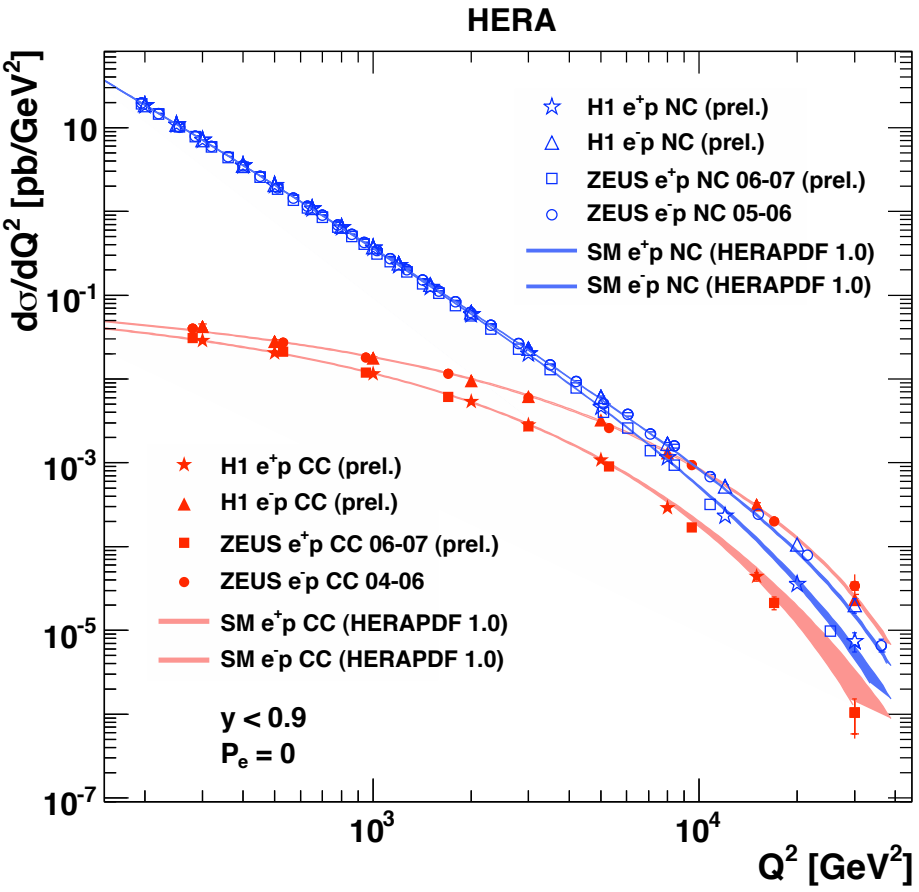

Figure 7.6: The Q^2 dependence of the unpolarized NC and CC cross sections measured by H1 for full HERA e^-p and e^+p data and by ZEUS for HERA-II. The results are compared with the corresponding Standard Model expectations determined from the HERAPDF 1.0 fit. The the inner and outer error bars represent respectively the statistical and total errors. The error band shows the Standard Model uncertainty by adding in quadrature the experimental uncertainty as derived from the fit, the model uncertainty and the parameterization uncertainty.

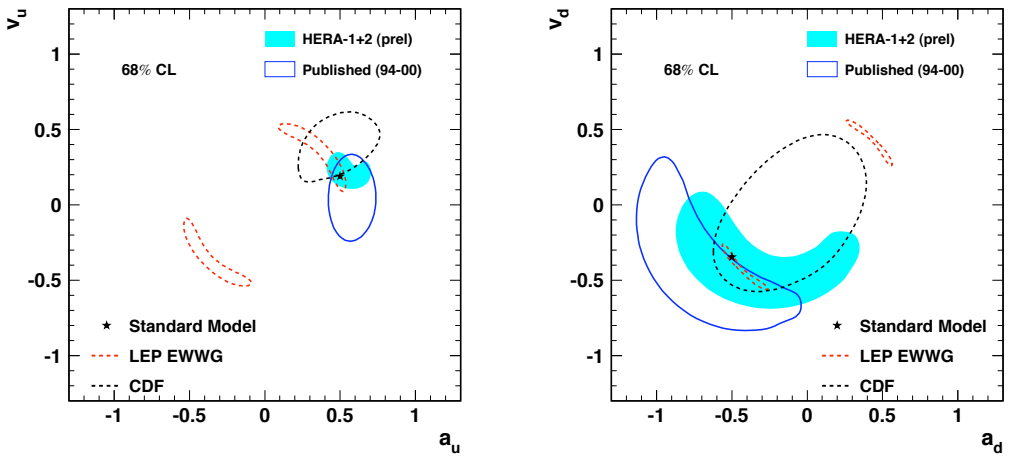

(a) (b)

Figure 7.7: Weak neutral couplings of u (a) and d (b) quarks to the Z boson in comparison with similar results from CDF and combined LEP experiments.

Chapter 8

Summary and Outlook

Both Neutral Current and Charged Current cross sections for full HERA-II data have been measured. The measurements performed in a large kinematic domain with the highest value of four-momentum transfer squared up to 30000 GeV^2 comparable with square of masses of Z and W boson allow the tests of both components of the Standard Model: QCD and the electroweak theories. The analyzed data are with integrated luminosities of 180.0 pb^{-1} and 149.1 pb^{-1} for e^+p and e^-p interactions respectively, which represent a factor of about 9 increase with respect to that of HERA-I for the e^-p interaction. The results of the combined data HERA-I and HERA-II have also been presented. The high luminosity, of $\sim$0.5 pb^{-1} per experiment (H1 or ZEUS) can provide a best precision measurement ever of the Deep Inelastic Scattering.

The single and differential cross sections of the Charged Current cross section measured in the kinematic region of $Q^2 > 300$ GeV^2 and $0.002 < x < 0.65$ have been compared with the expectation of the Standard Model estimated by the H1PDF 2009 fit and have been found to be in good agreement. The total Charged Current cross sections have been measured separately for e^- and e^+p, left- and right-handed data at $Q^2 > 400$ GeV^2 and $y < 0.9$. The cross sections with polarized electron beams from HERA-II together with the published cross sections from HERA-I with unpolarized beams show the linear dependence on the electron polarization. It is found that the cross section of the e^+p scattering at polarization $P_e = -1$ and that of the e^-p scattering at polarization $P_e = 1$ are compatible to zero. This confirms the linear dependence of the total Charged Current cross section on the electron (positron) beam polarization and the limit on the mass of the hypotherical right- (left-) handed boson W: there are no weak charged current interactions mediated by a hypothetical right- or left-handed W boson.

The results for the double differential reduced cross sections for the Charged Current process of the combined data have been presented and compared to the Standard Model prediction as well as the contribution from u-quark for the e^-p interaction or the contri-

bution from the d quark for e^+p interaction. It confirms that the Charged Current cross sections could be used to constrain the u or d quarks distribution function for a precise QCD analysis.

The double differential cross section of the Neutral Current process was measured in the kinematic range of $Q^2 > 200$ and $0.0032 < x < 0.65$ and was found to be in good agreement with the Standard Model prediction. The precision of the measurement is at level of a few per cent at low Q^2 where the systematic uncertainty dominates, and is limited by the statistical precision at very high Q^2.

The single differential cross section $\mathrm{d}\sigma/\mathrm{d}Q^2$ cover a large range in Q^2 and fall by six orders of magnitude with increasing Q^2 due to the propagator of the exchanged particles.

The polarization asymmetries $A^{\pm}$ determined from e^-p and e^+p cross sections allow the measurement of the vector- and axial-vector couplings of the leptons and the quarks. They demonstrate parity violation in NC interactions at a very small distance, down to about 10^{-18} m.

The neutral current double differential reduced cross sections measurement based on the combination of HERA-I and HERA-II have also been compared to the Standard Model. Again the difference of e^-p and e^+p cross section is confirmed. These cross sections were used to determine the proton structure function $x\tilde{F}_3$. The results on the extraction of $x\tilde{F}_3$ as well as its contribution $xF_3^{\gamma Z}$ which dominates at very high Q^2 have been found to be in fairly good agreement with the predictions.

Both the single differential cross section for charged and neutral currents have been compared to the predictions and it is found that, at zero polarization, the prediction of the unification of electromagnetic and weak forces is still valid in the framework of the Deep Inelastic Scattering.

Finally, the full HERA data were used to extract the coupling constants of the light quarks, u and d, to the Z-boson. The additional sensitivity of the HERA-II data to the couplings has significantly improved the precision achieved with the HERA-I data alone, providing the best determination in particular for the vector coupling of the u quark to the Z-boson.

These cross sections are being finalized and the final cross sections of H1 will be combined with the corresponding ones from ZEUS to achieve a unique high precision DIS cross section data. As demonstrated with HERAPDF 1.0 using the combined H1 and ZEUS data from HERA-I, the fully combined HERA data will have a profound impact on the LHC physics by providing the most precise parton distributions functions.

Moreover, HERA allows with a center-of-mass energy of $\sqrt{s} = 320$ GeV to resolve the

partonic structure down to distances as small as 10^{-18} m. Because of this large energy and the 4π acceptance of the detectors, it can cover a range in Bjorken x from nearly 10^{-5} to 1 and the momentum transfers squared Q^2 from the photoproduction limit $Q^2 = 0$ close to the maximum of $Q^2_{\text{max}} = s \simeq 10^5$ GeV^2. The x range corresponds to the full rapidity range of the LHC experiments. The HERA measurements, as illustrated in figure 8.1, can be used for the understanding of the LHC measurements and can be confronted with those especially for regions with $Q^2 > 100$ GeV^2.

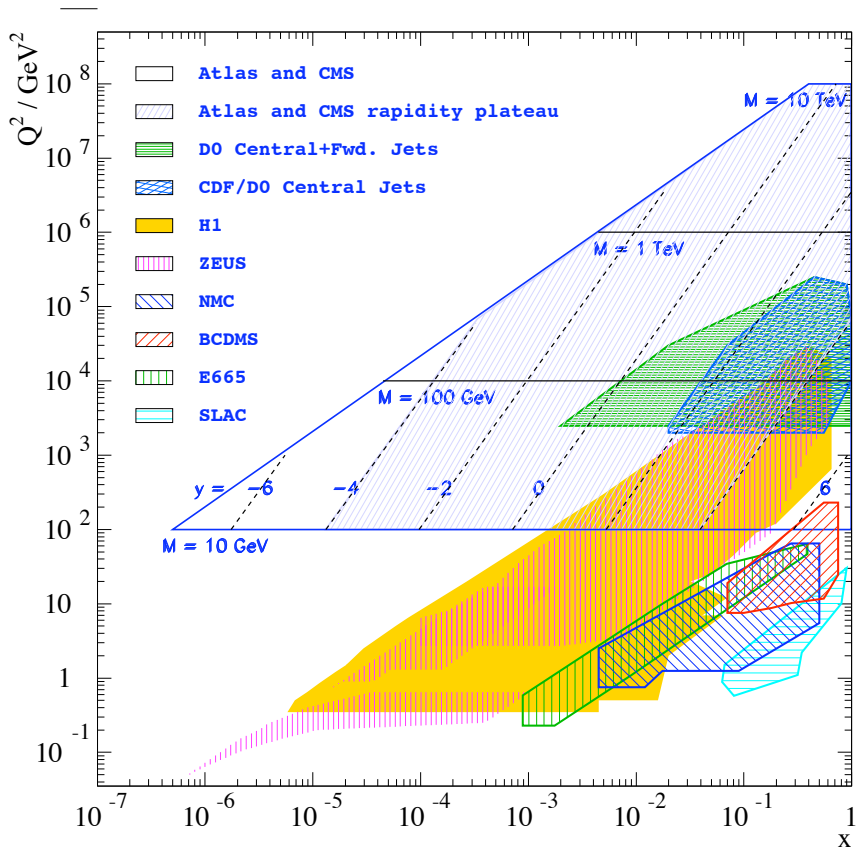

Figure 8.1: Schematic view of the kinematic coverage of recent deep inelastic scattering experiments including ZEUS and H1 from HERA, of the TEVATRON experiments and of the LHC experiments ATLAS and CMS.

Appendix A

Luminosity correction factor determined by QED Compton analysis

Period	Run range	Luminosity (pb^{-1}) (Database)	Factor (QED Compton)
0304 RH	356241-376562	18.6	0.98277 ± 0.02939
0304 LH	377533-386696	13.4	1.03835 ± 0.03571
0304 RH	387537-392213	8.0	0.97063 ± 0.04521
0405 LH	402992-414712	32.3	0.97399 ± 0.02231
0405 RH	415620-427474	28.1	1.00106 ± 0.02413
0405 LH	427813-436893	34.5	1.01643 ± 0.02240
06em LH	444094-458154	35.6	1.02349 ± 0.02180
06em RH	458841-466997	14.7	1.00089 ± 0.03482
0607 RH	468530-485679	51.9	1.01660 ± 0.01790
0607 LH	485715-485849	1.1	0.98691 ± 0.12148
0607 RH	486073-489866	18.7	1.05919 ± 0.03122
0607 LH	490135-500611	55.3	1.06993 ± 0.01773

Table A.1: Luminosity correction factors and corresponding statistical errors determined from QED Compton analysis for each subperiod.

Appendix B

Comparison data and MC for CC analysis

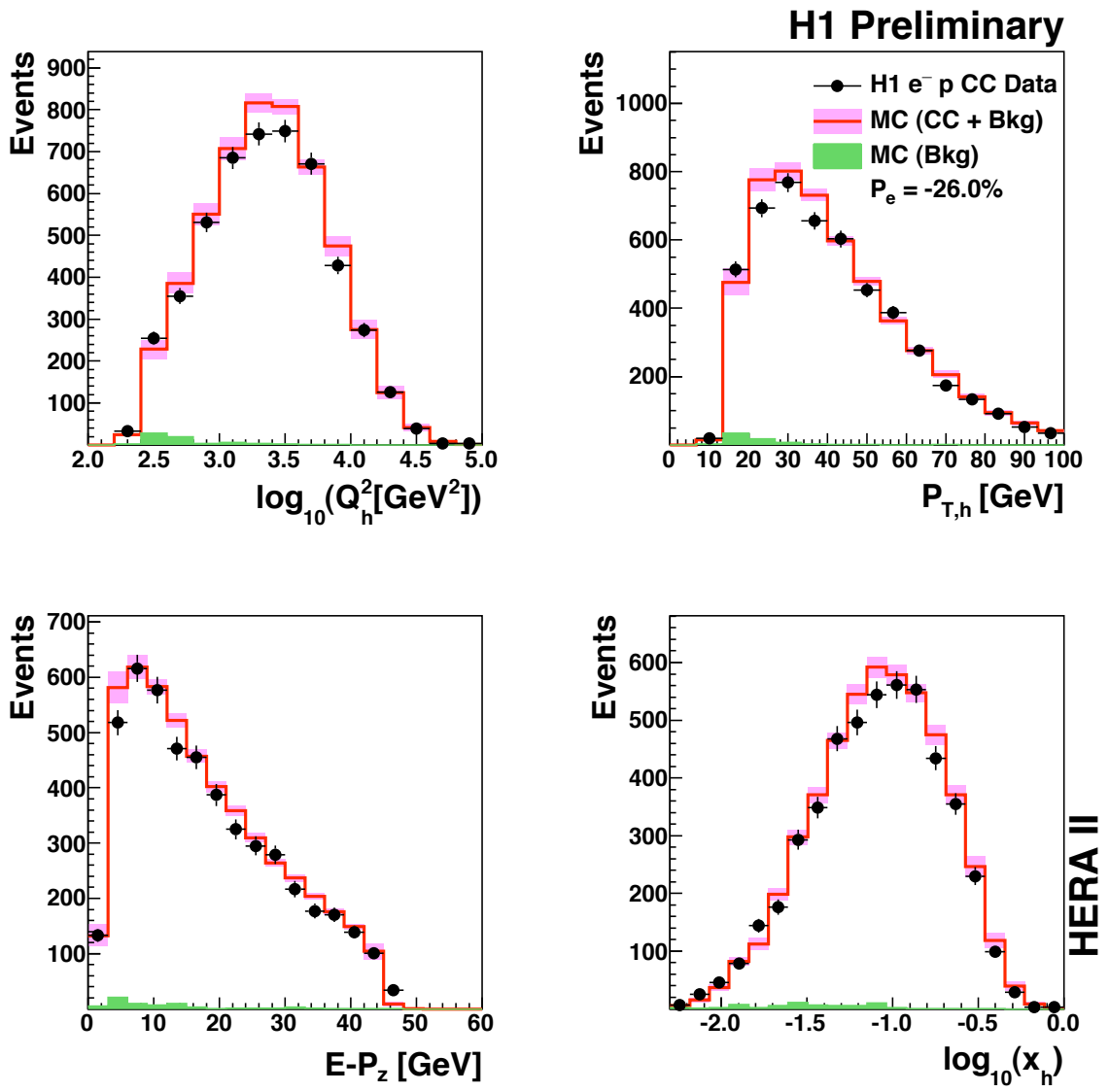

Figure B.1: Distributions $\log_{10}(Q_h^2)$, $P_{T,h}$, $E - P_z$ and $\log_{10}(x_h)$ for the e^-p left-handed data. The MC contributions from the Charged Current process and the ep background (bkg) processes are shown as open histograms with the latter contribution alone being shown as shaded histograms.

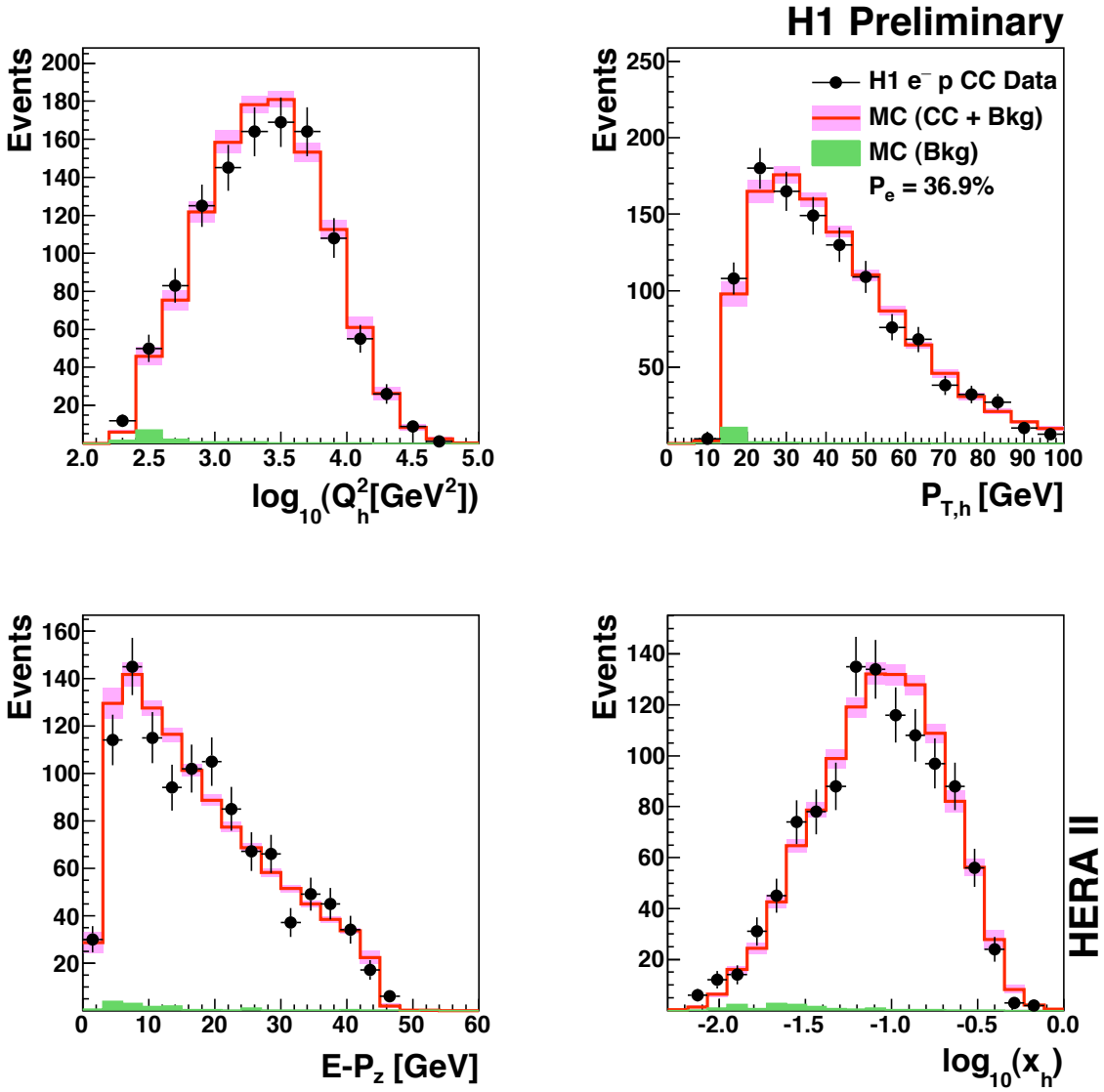

Figure B.2: Distributions $\log_{10}(Q_h^2)$, $P_{T,h}$, $E-P_z$ and $\log_{10}(x_h)$ for the e^-p right-handed data. The MC contributions from the Charged Current process and the ep background (bkg) processes are shown as open histograms with the latter contribution alone being shown as shaded histograms.

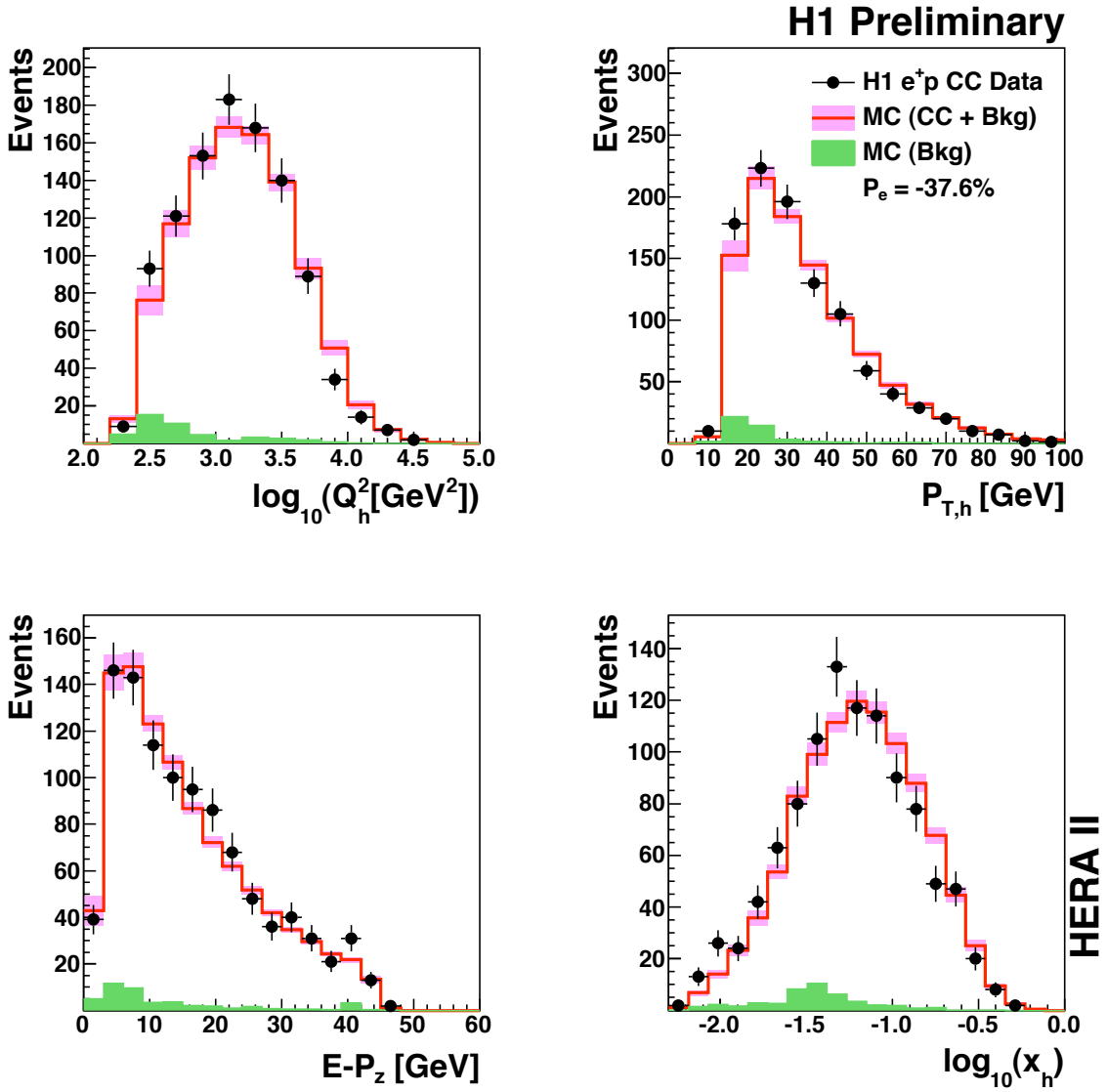

Figure B.3: Distributions $\log_{10}(Q_h^2)$, $P_{T,h}$, $E - P_z$ and $\log_{10}(x_h)$ for the e^+p left-handed data. The MC contributions from the Charged Current process and the ep background (bkg) processes are shown as open histograms with the latter contribution alone being shown as shaded histograms.

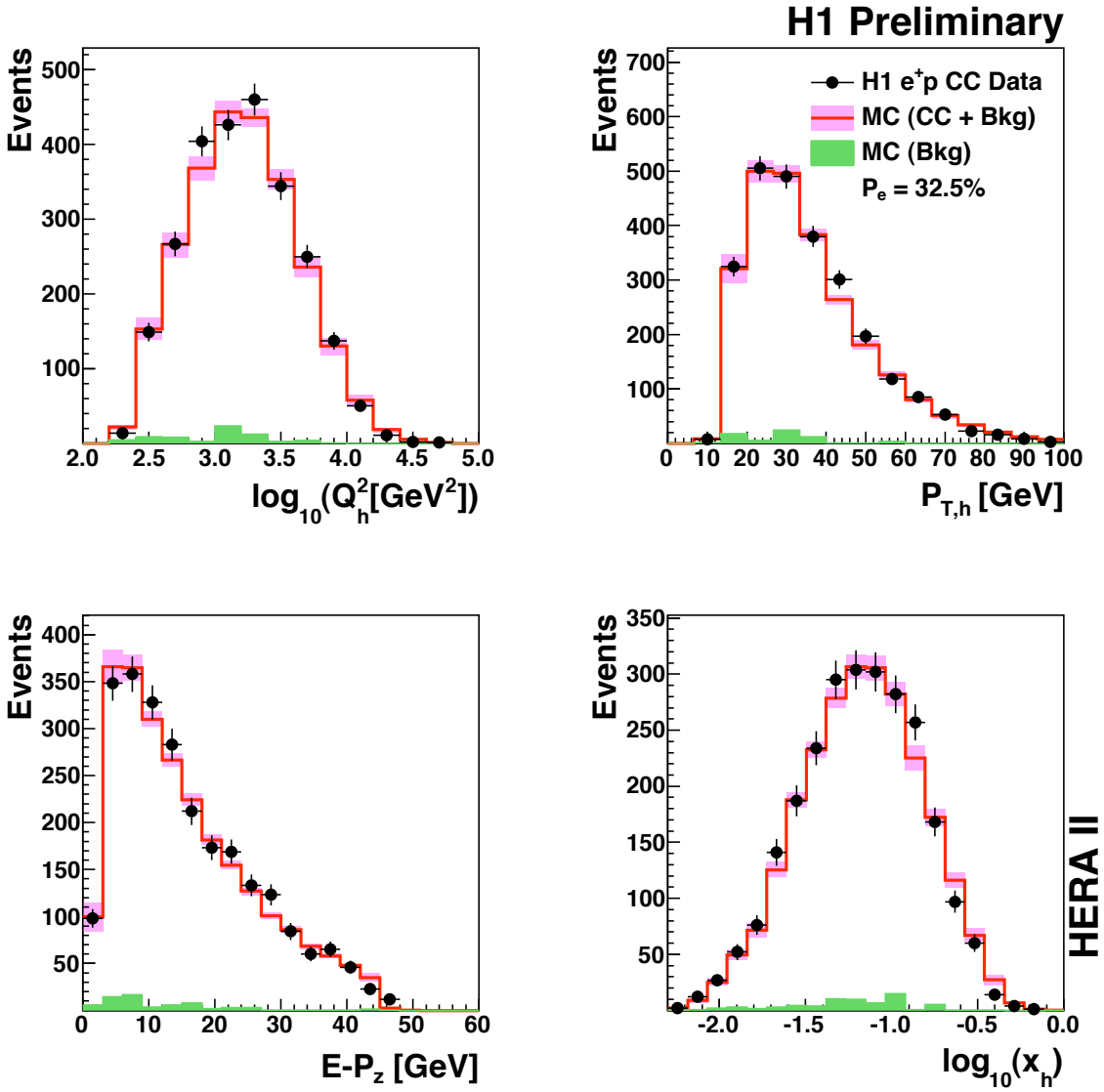

Figure B.4: Distributions $\log_{10}(Q_h^2)$, $P_{T,h}$, $E-P_z$ and $\log_{10}(x_h)$ for the e^+p right-handed data. The MC contributions from the Charged Current process and the ep background (bkg) processes are shown as open histograms with the latter contribution alone being shown as shaded histograms.

Bibliography

[1] E. Rutherford, *The Scattering of α and β Particles by Matter and the Structure of the Atom*, vol. 6, Philos. Mag., 1909.

[2] J. Chadwick, *The existence of a neutron*, 1932, Proceedings of the Royal Society, Series A, vol. 136, p. 692-708.

[3] J. Chadwick, *The Bakerian Lecture: The neutron*, 1933, Proceedings of the Royal Society, Series A, vol. 142, p. 1-25.

[4] R. Hofstadter, *The Electron Scattering Method and its Application to the Structure of Nuclei and Nucleons*, Elsevier Pub. Co., Amsterdam-London-New York, 1961, Nobel Lectures, Physics 1942-1962, p. 560-581.

[5] D. H. Corward *et al.*, *Electron-proton scattering at high momentum transfers*, SLAC-PUB-373, December 1967.

[6] E.D. Bloom *et al.*, Phys. Rev. Lett. **23** (1969), 930.

[7] M. Breidenbach *et al.*, Phys. Rev. Lett. **23** (1969), 935.

[8] M. Gell-Mann, Phys. Lett. **8** (1964), 214.

[9] R.P. Feynman, Proceedings of the 3rd Topical Conference on High Energy Collision of Hadrons, Stony Brook, N. Y. (1969).

[10] E. Fermi, *Attempt at a Theory of Beta-Rays*, Il Nouvo Cimento 11: 1-21, p. 1934.

[11] S. Bais, *The Equations. Icons of knowledge*, 2005.

[12] *"The Nobel Prize in Physics 1979"*, The Nobel Foundation, Retrieved 2008-12-16.

[13] F.J. Hasert *et al.* [Gargamelle Collaboration], Phys. Lett. **B46** (1973), 121–124.

[14] F.J. Hasert *et al.* [Gargamelle Collaboration], Phys. Lett. **B46** (1973), 138–144.

[15] G. Arnison *et al.* [UA1 Collaboration], Phys. Lett. **B122** (1983), 103.

[16] M.Banner *et al.* [UA2 Collaboration], Phys. Lett. **B122** (1983), 476.

[17] http://public.web.cern.ch/public/en/Research/SPS-en.html.

[18] Wikipedia, *The International Project HERA*, http://en.wikipedia.org/wiki/Hadron_Elektron_Ring_Anlage.

[19] I. Abt *et al.* [H1 Collaboration], *Gluing Silicon with Silicone*, Nucl. Instr. Meth. **A411** (1997), 310 and 348.

[20] [ZEUS Collaboration], *The ZEUS Detector. Status Report*, 1993.

[21] C. Adloff *et al.*, Eur. Phys. J. **C30** (2003), 1–32.

[22] A.C. Benvenuti *et al.* [BCDMS Collaboration], Phys. Lett. **B223** (1989), 485.

[23] M. Arneodo *et al.* [New Muon Collaboration], Phys. Lett. **B364** (1995), 107.

[24] R. Devenish and A. Cooper-Sarkar, *Deep Inelastic Scattering*, Oxford University Press, 2004.

[25] D. E. Groom *et al.* [Particle Data Group Collaboration], Eur. Phys. J. C. **15** (2000), 1.

[26] H. David Politzer, Phys. Rept. **14** (1974), 129–180.

[27] D. J. Gross and F. Wilczek, Phys. Rev. **D8** (1973), 3633–3652.

[28] Vernon D. Barger and R. J. N. Phillips, *COLLIDER PHYSICS*, REDWOOD CITY, USA: ADDISON-WESLEY (1987) 592 P. (FRONTIERS IN PHYSICS, 71).

[29] M. Peskin and D. Schroeder, *An Introduction to Quantum Field Theory*, Westview Press, 1995.

[30] F.D. Aaron *et al.* [H1 Collaboration], (2009).

[31] F. D. Aaron *et al.* [H1 Collaboration], Eur. Phys. J. **C65** (2010), 363.

[32] G. 't Hooft, Nucl. Phys. **B61** (1973), 455.

[33] S. Weinberg, Phys. Rev. **D8** (1973), 3497–3509.

[34] V.N. Gribov and L.N. Lipatov, Sov. J. Nucl. Phys. **15** (1972), 4338.

[35] G. Altarelli and G. Parisi, Nucl. Phys. **B126** (1977), 298.

[36] Yu. L. Dokshitzer., Sov.Phys. JETP **46** (1977), 641.

[37] F. D. Aaron *et al.* [H1 Collaboration], Eur. Phys. J **C64** (2009), 561.

[38] T. Ahmed *et al.*, Phys. Lett. **B299** (1997), 374.

[39] T.-M. Yan S.D. Drell, Phys. Rev. Lett. **25** (1970), 316–320.

[40] [H1 and ZEUZ Collaborations], *Events with an Isolated Lepton and Missing Transverse Momentum and Measurement of W Production at HERA*, 2009, Summited to JHEP.

[41] A. A. Sokolov and I. M. Ternov, Sov. Phys. Dokl. **8** (1964), 1203.

[42] T. Behnke *et al.*, *A new analysis for the transverse polarimeter at HERA-II*, contributed paper 120 to the European Physical Society International Conference on High Energy Physics, 2003, Aachen, Germany.

[43] F. Zomer, *A high power Fabry-Perot resonator for precision Compton Polarimetry with the longitudinally polarised lepton beams at HERA*, LAL 03-12, 2003, Habilitation à Diriger des Recherches.

[44] J. Bürger *et al.*, *The Central Jet Chamber of the H1 Experiment*, Nucl. Instrum. Meth. **A279** (1989), 217–222.

[45] S. Lueders, *CST/CIP$_{2000}$ Stand Alone Tracking and Vertexing*, 1999, H1-interal note H1-04/99-570.

[46] D. Pitzl *et al.*, *The H1 silicon vertex detector*, Nucl. Instrum. Meth. **A454** (2000), 334–349.

[47] I. Abt *et al.* [H1 Collaboration], *The Tracking, Calorimeter and Muon Detectors of the H1 Experiment at HERA*, Nucl. Instr. Meth. **A386** (1997), 348–396.

[48] B. Andrieu *et al.*, *The H1 Liquid Argon Calorimeter System*, Nucl. Instrum. Meth. **A336** (1993), 460–498.

[49] B. Portheault, *Première mesure des sections efficaces de courant chargé et neutre avec le faisceau de positron polarisé à HERA II et analyses QCD-électrofaibles*, Ph.D. thesis, Université Paris XI, 2005.

[50] C. Issever, K. Bornas, and D. Wegener, *An Improved Weighting Algorithm to Achieve Software Compensation in a Fine Grained LAr Calorimeter*, H1-internal note, H1-03/03-608, 2003.

[51] [H1 SPACAL Group], *The H1 Lead/Scintillating-Fibre Calorimeter*, Nucl. Instr. Meth. **A386** (1997), 397–408.

[52] H. Bethe and W. Heitler, Proc. Roy. Soc. **A146** (1934), 83.

[53] I. Abt *et al.* [H1 Collaboration], *The H1 detector at HERA*, Nucl. Instrum. Meth. **A386** (1997), 310–347.

[54] T. Frisson, *Mesure de la Luminosité pour l'Expérience H1*, Ph.D. thesis, Université Paris-Sud, 2006.

[55] Ch. Wissing *et al.*, *The H1 ToF System in 1996 and 1997*, 1998, H1-Internal Note, H1-01/98-533.

[56] T. Carli *et al.*, H1 Internal Note, H1-07/95-445.

[57] Kiesling Denby Fent *et al.*, *The H1 Neural Network Trigger Project*, (2000).

[58] J.C. Bizot and D. Hoffmann, *Strategy Studies for the H1 Topological L2-Trigger (L2TT)*, 1997, H1 internal note, H1-1/97-508.

[59] J. Naumann, *Entwicklung und test der dritten h1-triggerstufe*, Ph.D. thesis, Univ. Dortmund, 2003.

[60] K Müller and R. Beyer, *1996 L4 Filter Farm Selection Algorithm*, 1996, H1 internal note, H1-10/96/499.

[61] S. Bentvelsen *et al.*, *Reconstruction of* (x, Q^2) *and extraction of structure functions in neutral current scattering at HERA*, Proceedings of the Workshop: Physics at HERA, volume 1, pages 23-40. DESY. 1992.

[62] *Proceeding of the "Study of an ep Facility for Europe"*, DESY 79/48, 1979.

[63] W. Buchmüller and G. Ingelmann (eds.), *Reconstruction of* (x, q^2) *and extraction of structure functions in neutral current scattering at HERA*, DESY, 1992, vol. 1, 1992.

[64] U. Bassler and G. Bernardi, Nucl. Instrum. Meth. **A361** (1995), 197–208.

[65] F.D. Aaron *et al.* [H1 and ZEUS Collaborations], (2009).

[66] J. Meyer, *Guide for the h1 simulation program h1sim*, Internal Software-Note, 1989, 03-11/89, DESY.

[67] R. Brun *et al.*, CERNDD/EE/84-1 ed., 1987.

[68] [H1 Collaboration], H1 Reconstruction packages, available at https://www-h1.desy.de/icas/imanuals/h1rec/h1rec9/h1rec.html.

[69] G.A. Schuler and H. Spiesberger, *Proceedings of the Workshop "Physics at HERA"*, DESY **3** (1992), 1419.

[70] G. Ingelman, *Proceedings of the Workshop "Physics at HERA"*, DESY **3** (1992), 1366.

[71] H. Spiesberger A. Kwiatkowski and H. J. Möhring, Comput. Phys. Commun. **69** (1992), 155.

[72] L. Lönnblad, Comput. Phys. Commun. **71** (1992), 15.

[73] T. Sjöstrand and M. Bengtsson, Comput. Phys. Commun. **43** (1987), 367.

[74] A. D. Martin, W. J. Stirling, and R. G. Roberts, Phys. Rev. D **50** (1994), no. [hepph/9406315], 6734.

[75] T. Sjöstrand, Comput. Phys. Commun. **82** (1994), 74.

[76] H.L. Lai *et al.*, Eur. Phys. J. **C12** (2000), 375.

[77] M. Glück, E. Reya, and A. Vogt, Phys. Rev D **46** (1992), 1973.

[78] A. T. Doyle *et al.* (ed.), *A new generator forwide angle bremsstrahlung*, no. DESY-PROC-1999-02, 596, DESY, 1998, Monte Carlo Generators for HERA Physics.

[79] T. Abe, Comput. Phys. Commun. **136** (2001), 126.

[80] U. Bauer, J.A.M. Vermaseren, and D. Zeppenfeld, Nucl. Phys. **B375** (1992), 3.

[81] The H1 OO Group, *The H1 OO Physics Analysis Project*, December 2007, Version 3.2.2.

[82] R. Brun *et al.*, *ROOT, An Object-Oriented Data Analysis Framework, Version 5.22.00*, Geneva, 2009.

[83] *QHQTRK manual (Heavy Flavour track selection code by Lee West).*

[84] P. Bruel, *Recherche d'interactions au-delà du Modèle Standard à HERA*, Ph.D. thesis, Université Paris-Sud, 1998.

[85] H1 internal note H1-01/05-616, *An energy ow algorithm for Hadronic Reconstruction in OO: Hadroo2.*

[86] J. Cao and Z. Zhang, *Towards an Unbiased Measurement of Kinematic Variables at Low y Region*, H1-12/99-580.

[87] Z. Zhang, *New Insights into the proton structure with ep Collider HERA*, LAL 00-57, 2000, Habilitation à Diriger les Recherches.

[88] L. Goerlich and H.P. Wellisch, *Documentation of the LAr Clustering*, H1 Internal Note, H1-IN-204(12/1991).

[89] M. Jacquet and Z. Zhang *et al.*, *Absolute hadronic jet calibration of the H1 Liquid Argon calorimeter*, H1-04/99-571.

[90] S. Catani *et al.*, Nucl. Phys. **B377** (1992), 445.

[91] N. Brown and W. J. Stirling, Z. Phys. **C53** (1992), 629.

[92] E. Chabert *et al.*, *QBGFMAR: An Updated Phan Package for Cosmic and Halo Muon Topological Rejection in High P_T Physics Analysis*, H1-11/98-556.

[93] I. Negri *et al.*, *A Minimal Comprehensive Set of Muon Background Topological Finders for High P_T Physics Analysis*, H1-10/96-498.

[94] C. Veelken, *H1NonepBgFinder - Rejection of cosmic muon and beam-halo events in the H1OO framework*, H1-09/02-603.

[95] R. Plačakytė, *First Measurement of Charged Current Cross Sections with Longitudinally Polarised Positrons at HERA*, Ph.D. thesis, Ludwig-Maximilians-Universität München, 2006.

[96] G. Martin, *Untersuchung von Prozessen des geladenen und neutralen Stroms mit dem H1-Detektor bei HERA*, Ph.D. thesis, Universität Hamburg, 1997.

[97] A. Aktas *et al.* [H1 Collaboration], Phys. Lett. **B634** (2006), 173–179.

[98] A. Aktas, *Messung von polarisierten Wirkungsquerschnitten des geladenen Stroms bei HERA*, Ph.D. thesis, Universität Hamburg, 2005.

[99] F. Corriveau *et al.*, *A Calibration of the HERA Transverse Polarimeter for the 2003/2004 Data*, available at
http://www.desy.de/∼pol2000/documents/documents.html.

[100] W. Lorenzon [HERMES Collaboration], *7th International Workshop on Polarized Gas Targets and Polarized Beams*, 18-22 Aug 1997.

[101] V. Radescu, *The combined fit HERAPDF 1.0*, Proc. of XVII Int. Workshop on Deep-Inelastic Scattering and Related Topics, Madrid, Spain, April 2009.

[102] C. Adloff *et al.* [H1 Collaboration], Eur. Phys. J. **C13** (2000), 609–639.

[103] C. Adloff *et al.* [H1 Collaboration], Eur. Phys. J. **C19** (2001), 269–288.

[104] A. Dubak, Ph.D. thesis, Technische Universität München, 2003.

[105] B. Heinemann, *Measurement of Charged Current and Neutral Current Cross Section in Positron-Proton Collisions at* $\sqrt{s} \simeq 300$ *GeV*, Ph.D. thesis, Universität Hamburg, 1999.

[106] M. Gouzevitch, *Mesure de la constante de couplage forte* α_s *avec les jets hadroniques en Diffusion Inélastique Profonde*, Ph.D. thesis, Ecole Politechnique, 2008.

[107] F. James *et al.*, *MINUIT, Function Minimization and Error Analysis*, CERN Geneva, Switzerland.

[108] A. Nikiforov, Ph.D. thesis, Ludwig-Maximilians-Universität München, 2007.

[109] A. Maire *et al.* [H1 Collaboration], Internal presentation, nELAN group, 19/6/2007.

[110] S. Aid *et al.* [H1 Collaboration], Phys. Lett. **B379** (1996), 319–329.

[111] S. Aid *et al.* [H1 Collaboration], Nucl. Phys. **B470** (1996), 3.

[112] C. Adloff *et al.* [H1 Collaboration], Phys. Lett. **B568** (2003), 35.

[113] H1prelim-07-141. Preliminary result for Lepton Photon 2007 conference.

[114] [H1 Collaboration], Eur. Phys. J. **C63** (2009), 625–678.

[115] A. Aktas *et al.* [H1 Collaboration], Phys. Lett. **B632** (2006), 35.

[116] C. Pascaud and F. Zomer, *QCDFit manual*, LAL-95-05.

[117] W. Furmanski and R. Petronzio, Phys. Lett. **B97** (1980), 437.

[118] D. Acosta *et al.* [CDF Collaboration], Phys. Rev. **D71** (2005), 052002.

[119] [LEP and SLD Electroweak working groups], *A Combination of Preliminary Electroweak Measurements and Constraints on the Standard Model*, hep-ex/0412015 http://lepewwg.web.cern.ch/LEPEWWG/plots/summer2004/.

[120] G.P. Zeller *et al.* [NuTeV Collaboration], Phys. Rev. Lett. **88** (2002), 091802.

[121] S.C. Bennett and C.E. Wieman, Phys. Rev. Lett. **82** (1999), 2484.

Glossary

μODS : micro-ODS

ADC : Analog to Digital Converter

BBE : Backward Electromagnetic Barrel

CB : Central Barrel
CC : Charged Current
CIP : Central Inner Proportional Chamber
CIZ : Central Inner Z-chamber
CJC : Central Jet Chamber
COZ : Central Outer Z-chamber

DA : Double-Angle
DCA : Distance of Closest Approach
DESY : Deutches Elektronen SYnchrotron
DIS : Deep Inelastic Scattering
DST : Data Summary Tape
DTNV : Non-vertex-fitted track
DTRA : Vertex-fitted track

EM : Electromagnetic
ET : Electron Tagger

fADC : Fast Analog to Digital Converter
FB : Forward Barrel
FMD : Forward Muon Detector
FSR : Final State Radiation
FST : Forward Silicon Tracker
FTD : Forward Tracking Detector
FTT : Fast Track Trigger

H1OO : H1 Object-Oriented analysis framework
H1PDF2009 : H1 Parton Distribution Function 2009
HAT : H1 Analysis Tag
HERA : Hadron-Electron Ring Anlage
HFS : Hadronic Final State

ISR : Initial State Radiation

L2NN : Level 2 Neural Network Trigger
L2TT : Topological Trigger
LAr : Liquid-Argon
LH : Left-Handed
LPOL : Longitudinal Polarization
LW : Lee-West track

MC : Monte Carlo
MS : Minimal Subtraction scheme

NC : Neutral Current

ODS : Object Data Store

PD : Photon Detector
PDF : Parton Distribution Function
POT : Production Output Tape
PsCC : Pseudo-Charged-Current

QCD : Quantum Chromodynamics
QED : Quantum Electrodynamics
QPM : Quark-Parton Model

RH : Right-Handed

SpaCal : Spagetti Calorimeter
ST : Sub-Trigger

ToF : Time of Flight
TPOL : Transverse Polarization

Acknowledgement

This work arose in part out of my PhD student life that toke place since I came to the H1 group at the Laboratoire de l'Accélérateur Linéaire (LAL), Orsay. The final results would never be achieved without supports from people whom I own large acknowledgements.

I would like to express my sympathies to Professor Guy Wormser, director of the LAL, Orsay, for his kindness by accepting me to the laboratory and by accepting to be the president of the jury of the defence.

I am heartily thankful to my supervisor, Zhiqing Zhang, whose encouragement, patience, guidance and support from the initial to the final level enabled me to develop an understanding of the subject. His guidance helped me in all the time of study and also in writing of the thesis.

My sincere thanks also go to Violette Brisson, Marie Jacquet, Christian Pascaud, Victor Soskov and Fabian Zomer, members of the H1 group at LAL, for their encouragement, their availability for all of my questions or requirements, which are sometimes not very agreeable. I would like also to express my gratitude for their help by giving very useful comments for my defence.

I warmly thank to Li Gang, postdoc of the H1 Group, my fellow for the first two years, who gave me not only very useful advices on data analysis but also very interesting lectures on Chinese and beyond. Thanks for sharing with me "never ending" stories and discussions on the night trains to Hamburg.

I would also specially acknowledge the members of the high-Q^2 Physics Working Group: Sasha Glazov, Eram Rizvi, Andreii Nikiforov, Vladimir Shekelian, Stanislav Shuskevitch, Shiraz Habib. Their discussions, advices during the group meetings are always the key to guide me to a final results of this work and will be more than that. A special gratitude should be addressed to Sasha Glazov for his availability every time when I ask him for a recommendation letter. I gratefully thank Ringailė Plakakytė for her encouragements, advice. It is a pleasure to collaborate with you. My special thanks to Andreii Nikiforov and Stanislav Shuskevitch for sharing not only the data analysis techniques but also many beautiful tricks on softwares. I would like also to express my acknowledgement to the member of the new-ELAN group with their discussions and ad-

vices.

Besides the Physics working group, my work should not be fulfilled without helps from other people from the H1 Collaboration. For the first two years, it was Emmanuel Sauvan who never refused to answer any of my questions concerning the H1OO software, Marana package and also concerning the questions on Physics. I greatly appreciate his helps. I would like also express my gratitude to Cristinel Diaconu for his help not only by accepting to be a member of the jury in the defence of my thesis but also by giving me a great chance to continue the work at the H1 experiment.

My special acknowledgements must also be addressed to the other members of the H1 Collaboration: Claude Vallée, Bogdan Lobodzinski, Alan Campbell, Katja Krueger, Stefan Schmidt and the others. Specials thanks must also go to Laurent Schoeffel for his encouragements and for sharing very good moments while waiting for the night trains.

At a final step of a thesis, it is the defence which takes place and mine would not be realized without the acceptance of the other members of the Jury: Emi Kou and Mister Bertrand Laforge. I would like to specially thank Emi Kou for her explications with patience and corrections on the theoretical chapter and thank to Mister Bertrand Laforge for his very precise and detailed comments of my thesis.

I would like to address appreciations to Professor Tran Thanh Van, Professor François le Diberder and Sandrine Laplace for their encouragements. A special thank must go to Thi Nguyet Trinh for the chance she gave me to approach Particle Physics and for sharing of the difficult moments.

I would also like to address many thanks to the people of the Service de Missions et Service du personel of the Laboratoire de l'Accélérateur de Linéaire for their helps for every of my difficulties on the papers and for their helps for my missions to Hamburg. The special thanks would also be addressed to the people of the H1 group at DESY, Alla Grabovsky and Sabine Platz for their helps on the administrative procedures.

Finally, I would like a deep acknowledgement to my parents, my sister and my friends who are always besides me everytimes from the first to the final steps of my studies.

Résumé

Des mesures de sections efficaces des processus courant chargé et courant neutre ont été réalisées pour la première fois en utilisant l'ensemble des données accumulées à HERA-II avec un faisceau d'électrons ou de positrons polarisés en collision avec un faisceau de protons. Les données prises par le détecteur H1 à 319 GeV d'énergie dans le centre de masse correspondent à une luminosité intégrée de 149.1 pb^{-1} et 180.0 pb^{-1} pour les collisions e^-p et e^+p respectivement, et représentent une augmentation d'environ un facteur 10 et 2 respectivement par à rapport à la prise de données de HERA-I. Les sections efficaces mesurées couvrent un très grand domaine cinématique de plus de deux ordres de grandeur à la fois en Q^2 (jusqu'à 30000 GeV^2) et en x (jusqu'à 0.003). Les mesures sont comparées avec les prédictions du Modèle Standard montrant un très bon accord. La précision de la mesure de l'asymétrie sur la polarisation en fonction de Q^2 a confirmé l'observation précédente de la violation de parité dans le processus courant neutre pour une distance allant jusqu'à 10^{-18} m. Les sections efficaces intégrées pour $Q^2 > 400$ GeV^2 et pour des inélasticités $y < 0.9$ dans le processus courant chargé ont été mesurées pour quatre échantillons indépendants avec les faisceaux $e^\pm$ et à différentes valeurs de polarisation. Ces données et celles mesurées à HERA-I avec les faisceaux d'électrons et de positrons non-polarisés ont permis de vérifier la dépendance linéaire des sections efficaces du processus courant chargé en fonction de la polarisation, confirmant l'absence de courants droits dans les données en accord avec la prédiction du Modèle Standard.

Les nouvelles sections efficaces ont été combinées avec celles de HERA-I pour maximiser la précision de ces mesures. Les données combinées ont ensuite été utilisées pour déterminer la fonction de structure $xF_3^{\gamma Z}$ qui est pratiquement une mesure directe des quarks de valence. Les nouvelles sections efficaces ont aussi été utilisées avec celles de HERA-I dans un fit combinant à la fois les paramètres de la théorie électrofaible et de QCD pour extraire non seulement les densités de partons mais aussi les couplages des quarks légers u et d au boson Z. La précision obtenue sur les valeurs de ces couplages est bien meilleure que celle obtenue au Tevatron et au LEP, en particulier pour les couplages vectoriel et axial du quark u.

Mots-clés: Courant Chargé, Courant Neutre, DIS, Diffusion Profondément Inélastique, grand Q^2, QCD, polarisation, électron, positron, proton, fonction de structure, xF_3, électrofaible, DESY, HERA, H1.

Abstract

The inclusive cross sections for both charged and neutral current processes have been measured in interactions of longitudinally polarized electrons (positrons) with unpolarized protons using the full data samples collected by H1 at HERA-II. The data taken at a center-of-mass energy of 319 GeV correspond to an integrated luminosity of 149.1 pb^{-1} and 180.0 pb^{-1} for e^-p and e^+p collisions, representing an increase in statistics of a factor of 10 and 2, respectively, over the data from HERA-I. The measured double differential cross sections $\mathrm{d}^2\sigma/\mathrm{d}x\mathrm{d}Q^2$ cover more than two orders of magnitude in both Q^2, the negative four-momentum transfer squared, up to 30000 GeV^2, and Bjorken x, down to 0.003. The cross section data are compared to predictions of the Standard Model which is able to provide a good description of the data. The polarization asymmetry as a function of Q^2 is measured with improved precision, confirming the previous observation of P violation effect in neutral current ep scattering at distances down to 10^{-18} m. The total cross sections of the charged current process, for $Q^2 > 400$ GeV^2 and inelasticity $y < 0.9$ are measured for 4 independent data samples with $e^\pm$ beams and different polarization values. Together with the corresponding cross section obtained from the previously published unpolarized data, the polarization dependence of the charged current cross section is measured and found to be in agreement with the Standard Model prediction with the absence of right-handed charged current.

The cross sections are combined with previously published data from H1 to obtain the most precise unpolarized measurements. These are used to extract the structure function $xF_3^{\gamma Z}$ which is sensitive to the valence quark distributions down to low x values. The new cross sections have also been used in a combined electroweak and QCD fit to significantly improve the light quark couplings to the Z-boson than those obtained based on the HERA-I data alone.

Keywords: Charged Current, Neutral Current, DIS, Deep Inelastic Scattering, high Q^2, QCD, polarization, electron, positron, protron, structure function, xF_3, electroweak, DESY, HERA, H1.